Quantum Transport in Strongly Correlated Systems

A Density Matrix Renormalization Group Study

Bohr, Dan; Jauho, Antti-Pekka

Publication date:
2007

Document Version
Publisher's PDF, also known as Version of record

Quantum Transport in Strongly Correlated Systems

A Density Matrix Renormalization Group Study

Ph.D. Thesis

Dan Bohr

August 2007

Department of Micro and Nanotechnology
Technical University of Denmark

Quantum Transport in Strongly Correlated Systems – A Density Matrix Renormalization Group Study

Ph.D. Thesis, Technical University of Denmark.

Department of Micro and Nanotechnology
Ørsteds Plads
Building 345east
Technical University of Denmark
DK-2800 Kgs. Lyngby
Denmark
E-mail: dab@mic.dtu.dk
Web: http://www.mic.dtu.dk/

Typeset in LaTeX 2_ε

Abstract

In the past decade there has been a trend towards studying ever smaller devices. Improved experimental techniques have made new experiments possible, one class of which is electron transport through molecules and artificially manufactured structures like quantum dots. In this type of systems screening plays a much less significant role than in bulk systems due to the reduced size of the objects, therefore making it necessary to consider the importance of correlations between electrons.

The work presented in this thesis deals with quantum transport through strongly correlated systems using the density matrix renormalization group (DMRG) method. We present two DMRG setups for calculating the linear conductance of strongly correlated nanostructures in the infinitesimal source-drain voltage regime. The first setup describes the leads by modified real-space tight-binding chains, whereas the second describes the leads in momentum-space. We benchmark each of these schemes against exact Greens function results for the conductance in the non-interacting limit, thus demonstrating the accuracy of the lead descriptions.

We first use the DMRG implementations to calculate the conductance of an interacting spinless resonant 7 site chain, studying the effect of repulsive interaction inside the chain. We demonstrate that both weak and strong interactions inside the chain lead to Coulomb blockade renormalization of the resonances in the conductance spectrum. Additionally the strongly interacting case sharpens the resonances significantly, such that strong interaction inside the chain tends to *suppress* the off-resonance transport.

Next we consider interacting resonant level models, studying the effect of repulsive interaction on the contact links. We demonstrate that even a small leak of the interaction in the system onto the contact links leads to a strong *enhancement* of the off-resonance transport, and further that this behavior is non-monotonic. By considering both a single level model and short interacting chains we demonstrate that the off-resonance transport enhancement is stronger than the corresponding suppression when having the interaction inside the chain, and conjecture that the enhancement by interacting contacts is universal. This result challenges the commonly used division between interacting transport region and non-interacting leads, and shows that care should be taken when making this partitioning, particularly

regarding the interaction.

Finally we consider a spintronics model known as the ferromagnetic Anderson model with an applied magnetic field. The model uses spin-polarized leads and the magnetic field is applied to the transport level at an angle with the direction of polarization. Thus both coherence and correlation effects are important in this model, and the methods applied should be able to handle both these effects rigorously. We present the DMRG setup for this model and benchmark against existing Greens function results for the model. Then we present initial DMRG results demonstrating the ability of the DMRG setup to provide accurate results for this model. We discuss the effects of the various parameters in the model, and finally compare perturbative results in the cotunneling regime with the DMRG results, and thereby quantitatively confirm the range of validity of the perturbative approach.

Dansk resume

I det seneste årti har der været en tendens til at studere stadigt mindre komponenter. Gennem forbedrede eksperimentelle teknikker er det blevet muligt at studere nye eksperimenter, hvoraf en type er elektron transport gennem molekyler og kunstigt fremstillede strukturer, såsom kvanteprikker. I denne type systemer spiller screening en meget mindre rolle end i makroskopiske systemer på grund af den betydeligt reducerede størrelse af disse objekter, således at det er nødvendigt at overveje vigtigheden af korrelationer mellem elektronerne.

I denne afhandling behandles emnet elektron transport gennem stærkt korrelerede systemer ved brug af metoden "the density matrix renormalization group" (DMRG). Vi præsenterer to setups for beregning af konduktansen af stærkt korrelerede nanostrukturer ved lineært påtrykt spænding. Det første setup anvender en real-rums repræsentation af elektroderne i form af tight-binding kæder, hvorimod det andet setup repræsenterer elektroderne i impuls-rummet. Vi tester nøjagtigheden af begge disse setups ved sammenligning med eksakte Greens funktion resultater for konduktansen i den ikke-vekselvirkende grænse, og demonstrerer derved nøjagtigheden af de anvendte elektrode beskrivelser.

Vi anvender først DMRG implementationerne til at beregne konduktansen for en spinløs 7 niveau kæde, og fokuserer på effekten af frastødende vekselvirkning inde i kæden. Vi viser at både svag og stærk vekselvirkning inde i kæden medfører en Coulomb blokade renormalisering af resonanserne i konduktans spektret. Derudover er resonanserne i det stærkt vekselvirkende tilfælde betydeligt skarpere end i det ikke-vekselvirkende tilfælde, således at stærk vekselvirkning inde i nanostrukturer *undertrykker* elektron transport når systemet ikke er præcis resonant.

Derefter behandles vekselvirkende korte resonante kæder, hvor vi fokuserer på betydningen af frastødende vekselvirkning på kontakterne. Vi viser at selv en lille spredning af vekselvirkningen fra systemet ind i kontakterne giver en stærk *forøgelse* af transporten når systemet ikke er præcis resonant, samt at denne afhængighed ikke er monoton. Vi behandler både enkelt niveau modeller samt korte resonante kæder, og viser derved at transport forøgelsen ved vekselvirkende kontakter er stærkere end den tilsvarende transport undertrykkelse ved et stærkt vekselvirkende system,

hvilket indikerer at transport forøgelsen ved vekselvirkende kontakter er universel. Mange teoretiske metoder anvender en principiel sondring mellem vekselvirkende transport region og ikke-vekselvirkende elektroder. Vores resultat viser at stor påpasselighed skal udvises når denne deling fastlægges, især med hensyn til vekselvirkninger.

Endeligt studerer vi en spintronik model kendt som den ferromagnetiske Anderson model med et påtrykt magnet felt. I denne model er elektroderne spin-polariserede og transport niveauet påvirkes af et magnetisk felt der er vinklet i forhold til spin-polariseringens retning. Såvel korrelationer som kohærens spiller en væsentlig rolle for denne model, således at teoretiske metoder anvendt på modellen skal kunne håndtere begge disse effekter korrekt. Vi præsenterer DMRG opsætningen for denne model, og tester denne mod eksisterende eksakte Greens funktion resultater i den ikke-vekselvirkende grænse. Derefter viser vi de første DMRG resultater og demonstrerer derved at opsætningen giver nøjagtige resultater for denne model. Dernæst diskuterer vi de forskellige parametre i modellen, og endeligt sammenligner vi DMRG resultaterne med perturbativ resultater i ko-tunnellerings grænsen, hvorigennem vi kvantitativt bekræfter gyldigheden af de perturbative resultater for modellen.

Foreword

The present thesis is submitted in candidacy for the Ph.D. degree at the Technical University of Denmark. It is the result of part of my work at the Department of Micro and Nanotechnology (MIC) in the period August 2004 to July 2007 under supervision of Professor Antti-Pekka Jauho.

It has been a personal challenge for me to carry out this project. My background is not within numerics, so engaging in a heavily numerical project using a method which nobody in the group at MIC was familiar with has been quite challenging. But after three years work I now have the pleasure to present the results of my work in this thesis.

In the beginning of my Ph.D. studies in August 2004 I was fortunate to meet Dr. Peter Schmitteckert on a DMRG conference in Leiden. I had brought a poster explaining my Ph.D. project about transport calculations using DMRG. During the poster session Peter came by and explained that he was working along the same lines and I could either come work with him in Karlsruhe, or he would do and publish all the things stated on my poster before me. Naturally this was a good offer in disguise, and I had no trouble accepting it. Thinking back on how things have evolved it was definitely a good choice, and as a consequence I have spent around 10 months in Karlsruhe throughout the past three years. It was always a pleasure to visit the Institut für Theorie der Kondensierten Materie (TKM) in Karlsruhe, both personally and professionally. I feel indebted to Peter for our collaboration during this project, and for always providing a good and personal atmosphere for my visits at the TKM. Karlsruhe has been a remarkable place for me to visit as a student with the constant flow of people and an almost endless series of interesting talks.

I would like to thank the people in the theory group at MIC, nobody mentioned – nobody forgotten, for the pleasant atmosphere at group meetings and social arrangements. It has been my pleasure to share an office with Christian Flindt most of the three years, and over the years I have had many interesting discussions both with him and with Thomas Frederiksen. It is with a feeling of ambivalence I see myself, friends, and fellow students, also from the undergraduate studies, scattered all over the world, and I hope we manage to stay in touch in the years to follow.

Acknowledgements

Significant parts of this project were carried out in close collaboration with Dr. Peter Schmitteckert at the Institut für Theorie der Kondensierten Materie (TKM), Universität Karlsruhe. The DMRG calculations carried out within my Ph.D. and presented in this thesis were all performed using the `NRG++` implementation of Dr. Schmitteckert, and carried out mainly on computers provided by him and the TKM. A large part of the calculations was performed on the XC4000 and XC6000 of the Scientific Supercomputing Center (SSC) Karlsruhe on a grant received by Dr. Schmitteckert. I would like to thank Peter for all the effort he put into this project in general, and for the many useful comments and suggestions to the manuscript for this thesis in particular.

I would also like to thank Dr. Tomáš Novotný (Prague, Czech Republic) for his support and effort in getting the FAB project running. Ph.D. student Jonas Nyvold Pedersen (Lund, Sweden) deserves acknowledgement for his significant contribution to my understanding of the FAB model, and willingness to answer the large amount of questions from my side. He also provided the Greens function and cotunneling results which I have compared my DMRG results for the FAB model to, and helped proof read the chapter on the FAB model.

The close collaboration with Peter Schmitteckert in Karlsruhe would not have been possible without a substantial financial support from my institute, the Department of Micro and Nanotechnology, at the Technical University of Denmark, enabling me to travel and to partake in relevant conferences.

This project was supported financially also by the European Commission under the HPC-EUROPA program, project RII3-CT-2003-506079, through a 10 weeks visit at the TKM in Karlsruhe, including calculational time on the HLRS in Stuttgart. In particular the IRLM project and the FAB project benefitted from this support.

A special thanks goes to Verena Körting for her tireless effort in proof reading the manuscript that eventually turned into this thesis. She also deserves thanks for her general support in the times when I needed it, in particular during the hectic last months of the project.

Finally I would like to thank my supervisor Professor Antti-Pekka Jauho for introducing me to this interesting computational method and giving me the opportunity to carry out my Ph.D. work in his group for the past three years.

ooOoo

Kgs. Lyngby
July 31, 2007 Dan Bohr

Contents

List of Figures

List of Tables

List of Symbols

List of the most commonly used symbols and their meanings. Deviations from this list are explained locally in the text.

Hamiltonian

σ	Spin index, $\sigma = \{\uparrow, \downarrow\}$
$\vec{\tau}$	Vector of Pauli matrices
P, P_ℓ	Spin polarization of the lead ℓ
H_0	Interacting Hamiltonian without *voltage* perturbation
δH	Voltage perturbation, $\delta H = \frac{-eV_{\mathrm{SD}}}{2}(N_L - N_R)$
E_0	Ground state energy of H_0
N_ℓ	Density operator of lead ℓ
$\mid \psi\rangle$	State vector of the state ψ
$\mid \psi_0\rangle$	Ground state of the Hamiltonian H_0
V	Nearest neighbor density-density interaction
γ	Leaking of the interaction onto the contact links
t	Nearest neighbor hopping matrix elements
$t_{L/R}$	Hopping matrix element coupling the nanostructure to the left/right lead
t'	Notation used when $t_L = t_R \equiv t'$
t_D	Hopping matrix element within the nanostructure ('Dot')
U	Onsite Hubbard interaction between the spin species
ε_d	Bare energy level for the nanostructure
μ_g	Gate potential for the nanostructure

ω	Frequency, fourier transform of time
$\vec{B}$	Magnetic field of strength $B =\mid \vec{B} \mid$

General abbreviations and concepts

`NRG++`	DMRG implementation used in this work
DMRG	Density matrix renormalization group, Chap. 2.2
ED	Exact diagonalization, Chap. 2.6
GF	Greens function, Chap. 2.5
IRLM	Interacting resonant level model, Chap. 3.2
FAB	Ferromagnetic Anderson model with an applied magnetic field, Chap. 4.1
$\mathrm{Re}\,[A]$	Real part of A
$\mathrm{Im}\,[A]$	Imaginary part of A
$\mathrm{Tr}\,[A]$	Trace of the matrix A

General parameters

ε_F	Fermi energy
μ_0	Fitted Lorentzians located at gate potential $\mu = \mu_0$
ρ	Reduced density matrix for the system block
η	Finite size broadening parameter
M_S	Number of sites in the nanostructure
M_L	Number of sites in the leads
M	Total number of lead and system sites
$g_{J_\ell J_{\ell'}}$	Conductance calculated from the current-current correlator
$g_{J_\ell N}$	Conductance calculated from the current-density correlator
J_ℓ	Particle current operator at link ℓ
V_{SD}	Source-drain voltage
I	Electric current
w	Fitted Lorentzians have half width w at half maximum

$L_A(w, \mu_0)$	Area normalized Lorentzian: $L_A(w, \mu_0) = \frac{1}{\pi} \frac{w}{(\mu-\mu_0)^2+w^2}$
$L_H(w, \mu_0)$	Height normalized Lorentzian: $L_H(w, \mu_0) = \frac{1}{1+\frac{(\mu-\mu_0)^2}{w^2}}$

Constants

h	Planck's constant
$\hbar$	Planck's constant divided by 2π
e	Charge of the electron
m	Mass of the electron

Greens functions

$G^r_{i,j}$	Retarded single particle Greens function
$G^a_{i,j}$	Advanced single particle Greens function
A_σ	Spectral function for spin σ
$G^<_{i,j}$	Lesser single particle Greens function
$G^>_{i,j}$	Greater single particle Greens function
$\mathbf{\Gamma}_{L/R}$	Broadening matrix due to the left/right leads

Real-space

DBC	Damped boundary conditions
d	Damping factor defining the exponential damping
M_D	Number of damped sites

Momentum-space

M_{Add}	Number of lead sites represented in real-space
M_E	Total number of real-space sites
M_{L_0}	Number of logarithmically discretized states in the momentum-space lead
Λ	Factor defining the logarithmic discretization
M_{L_1}	Number of linearly discretized states on the low-energy scale in the momentum-space lead
t_k	Discretization dependent hopping matrix element coupling real- and momentum-space parts

$L(k)$	Level distribution function, $-\frac{D}{2} < k < \frac{D}{2}$ for the linear band and $0 < k < \pi$ for the cosine-band
D	Band cutoff in the momentum-space lead, $-D < \varepsilon < D$

Chapter 1

Introduction

1.1 History

Curiosity is one of mankind's most powerful properties. It has lead us to the search for explanations and connections in the surrounding world leading to an ever increasing level of understanding of the world around us. From the more basic understanding of the macroscopic world this quest for understanding has evolved into modern science, one branch of which is physics.

It is hard to define a sharp starting point for the solid state branch of physics, but one threshold would be the early models of solids by Ernest Rutherford [1]. Since then the field of solid state physics has evolved over the successful atomic model due to Niels Bohr and to the complete understanding of the periodic table of the elements and a thorough understanding of bulk materials in terms of electrical and mechanical properties.

For many years the theoretical models used in the description of electronic matter were mathematically simple, the primary reason being the neglect of electronic interaction effects. The theories by Drude and Sommerfeld [2] are examples of such models, considering non-interacting particles in a constant potential. Despite their simplicity these models are capable of explaining a variety of phenomena in solids – a success that can be traced to the existence of screening that effectively limits the interaction between particles [2].

Despite the success of these simple models they far from cover all observed phenomena. For instance the different electric behaviors of metals and semiconductors are not described by these models, and until the formulation of Bloch's theory of electron waves in lattices in 1928 [3], introducing the concept of bandstructures, these questions remained unanswered.

However successful the theory of the non-interacting electron gas is, there are phenomena not describable from this starting point. One prominent example studied extensively in the solid state community since the 1950's is superconductivity. This phenomenon, that below a certain temperature the resistance of certain materials drops to zero, was discovered accidentally by the group of Kamerlingh Onnes in 1911. Much effort was put into developing an understanding of this phenomenon which in the end lead to the formulation of the Bardeen-Cooper-Schrieffer (BCS) theory of conventional superconductors in 1957 [4]. Interestingly the BCS theory is a weakly interacting theory that does not rely on the strong Coulomb repulsion between the electrons, but rather on interaction with the lattice. The lesson learned from this field was that despite the success of the non-interacting electron gas there exist phenomena, like superconductivity, that cannot be described using this limit as a starting point, and where new ideas are needed.

Based on the understanding of metals and semiconductors a whole industry eventually grew out of condensed matter physics. Historically the technological development within the semiconductor industry has progressed almost exponentially, as predicted in 1965 by co-founder of Intel Corporation

Gordon E. Moore and therefore often referred to as Moore's law [5]. This advance has been related to a miniaturization of the individual electronic components, an approach that has been very successful historically.

Within basic science a similar miniaturization trend has been observed. A fundamental question to ask is what happens when a current is passed through some device, which could be a molecule, an engineered structure, or something else. As experimental techniques improved ever smaller such devices were considered, and attempts to treat these systems theoretically using existing models eventually failed. The explanation of this failure is two fold: (1) The devices become quantized as the quantum regime is reached, and (2) screening is reduced due to the reduced density of electrons [2]. Without screening electrons interact through the full long range Coulomb interaction leading to much stronger correlation between the electrons. A simple example is the quantum dot in the Coulomb blockade regime, where the transport through the dot depends on the actual, rather than the average, charge on the dot. Thus small devices are potentially both quantized and correlated, such that many interesting quantum phenomena may occur in these setups.

This emerging field initially denoted by mesoscopic physics eventually developed into nanoscopics and molecular electronics. As of present much attention is being devoted to transport through real molecules, for example the buckyball C_{60} [6, 7] and benzene [8, 9]. At the academic level such devices are interesting due to the physics involved and at the technological level they are interesting as candidates for the building blocks of future electronics.

Theoretically and mathematically the area of transport in quantum systems is difficult for several reasons. The quantum nature of these systems makes an exact numerical description unfeasible due to the exponentially large Hilbert space. On the other hand the possibility for reduced screening may make the mathematically simple approximations such as mean-field theory insufficient as the few particle nature of these devices (as opposed to thermodynamically many) require a correct treatment of interaction and correlation effects between the electrons. Or in other words a more rigorous quantum mechanical treatment may be required.

In a transport setup a further complication is added in the form of non-equilibrium conditions. Whereas equilibrium quantum mechanics is a well established field there are still many open questions in non-equilibrium transport. An essential difference between the two is the distribution of states; where equilibrium uses the Boltzmann thermal weight it is not a priori obvious what distribution to use in non-equilibrium. Also the tools applicable are very different; where the variational principle has been very successful for equilibrium situations, such an approach cannot easily be generalized to non-equilibrium. For instance in a transport setup this is illustrated by the fact that energy is gained by moving particles between the reservoirs.

Many different schemes to treat electronic transport have been suggested and it is not yet clear how these different approaches are connected, or if they indeed agree in the relevant limits. Combining further interaction effects and non-equilibrium transport leads to a physical regime where little knowledge is well established and much work is still to be done.

In Chap. 2 we discuss briefly some of the alternative approaches to the kind of systems studied here, in particular perturbative methods, the flow equation method, the functional renormalization group method, embedding methods, numerical renormalization group based methods, quantum Monte-Carlo based calculations, and density functional theory based methods.

1.2 The density matrix renormalization group

The idea of renormalization in solid state physics can be traced back to Kadanoff in the 60's [10] who employed a blocking procedure for spin clusters to formulate scaling relations for critical exponents. Although not really rigorous Kadanoff's spin blocking provides a very nice picture of the idea of renormalization procedures – to reduce the number of degrees of freedom without changing the mechanisms of the model but at the cost of changed coupling constants. Iterating the blocking scheme one hopes to eventually end up with a model that represents the physics of the original model but with a manageable number of degrees of freedom. In other words some degrees of freedom have been truncated to yield a more feasible model describing the same physics.

One very successful implementation of renormalization is Wilson's Numerical Renormalization Group, NRG [11, 12]. Probably NRG is most famous for solving the Kondo model but over the years much effort has been put into expanding the applicability of NRG to new problems and properties, for instance the calculation of transport phenomena [13]. The NRG uses a blocking scheme in momentum-space, adding well separated energy shells to the system, and selects the states to keep by energy.

If one considers a real-space blocking scheme rather than the momentum-space blocking of NRG and uses the NRG state selection by energy, the procedure fails. Analyzing the problem related to the joining of two real-space blocks leads to the conclusion that the hard wall boundary conditions in combination with the NRG state are closely related to the failure. The NRG state selection uses the lowest energy eigenstates to represent the physics at small energy-scales – wavefunctions of which *all* have nodes at the hard wall boundary. Thus joining the wavefunctions of two real-space blocks in an attempt to form the ground state wavefunction of the joined block yields the inherently erroneous feature of a node in the joined wavefunction – illustrating the problem of using state selection by energy in the real-space blocking.

An analysis like this lead Stephen R. White to the conclusion that another setup was needed for the real-space blocking. Some of the boundary problems can be remedied by using (a combination of) different boundary conditions but the underlying problem that the low-energy wavefunctions of subblocks do not constitute good building blocks for the (low-energy) wavefunction of the joined block remains [14]. Inspired by his attempts to resolve these issues by different boundary conditions White realized that a *superblock* configuration would remedy the problem, and eventually he formulated the density matrix renormalization group (DMRG) method [15, 16], originally published in 1992. The general idea is to consider a system in the presence of an environment rather than considering an isolated system – or in terms of blocks to consider a superblock consisting of a system and an environment block. As we show in App. A the projection onto the system block in the superblock setup turned out to be equivalent to a singular value decomposition of the wavefunction, which can be given an interpretation in terms of the probability of a given eigenstate of the reduced density matrix for the system in the presence of the environment. Thus the DMRG states are the most probable eigenstates of the reduced density matrix and White denoted this new scheme the density matrix renormalization group method, although strictly speaking the transformations employed by the DMRG method do not form a mathematical group.

In its original formulation DMRG is an iterative scheme seeking an optimally projected Hilbert space. Originally it is formulated as a ground state method in the sense that it optimizes the description of expectation values in the ground state, or at least a few states, and DMRG can be viewed as an iterative variational optimization for these quantities.

DMRG has received much attention in later years due to its capability to handle strong correlations. Substantial effort has been put into expanding the capabilities of the method to calculate dynamical properties [17, 18, 19], extensions to two-dimensional systems [20, 21, 22], and real-time evolution of systems [23, 24, 25], and today DMRG constitutes a very powerful numerical technique applicable in a wide range of situations.

1.3 Outline

This work is aimed at studying the effect on transport properties of interaction, particularly the limit of strong interaction. This work is limited to the linear response regime for the applied source-drain voltage. However, it is based on *direct* calculations of transport properties and does *not* rely on extracting non-equilibrium properties from equilibrium quantities. Thus all results presented in this work are approximation-free to the degree that finite system numerics can describe transport properties and to the truncation error implicit in the density matrix renormalization method used.

The philosophy is to consider simplified models incorporating the essential physical elements, correlations and coherence, and through the study of these models gain an understanding of the physics of such systems. Current experiments do allow the study of one-dimensional systems [26] such that despite their simplicity the models studied theoretically here may provide insight into the transport properties of experimentally studied systems.

The outline of the thesis is as follows: In Chap. 2 we present the theory behind this work. We introduce the transport setup in Chap. 2.1, and motivate the use of the DMRG method in this work. The DMRG itself is introduced in Chap. 2.2, in particular the correction vector method is considered. In Chap. 2.3 we review the two representations of the leads used in this work, in real- and momentum-space, and discuss the strengths and weaknesses of the two approaches. In particular the formulation of a momentum-space representation for the leads is discussed in detail.

The work here has been centered on the linear response approach for the source-drain voltage and in Chap. 2.4 we derive the general Kubo formula, and discuss the resolvent formulations of the Kubo formula for conductance. In Chap. 2.5 we proceed and derive resolvent formulations for the single particle Greens functions. A few details regarding the discretization are discussed, and finally the conductance evaluation from the spectral function is derived.

When developing new calculational schemes it is essential to benchmark these against well established results. In Chap. 2.6 two different benchmarking schemes are discussed, the exact diagonalization used to benchmark the DMRG truncation, and the Greens function method used to benchmark the finite size effects. Furthermore the exact diagonalization scheme aids in fast determinations of free parameters of the model, as discussed in Chaps. 3 and 4.

Proceeding to the physics part of the thesis we first consider spinless models in Chap. 3. This part of the thesis is divided into two subparts: The first deals with a resonant 7 site chain, and considers the effect of interaction mainly inside the transport region. Using the real-space setup we show that a strong repulsive interaction inside the transport region suppresses the off-resonance transport, and provide a simple picture for the Coulomb blockade renormalization of the resonances. Finally by recalculating some of the results using the momentum-space setup we demonstrate the improved energy resolution of the momentum-space setup compared to the real-space setup.

The second part deals with short resonant chains and investigates the effect of interaction on the contact links. For the resonant 7 site chain it is shown that strong interaction inside the chain leads to a suppression of the off-resonance transport. In this part we show that spreading the interaction onto the contact links leads to a significant and non-monotonic enhancement of the off-resonance transport. By considering chains of one,

three, and five sites we demonstrate that this enhancement is stable, such that even a small 'leak' of the interaction onto the contacts influences the transport strongly, and conjecture that this feature is universal. This in turn challenges the common distinction between interacting transport region and non-interacting leads, and shows that care should be taken when making this division, particularly regarding the interaction.

In Chap. 4 we consider a spintronics model known as the ferromagnetic Anderson model with an applied magnetic field. This model exhibits both coherence and correlation effects and is hence a challenge to treat theoretically. A different approach was taken to calculate the transport properties of this model, using the Meir-Wingreen formula, rather than the direct evaluation of the Kubo formula. We present the DMRG scheme for calculating the spectral function, and further the conductance from the spectral function using the Meir-Wingreen formula [27].

The model itself is presented in Chap. 4.1.1, and transcribed to a tight-binding description in Chap. 4.1.2. In Chap. 4.1.3 and 4.1.4 we review the implementation of the polarization and the DMRG setup for the model. In Chap. 4.1.5 we present analytical results provided by Ph.D. student Jonas N. Pedersen (Lund, Sweden) which are used to benchmark and compare to the DMRG calculations. In Chap. 4.1.6 we benchmark the setup against these results in the non-interacting limit. Having verified the description of the leads we proceed and present DMRG calculations for a range of parameters and discuss the effects of the different parameters in the model. In Chap. 4.1.7 we compare perturbative cotunneling results provided by Ph.D. student Jonas N. Pedersen to the DMRG results and confirm the range of validity of the perturbation theory.

In Chap. 5 we conclude the thesis by a summary of the main results presented, and a short discussion of the open ends and possible extensions to the presented work. Finally in Apps. A-D we provide detailed derivations and implementation details. In App. A we discuss the DMRG state selection and algorithms. App. B contains the derivation of the resolvent formulations used throughout this work. In App. C we discuss the Greens function calculation in the non-interacting limit of the spinless resonant chains considered in Chap. 3, and in App. D we discuss a few implementation details and the hardware used during this project.

Chapter 2

Theory

In this chapter we review the calculational scheme and techniques developed and used in this work. First we introduce the transport setup and discuss the conductance which we consider throughout this work. We mention briefly some other methods applicable to the kind of systems considered in this work and discuss strengths and limitations. Then we introduce the numerical method used in this work, the density matrix renormalization group (DMRG) method, and discuss particular aspects used in this context. We then derive the Kubo formula for conductance and the resolvent form of the single particle Greens functions, and discuss their evaluation using the DMRG. Finally we illustrate the benchmarks used for the developed DMRG setup, in terms of exact diagonalization and Greens functions, both in the non-interacting limit.

2.1 Introduction to transport

In this chapter we introduce the transport setup that all work presented in this thesis revolves around. We discuss the physical mechanism behind the steady state transport, and the measure used in quantifying the transport.

In a transport setup the device is connected to a current or voltage source that applies a source-drain voltage V_{SD} across the device, and drives a current I through it, as illustrated in Fig. 2.1. When the dimensions of the device become sufficiently small the quantum nature of the device manifests itself, such that the device is considered a finite system with quantized energy levels. Typically a gate potential μ_g is applied to the device that shifts these

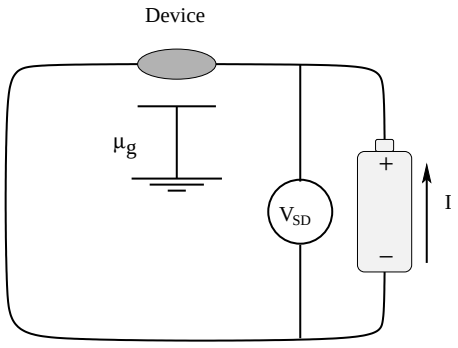

Figure 2.1: Generic two-terminal transport setup, where a source-drain voltage V_{SD} is applied across, and an electric current I is driven through the device. To the device is applied a gate potential μ_g which can shift the energy levels in the device up and down, depending on the sign of the potential.

discrete energy levels up and down in energy, depending on the sign of the applied potential.

We specialize further to the zero temperature limit $T = 0$. The low density of electrons in the device reduces the screening and makes it necessary

to consider the importance of correlations. By contrast the leads are usually macroscopic and it is common to treat them as non-interacting, and since the combined lead and current (or voltage) supply is a much larger system than the device it is usually assumed that the leads are continuous and structureless reservoirs of particles in local equilibrium. The coupling of the leads to the device is modeled by a hopping process in the quantum mechanical model of the setup, as will be explained in Chap. 2.3, and we consider steady state situations such that there are no displacement currents, and only tunneling currents are present.

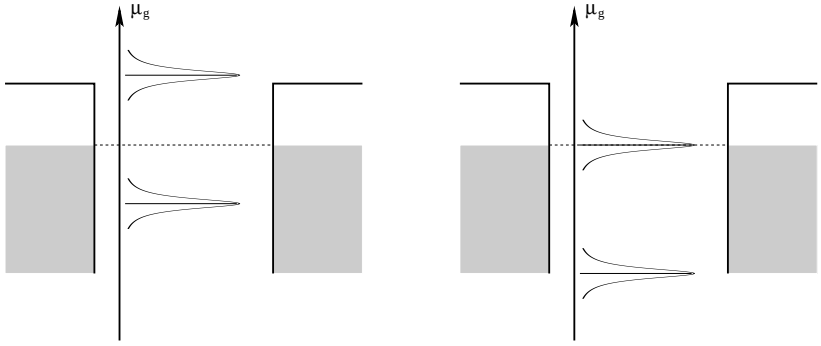

(a) When no levels are close to being on-resonance the electron transport mediated by the device is suppressed.

(b) Applying a gate potential that tunes a level on-resonance opens up transport through that level.

Figure 2.2: Schematic illustration of the transport mechanism; having all levels off-resonance suppresses transport, while having a level nearly on-resonance opens transport through that level. A gate potential applied to the device shifts the levels in the device, such that a full scan of the gate potential yields a series of peaks in the current. Notice that the levels illustrated in the figure need not be single particle levels, but can be many particle levels. The figure indicates that the levels acquire a width when coupled to the leads.

In the weak coupling limit the energy levels acquire only a modest width from the broadening by the leads, and the transport mechanism can be illustrated as follows: The direct tunneling between the leads is exponentially suppressed by the distance between the electrodes and the device is needed to mediate the electron transfer. From energy conservation arguments only the electrons inside the bias window partakes in the transport, such that for infinitesimal source-drain voltages, as considered in this thesis, the transport takes place at the Fermi edge. Hence if all levels in the device are far away from the Fermi edge, as illustrated in Fig. 2.2(a), transport is suppressed and no current flows. Applying now a gate potential to the device such that a single level is on-resonance, as illustrated in Fig. 2.2(b), transport is allowed and a current flows. Since the levels inside the device acquire a finite width due to the coupling to the leads, the level need not be precisely

resonant to allow transport, such that shifting a level into resonance by the gate potential yields a smooth transition from a low current to a high current situation. Keeping the source-drain voltage fixed a full scan of the gate potential is hence expected to reveal a series of smooth peaks in the current, a maximum occurring each time a level is tuned exactly on-resonance, and a valley when all levels are off-resonance. Another measure than the current, used in describing the transport is the conductance, either the linear- or the differential conductance, defined respectively as

$$g_{\text{lin}} = \frac{I(V_{\text{SD}})}{V_{\text{SD}}}, \tag{2.1a}$$

$$g_{\text{diff}} = \frac{\partial I(V_{\text{SD}})}{\partial V_{\text{SD}}}. \tag{2.1b}$$

The challenge considered in this work is the non-perturbative quantum mechanical treatment of transport through strongly correlated systems. This task contains two different complications, the transport, or non-equilibrium, and the correlations. Each of those is a complicated topic in itself, and no methods are well established as providing general insight into transport setups where both coherence and correlations are significant.

In this work we relax the first complication a bit, and consider linear response in the source-drain voltage $V_{\text{SD}} \to 0$, such that the transport takes place only at the Fermi edge. In this limit the linear and differential conductances are identical, and henceforth referred to simply as the conductance. A similar behavior as for the current itself is found for the conductance, such that having a level of the device on-resonance with the leads allows transport and hence gives a high conductance, while having all levels in the device off-resonance with the leads results in a low conductance. When the system is fully transparent the conductance is maximal and has the value of a conductance quantum, e^2/h, per channel.

2.1.1 Alternative methods

We would like to briefly mention a few other applicable methods for the kind of systems we consider in this work. The calculation of conductance for strongly correlated systems has two different challenges, the interaction and the applied source-drain voltage. The following list is not intended to be complete, rather to mention some alternative methods.

Perturbation theory

When approaching a complicated system perturbation theory may be useful. The key idea is to include increasing orders of some perturbation to a known state, providing an increasingly more accurate description. For the conductance there exists a number of approaches from which we mention

two prominent examples important in this work. (1) The linear response (Kubo) formula [28], and (2) the Keldysh theory [29, 30, 27].

(1) The Kubo formula provides an exact result for the first order correction in some perturbation. The use of the Kubo formula in this work is for the response of the current to linear order in the applied source-drain voltage. The advantage of the Kubo formula in this connection is that no assumptions are made regarding the unperturbed system, only a suitable method is needed to treat the ground state of this system, such that e.g. all correlation effects can be kept exactly within this setup, leading to a principally exact method.

(2) The Keldysh theory is a powerful tool for finite temperatures and voltages. While formally exact the Keldysh results in practice often involve two different perturbative expansions, in the Coulomb interaction *and* in the coupling of the transport region and leads. Thus even calculating the ground state of the unbiased and interacting system involves a perturbative expansion, on top of which the complication of a voltage perturbation should be added.

Higher order resummation schemes in turn lead to the renormalization group (RG) methods, where the leading order contributions are taken into account, either numerically or analytically.

Flow equation method

Analytical renormalization group methods that include an energy dependence should be mentioned in this connection because they are applicable to large voltage situations in transport setups, and an example is the flow equation method.

The flow equation method [31] consists of a series of infinitesimal unitary transformations to make the Hamiltonian successively more energy diagonal, leading eventually to a diagonal effective Hamiltonian. Thus the method retains information on all energy scales, which makes it well suited for finite bias transport calculations. An obvious advantage of the flow equation method is that knowledge of the energy eigenvalues of the Hamiltonian provides *exact* time evolution, and hence long-time behavior can be studied.

The flow equation approach is in principal exact, but in practical calculations the perturbative expansion of the generator for the diagonalization transformation is truncated. Thus the method is perturbative in the interaction and in practice it works well when the systems are not too strongly correlated.

Functional renormalization group

In the functional renormalization group [32] the starting point is an exact hierarchy of RG equations, that in principal facilitates approximation free

calculations. However in practical applications this hierarchy is truncated, often at the second order correction for the interaction vertex [33].

Contrary to the flow equation method the functional RG problem for finite bias transport situations has not yet been solved. Furthermore due to the truncation the functional RG is in practice perturbative in the interaction.

Embedding methods

Another class of approaches to steady state transport with infinitesimal source-drain voltage are the embedding methods suggested in Refs. [35, 36], where the system through which transport is studied is embedded in a large lead, and the combined system is closed to a ring. Passing a flux through the ring one can calculate the flux dependent ground state energy, and from this the current in the ring and the transmission amplitudes [37]. Finally by using the Landauer formula [38, 27] the linear conductance of the system can be calculated. Only single channel physics in the linear source-drain voltage regime can be treated within this method, and the applicability of the method depends on the ground state calculation. Refs. [39, 40, 41] use the DMRG to evaluate the ground state, resulting in an overall method that is able to handle correlated systems. Since an essential step in the conductance calculation is a scaling to large lead sizes the method is expensive when using direct numerical methods like DMRG, which limits the system sizes that can be treated.

A different kind of embedding method was used in Refs. [42, 43], where an exact diagonalization of an extended molecule, consisting of the transport region and part of the leads, is combined with a perturbative coupling of the remaining parts of the leads represented by appropriate self-energies. The overall method is thus perturbative, and only provides reliable results when the correlation cloud is kept within the extended molecule that is treated exactly.

Numerical renormalization group

There are several approaches to the conductance using NRG. However, all NRG based calculations are limited by the logarithmical discretization, and cannot use more general discretization schemes since the NRG relies on a clear separation of energy scales. While well suited for Fermi edge physics the logarithmic discretization is not well suited for calculations away from the Fermi edge where the logarithmic discretization is inherently coarse-grained. For more complicated setups, for example resolving the finite frequency spectral function, a flexible discretization scheme is needed, such that the discretization can be tailored to the problem at hand.

One approach to the conductance is to extract phaseshifts from the NRG

[44, 45, 46, 47] and evaluate the conductance from this [48]. The extraction of phase shifts is, however, limited to a completely symmetric setup.

Another approach using the NRG is to evaluate the spectral functions [49] and use the Meir-Wingreen formula [27] to evaluate the conductance. This approach is thus limited to systems having proportional coupling to the leads.

Quantum Monte-Carlo

Considering the linear source-drain voltage transport regime, the Kubo formula for conductance applies, and various methods can be used to evaluate it. Using the quantum Monte-Carlo method to evaluate the linear response result yields a principally approximation free method. In Ref. [50] quantum Monte-Carlo simulations were used to evaluate a linear response correlator similar to the ones used in this work. The calculation was performed for a bosonic system obtained by a Jordan-Wigner transformation of the original one-dimensional fermionic model. The Monte-Carlo calculations were performed for imaginary frequencies, and followed by an extrapolation to zero frequency to get the DC conductance. The Monte-Carlo calculations rely on a finite but low temperature. This in turn limits the size of the interacting system for which a reliable zero frequency extrapolation of the conductance can be performed since smaller frequencies, and hence smaller temperatures, are needed.

Density functional theory

We also mention the density functional theory (DFT) [51, 52], although the limit considered in this work is quite different from the limit considered in DFT based calculations.

In DFT it is used that there is an exact connection between the electron density and the ground state of a given system, such that a variational search for the density in principle leads to a variational determination of the ground state. By mapping the physical problem onto an effective non-interacting problem (the Kohn-Sham system) the wavefunction, and hence the density can be found. In practise this involves a self-consistency between the interacting electron density and the non-interacting Kohn-Sham Hamiltonian. This scheme is in principle exact, but the functional linking the ground state density and the ground state energy is not exactly known, in particular the exchange-correlation functional is unknown. Thus approximations for this functional are used, leading to an overall approximate theory.

The strength of ground state DFT is that it is an *ab initio* approach, where only very fundamental parameters are used as input, such that everything else is determined by the calculation itself. DFT has been very successful for electronic structure calculations on large samples, where geometrical

relaxation of a structure can be used to calculate e.g. crystal structures or phonon modes [53].

In practice DFT is only applicable in the absence of strong correlations, since the interaction is often treated at the mean-field level within the local density approximation (LDA). Recently the exact functionals for the DFT on a lattice have been calculated using DMRG [54], in order to investigate whether the ground state DFT is sufficient to describe linear transport from a Kubo formula for the Kohn-Sham particles.

This work

In this work we focus on linear response in the applied source-drain voltage, which implies focusing on physics taking place at the Fermi edge of the leads. The linear response in source-drain voltage limits the scope of the method, such that high-bias situations are not described by this setup. On the other hand we devise a non-perturbative direct calculational method capable of treating both correlations and coherence rigorously. To this end we use the density matrix renormalization group (DMRG) method, and combine it with either a linear response (Kubo) approach in source-drain voltage, or an evaluation of the single particle Greens functions. Using the Meir-Wingreen formula [27] the conductance in the linear source-drain voltage limit can be calculated from the zero frequency spectral function.

The developed scheme benefits from a high degree of freedom in choosing the discretization. For our purpose of linear response conductance it turns out to be crucial to have a *linear* discretization on the low-energy scale close to the Fermi edge, as is discussed in Chap. 2.4.3. Thus this method is applicable in some situations where the methods above are not since we treat both correlations and coherence non-perturbatively, and likewise inapplicable in some situations where the same methods above do apply, the most obvious limitation being the DC linear response in the applied source-drain voltage. Further, since the DMRG approach is non-perturbative, this method provides a unified description of the weakly and strongly interacting, as well as the weakly and strongly coupled limits.

In the next sections we review the different parts of this method, in particular the DMRG method, and the Kubo formula for linear response in general and for conductance in particular. Finally we consider the evaluation of the single particle Greens functions using the DMRG setup. From the Greens functions eg. the conductance can be evaluated using the Meir-Wingreen formula, and we discuss this method briefly.

2.2 The density matrix renormalization group

Theoretical calculations on quantum mechanical models often involve some level of approximation. The reason for this is found when attempting exact

numerical calculations, as the Hilbert space of quantum models grows exponentially with the size of the system considered. Hence exact calculations soon face the problem that the Hilbert space becomes larger than what is feasible for the purpose at hand or even possible on the computers available. In many situations it is intuitively clear that not all information contained in the full description is relevant in certain limits, and hence a truncation is necessary as well as possible.

The density matrix renormalization group (DMRG) method is one choice of a truncation scheme applicable to quasi-one-dimensional systems. In the original formulation by White [15, 16] the DMRG is an iterative scheme seeking an optimally projected Hilbert space for ground state properties. The source of inspiration for White was the failure of a real-space blocking scheme when using a state selection by energy [14]. He traced this failure to the hard-wall boundary conditions of the isolated real-space blocks, and eventually formulated a real-space blocking scheme by adding an environment to the system. For this blocking scheme he showed that the optimal states to keep for the *system* are the most probable eigenstates of the reduced density matrix – leading to the name density matrix renormalization group.

The work presented in this thesis uses the DMRG extensively. In this part we first present some terminology and basic concepts, and then proceed to review the two different implementations used in this work. In App. A we derive the state selection used in DMRG, and discuss the two algorithms. For further details on DMRG we refer to the original papers by White, Refs. [15, 16], or one of the many reviews of the method, for instance Refs. [14, 55, 56, 57, 58].

Figure 2.3: General superblock configuration, consisting of a system and an environment. The optimal states to keep for the system are the most probable eigenstates of the reduced density matrix, found by tracing out the environment degrees of freedom.

2.2.1 Basic concepts

In the original formulation DMRG is an iterative method for optimizing the basis to describe certain properties on a decimated Hilbert space. Since then the method has been expanded to target many different physical setups and situations, among others the description of finite frequency properties [17] and also time evolution has been treated using DMRG [23, 24, 25]. In this work we use the correction vector DMRG [59, 18, 19] to evaluate resolvent equations, as will be explained in Chap. 2.2.3. In order to clarify the ex-

planation of the method presented in this chapter we start by introducing some basic concepts and terminology used in the DMRG community and throughout this chapter.

The DMRG seeks an optimally projected Hilbert space by iteratively calculating the optimal basis states for the system using the reduced density matrix. The states used in the construction of the reduced density matrix are denoted *target* states. Multiple states can be targeted simultaneously and a faithful description can only be expected for the target states. In general adding more target states to the reduced density matrix reduces the accuracy for a fixed number of DMRG states kept in the truncation. The number of states that successfully can be put into the density matrix is limited, and DMRG is thus often referred to as a few state method. One consequence is that the description of finite temperatures is possible, but only in the low temperature limit where a few states in the Boltzmann distribution suffices. In this work we only consider the strict zero temperature limit.

The basic DMRG setup is a *superblock* consisting of a *system* block and an *environment* block, as seen in Fig. 2.3. The essential ingredients of the DMRG scheme are the enlargement of one of the blocks, and the truncation back to a given number of states for this block. A DMRG step thus consists of adding to the system block (typically) a single site and then truncating back to a given basis size. The selection mechanism for the truncation is the magnitude of the eigenvalues of the reduced density matrix ρ for the *system*, found by tracing out the environment degrees of freedom, and the kept states can be given a probabilistic interpretation since ρ is trace normalized. The reduced density matrix represents the system in the presence of a bath that has been traced out, and hence mimics the coupling to a bath.

2.2.2 Algorithms

Using this truncation procedure in a systematic way leads to the essential DMRG algorithms denoted the infinite and finite lattice algorithm. In the infinite system algorithm the superblock is enlarged in each step, whereas the finite system algorithm keeps the size of the superblock fixed. The finite lattice algorithm consists of a number of sweeps where the role of system and environment is reversed after each such sweep, and where the division between the system and environment is shifted a single site at each step in the sweep, as illustrated in Fig. 2.4. In this fashion the DMRG iteratively optimizes the description of the target states used in the construction of the reduced density matrix. For a more elaborate review of the DMRG truncation, state selection, and algorithms we refer to App. A.

Typically one truncates to a fixed number of states per block but this is just one possible choice. Another choice is to keep the size of the *target space* fixed, that is the subspace of the full Hilbert space of the superblock within which the target state is calculated. These two schemes differ in

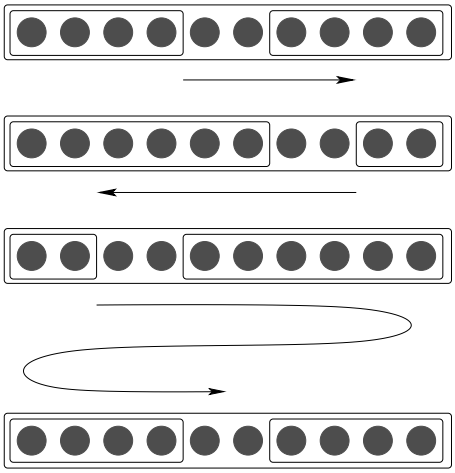

Figure 2.4: Illustration of the finite lattice DMRG algorithm. Each step in the algorithm moves the point of division between the system- and environment blocks by one site, and truncates the Hilbert space of the system block to the desired size. When the end of the superblock is reached the role of system and environment is reversed. The sweeping is usually continued until convergence has been reached.

the strongly asymmetric superblock configuration, where one block is much larger than the other. Consider for instance a situation where one block, denoted A, is very small and the remaining part of the superblock, denoted B, is large. Then also the corresponding particle numbers of the two blocks are very different, $N_A \ll N_B$. To target a subspace of the full Hilbert space of a fixed particle number, $N = N_A + N_B$, the subspace of block B used in the construction of the target space must be enlarged to cover larger particle numbers N_B in order to 'compensate' for the small N_A, compared to the case where the blocks are of more equal size. This illustrates the difference in the two truncation schemes.

Whenever truncations are made it is relevant to ask what is the importance of the part that is discarded, or equivalently how reliable are the results coming from the calculation. In DMRG a commonly used measure of the truncation error is the *weight* of the discarded states of the reduced density matrix ρ. Since ρ is trace normalized this is indeed a measure that goes to zero in the limit of keeping all states, and goes to one in the limit of discarding everything. But it is an *indirect* measure that does not reveal information about the error committed for an arbitrary operator, and as such it is more to be considered a guideline to the error than an actual error measure. It is a further complication that the DMRG consists of a high number of steps employing a truncation at each step. Having an error estimate for a single step therefore does not necessarily give an estimate for the full calculation.

Another commonly used measure for the truncation error is the dis-

carded entropy, calculated as $S_D = -\mathrm{Tr}_{\text{Disc. States}}[\rho \log \rho]$. This measures the amount of bipartite entanglement between the blocks for the discarded states but as the discarded weight it is an indirect measure.

2.2.3 Correction vectors

In order to evaluate resolvent equations like the conductance or the single particle propagator considered in Chap. 3 and 4 within the DMRG framework a few considerations must be made. To evaluate these resolvents the correction vector DMRG [59, 18, 19] is used.

In general the resolvent equations considered in this work have the form

$$\langle\psi_0|A\frac{1}{f(H_0, E_0, \omega, i\eta)}B|\psi_0\rangle, \tag{2.2}$$

where $f(H_0, E_0, \omega, i\eta)$ is a generic, typically polynomial, function of the Hamiltonian (H_0), the ground state energy (E_0), frequency (ω), and the finite size broadening parameter (η). Rather than inverting the Hamiltonian matrix to calculate the resolvent in Eq. (2.2) the problem is rephrased as a linear set of equations,

$$\begin{aligned}\frac{1}{f(H_0, E_0, \omega, i\eta)}B|\psi_0\rangle &= |\phi_B\rangle \quad \Rightarrow \\ B|\psi_0\rangle &= \left[f(H_0, E_0, \omega, i\eta)\right]|\phi_B\rangle.\end{aligned} \tag{2.3}$$

It is cheaper to solve this linear system for $|\phi_B\rangle$ using a linear solver, than explicitly inverting the Hamiltonian matrix. Having solved for the real and imaginary parts of the correction vectors $|\phi_{A,B}\rangle = |\phi^R_{A,B}\rangle + i|\phi^I_{A,B}\rangle$, the resolvents can be evaluated as vector overlaps, for instance for the resolvent in Eq. (2.2)

$$\langle\psi_0|A\frac{1}{f(H_0, E_0, \omega, i\eta)}B|\psi_0\rangle = \langle\psi_0|A|\phi_B\rangle. \tag{2.4}$$

In the DMRG calculations we target apart from the ground state $|\psi_0\rangle$ also the real and imaginary parts of the relevant correction vectors $|\phi_A\rangle$ and $|\phi_B\rangle$, as well as the states $A|\psi_0\rangle$ and $B|\psi_0\rangle$ to ensure that the DMRG basis is suitable for describing all these states properly [18, 19]. Thus we target typically 7 states in the DMRG calculations and specific examples hereof are given for the Kubo formula in Chap. 2.4 and for the Greens functions in Chap. 2.5.

2.3 DMRG implementations

This work has been centered around using the linear response formula for conductance within different models. However in order to achieve the energy

resolution needed to perform physically relevant calculations care should be taken in the representation of leads used, the development of which constitutes a significant part of this work. The central task in this connection is to reduce the effects of the finite system, such that a finite and small number of lead sites can model the continuous lead properly. The implementations reviewed in the present thesis are those implemented by Peter Schmitteckert in his DMRG code `NRG++`, which is the code used in all calculations presented in this thesis.

Since the DMRG is generically a few state method the description of finite temperatures is limited; in principle finite but low temperatures could be described. We have not investigated the temperature dependence in this work, but limit the focus to the strict zero temperature limit, such that all averages reduce to ground state averages. Hence in all calculations presented in this thesis the zero temperature limit is understood, although sometimes not specified explicitly.

We first discuss some issues for describing physics on finite size systems. This discussion is intended to highlight some of the issues to be taken into account when implementing this setup. In this work we have applied two different description of the leads, in real- and momentum-space, and we review both setups in some detail, discussing advantages and disadvantages of each setup. In particular we discuss the discretization used in the momentum-space representation of the leads.

2.3.1 Physics on finite size systems

The main challenge in describing transport within the setup used here is the description of the leads. As discussed in Chap. 2.1 the leads and voltage supply are so large that they are considered infinite. Using a method like the DMRG only finite, and often quite small, systems can be treated. Hence the main challenge is the discretization of the continuous leads to describe the continuum using a small number of sites.

In finite system physics a generic feature is the broadening parameter, in this work denoted η, due to the finite size of the system. This broadening is necessary in order to model the continuum of the infinite leads on a finite system, such that the finite η mimics the missing (infinite) part of the lead. On the other hand η also sets a scale below which physics is no longer described correctly because of the very same broadening. In this context the broadening is thus limited by physical arguments, from below because it has to be larger than the finite size level splitting to allow transport, and from above by the broadening it introduces into the system.

One manifestation of the finite size of the system is that different calculations of the same physical property, e.g. conductance, may result in slightly different results. Naturally, significant deviations would be a sign that the physics is not resolved properly, but small deviations are expected and also

found numerically. Furthermore, different approaches to the same physical quantities may exhibit different finite size scalings, such that one approach may be superior compared to another in terms of speed or accuracy. Explicit examples of these effects are discussed in Chaps. 3 and 4.

Different approaches have different ways of dealing with the broadening by η. In this work we present two different possibilities of describing the leads within the DMRG framework, one being in real-space, the other being in momentum-space. The momentum-space approach is in most aspects superior to the real-space approach but we nevertheless review both as the momentum-space approach requires more consideration in the numerical implementation. The real-space approach is straight forward to implement but has a number of numerical issues that need attention, in particular when attempting to resolve narrow resonances. At the end of the day the resolution attainable with the real-space method is limited compared to the momentum-space method.

2.3.2 Particle-hole symmetry

This work considers the dependence of interaction on the transport properties, specifically the conductance. When specifying the interaction there is a choice to be made between using particle-hole symmetry or not. The difference between the two is an interaction dependent compensating potential.

For example the particle-hole-symmetric density-density interaction between sites i and j is

$$V\Big(n_i - \frac{1}{2}\Big)\Big(n_j - \frac{1}{2}\Big) \;=\; V\Big(n_i n_j - \frac{1}{2}(n_i + n_j) + \frac{1}{4}\Big), \tag{2.5}$$

where $n_\ell = c_\ell^\dagger c_\ell$ is the local density operator of site ℓ. The term $n_i n_j$ is the non-particle-hole-symmetric interaction and the term $-\frac{1}{2}(n_i + n_j)$ is the compensating potential. The constant background term is neglected.

In this work we mainly use particle-hole-symmetric interactions. For the resonant chains with an odd number of sites we consider in this work the particle-hole-symmetric interaction has the advantage that the central resonance of the spectrum is pinned at zero gate potential, because of the compensating potential. Thus benchmark calculations for the resonant value for this resonance is possible without having to locate the resonance first.

For some models the effect of the compensating potential is merely a shift of the conductance spectrum whereas the spectrum itself is unchanged. For those models the particle-hole symmetry is a calculational convenience that does not change the physics. For other models the behavior changes depending on whether the interaction is particle-hole-symmetric or not.

2.3.3 Real-space leads

The real-space approach was published in Ref. [60], and many results presented in this part of the chapter is based on that paper. Perhaps the simplest approach to modeling the leads is as finite one-dimensional non-interacting tight-binding chains, as illustrated in Fig. 2.5. The DMRG was originally formulated for one-dimensional chains and is directly applicable.

However for unmodified tight-binding chains the finite level splitting, that sets the scale for the broadening parameter η, scales inversely proportional with the system size, M^{-1}, which means that to reduce the magnitude of η significantly a much bigger system is needed. Further, since DMRG is a relatively expensive numerical method, such a direct approach gives only a poor resolution.

To reduce the finite size effects a number of modifications to the tight-binding chain description of the leads are needed, and in this setup we use a scaling of the boundaries to reduce the finite size effects of the setup.

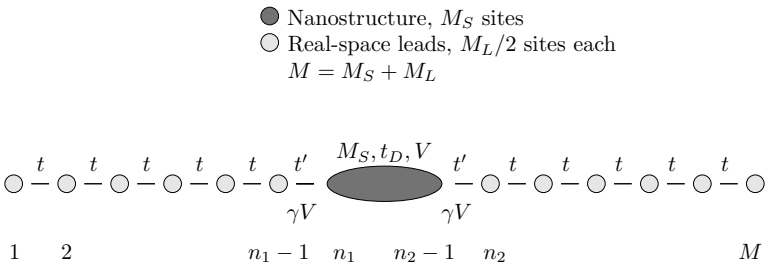

Figure 2.5: Real-space DMRG setup: The leads are modeled by non-interacting tight-binding leads coupled to the interacting nanostructure by hopping matrix elements $t' = t_{L/R}$. The hopping and interaction inside the nanostructure is denoted t_D and V respectively, and the leaking of interaction into the contacts is controlled by γ. Scaling of the boundaries is necessary to reduce the finite size effects, as discussed in the main text.

Scaled boundaries

As discussed in Chap. 2.3.1 the magnitude of the broadening parameter η is bounded by physical arguments; from below by the fact that it should be larger than the finite size level splitting to allow transport, and from above by the broadening of physical results by any finite η, and should thus be significantly smaller than the width of the resonances that is sought resolved.

To improve the finite size scaling and to facilitate the use of sufficiently short leads we use exponentially damped boundary conditions (DBC), decreasing the last M_D hopping matrix elements exponentially towards the

end of the leads as illustrated for the right lead in Eq. (2.6),

$$[-t,\cdots,-t,\underbrace{-t,\cdots,-t}_{M_D}] \;\rightarrow\; [-t,\cdots,-t,\underbrace{-td,-td^2,\cdots,-td^{M_D}}_{M_D}], \quad (2.6)$$

where $d < 1$ is a damping parameter defining the rate of the exponential damping. The damping introduces two more parameters in the model, the number of damped links M_D and the damping factor d, and these must take values such that physical quantities do not depend sensitively on the particular choice. An example of the determination of d and the corresponding η is given in Chap. 3.1.

Modified boundary conditions to reduce finite size effects in connection with DMRG were introduced by Vekic and White [61, 62] under the name of soft boundary conditions. Note that the exponential damping used here is essentially a real-space representation of the Wilson chain used in the NRG, and hence models a logarithmic discretization around $\varepsilon_F = 0$ for half filling. This 'exponentially dense' spectrum around the Fermi energy is the main rationale for using these boundaries, see also App. D where we show by use of exact diagonalization the effect of the damped boundaries on the energy spectrum in the non-interacting case.

The improvement of the finite size scaling relies on two properties of the DBC's: (1) They allow for the use of a smaller η, and (2) serve as a particle bath for the nanostructure. The first property is due to the exponentially small finite size level splitting at the Fermi energy at half filling when using the DBC's. The second property can be understood from the fact that the energy cost of adding or removing a particle from the damped region is of the order of the kinetic energy given by the exponentially small hopping matrix element.

In principle these two properties of the DBC's could be obtained by using longer undamped leads. However these leads would have to be unrealistically long to reach the same finite size level splitting as facilitated by the DBC's, such that this approach is impossible within a direct and expensive numerical scheme like DMRG.

Scaling sweeps

While physically desirable the damped boundary conditions involve several numerical challenges. The gradual decoupling of the outermost part of the leads makes the Hamiltonian matrices worse conditioned, leading to harder linear systems to solve in the resolvent equations.

Physically strong damping is desired, but numerically this involves problems. In order to make use of the particle bath property of the damped regions particles must be moved from the gated nanostructure to the damped regions. Hence we face a paradox: strong damping makes for a better particle bath, but also makes it much harder to move the particles from the

nanostructure to the damped region due to the decoupling involved. Hence particles or holes may become trapped on the far end of the Wilson chain because of the decoupling, and this trapping of fermions on the damped chain slows down the rate of convergence significantly. This is the main problem of the real-space approach.

In order to compensate for this trapping of fermions we turn on the damping in steps and perform *scaling sweeps*. That is, we first perform a full DMRG calculation including finite size sweeps on the undamped system, and then turn on the damping in a series of steps. For each step we perform a number of finite size DMRG sweeps, thus allowing the DMRG to gradually optimize the basis for the damped system.

The scaling sweeps make the overall method more stable for moderate and strong damping since it prevents the system from getting trapped in local minima due to the damping. However it is numerically costly as we end up performing many additional DMRG sweeps compared to the undamped system. Even when using the scaling sweeps there is an upper limit to the energy resolution attainable as the calculational time increases significantly when increasing the damping, and batch queue limitations usually sets an upper limit on the calculational time available. For very strong damping the convergence rate is so slow that the system effectively becomes trapped, and the calculation never converges.

Energy resolution

The advantage of the real-space setup is that the standard DMRG algorithms are fairly directly applicable. However there are still a number of challenges in making the real-space setup produce meaningful results. The finite size effects are significant and must be reduced by the means described above. However in practice there is a limit to how far this scheme can be pushed in terms of finite size splitting – and hence energy resolution. In principle the resolution of the real-space setup is determined by the scaling of the boundaries, but in practice the calculational time and stability of the calculation imposes a limit.

The limitations of the real-space approach is essentially a limitation of the magnitude of η. In the evaluation of the Kubo formula for conductance the limited resolution manifests itself as an on-resonance conductance below the unitary limit due to the broadening introduced by η. Furthermore the evaluation of the two different correlators for the conductance start to differ significantly. As these expressions deal with the same physical quantity, this is a consequence of the different finite size scaling of these two calculations.

Also it should be mentioned that using leads that are not half filled is in principle possible but cumbersome as it is not obvious what the corresponding real-space representation is, and one would have to perform a tri-diagonalization procedure to produce a tight-binding representation.

Nevertheless the DMRG setup using a real-space representation of the leads can yield interesting results, and in Chap. 3.1 we show examples of correlated physics calculated using this setup.

2.3.4 Momentum-space leads

In many aspects the real-space approach is not optimal in a transport setup where one wants to model continuous leads and capture physics at very low-energy-scales. A more natural setup is to use a momentum-space representation for the leads, which additionally gives the flexibility to choose the discretization appropriately for the calculation at hand. However DMRG is generally known to perform poorly in momentum-space [63] and for long range hopping and interactions [14], including the so-called 'star' configurations where a single site couples to many sites as is relevant when joining a real-space site to the momentum-space lead.

One of the reasons for the generally poor performance of DMRG in momentum space is the non-locality of hopping and interaction terms, making the structure similar to higher dimensional systems in real-space. Another complication is that operators that are local in real-space become non-local in momentum-space. Thus in the `NRG++` implementation e.g. the current operator is kept in real-space in order not to complicate the implementation unnecessarily. To ensure this and to provide a handle to cover also local (high-energy) physics close to the nanostructure, a portion of the leads consisting of M_{Add} sites is kept in real-space. The setup is illustrated in Fig. 2.6, where each lead consists of a real-space part joined with a momentum-space part.

Contrary to the naive expectation the momentum-space representation for the lead implemented in `NRG++` works very well, and provides a very flexible description of the leads, such that the discretization can be fine-tuned to the problem at hand. In Chap. 3.1.3 we compare results using the real- and momentum-space representations of the leads, demonstrating the higher accuracy in the latter setup.

Momentum transformation

To transfer the leads to momentum-space we first take the continuum limit of an infinitely long lead,

$$-t \sum_{i=1}^{n_1-1} (c_i^\dagger c_{i-1} + \mathrm{h.c.}) \;\rightarrow\; -t \sum_{i=-\infty}^{\infty} (c_i^\dagger c_{i-1} + \mathrm{h.c.}). \tag{2.7}$$

Later we show that the lead decouples into odd and even combinations of the left and right movers thus compensating for taking an infinite rather

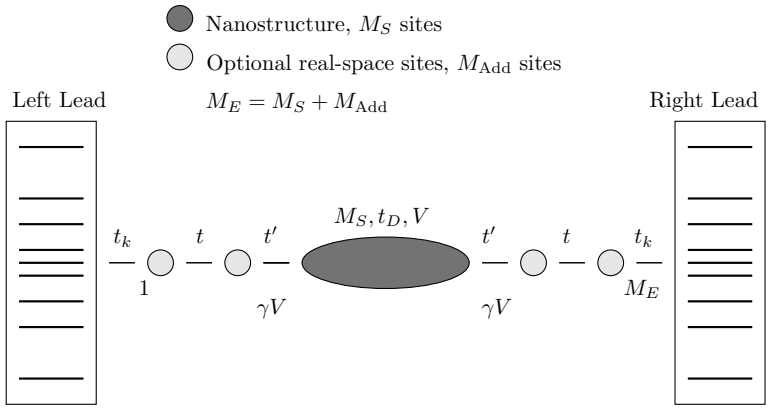

Figure 2.6: Momentum-space DMRG setup: The interacting nanostructure is coupled to non-interacting leads via hopping matrix elements $t' = t_{L/R}$. The hopping matrix elements and interaction inside the nanostructure is given by t_D and V respectively, and the leaking of interaction into the contacts is governed by γ. The leads are modeled by M_{Add} sites kept in real-space, close to the nanostructure, and then coupled to momentum-space leads via discretization dependent hopping matrix elements t_k, such that the real-space site couples to *all* momentum-space sites. There is full flexibility to choose the discretization scheme appropriate for the calculation, and the direct coupling to the low-energy sector prevents problems with trapping of fermions in the low-energy sector. A non-linear discretization of the momentum-space is indicated, and we use the indices 1 and M_E for the first and last sites in the real-space part of the setup.

than semi-infinite lead. Fourier transforming this expression yields

$$-t \sum_{i=-\infty}^{\infty} (c_i^\dagger c_{i-1} + \text{h.c.}) \;\rightarrow\; \int_{-\pi}^{\pi} \mathrm{d}k\; \varepsilon_k c_k^\dagger c_k = \int_0^{\pi} \mathrm{d}k\; \varepsilon_k c_k^\dagger c_k, \qquad (2.8)$$

where ε_k for the tight-binding chain is the cosine dispersion relation. Generalizing Eq. (2.8) to arbitrary dispersion relations, assuming symmetry of the band, this is the continuum form which should be rediscretized in order to put it on a lattice.

When rediscretizing it is essential to be able to target both the low- and high-energy parts of the band. Further it should be kept in mind that a highly non-linear discretization scheme is the aim in this context.

Rediscretization: Preserving statistics

In order for the discretization of the momentum lead to be physically meaningful, and hence relevant in this connection, the statistics of the particles must be preserved. Hence starting from a fermionic operator statistics in the continuous momentum-space the statistics of the discretized momentum-space operators should remain fermionic.

Defining the discretization as

$$\begin{aligned} c_{k_l} &= \frac{1}{\sqrt{d_l}} \int_{k_l^-}^{k_l^+} \mathrm{d}k \; c_k \\ &\equiv \sqrt{d_l} c_{\overline{k}_l}, \end{aligned} \tag{2.9}$$

where $d_l = k_l^+ - k_l^-$ is the width of the l'th interval of the discretized k-space and $k_l^- < \overline{k}_l < k_l^+$, we find

$$\begin{aligned} \left\{ c_{k_l}, c_{k_{l'}}^\dagger \right\} &= \frac{1}{\sqrt{d_l d_{l'}}} \int_{k_l^-}^{k_l^+} \int_{k_{l'}^-}^{k_{l'}^+} \mathrm{d}k \; \mathrm{d}k' \; \left\{ c_k, c_{k'}^\dagger \right\} \\ &= \frac{1}{\sqrt{d_l d_{l'}}} \int_{k_l^-}^{k_l^+} \int_{k_{l'}^-}^{k_{l'}^+} \mathrm{d}k \; \mathrm{d}k' \; \delta(k, k'). \end{aligned} \tag{2.10}$$

Now observing that $k = k'$ implies that $l = l'$ we finally have

$$\begin{aligned} \left\{ c_{k_l}, c_{k_{l'}}^\dagger \right\} &= \begin{cases} \frac{1}{d_l} \int_{k_l^-}^{k_l^+} \mathrm{d}k, & l = l', \\ 0, & l \neq l'. \end{cases} \\ &= \begin{cases} 1, & l = l', \\ 0, & l \neq l'. \end{cases} \end{aligned} \tag{2.11}$$

Hence, according to Eq. (2.11), weighting each discretized k-operator with $w_l = \sqrt{d_l}$ as in Eq. (2.9) we have a discretization that preserves the anticommutation rules of the fermions. Notice that as a highly non-linear discretization scheme is the main goal of the momentum-space leads it is important to calculate the weighting factors for each discrete momentum-space operator.

Right and left movers

The momentum transformation also implies a change in the hopping matrix elements between the real- and momentum-space parts. Denoting temporarily the operator for the last site in the real-space by d, and the first site in the real-space lead that we wish to transform into momentum-space by c_0 we find

$$\begin{aligned} t d^\dagger c_0 &\rightarrow t d^\dagger \frac{1}{\sqrt{2\pi}} \int_{-k_0}^{k_0} \mathrm{d}k \; c_k \\ &= \frac{t d^\dagger}{\sqrt{2\pi}} \int_0^{k_0} \mathrm{d}k \; (c_k + c_{-k}) \\ &\equiv \frac{t d^\dagger}{\sqrt{\pi}} \int_0^{k_0} \mathrm{d}k \; c_{k,+}, \end{aligned} \tag{2.12}$$

where new particles have been defined by even and odd combinations of the left and right movers as

$$c_{k,\pm} \;=\; \frac{1}{\sqrt{2}}(c_k \pm c_{-k}). \tag{2.13}$$

Hence using the discretization weight of the momentum-space operators in Eq. (2.9), $w = \sqrt{d_k}$, the coupling of the real- and momentum-space parts of the leads is via hopping elements

$$t_k \;=\; t\sqrt{\frac{d_k}{\pi}}, \tag{2.14}$$

where t is the real-space hopping parameter, and it should be recalled that the discretization can be non-linear and hence the hopping is k-dependent due to the varying interval size.

The rationale for defining these new particles, $c_{k,\pm}$, is a reduction of the effective Hilbert space. As shown in Eq. (2.12) the kinetic part of the real-space Hamiltonian couples only to the even sector of the momentum-space leads, represented by the $c_{k,+}$ operators. Assuming symmetry of the band we find

$$\begin{aligned}\int_{-k_0}^{k_0} \mathrm{d}k\ \varepsilon_k c_k^\dagger c_k \;&=\; \int_{-k_0}^{0} \mathrm{d}k\ \varepsilon_k c_k^\dagger c_k + \int_{0}^{k_0} \mathrm{d}k\ \varepsilon_k c_k^\dagger c_k \\ &=\; \int_0^{k_0} \mathrm{d}k\ (\varepsilon_k c_k^\dagger c_k + \varepsilon_{-k} c_{-k}^\dagger c_{-k}) \\ &=\; \int_0^{k_0} \mathrm{d}k\ \varepsilon_k (c_k^\dagger c_k + c_{-k}^\dagger c_{-k}).\end{aligned} \tag{2.15}$$

In terms of the new particles we find

$$\begin{aligned}c_k^\dagger c_k + c_{-k}^\dagger c_{-k} \;&=\; \frac{1}{2}(c_{k,+}^\dagger + c_{k,-}^\dagger)(c_{k,+} + c_{k,-}) + \frac{1}{2}(c_{k,+}^\dagger - c_{k,-}^\dagger)(c_{k,+} - c_{k,-}) \\ &=\; c_{k,+}^\dagger c_{k,+} + c_{k,-}^\dagger c_{k,-},\end{aligned} \tag{2.16}$$

which shows that the Hamiltonian contains both subspaces but does not *mix* them. In Eq. (2.12) it was shown that the hopping Hamiltonian only couples to the even sector. Thus the Hilbert space of the odd sector of the leads decouples from the remaining Hilbert space, and can hence be neglected completely, enabling a significant reduction of the lead size and hence a faster setup.

Energy resolution

The main problem of the real-space setup is the gradual decoupling of real-space sites when using the damped boundary conditions, leading to trapping

of fermions on the Wilson chains. In the momentum-space setup no scaling sweeps are necessary as the real-space part of the setup couples directly to all energy sectors in the momentum-space leads. A direct consequence of this is that a much smaller finite size level splitting can be used, such that much lower energy-scales can be addressed in the leads. In turn this leads to a significantly increased energy resolution, or for fixed energy resolution a faster setup.

The momentum-space method can hence resolve resonances that are inaccessible to the real-space setup, or be used for significantly faster calculations of broader resonances. The flexibility regarding the choice of band structure in principle enables a higher-dimensional description of the leads, limited however to single channel physics. So far we have not investigated this point further.

Finally the flexibility in the choice of discretization makes more sophisticated discretization schemes possible. In Chap. 2.5.2 we discuss an example of a double-dense discretization scheme, with two fine-grained points in the band.

2.3.5 Single lead mapping – proportional coupling

In the case of proportional coupling and linear response source-drain bias, the two leads can be combined in even and odd combinations that are not mixed by the Hamiltonian of the leads. We show in this section that the hopping Hamiltonian couples only to the even combination of the leads, such that a single lead suffices.

The coupling matrices $\mathbf{\Gamma}_{i,j} = 2[t_i t_j^*]$ are matrices in the indices of the transport region, and model the broadening of the levels by the coupling to the leads. The simplest case of proportional coupling is when the transport region is a single site, since then the coupling matrices $\Gamma_{i,j} = 2t_i t_j^*$ reduce to real numbers that are always proportional, rather than (in general) complex matrices. Specializing to this case, $M_S = 1$, and denoting temporarily the left and right lead operators by a and b respectively we have the Hamiltonian,

$$H_a = \sum_a \varepsilon_a a^\dagger a, \tag{2.17a}$$

$$H_b = \sum_b \varepsilon_b b^\dagger b, \tag{2.17b}$$

$$H_C = -t_a(a^\dagger d + d^\dagger a) - t_b(b^\dagger d + d^\dagger b). \tag{2.17c}$$

Defining the rotation to new particles as

$$\begin{pmatrix} c_+ \\ c_- \end{pmatrix} = \frac{1}{\sqrt{t_a^2 + t_b^2}} \begin{pmatrix} t_a & t_b \\ t_b & -t_a \end{pmatrix} \begin{pmatrix} a \\ b \end{pmatrix}, \tag{2.18}$$

the reverse transformation is

$$\begin{pmatrix} a \\ b \end{pmatrix} = \frac{1}{\sqrt{t_a^2 + t_b^2}} \begin{pmatrix} t_a & t_b \\ t_b & -t_a \end{pmatrix} \begin{pmatrix} c_+ \\ c_- \end{pmatrix}. \tag{2.19}$$

Defining additionally the proportionality factor as

$$\lambda \;=\; \frac{t_a^2}{t_b^2}, \tag{2.20}$$

the reverse transformation is

$$\begin{pmatrix} a \\ b \end{pmatrix} = \begin{pmatrix} \sqrt{\frac{\lambda}{1+\lambda}} & \sqrt{\frac{1}{1+\lambda}} \\ \sqrt{\frac{1}{1+\lambda}} & -\sqrt{\frac{\lambda}{1+\lambda}} \end{pmatrix} \begin{pmatrix} c_+ \\ c_- \end{pmatrix}. \tag{2.21}$$

Denoting the prefactors as $\alpha = \sqrt{\frac{\lambda}{1+\lambda}}$ and $\beta = \sqrt{\frac{1}{1+\lambda}}$ respectively the lead Hamiltonian transforms as

$$\begin{aligned} H_a + H_b \;=\; & \sum_a \varepsilon_a (\alpha c_+^\dagger + \beta c_-^\dagger)(\alpha c_+ + \beta c_-) \\ & + \sum_b \varepsilon_b (\beta c_+^\dagger - \alpha c_-^\dagger)(\beta c_+ - \alpha c_-) \\ = \; & \sum_{a,b} \varepsilon (c_+^\dagger c_+ + c_-^\dagger c_-) \end{aligned} \tag{2.22}$$

where it has been assumed that the leads are identical, $\varepsilon = \varepsilon_a = \varepsilon_b$, and it was used that $\alpha^2 + \beta^2 = 1$. Notice that in finite voltage calculations this single lead mapping is no longer valid since the chemical potentials of the leads are different in this case.

Similarly the combination that enters the contact Hamiltonian Eq. (2.17c) transforms as

$$\begin{aligned} t_a a^\dagger + t_b b^\dagger \;&=\; t_a \sqrt{\frac{\lambda}{1+\lambda}} c_+^\dagger + t_a \sqrt{\frac{1}{1+\lambda}} c_-^\dagger + t_b \sqrt{\frac{1}{1+\lambda}} c_+^\dagger - t_b \sqrt{\frac{\lambda}{1+\lambda}} c_-^\dagger \\ &=\; \big(t_a \sqrt{\frac{\lambda}{1+\lambda}} + t_b \sqrt{\frac{1}{1+\lambda}}\big) c_+^\dagger, \end{aligned} \tag{2.23}$$

where $t_b^2 \lambda = t_a^2$ was used to show that the c_- part vanishes.

From Eqs. (2.23) and the corresponding hermitian conjugate it is obvious that only the even combination, c_+, couples to the d-level. Thus the odd combination, c_-, can be neglected as it does not couple to the level and the lead Hamiltonians do not mix odd and even combinations, and we are left with an effective single lead description.

The two lead model with proportional coupling in the matrix sense can also be mapped onto a single lead model using a generalized version of the

single level case illustrated above. In this thesis, however, the single level suffices, and the modification of the hopping matrix element is

$$t_{a,b} \;\rightarrow\; t_a\sqrt{\frac{\lambda}{1+\lambda}} + t_b\sqrt{\frac{1}{1+\lambda}}, \tag{2.24}$$

or in the case of identical coupling $t_a = t_b = t$ simply,

$$t_{a,b} \;\rightarrow\; \sqrt{2}\, t, \tag{2.25}$$

This mapping effectively reduces the size of the leads by a factor of two – and hence provides much faster DMRG calculations. However the proportional coupling in the matrix sense, $\mathbf{\Gamma}_L = \lambda \mathbf{\Gamma}_R$, is a strong limitation to which models can be considered.

It should be mentioned that the Kubo formula for conductance, Eqs. (2.41) and (2.42), relies on representing a current operator. Putting this current operator on the link between the lead and the nanostructure it couples to both combinations of the leads. Therefore to evaluate the Kubo formula within a single lead setup an additional requirement is to keep the current operators within the nanostructure itself.

For the resonant chains considered in Chap. 3 the single lead mapping is invalid since the Γ-matrices are not proportional for this model. For the single resonant level, where the Γ-matrices reduce to numbers, the current operator cannot be placed inside the transport region, again invalidating the single lead mapping for the Kubo setup. For the ferromagnetic Anderson model with an applied magnetic field, considered in Chap. 4, we evaluate the conductance via the Meir-Wingreen formula, and hence do not rely on current operators, and the single lead mapping is indeed used for this model.

2.4 Linear response theory

The theory of systems in equilibrium has undergone an extensive development since the formulation of quantum mechanics. A wide range of results and methods have emerged and in general equilibrium techniques are well established.

By contrast, non-equilibrium transport in strongly correlated systems is far from well understood. A variety of methods have been applied with various success and the validity and consistency is in general not well established. Examples of well established methods include the non-equilibrium Greens function technique [27] and the Landauer-Büttiker approach [38, 28, 27], while examples of more recent developments are scattering Bethe-ansatz [64, 65], flow equation methods [31], and time evolution using DMRG [23, 24, 25].

Linear response theory is a useful method to approach the regime of non-equilibrium in a controlled way and using the well known set of techniques

from equilibrium quantum mechanics. In linear response properties are expressed to lowest order in some perturbation, such that physical observables are expressed in terms of averages for the *unperturbed* system.

In principle linear response theory facilitates an approximation-free theory in the sense that no further approximations than the linear response are needed. The quantity in which the linear response is taken can be chosen to suit the problem at hand. In this work we evaluate the linear response of the current in applied source-drain voltage using the DMRG method. The DMRG is capable of handling strong interactions between particles, such that the unperturbed Hamiltonian contains the *full* quantum description. The calculational scheme presented here is a true transport calculation in the sense that we do not rely on extracting transport properties from the ground state itself: The excitations necessary for the transport are generated by η.

In this part of the chapter we review the linear response result for conductance that much of the work presented in this thesis is revolving around. First the general Kubo formula is derived following Ref. [28], and the specific example of the conductance is discussed. Finally some aspects of the discretization within the DMRG framework are discussed.

2.4.1 General Kubo formula

The starting point of the derivation is a system in equilibrium described by the Hamiltonian $H = H_0$, and the corresponding density matrix $\rho_0 = e^{-\beta H_0}$. For systems in equilibrium quantum mechanical expectation values are computed as

$$\begin{aligned} \langle \mathcal{O} \rangle &= \frac{1}{Z_0} \mathrm{Tr}\left[\rho_0 \mathcal{O}\right] \\ &= \frac{1}{Z_0} \sum_n \langle n| \mathcal{O} |n\rangle \, e^{-\beta E_n}, \end{aligned} \tag{2.26}$$

where

$$\rho_0 = e^{-\beta H_0} = \sum_n |n\rangle \langle n| \, e^{-\beta E_n}, \tag{2.27}$$

is the density matrix, $Z_0 = \mathrm{Tr}\left[\rho_0\right]$ is the partition function, and $|n\rangle$ is a complete set of eigenstates for the Hamiltonian H_0.

Turning on a general but weak time dependent perturbation $\delta H(t)$ at time t_0, the Hamiltonian is

$$H(t) = H_0 + \delta H(t)\theta(t - t_0), \tag{2.28}$$

and the time evolution of the system for times $t > t_0$ is governed by the full Hamiltonian $H(t)$. Note that no assumptions are made regarding the

structure of the unperturbed Hamiltonian H_0, which hence may include correlations and other complications.

Since the perturbation is weak the distribution of states remains unchanged when the perturbation is applied but the states evolve according to the full Hamiltonian. The time evolution of the eigenstates, $|n(t)\rangle$, and hence of the density matrix $\rho(t)$, is governed by the Schrödinger equation using the full Hamiltonian and we have

$$\langle \mathcal{O}(t) \rangle \;=\; \frac{1}{Z_0} \sum_n \langle n(t)| \, \mathcal{O} \, |n(t)\rangle \, e^{-\beta E_n}. \tag{2.29}$$

Since we focus on a weak perturbation the interaction picture is well suited and the time-evolution operator is

$$\hat{U}(t, t_0) \;=\; T_t \left(e^{-i \int_{t_0}^{t} \mathrm{d}t' \delta \hat{H}(t')} \right), \tag{2.30}$$

where $\hat{\mathcal{O}}$ is used to denote the interaction picture representation of the operator $\mathcal{O}$, and T_t is the time ordering operator. An expansion of the time-evolution operator to linear order in the perturbing Hamiltonian δH yields

$$\begin{aligned} |n(t)\rangle \;&=\; e^{-iH_0 t} \, |\hat{n}(t)\rangle \\ &=\; e^{-iH_0 t} \hat{U}(t, t_0) \, |\hat{n}(t_0)\rangle \\ &\simeq\; e^{-iH_0 t} \left(1 - i \int_{t_0}^{t} \mathrm{d}t' \delta \hat{H}(t') \right) |\hat{n}(t_0)\rangle \, , \end{aligned} \tag{2.31}$$

where $|\hat{n}(t)\rangle$ denotes the interaction picture states, and $|\hat{n}(t_0)\rangle = |n\rangle$ is the distribution due to the unperturbed Hamiltonian H_0. With this expression and keeping only terms up to linear order in the perturbing Hamiltonian δH the physical observable evolves as,

$$\begin{aligned} \langle \mathcal{O}(t) \rangle \;&=\; \langle \mathcal{O} \rangle_0 - i \int_{t_0}^{t} \mathrm{d}t' \frac{1}{Z_0} \sum_n e^{-\beta E_n} \, \langle n| \, \hat{\mathcal{O}}(t) \delta \hat{H}(t') - \delta \hat{H}(t') \hat{\mathcal{O}}(t) \, |n\rangle \\ &=\; \langle \mathcal{O} \rangle_0 - i \int_{t_0}^{t} \mathrm{d}t' \left\langle \left[\hat{\mathcal{O}}(t), \delta \hat{H}(t') \right] \right\rangle_0 , \end{aligned} \tag{2.32}$$

or in terms of the change due to the perturbation $\delta \langle \mathcal{O}(t) \rangle = \langle \mathcal{O}(t) \rangle - \langle \mathcal{O} \rangle_0$

$$\delta \langle \mathcal{O}(t) \rangle \;=\; -i \int_{t_0}^{t} \mathrm{d}t' \left\langle \left[\hat{\mathcal{O}}(t), \delta \hat{H}(t') \right] \right\rangle_0 , \tag{2.33}$$

which is the Kubo formula in the time domain. The notation $\langle \ldots \rangle_0$ denotes average with respect to the unperturbed Hamiltonian H_0.

Here the aim is to study steady state properties rather than transients, and the perturbation is thus assumed to be switched on in the infinite past, $t_0 \to -\infty$, leading to the Kubo formula

$$\delta \langle \mathcal{O}(t) \rangle \;=\; -i \int_{-\infty}^{t} \mathrm{d}t' \left\langle \left[\hat{\mathcal{O}}(t), \delta \hat{H}(t') \right] \right\rangle_0 . \tag{2.34}$$

The strength of the Kubo formula is that it facilitates approximation-free calculations in the non-equilibrium given by $H(t)$, using the framework of equilibrium quantum mechanics – i.e., averages given by H_0.

In all work presented in this thesis Fourier transformed versions of the Kubo formula for conductance are used. The general derivation of the frequency resolved Kubo formula is not relevant here, and we refer instead to App. B where the specific resolvents used in this work are derived in detail. In the following section we discuss the resolvent formulation of the Kubo formula for conductance, and refer to App. B for a full derivation.

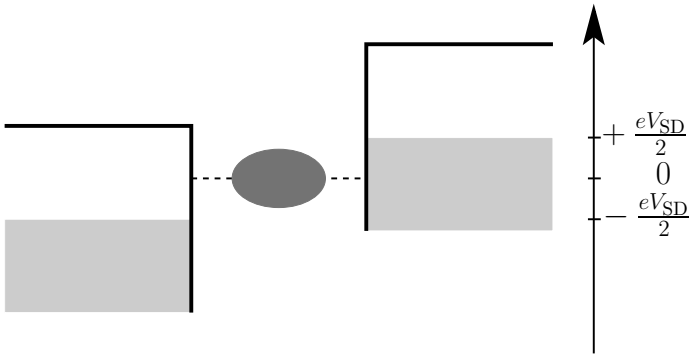

Figure 2.7: Illustration of the voltage perturbation applied to the system. The chemical potentials of the left and right leads are shifted symmetrically down and up respectively, by half the applied source-drain voltage $\frac{eV_{\mathrm{SD}}}{2}$.

2.4.2 Conductance

In this section we discuss the resolvent expressions for the linear response conductance of a given system. The perturbation we apply to the system and calculate the linear response in, is an infinitesimal source-drain voltage,

$$\delta H(t) \;=\; -eV_{\mathrm{SD}}(t)N, \quad |V_{\mathrm{SD}}| \to 0, \tag{2.35}$$

$$N \;=\; \frac{1}{2}(N_L - N_R), \tag{2.36}$$

where $N_{L/R}$ is the density operator of the left/right lead, such that δH corresponds to shifting the left and right lead chemical potentials down and up symmetrically by $\frac{eV_{\mathrm{SD}}}{2}$, as illustrated in Fig. 2.7.

The conductance is calculated from the linear response in electric current to the applied voltage perturbation

$$\big\langle I(t)\big\rangle \;=\; \big\langle I\big\rangle_0 - i\int_{-\infty}^{t} \mathrm{d}t' \big\langle\psi_0\big|[\hat{I}(t), \delta\hat{H}(t')]\big|\psi_0\big\rangle, \tag{2.37}$$

where the particle and electric current operators at the i'th link are

$$J_i = -i(t_i^* c_{i-1}^\dagger c_i - t_i\, c_i^\dagger c_{i-1}), \tag{2.38}$$
$$I_i = -eJ_i. \tag{2.39}$$

Note that we derive a linear response result in the source-drain voltage $V_{\rm SD}$, and the 'simple' Hamiltonian H_0 thus contains all interactions and correlations. The advantage of using the DMRG method to evaluate the Kubo formula is that the DMRG can handle strong correlations, such that the 'simple' Hamiltonian H_0 contains a full quantum description of the system, including the full Coulomb interaction.

The DC linear conductance is defined in terms of the zero frequency component of the Fourier transform of the averaged electric current, as in Eq. (2.1),

$$g = \frac{\big\langle I(V_{\rm SD},\omega)\big\rangle}{V_{\rm SD}(\omega)}\Big|_{\omega\to 0, V_{\rm SD}\to 0}. \tag{2.40}$$

Fourier transforming the linear response result for the current in Eq. (2.37) and dividing by the source drain voltage leads to two different expressions for the conductance, in terms of current-current, and current-density correlators. In App. B we derive by repeated use of the Lehmann representation these two different resolvent forms for the linear response for conductance, to which the DMRG can be applied.

The first form is in terms of current-current correlators, given by

$$g_{J_iJ_j} = \frac{e^2}{h}\,\langle\psi_0|\, J_i \frac{8\pi\eta(H_0-E_0)}{\big((H_0-E_0)^2+\eta^2\big)^2} J_j\,|\psi_0\rangle\,, \tag{2.41}$$

where H_0 is the Hamiltonian without the voltage perturbation, E_0 is the ground state energy, η is the finite size broadening parameter discussed in Chap. 2.3.1, and J_ℓ is the current operator on the ℓ'th link as defined in Eq. (2.38). In principle the current operators can be positioned arbitrarily in the real-space part of the setup, but in general the best results are obtained close to the nanostructure. Note that the two current operators can be placed at the same link.

The second resolvent form is in terms of current-density correlators, given by

$$g_{J_iN} = -\frac{e^2}{h}\,\langle\psi_0|\, J_i \frac{4\pi i\eta}{(H_0-E_0)^2+\eta^2} N\,|\psi_0\rangle\,, \tag{2.42}$$

where H_0, E_0, η, and J_ℓ have the same meanings as above, and where N is the density operator given in Eq. (2.36). Again the current operator can be placed anywhere in the real-space part of the system.

As discussed in Chap. 2.3.1, there may be deviations between the two different resolvents, (2.41) and (2.42), even though they measure the same physical quantity. Also the position of the current operators can have an impact on the resulting conductance, and as commented above the best results are usually found putting the current operators close to the nanostructure. The different calculations should be compared and if there are substantial deviations it is a sign that finite size effects are significant, and a better resolution should be attempted.

In order to calculate the current-current and current-density correlators in Eqs. (2.41) and (2.42) within the DMRG setup we target the ground state $|\psi_0\rangle$, the operator states $N|\psi_0\rangle$ and $J_\ell|\psi_0\rangle$, and the correction vectors $|\phi_\ell\rangle = \left[H_0 - E_0 + i\eta\right]^{-1} J_\ell|\psi_0\rangle$.

Denoting the real and imaginary parts of the correction vectors by $|\phi_\ell^R\rangle$ and $|\phi_\ell^I\rangle$ respectively such that $|\phi_\ell\rangle = |\phi_\ell^R\rangle + i|\phi_\ell^I\rangle$, the current-current and current-density correlators can be calculated from the target states as

$$g_{J_iJ_j} = -\frac{8\pi e^2}{h}\langle\phi_j^I|\phi_i^R\rangle, \tag{2.43}$$

$$g_{J_iN} = \frac{4\pi e^2}{h}\langle\phi_i^R|N|\psi_0\rangle, \tag{2.44}$$

where it was used that in the `NRG++` implementation used in this work the creation and annihilation operators are real, making the density state $N|\psi_0\rangle$ real and the current operator state $J_\ell|\psi_0\rangle$ imaginary, as also discussed in App. D.

2.4.3 Discretization details

When doing calculations like linear transport on finite systems the discretization of the lead is crucial for the accuracy of the results. The transport takes place close to the Fermi level and the discretization scheme should support this. However it has turned out to be important to represent also the higher energy states in the band, although the discretization needed there is less fine-grained.

We work with two different bands, the linear band, $\varepsilon_k = 2k$ for $-D/2 < k < D/2$, and the cosine-band $\varepsilon_k = -D\cos k$ for $0 < k < \pi$, where D is a band cutoff such that the band ranges in energies $-D < \varepsilon_k < D$. A central parameter when one defines the band is what we denote the Fermi velocity, defined as the slope of the dispersion at the Fermi edge, $v_F = \partial_k\varepsilon_k\big|_{k=k_F}$. For the linear band the slope is kept fixed, while the slope of the cosine-band as defined above is scaled by the bandwidth. Notice that we have shifted the linear band such that the Fermi edge is at zero energy and $k_F = 0$.

For the conductance calculations using the momentum-space representation of the leads the discretization scheme used is inspired by the logarithmic

discretization used in NRG and can be summarized as follows: (1) M_{L_0} logarithmically discretized points dense around ε_F, given by the scaling factor Λ, (2) M_{L_1} linearly discretized points at the low-energy scale close to and symmetrically around ε_F, and (3) additional M_{Add} real-space sites added around the nanostructure to account for local (high-energy) physics. Thus in summary we have $M_E = M_S + M_{\mathrm{Add}}$ real-space sites, and $M_L = M_{L_0} + 2M_{L_1}$ momentum-space sites in each lead.

The calculations presented in this thesis all deal with Fermi surface physics and the above discretization scheme suffices. It is essential to have the *linear discretization* on the *low-energy scale* in order to get the unitary conductance on-resonance. Note that exactly the linear discretization is beyond the capability of the NRG, where only the logarithmic discretization is possible.

For more complicated problems involving resolvents at energies away from the Fermi edge more sophisticated discretization schemes are needed. An example of this, discussed in more detail in Chap. 2.5.2, is the finite frequency spectral function, where energies at the Fermi edge *and* energies corresponding to the frequency must be resolved properly, which is again beyond the NRG type discretizations.

2.5 Single particle Greens functions

In this section we show how the single particle Greens functions can be evaluated within the DMRG framework. In order to apply the DMRG setup the Greens functions must be rephrased in terms of resolvent equations. It turns out that the lesser and greater Greens functions are formulated in terms of the same resolvents as the retarded Greens function, and hence a DMRG evaluation of those resolvents provides access to *all* Greens functions for a given set of parameters.

Formally the Kubo formula is similar to the single particle propagator, only a single annihilation or creation operator plays the role previously held by the current operators. One technical difference is that the creation and annihilation operators do not preserve the number of particles and hence the Hamiltonian in the resolvent sees a different target space compared to the conductance calculations.

Here we describe in some detail the resolvent formulation of the Greens functions, and discuss particular issues in the DMRG evaluation of those. Further we review the evaluation of the conductance from the spectral function, and discuss the limitations implicit in this approach to calculate the conductance.

2.5.1 Resolvent formulation

In order to formulate resolvent equations for the single particle Greens functions we Fourier transform and introduce the usual broadening parameter η needed in any finite system physics to broaden the δ-peaks. The fermionic Greens functions are defined by

$$
\begin{aligned}
G^{>}_{i,j}(t,t') &= -i\big\langle c_i(t)c_j^\dagger(t')\big\rangle, && \text{(2.45a)}\\
G^{<}_{i,j}(t,t') &= i\big\langle c_j^\dagger(t')c_i(t)\big\rangle, && \text{(2.45b)}\\
G^{r}_{i,j}(t,t') &= -i\theta(t-t')\big\langle\big\{c_i(t),c_j^\dagger(t')\big\}\big\rangle, && \text{(2.45c)}\\
G^{a}_{i,j}(t,t') &= i\theta(t'-t)\big\langle\big\{c_i(t),c_j^\dagger(t')\big\}\big\rangle, && \text{(2.45d)}
\end{aligned}
$$

where we use i and j to denote the position in the lattice, possible spin indices have been suppressed, and where $\{A,B\} = AB + BA$ denotes the anticommutator of operators A and B. In the zero temperature limit considered here the average reduces to a ground state average.

We consider first the single particle propagator, or retarded Greens function, and rewrite it in a single exponential,

$$
\begin{aligned}
G^{r}_{i,j}(t,t') &= -i\theta(t-t')\Big(\big\langle\psi_0\big|e^{iH_0t}c_i\,e^{-iH_0t}e^{iH_0t'}c_j^\dagger e^{-iH_0t'}\big|\psi_0\big\rangle\\
&\qquad +\big\langle\psi_0\big|e^{iH_0t'}c_j^\dagger e^{-iH_0t'}e^{iH_0t}c_i\,e^{-iH_0t}\big|\psi_0\big\rangle\Big)\\
&= -i\theta(t-t')\Big(\big\langle\psi_0\big|c_i\,e^{i(E_0-H_0)(t-t')}c_j^\dagger\big|\psi_0\big\rangle\\
&\qquad +\big\langle\psi_0\big|c_j^\dagger e^{-i(E_0-H_0)(t-t')}c_i\,\big|\psi_0\big\rangle\Big), \qquad \text{(2.46)}
\end{aligned}
$$

where it is explicit that the Greens function depends only on a single time argument. Hence the Fourier transform is

$$
\begin{aligned}
G^{r}_{i,j}(\omega) &= -i\int_0^\infty dt\Big(\big\langle\psi_0\big|c_i\,e^{i(E_0-H_0)t}c_j^\dagger\big|\psi_0\big\rangle\\
&\qquad +\big\langle\psi_0\big|c_j^\dagger e^{-i(E_0-H_0)t}c_i\,\big|\psi_0\big\rangle\Big)\; e^{i(\omega+i\eta)t}\\
&= \big\langle\psi_0\big|c_j^\dagger\frac{1}{H_0-E_0+\omega+i\eta}c_i\big|\psi_0\big\rangle\\
&\qquad -\big\langle\psi_0\big|c_i\,\frac{1}{H_0-E_0-\omega-i\eta}c_j^\dagger\big|\psi_0\big\rangle, \qquad \text{(2.47)}
\end{aligned}
$$

where the broadening, or convergence, parameter η has been introduced. This is the desired resolvent form of the retarded Greens function G^r to which the DMRG can be applied. The advanced Greens function can be calculated from the retarded as $G^a = [G^r]^\dagger$, and hence needs no further consideration.

Similar manipulations apply for the greater Greens function,

$$\begin{aligned} G^{>}_{i,j}(t,t') &= -i\langle\psi_0|e^{iH_0t}c_i e^{-iH_0t}e^{iH_0t'}c_j^\dagger e^{-iH_0t'}|\psi_0\rangle \\ &= -i\langle\psi_0|c_i e^{-i(H_0-E_0)(t-t')}c_j^\dagger|\psi_0\rangle, \end{aligned} \tag{2.48}$$

such that

$$\begin{aligned} G^{>}_{i,j}(\omega) &= -i\int_{-\infty}^{\infty} dt\langle\psi_0|c_i e^{-i(H_0-E_0)t}c_j^\dagger|\psi_0\rangle\ e^{i\omega t} \\ &= -2\pi i\langle\psi_0|c_i\,\delta(\omega+E_0-H_0)c_j^\dagger|\psi_0\rangle \\ &= -2i\langle\psi_0|c_i\,\frac{\eta}{(\omega+E_0-H_0)^2+\eta^2}c_j^\dagger|\psi_0\rangle \\ &= -2i\ \mathrm{Im}\left[\langle\psi_0|c_i\frac{1}{H_0-E_0-\omega-i\eta}c_j^\dagger|\psi_0\rangle\right], \end{aligned} \tag{2.49}$$

where the δ-function has been represented as an area normalized Lorentzian of width η in order to broaden the δ-function due to the finite size of the system. Note in particular that this resolvent is the same as for the retarded Greens function Eq. (2.47).

Similarly the lesser Greens function is,

$$G^{<}_{i,j}(t,t') = i\langle\psi_0|e^{iH_0t'}c_j^\dagger e^{-iH_0t'}e^{iH_0t}c_i e^{-iH_0t}|\psi_0\rangle, \tag{2.50}$$

which gives the resolvent form

$$G^{<}_{i,j}(\omega) = -2i\ \mathrm{Im}\left[\langle\psi_0|c_j^\dagger\frac{1}{H_0-E_0+\omega+i\eta}c_i|\psi_0\rangle\right]. \tag{2.51}$$

Note again that this is the same resolvent as for the retarded Greens function Eq. (2.47). Thus if these two resolvents,

$$\langle\psi_0|c_j^\dagger\frac{1}{H_0-E_0+\omega+i\eta}c_i|\psi_0\rangle, \tag{2.52a}$$

$$\langle\psi_0|c_i\frac{1}{H_0-E_0-\omega-i\eta}c_j^\dagger|\psi_0\rangle, \tag{2.52b}$$

are calculated using DMRG information on *all* four Greens functions is available from the resolvents. Note however that individual calculations are necessary for each frequency ω.

In the DMRG calculations of the propagators we target the ground state $|\psi_0\rangle$, the operator states $c_j^\dagger|\psi_0\rangle$ and $c_i|\psi_0\rangle$, and the real and imaginary parts of the correction vectors $|\phi_i\rangle = \left[H_0-E_0+\omega+i\eta\right]^{-1}c_i|\psi_0\rangle$ and $|\phi_j\rangle = \left[H_0-E_0-\omega-i\eta\right]^{-1}c_j^\dagger|\psi_0\rangle$, from which the resolvents are calculated

as

$$\langle\psi_0|c_j^\dagger \frac{1}{H_0 - E_0 + \omega + i\eta} c_i|\psi_0\rangle = \langle\psi_0|c_j^\dagger \mathrm{Re}\left[|\phi_i\rangle\right] + i\langle\psi_0|c_j^\dagger \mathrm{Im}\left[|\phi_i\rangle\right], \tag{2.53a}$$

$$\langle\psi_0|c_i \frac{1}{H_0 - E_0 - \omega - i\eta} c_j^\dagger|\psi_0\rangle = \langle\psi_0|c_i \mathrm{Re}\left[|\phi_j\rangle\right] + i\langle\psi_0|c_i \mathrm{Im}\left[|\phi_j\rangle\right]. \tag{2.53b}$$

2.5.2 Discretization details

In the evaluation of the spectral function the fine-grained discretization around the Fermi energy alone no longer suffices. The fine-grained discretization around ε_F is still needed to get an accurate ground state, but the resolvents in Eqs. (2.52) target energies at $E_0 \pm \omega$, such that a fine-grained discretization is necessary at those energies as well.

In the real-space DMRG setup it is quite cumbersome but in principle possible to use such a 'double dense' discretization, while in the standard NRG [66] it is not possible as the NRG relies on a clear separation of energy-scales due to the state selection by energy. Using the momentum-space leads in the DMRG setup the discretization can easily be tailored to suit the problem at hand.

To provide the flexibility of having a fine-grained discretization around multiple points a different approach than used for the Kubo setup to the discretization has been implemented. The general idea is to use a *level distribution function*, $L(k)$, rather than constructing the discretization directly. Using the linear band as an example, and given some function $L(k)$ on the momentum interval $k \in [-\frac{D}{2}, \frac{D}{2}]$ the N points in the discretization are determined by dividing the axis into $N+1$ intervals of constant area below the curve. An example is given in Fig. 2.8 where a doubly dense distribution function is illustrated together with the resulting discretization.

Hence using a constant distribution function, $L(k) = C$, gives a linear discretization, while using a doubly peaked distribution gives a discretization that is dense around two different points. Further, the actual lineshape of each peak determines the details of the dense distribution, such that using a lineshape that is essentially constant in a range close to the peak would mimic a linear discretization on the energy scale close to the condensation point.

For the single particle Greens function calculations we use a doubly peaked level distribution function for each term in G^r. Without specifying the line shape of the peaks the doubly dense level distribution function can be represented as

$$L(k) \;=\; \alpha_0 C + \alpha_1 L_1(k, k_1, w_1) + \alpha_2 L_2(k, k_2, w_2), \tag{2.54}$$

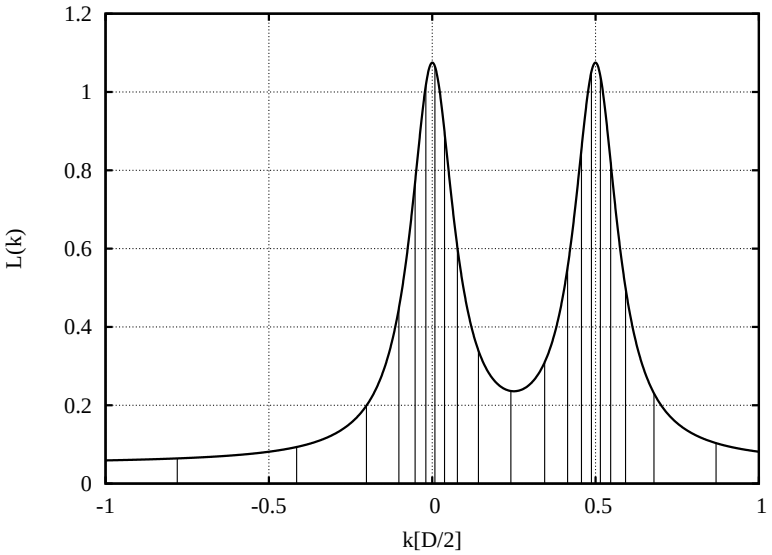

Figure 2.8: Example of a double dense level distribution function for discretizing the leads in the case of a linear band. $L(k)$ is dense around $k_F = 0$ and $k = 0.5$ (in units of $\frac{D}{2}$) relevant for describing eg. one term in the spectral function at frequency $\omega = 1$.

where $L_\ell(k, k_\ell, w_\ell)$ means some peaked function centered at $k = k_\ell$ and with the parameter $w = w_\ell$ controlling the width. Adjusting the widths w_ℓ, positions k_ℓ, and weights α_ℓ hence provides control over the discretization scheme. In order to compare different choices of discretization it is usually required additionally that $\sum_\ell \alpha_\ell = 1$. The specific details of the peaked functions L_ℓ depend on the problem at hand.

2.5.3 Spectral function

The spectral function is defined from the retarded Greens function as the imaginary part of G^r, such that the frequency dependent spectral function, $A(\omega)$, can be expressed as

$$\begin{aligned} A_{i,j}(\omega) &= -2\mathrm{Im}\left[G^r_{i,j}(\omega)\right] \\ &= -2\Big(\mathrm{Im}\Big[\langle\psi_0|c_j^\dagger \frac{1}{H_0 - E_0 + \omega + i\eta} c_i|\psi_0\rangle\Big] \\ &\quad -\mathrm{Im}\Big[\langle\psi_0|c_i \frac{1}{H_0 - E_0 - \omega - i\eta} c_j^\dagger|\psi_0\rangle\Big]\Big), \end{aligned} \tag{2.55}$$

where typically only the diagonal components are considered.

For a number of models access to the spectral function is an interesting quantity in itself as it for example provides information on the lifetime of quasi-particle excitations.

In connection with transport it also contains information. For a certain class of models, those who have proportional coupling matrices to the left and right leads, the conductance can be evaluated from the spectral function via the Meir-Wingreen formula [29, 67]. We review this procedure in Chap. 2.5.4, and use it explicitly for the ferromagnetic Anderson model with an applied magnetic field in Chap. 4.1. The motivation for using this approach rather than the direct evaluation of the Kubo formula is a different finite size scaling; for some models the spectral function scales better with the lead size than the Kubo formula, and further for the proportional coupling models it can be evaluated within a single lead setup (see also Chap. 2.3.5), and hence this approach may enable faster or more accurate calculations.

2.5.4 Conductance from the spectral function

In this section we review how to calculate the conductance in linear response using the retarded single particle Green function, following Haug and Jauho [27]. Such an approach is relevant since the calculation of the propagator has a better finite size scaling and for some models does not require a two terminal setup, but rather a single lead suffices in the linear source-drain voltage limit. However the derivation given here takes its starting point in a standard two lead setup – as the single lead mapping is merely a calculational trick to get the propagator numerically easier.

The current *out of* the left and right contacts is given by the time derivative of the occupation number operator for the contacts,

$$I_{L/R} \;=\; -e\langle \dot{N}_{L/R}\rangle = -\frac{ie}{\hbar}\langle [H_0, N_{L/R}]\rangle, \tag{2.56}$$

where H_0 is the full Hamiltonian and N_ℓ is the occupation number operator for the relevant lead. Calculating this commutator it can be shown that the current can be expressed in terms of the equal time lesser hybrid Greens function $D^{<}_{d_1 c_{n_1}}(t,t) = i\langle c^\dagger_{n_1}(t) d_1(t)\rangle$. By calculating the equations of motion for the corresponding time ordered Greens function $D^{t}_{d_1 c_{n_1}}$, and extracting the lesser component the current through the left and right contact can be expressed in terms of the Greens functions and coupling matrices of the transport region as,

$$\begin{aligned} I_{L/R} = \frac{ie}{\hbar}\int \frac{\mathrm{d}\omega}{2\pi} \\ \mathrm{Tr}\left[\mathbf{\Gamma}^{L/R}\mathbf{G}^{<}(\omega) + n_F^{L/R}(\omega)\mathbf{\Gamma}^{L/R}\big[\mathbf{G}^{r}(\omega) - \mathbf{G}^{a}(\omega)\big]\right], \end{aligned} \tag{2.57}$$

where n_F^α is the Fermi function of lead α, and the boldface notation indicates that the Greens functions and Γ's are matrices in the transport region

indices,

$$\mathbf{G} \;=\; [G_{i,j}], \tag{2.58}$$
$$\mathbf{\Gamma} \;=\; [2t_i\, t_j^*], \tag{2.59}$$

and where the time dependent fermionic Greens functions where defined in Eq. (2.45).

A few remarks are in order regarding the current expression in Eq. (2.57). First of all it is valid for *arbitrary* interactions within the transport region, and secondly it is valid for *any* applied bias. The complication arises when trying to calculate the Greens functions, where approximations are often made in order to get closed form expressions when using analytical tools. The retarded and advanced Greens functions fulfill Dyson equations,

$$\mathbf{G}^{r/a} \;=\; \mathbf{G}_0^{r/a} + \mathbf{G}_0^{r/a}\; \mathbf{\Sigma}^{r/a}\; \mathbf{G}^{r/a}, \tag{2.60}$$

whereas the lesser Greens function obeys the Keldysh equation which, neglecting a boundary term describing transient behavior, reads

$$\mathbf{G}^{<} \;=\; \mathbf{G}^{r}\; \mathbf{\Sigma}^{<}\; \mathbf{G}^{a}. \tag{2.61}$$

Thus this formalism relies on the definition of self-energies $\mathbf{\Sigma}$ that capture the physics of the model, and the solution of this coupled set of matrix equations.

The current was defined as the current *out* of each contact. In steady state, which is the target here, the current through the two contact links are thus equal apart from an opposite sign, and hence we can 'symmetrize' the current using $I_L = -I_R$ and

$$I \;=\; xI_L - (1-x)I_R, \tag{2.62}$$

where $x \in [0,1]$ can be chosen arbitrarily. Thus the current becomes

$$\begin{aligned} I \;=\; \frac{ie}{\hbar}\int \frac{\mathrm{d}\omega}{2\pi}\mathrm{Tr}\Big[&\big[x\mathbf{\Gamma}^L - (1-x)\mathbf{\Gamma}^R\big]\mathbf{G}^{<}(\omega) \\ &+\big[xn_F^L(\omega)\mathbf{\Gamma}^L - (1-x)n_F^R(\omega)\mathbf{\Gamma}^R\big]\big[\mathbf{G}^r(\omega) - \mathbf{G}^a(\omega)\big]\Big]. \end{aligned} \tag{2.63}$$

Out of equilibrium the fluctuation-dissipation theorem no longer applies, and the lesser Greens function must be calculated separately. However specializing to the case of proportional coupling, $\mathbf{\Gamma}^L = \lambda\mathbf{\Gamma}^R$, a simpler expression for the current can be given. Note that proportional coupling is a quite severe restriction since $\mathbf{\Gamma}^{L/R}$ are *matrices*. With this restriction we find the current

$$\begin{aligned} I \;=\; \frac{ie}{\hbar}\int \frac{\mathrm{d}\omega}{2\pi}\mathrm{Tr}\Big[&\mathbf{\Gamma}^R\big[\lambda x - (1-x)\big]\mathbf{G}^{<}(\omega) \\ &+\mathbf{\Gamma}^R\big[\lambda x n_F^L(\omega) - (1-x)n_F^R(\omega)\big]\big[\mathbf{G}^r(\omega) - \mathbf{G}^a(\omega)\big]\Big]. \end{aligned} \tag{2.64}$$

The troublesome term involving the lesser Greens function can be eliminated by choosing x as $x = 1/(1+\lambda)$, and using further that

$$\frac{\lambda}{1+\lambda} \;=\; \frac{\lambda \mathbf{\Gamma}^R}{\mathbf{\Gamma}^R + \lambda \mathbf{\Gamma}^R} = \frac{\mathbf{\Gamma}^L}{\mathbf{\Gamma}^R + \mathbf{\Gamma}^L}, \tag{2.65}$$

we find

$$I \;=\; \frac{ie}{\hbar} \int \frac{\mathrm{d}\omega}{2\pi} \big[n_F^L(\omega) - n_F^R(\omega) \big] \,\mathrm{Tr} \left[\frac{\mathbf{\Gamma}^R \mathbf{\Gamma}^L}{\mathbf{\Gamma}^R + \mathbf{\Gamma}^L} \big[\mathbf{G}^r(\omega) - \mathbf{G}^a(\omega) \big] \right]. \tag{2.66}$$

Specializing further to linear response in the source-drain voltage the difference in Fermi functions reduces to a δ-function, $n_F^L - n_F^R = eV_{\mathrm{SD}}\delta(\omega)$. Considering for simplicity the case of a single level in the transport region such that the Γ-matrices reduce to simple numbers, we finally find the conductance in terms of the zero frequency spectral function,

$$g \;=\; \frac{e^2}{h} \frac{\Gamma^R \Gamma^L}{\Gamma^R + \Gamma^L} A(\omega = 0), \tag{2.67}$$

where $A(\omega) = -2\,\mathrm{Im}\,[G^r(\omega)]$ is the spectral function of the transport level. Inserting finally $\Gamma^{L/R} = 2|t_{L/R}|^2$ we find the Meir-Wingreen formula [38, 27] for the DC linear response conductance

$$g \;=\; \frac{e^2}{h} \frac{2|t_R|^2 |t_L|^2}{|t_R|^2 + |t_L|^2} A(\omega = 0), \tag{2.68}$$

where we have retained separate notations for left and right leads.

Hence the conductance can be calculated from the spectral function for models with proportional coupling, such that the single lead mapping and the better finite size scaling of the single particle propagator can be utilized. For some models this is a more feasible path to calculations as the finite size scaling for the spectral function is different than for the Kubo formula. For example this approach is taken for the ferromagnetic Anderson model with an applied magnetic field considered in Chap. 4.1.

2.6 Benchmarking the DMRG scheme

When developing new methods it is essential to have rigorous and non-trivial benchmarks to evaluate the accuracy of the methods. In the case of the DMRG scheme used here there are two different sources of error to consider: (1) The error made by the DMRG truncation procedure, and (2) the error due to the use of a finite system to calculate transport properties. These two different issues are addressed by two different techniques.

The exact diagonalization in the case of free fermions facilitates a benchmark for the DMRG truncation since the evaluation is using the same discretization scheme and hence exhibits the same finite size effects as the

DMRG setup. It should be noted that the non-interacting case is *not* a special case for the DMRG where it performs significantly better, and therefore it is a rigorous benchmark to test DMRG against exact diagonalization calculations in this limit. Furthermore the exact diagonalization calculations are fast such that the determination of the parameters for the discretization is easy.

The finite system issue can be addressed using Greens function calculations to evaluate the exact conductance in the non-interacting and infinite lead limit – hence addressing the finite size error. In total we can thus address the significance of both types of errors and provide a complete and rigorous benchmark for the DMRG method.

In the following sections we review in some detail these two benchmarks for the DMRG procedure.

2.6.1 Exact diagonalization – non-interacting systems

In this section we demonstrate how the exact diagonalization procedure can be used to evaluate the same resolvents as we evaluate in the DMRG scheme. Since the exact diagonalization idea can be used equally well for spinful and spinless models we give here a unified description of the exact diagonalization idea as used in this work. Note that spinful models without spin-flips decompose into 'spinless' components that are identical, and hence these cases reduce to the spinless calculation.

The overall idea is to use the single particle basis which grows linearly rather than exponentially with the system size. Hence for the system sizes relevant in the DMRG calculations a full diagonalization is feasible. An example is a normal nearest-neighbor hopping chain (tight-binding chain) which would result in a tri-diagonal Hamiltonian of a size that can be diagonalized exactly.

With the matrices containing the eigenstates of the Hamiltonian, denoted U, the basis change to the diagonal basis is

$$c_\ell^\dagger = \sum_k U_{\ell,k}^* c_k^\dagger, \tag{2.69a}$$

$$c_\ell = \sum_k U_{\ell,k} c_k, \tag{2.69b}$$

where the operator $c_k^\dagger$ is in the diagonal basis of the Hamiltonian and ℓ denotes a position in the original non-diagonal setup. The single particle energies ε_k of the states k are known from the diagonalization. It should be noted that the label k is used as an index and need not represent a physical momentum.

The exact diagonalization schemes for the Kubo formula for conductance and for the Greens functions reviewed next are implemented in the `NRG++`

DMRG code, and used as a benchmark in the relevant limit. In Chaps. 3 and 4 we present example calculations.

Conductance

To proceed all relevant operators should be rotated to the diagonal basis, for example

$$c_\ell^\dagger \, c_{\ell'} \;=\; \sum_{p,q} U^*_{\ell,p} U_{\ell',q} c_p^\dagger c_q, \tag{2.70}$$

such that the particle current operator transforms as

$$\begin{aligned} J_i \;&=\; -it_i(c_{i-1}^\dagger c_i - c_i^\dagger c_{i-1}), \\ &=\; -it_i \sum_{p,q} (U^*_{i-1,p} U_{i,q} - U^*_{i,p} U_{i-1,q}) c_p^\dagger c_q. \end{aligned} \tag{2.71}$$

In the diagonal basis the ground state of the Hamiltonian is a simple Fermi sea,

$$\big|\psi_0\big\rangle \;=\; \prod_{k<k_F} c_k^\dagger \, |-\rangle \,, \tag{2.72}$$

where $|-\rangle$ denotes the vacuum state, and hence the linear response conductance can be evaluated explicitly. As we show in App. A the linear response conductance can be expressed as

$$g_{J_i J_j} \;=\; \frac{e^2}{h} \, \langle\psi_0| \, J_i \frac{8\pi\eta(H_0 - E_0)}{\big((H_0 - E_0)^2 + \eta^2\big)^2} J_j \, |\psi_0\rangle \,, \tag{2.73a}$$

$$g_{J_i N} \;=\; -\frac{e^2}{h} \, \langle\psi_0| \, J_i \frac{4\pi i\eta}{(H_0 - E_0)^2 + \eta^2} N \, |\psi_0\rangle \,. \tag{2.73b}$$

To proceed further we first identify the action of the current operator on the ground state,

$$J_i\big|\psi_0\big\rangle \;\propto\; \sum_{p,q} (U^*_{i-1,p} U_{i,q} - U^*_{i,p} U_{i-1,q}) c_p^\dagger c_q \prod_{k<k_F} c_k^\dagger \, |-\rangle \,, \tag{2.74}$$

such that the state generated is a single particle excitation of the ground state, exciting a particle from state q inside the Fermi sea to state p above the Fermi sea. Thus the action of the Hamiltonian on this state is

$$H_0 J_i\big|\psi_0\big\rangle \;\sim\; (E_0 - \varepsilon_q + \varepsilon_p) J_i\big|\psi_0\big\rangle, \tag{2.75}$$

and any resolvent function of the Hamiltonian, $f(H_0 - E_0)$, where E_0 is the energy of the Fermi sea, can be evaluated within the current-current

correlator setup as

$$\begin{aligned}
&\langle\psi_0|J_i\ f(H_0-E_0)J_j|\psi_0\rangle = \\
&\quad -t_i t_j \sum_{p,q} n_F(\varepsilon_q)\left(1-n_F(\varepsilon_p)\right) f(\varepsilon_p-\varepsilon_q) \\
&\quad \left(U_{i-1,p}U^*_{i,q}-U_{i,p}U^*_{i-1,q}\right)\left(U^*_{j-1,p}U_{j,q}-U^*_{j,p}U_{j-1,q}\right), \qquad (2.76)
\end{aligned}$$

where the Fermi functions n_F assure that particles within the Fermi sea are excited to vacant states above the Fermi sea. Hence the conductance can be evaluated once the transformation matrices have been calculated.

Similar considerations apply to the density operator N,

$$N|\psi_0\rangle \;=\; \frac{1}{2}\sum_{p,q}\Big(\sum_{\ell\in L}U^*_{\ell,p}U_{\ell,q}-\sum_{\ell\in R}U^*_{\ell,p}U_{\ell,q}\Big)c^\dagger_p c_q \prod_{k<k_F} c^\dagger_k|-\rangle, \quad (2.77)$$

such that any resolvent function of the Hamiltonian, $f(H_0-E_0)$, may be evaluated in the current-density correlator as

$$\begin{aligned}
&\langle\psi_0|J_i f(H_0-E_0)N|\psi_0\rangle = \\
&\quad \frac{-it_i}{2}\sum_{p,q} n_F(\varepsilon_q)\left(1-n_F(\varepsilon_p)\right) f(\varepsilon_p-\varepsilon_q) \\
&\quad \left(U_{i-1,p}U^*_{i,q}-U_{i,p}U^*_{i-1,q}\right)\Big(\sum_{\ell\in L}U^*_{\ell,p}U_{\ell,q}-\sum_{\ell\in R}U^*_{\ell,p}U_{\ell,q}\Big). \qquad (2.78)
\end{aligned}$$

The expressions Eqs. (2.76) and (2.78) enable an exact diagonalization evaluation of the current-current and current-density correlators for the conductance.

The single particle propagator

Similar transformations as for the conductance can be used for the single particle Greens functions. We consider the retarded Greens function in the resolvent form,

$$\begin{aligned}
G^r_{i,j}(\omega) \;&=\; \langle\psi_0|c^\dagger_j\frac{1}{H_0-E_0+\omega+i\eta}c_i|\psi_0\rangle \\
&\quad -\langle\psi_0|c_i\frac{1}{H_0-E_0-\omega-i\eta}c^\dagger_j|\psi_0\rangle, \qquad (2.79)
\end{aligned}$$

as an evaluation of these resolvents enables evaluation of all the single particle Greens functions.

Using again the known ground state in the diagonal basis the Hamiltonian in the two terms in Eq. (2.79) sees a Fermi sea with an extra particle or hole. Thus the two terms in G^r can be expressed as

$$\langle\psi_0|c^\dagger_j\ f(H_0-E_0)c_i|\psi_0\rangle \;=\; \sum_p U^*_{j,p}U_{i,p}\ f(-\varepsilon_p)n_F(\varepsilon_p), \qquad (2.80)$$

and

$$\langle\psi_0|c_i\ f(H_0-E_0)c_j^\dagger|\psi_0\rangle\ =\ \sum_q U^*_{j,q}U_{i,q}\ f(\varepsilon_q)(1-n_F(\varepsilon_q)), \quad (2.81)$$

where the Fermi functions assure that filled states from the Fermi sea are annihilated or vacant states above the Fermi sea are filled. Thus the retarded Greens function can be expressed as

$$\begin{aligned} G^r_{i,j}(\omega) &= \sum_p U^*_{j,p}U_{i,p}\ \frac{n_F(\varepsilon_p)}{\omega-\varepsilon_p+i\eta} - \sum_q U^*_{j,q}U_{i,q}\ \frac{1-n_F(\varepsilon_q)}{-(\omega-\varepsilon_q+i\eta)} \\ &= \sum_p U^*_{j,p}U_{i,p}\ \frac{1}{\omega-\varepsilon_p+i\eta}. \end{aligned} \quad (2.82)$$

Since the lesser, greater and advanced Greens functions are given in terms of the same resolvents as the retarded Greens function, the expressions in Eqs. (2.80) and (2.81) can also be used to evaluate the remaining Greens functions.

2.6.2 Greens function approach – non-interacting systems

In this section we discuss briefly the Greens function result for one class of systems considered in this work, namely the spinless resonant chains in the symmetrically coupled case, $t' = t_L = t_R$. The calculation uses semi-infinite tight-binding chains as leads. In App. C we show in more detail how the non-equilibrium Greens function method [27] can be used to evaluate the conductance of an M_S site linear resonant chain, see also Chap. 3.

In summary the DC conductance is given by the expression

$$\begin{aligned} g &= \frac{I}{V_{\rm SD}} \\ &= \frac{e^2}{h}t'^2 \mathrm{Im}\left[g^r_{11}\right] \times \Big\{ \mathrm{Im}\left[G^r_{d_0d_0}\right] \\ &\quad + t'^2 \left|G^r_{d_0d_0}\right|^2 \mathrm{Im}\left[g^r_{11}\right] t^2 \left|g^r_{11}\right|^2 \Big[\prod_{i=1}^{M_S-1} \Big| \frac{t_D^2}{\omega-\mu_g-\Sigma_{R_i}} \Big|^2 - 1 \Big] \Big\} \Big|_{\omega=0}. \end{aligned} \quad (2.83)$$

where the Greens functions are given by

$$G^{r/a}_{d_0d_0}(\omega) = \frac{1}{\omega-\mu_g-\Sigma^{r/a}_{d_0d_0}(\omega)}, \quad (2.84)$$

$$G^{r/a}_{R_{i-1}}(\omega) = \frac{1}{\omega-\mu_g-\Sigma^{r/a}_{R_{i-1}}(\omega)}, \quad (2.85)$$

$$g^{r/a}_{11}(\omega) = \frac{1}{\omega-\Sigma^{r/a}(\omega)}. \quad (2.86)$$

The index d_0 denotes the first site in the resonant chain and $G_{d_0 d_0}$ is the corresponding diagonal Greens function.

The self-energies of the Greens functions are built starting from the right side of the chain ('R') by iteration in the index R_i as,

$$\Sigma_{d_0 d_0}(\omega) = \frac{t_D^2}{\omega - \mu_g - \Sigma_{R_{M_S-1}}(\omega)}, \tag{2.87}$$

$$\Sigma_{R_i}(\omega) = \frac{t_D^2}{\omega - \mu_g - \Sigma_{R_{i-1}}(\omega)}, \tag{2.88}$$

$$\Sigma_{R_1}(\omega) = \frac{t'^2}{\omega - \Sigma(\omega)}, \tag{2.89}$$

and where the retarded self-energy of the lead, $\Sigma^r(\omega)$, is finally given by

$$\Sigma^r(\omega) = \frac{\omega - \sqrt{\omega^2 - 4t^2}}{2}, \tag{2.90}$$

such that the lead self-energy has a finite imaginary part inside the cosine-band $|\omega| < 2t$.

This enables the calculation of the conductance of a non-interacting resonant chain coupled to semi-infinite tight-binding leads for symmetric coupling.[1] In App. C the Matlab implementation of the Greens function calculation of the conductance of resonant chains is shown, and we also give a comparison of the exact diagonalization and Greens function solutions to a non-interacting resonant 7 site chain weakly coupled to two tight-binding leads, demonstrating that the two approaches agree perfectly.

In Chaps. 3 and 4 we show explicit examples of the exact diagonalization and Greens function approaches to the conductance of non-interacting systems.

[1] The symmetric coupling is not strictly a demand – having $t_L \neq t_R$ would only result in different self-energies.

Chapter 3

Spinless models

In this chapter we present work performed within spinless models. Spinless models neglect the complication of the spin degree of freedom of the electrons and can be used to describe situations where only the charge degree of freedom matters. Usually DMRG performs very well for this class of models as the spinless site basis is small.

The models are presented in 'chronological' order, such that the oldest work using the real-space leads is presented first, followed by more recent work using the momentum-space leads. For the different models considered in this chapter we present calculations of the Kubo formula for conductance in the DC-limit, discussed in Chap. 2.4.2,

$$g_{J_iJ_j} = \frac{e^2}{h} \langle\psi_0| J_i \frac{8\pi\eta(H_0 - E_0)}{\left((H_0 - E_0)^2 + \eta^2\right)^2} J_j |\psi_0\rangle , \tag{3.1a}$$

$$g_{J_iN} = -\frac{e^2}{h} \langle\psi_0| J_i \frac{4\pi i\eta}{(H_0 - E_0)^2 + \eta^2} N |\psi_0\rangle . \tag{3.1b}$$

The scale on which we measure all other parameters is set by the hopping matrix element in the tight-binding leads such that $t = 1$ and everything else is measured in units of t. The momentum-space representation of the leads that is used in some calculations is chosen to represent the real-space lead with hopping matrix element t such that again $t = 1$ sets the scale.

We first consider a resonant 7 site chain. This chain length was chosen long enough to be an extended system, and short enough to be treated within the real-space DMRG setup. Due to the odd number of sites a resonance is pinned at zero gate potential by the particle-hole-symmetric interaction, such that benchmark calculations for the on-resonance conductance are possible without having to locate the resonance first. For this model we investigate the effects on the conductance of having repulsive interactions mainly inside the nanostructure. We show that strong interactions inside the chain sharpens the resonances, and that this model displays Coulomb blockade behavior.

We then proceed with a simpler model, consisting of a single resonant level interacting with the first sites in each lead via a density-density interaction on the contact links. Despite the simplicity of this model it shows an interesting and unexpected non-monotonic behavior of the resonance width versus the interaction strength on the contacts.

Finally in order to investigate if the non-monotonic behavior of the single level model is unique to this simple model we consider short linear chains consisting of 3 and 5 sites. These models have two interaction strengths, the interaction inside the system, and the leaking of interaction onto the contact links. Thus we have two oppositely directed effects for the off-resonance transport, a suppression due to the interaction within the chain, and an enhancement due to the leaking interaction on the contacts, and we show that the enhancement is stronger than the suppression.

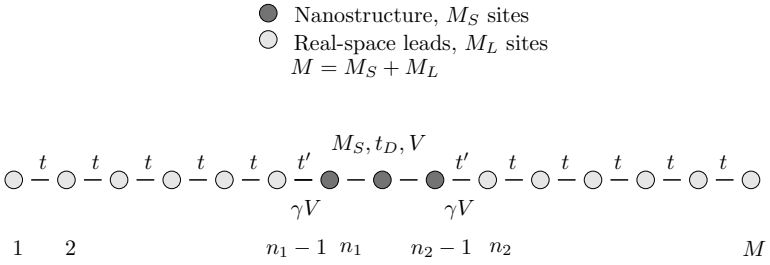

Figure 3.1: Interacting resonant chain with M_S sites (here $M_S = 3$ shown), coupled to non-interacting real-space tight-binding leads. The total system size is denoted M, the number of lead sites is M_L. The intradot and intralead hopping elements are t_D and t respectively, while the hopping matrix elements between the chain and leads are $t' = t_L = t_R$. The interaction V is confined within the resonant chain and the parameter γ controls the leaking of the interaction onto the contact links. The sites in the leads that are connected to the resonant chain are denoted $n_1 - 1$ and n_2.

For the resonant 3 site chain we consider additionally the resonance at finite gate potential, and show that it exhibits a similar, although less pronounced, behavior compared to the resonance at zero gate potential.

3.1 Interacting resonant 7 site chain

In this section we consider an interacting resonant $M_S = 7$ site chain, coupled to non-interacting leads via weak links. The rationale for studying this chain length is that the system is large enough to have an interesting structure, and small enough to be treated within the developed DMRG framework using real-space leads. The advantage of having an odd number of sites in the chain is that the central resonance is pinned at zero gate potential by virtue of the particle-hole-symmetric interaction, such that the discretization of the leads can easily be tested at the resonant value.

Apart from the comparison of the real- and momentum-space setups at the end of the section all calculations presented for $M_S = 7$ were performed using the real-space representation of the leads in the DMRG evaluation of the conductance. We present some level of detail regarding the parameter determination for the leads as this is crucial for the success of these calculations. The essential results presented in this section were published in Ref. [60].

The model we consider is an interacting linear chain connected to non-interacting real-space leads via weak links, denoted $t_{L/R}$. We denote by S the system (the resonant chain), and by L/R the left and right lead respectively. The general setup is shown in Fig. 3.1 and using the notation in the figure

the Hamiltonian $H = H_L + H_R + H_S + H_C$ is

$$H_{L,R} = -t \sum_{i,i-1\in\{L,R\}} (c_i^\dagger c_{i-1} + c_{i-1}^\dagger c_i), \tag{3.2a}$$

$$\begin{aligned} H_S = &\sum_{j\in S} \mu_g c_j^\dagger c_j - \sum_{j,j-1\in S} t_D (c_j^\dagger c_{j-1} + c_{j-1}^\dagger c_j) \\ &+ \sum_{j,j-1\in S} V\Big(n_j - \frac{1}{2}\big)\big(n_{j-1} - \frac{1}{2}\Big), \end{aligned} \tag{3.2b}$$

$$\begin{aligned} H_C = &-t_L (c_{n_1-1}^\dagger c_{n_1} + \text{h.c.}) - t_R (c_{n_2-1}^\dagger c_{n_2} + \text{h.c.}) \\ &+\gamma V\Big(\big(n_{n_1-1} - \frac{1}{2}\big)\big(n_{n_1} - \frac{1}{2}\big) + \big(n_{n_2-1} - \frac{1}{2}\big)\big(n_{n_2} - \frac{1}{2}\big)\Big), \end{aligned} \tag{3.2c}$$

where V is the particle-hole-symmetric interaction strength, $n_\ell = c_\ell^\dagger c_\ell$ is the local density operator at site ℓ, t_D is the hopping matrix element within the dot, t is the hopping matrix element in the leads, γ controls the leak of interaction into the contacts, $t_{L/R}$ are the (weak) links connecting leads and dot, and μ_g is a gate potential applied to the resonant chain.

We show in this part of the chapter that strong interaction within the resonant chain suppresses the width of the resonances, and further that we find a Coulomb blockade renormalization of the resonance position by the interaction, demonstrating Coulomb blockade from a microscopic model. But first the free parameters of the model must be determined.

3.1.1 Parameter determination

Before actual numerical calculations can be performed the free parameters of the real-space setup, the number of damped links M_D, the damping factor d, and the finite size broadening η, must be determined, see Chap. 2.3.3 for definitions. This is done using exact diagonalization calculations for the non-interacting systems, specifically benchmarking the resonant value of the conductance at $\mu_g = 0$. Due to the bath property of the damped boundary conditions it is safe to assume that half filling is nearly maintained in the parts of the leads that are close to the chain. By contrast the strongly damped regions act like particle baths and therefore cannot maintain half filling for finite gate potential.

The reference result used in the determination of the parameters is the resonant value pinned at $\mu_g = 0$ by the particle-hole symmetry. Performing exact diagonalization calculations of the resonant value of the conductance and varying the value of η we obtain the plot in Fig. 3.2(a). The plot nicely illustrates the discussion of the finite size broadening given in Chap. 2.3.1; for $\eta \to 0$ no transport takes place, and the conductance is identically zero in this limit. Turning up the value of η eventually broadens the levels sufficiently to allow transport. A region where the resonant value of the conductance does not depend sensitively on the actual choice of η is found, as seen

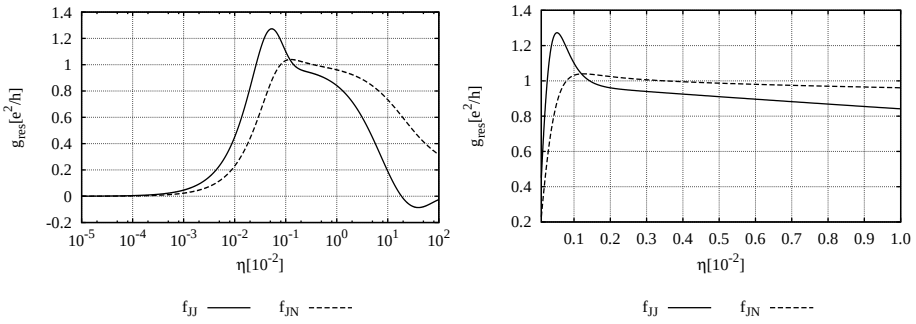

(a) (b)

Figure 3.2: Example of an exact diagonalization calculation of the resonant value of the conductance $g_{\rm res}$ versus the finite size broadening η, (a) on a logarithmic scale, (b) on a linear scale of the physically relevant interval. Calculation using the parameters $M_S = 7$, $t' = t_{L/R} = 0.5$, $M_D = 30$, and $M = 102$. This calculation shows signs of finite size effects in the difference between the current-current and the current-density calculations of the conductance.

on a non-logarithmic scale in Fig. 3.2(b), and we choose η within this range. Increasing further the value of η we get again a reduced on-resonance value of the conductance due to the significant broadening introduced by the large η, and eventually the physics is no longer described satisfactorily.

Similar considerations are made regarding the damping, and for fixed number of damped links M_D we find a range of d values that produce essentially identical physical results, as shown in the example in Fig. 3.3, indicating the range of validity of the DBC's. Additionally we find that the actual value of M_D is not significant (for $M_D \gtrsim 30$) as long as the corresponding value of the damping factor d is tuned such that the damping at the edge reaches values of the same order of magnitude. The leads used are sufficiently long to keep the damped region separated from the chain, thus allowing Friedel oscillations at the edge of the chain to decay before reaching the damped region. For all calculations presented in this chapter the values $M_D = 30$ and $d = 0.8$ are used while the specific value of η varies somewhat between the calculations.

These example calculations shown in Figs. 3.2 and 3.3 for the parameter determination show signs of finite size errors in the deviation between the current-current result, f_{JJ}, and the current-density result, f_{JN}. In Chap. 3.1.2 we discuss the finite size effects for the results presented, and in Chap. 3.1.3 we show that the momentum-space representation of the leads gives much better resolution.

It should be mentioned that the damped boundary conditions make the convergence rate in numerical calculations much slower. A finite gate potential, μ_g, changes the particle number in the structure and the excess particles

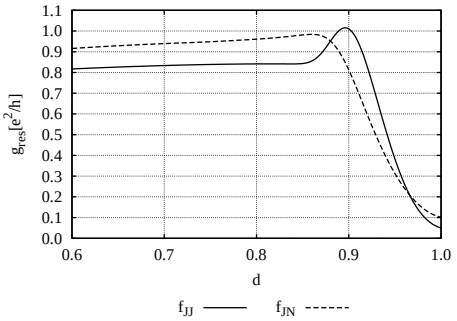

Figure 3.3: Example of an exact diagonalization calculation of the resonant value of the conductance $g_{\rm res}$ versus the damping factor d. The parameters used are $M_S = 7$, $t' = t_{L/R} = 0.5$, $M_D = 30$, and $M = 102$. This calculation shows signs of finite size effects in the difference between the current-current and the current-density calculations of the conductance.

come from the bath property of the DBC's. We therefore face the problem that the damping should be sufficiently strong to provide a reasonable particle bath but at the same time a strong damping decreases the coupling of the strongly damped region to the rest of the system. To remedy the slow convergence in the DMRG calculations we turn on the damping in steps and perform several finite system DMRG sweeps for each such damping step. In other words, we perform a complete finite lattice calculation employing typically 11 sweeps and then initiate the scaling sweeps. The damping is typically turned on in 4 steps, $d = 0.95, 0.9, 0.85, 0.8$, and between each step 4-5 DMRG sweeps are performed. This allows DMRG to gradually optimize the basis to include the damping in the leads and provides a more gradual decoupling of the damped regions from the rest of the system, thus improving the convergence rate at the cost of more DMRG iterations.

Despite this effort to improve the convergence rate the resolvent equations for the conductance are still ill-conditioned and standard solvers like the Conjugate Gradient Method do not converge [60]. The DMRG calculations presented in Fig. 3.4 and Fig. 3.5 were done keeping up to $m = 1200$ states per block in the DMRG truncation. We do not fix the number of states per block to be m but rather fix the dimension of the target space to be at least m^2, see also Chap. 2.2.1 for further details. In the calculations presented here this corresponds to an increase of block states of typically $15\% - 30\%$ [60].

With the free parameters of the model determined we proceed to present results calculated with the real-space setup for the interacting resonant $M_S = 7$ site chain.

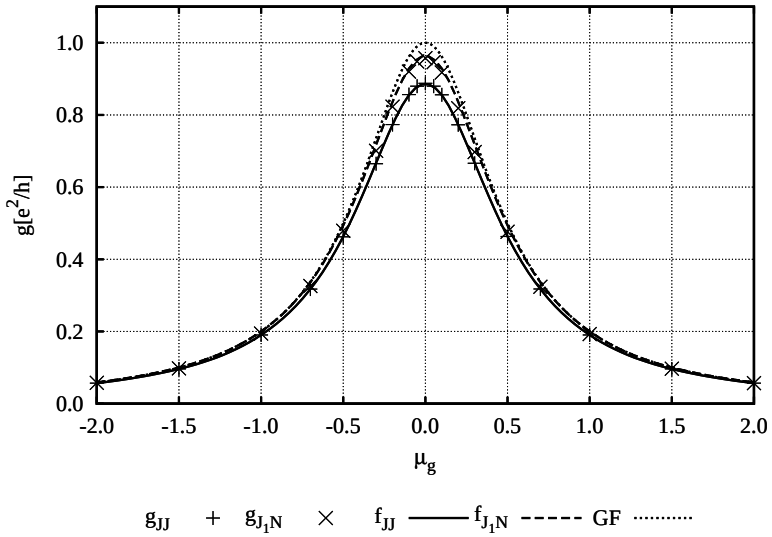

(a) Single resonant level, $M_S = 1$ and $M = 102$. g's denote DMRG results, f's denote exact diagonalization results, and GF denotes the exact Lorentzian result in the infinite lead limit.

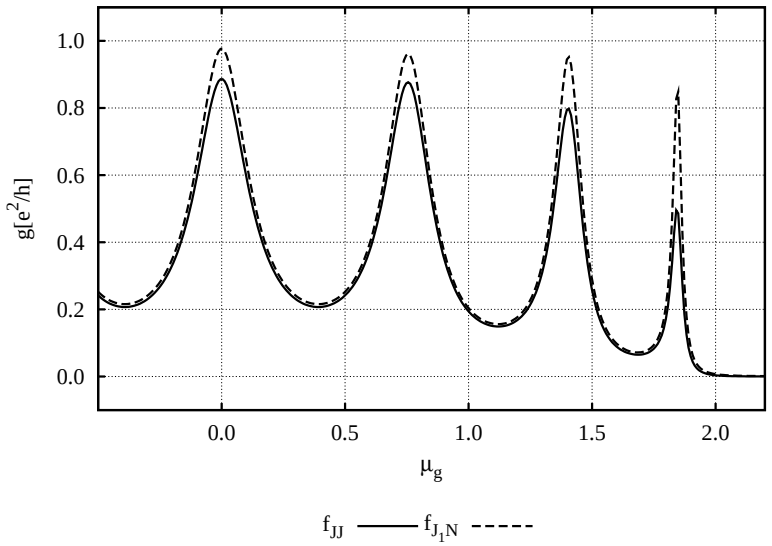

(b) Seven site chain, $M_S = 7$ and $M = 150$, in the non-interacting limit, $V = 0.0$. The conductance spectrum is symmetric around zero gate potential, and we show only the positive part. In the weak coupling limit the position of the resonances is given by the energy levels of the isolated structure. Figure based on an exact diagonalization calculation.

Figure 3.4: Conductance, g, versus external potential μ_g (a) for a single resonant level and (b) for an extended chain consisting of seven sites in the non-interacting limit. g's denote DMRG results and f's denote exact diagonalization results, while JJ denotes the current-current correlator and $J_\ell N$ denotes current-density correlators. The calculations were performed with the real-space DMRG setup and parameters $t' = t_{L/R} = 0.5$, $t_D = 1$, $M_D = 30$, $d = 0.8$, and $\eta = 1/M$.

3.1.2 Results

Here we present DMRG and, in the non-interacting limit, exact diagonalization calculations for a single resonant level, Fig. 3.4(a), and a resonant $M_S = 7$ site chain, coupled symmetrically to non-interacting left and right leads. For the extended structure we present results in the non-interacting limit, Fig. 3.4(b), and for weak and strong interaction, Fig. 3.5(a) and 3.5(b). As discussed in Chap. 2.3.2 we use a particle-hole-symmetric interaction, resulting in a conductance spectrum that is symmetric around $\mu_g = 0$, and we therefore show results for positive gate potential only.

The spinless single resonant level is generically non-interacting and serves as a testing ground for the approach.[1] The exact result for the conductance in the symmetrically coupled case can be shown to be a Lorentzian of full width $4t'^2$ at half maximum, where $t' = t_L = t_R$. In Fig. 3.4(a) we show exact diagonalization and DMRG calculations for the single resonant level and the two sets are indistinguishable. This verifies that the truncation error introduced by the DMRG is negligible. Furthermore we have plotted the exact Lorentzian result, and the agreement between the three curves is good, demonstrating the level of accuracy of the Kubo approach with real-space leads.

The expected shape of the broadened peak is that of an area normalized Lorentzian L_A of half-width η convoluted with the unbroadened physical result [60]. From Greens function calculations the exact result for the single resonant level is a height normalized Lorentzian L_H, and thus the result broadened by η is

$$g(\mu_g) \;=\; (L_A * L_H)(\mu_g) = \frac{\Gamma}{2}\frac{\eta + \Gamma/2}{(\mu_g - \mu_0)^2 + (\eta + \Gamma/2)^2}. \tag{3.3}$$

While not reaching the unitary limit $g_{\mathrm{res}}[e^2/h] = 1$ the DMRG approach gets close. Performing a linear expansion in η of Eq. (3.3) yields the value on-resonance $g_{\mathrm{res}} \approx 1 - 2\eta/\Gamma$, and inserting for the resonant level in Fig. 3.4(a) the values of η and $\Gamma = 2t'^2$ yields $g_{\mathrm{res}} \approx 0.96$. Comparing this value to the DMRG data for $M_S = 1$ shows that this result agrees with the resonant value found using the current-density correlator. By contrast the current-current correlator displays an additional broadening, also apparent from the expression in Eq. (3.1), due to the linear expansion in frequency performed when taking the DC limit, as shown in App. B.

Although the physical conductance of a system is independent of the method used in calculating it we find a systematic difference between the current-current and the current-density correlators in the real-space setup

[1] In Sec. 3.2 we consider the IRLM, a resonant level including Coulomb interaction of the level with the first lead sites. Here the level is treated as non-interacting and used only as a benchmark system.

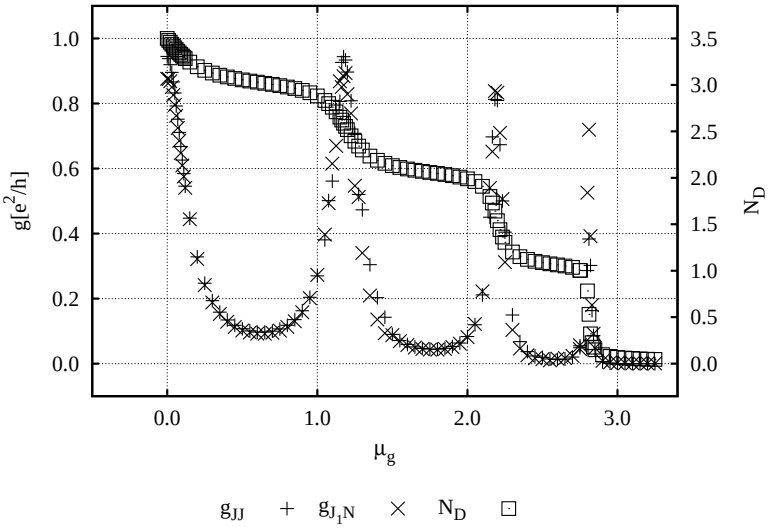

(a) Seven site chain, $M_S = 7$ and $M = 150$, in the weakly interacting regime, $V = 1.0$.

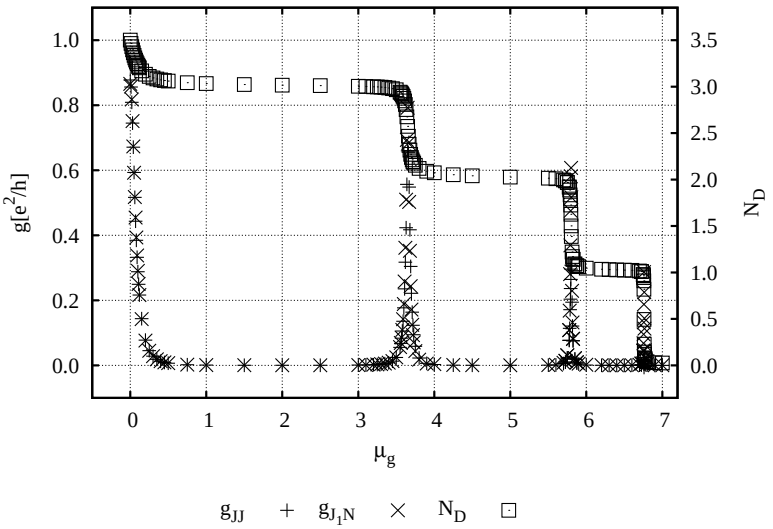

(b) Seven site chain, $M_S = 7$ and $M = 150$, in the strongly interacting regime, $V = 5.0$. Notice the offset of resonance positions of the order V as compared to the non-interacting case.

Figure 3.5: Conductance, g, and number of particles on the dot, N_D, versus external potential μ_g for a resonant 7 site chain. JJ denotes the current-current correlator, and $J_\ell N$ denotes the current-density correlator. The calculations were performed using the real-space setup with parameters $t' = t_{L/R} = 0.5$, $t_D = 1$, $M_D = 30$, $d = 0.8$, and $\eta = 1/M$. The interaction on the chain is smoothed over the contacts with $\gamma = 0.5$.

calculations, a difference attributed to the finite size of the system. Specifically close to resonances the current-density correlator generally gives better results, which is due to the additional energy dependent broadening given by $H_0 - E_0$ in the current-current correlator. The opposite is true in the tails where the current-current correlator is more reliable since it is less sensitive to changes in the density of the leads.

Both sets of DMRG data deviate from the unitary value for the conductance on-resonance because of the broadening due to the finite system. Because of the numerical problems involved in the scaled boundaries of the real-space setup it is limited how much can be gained by using larger systems or stronger damping. In Chap. 3.1.3 we present results for the resonant $M_S = 7$ site chain using the momentum-space representation of the leads. The comparison shows the significantly improved resolution of the momentum-space setup due to the reduced finite size effects in this setup.

But first we discuss the position and width renormalization of the resonances.

Resonance position

In the weak coupling limit the position of the resonances is given by the energy levels of the isolated system, found for instance by diagonalization of the Hamiltonian of the isolated chain. Thus the position of the resonances is determined by the parameters of the chain, t_D and V, while the width is determined by the broadening due to the leads, $t' = t_{L/R}$.

The position of the resonances is hence described by the addition spectrum, for instance for going from $N_D - 1$ to N_D particles on the dot gives a resonance at the gate potential

$$\mu_g^{N_D-1\to N_D} \;=\; E_0^{N_D-1} - E_0^{N_D}, \tag{3.4}$$

where $E_0^{N_D}$ is the energy of the isolated chain occupied by N_D particles. For example in Fig. 3.5 the particle number is changed by one each time a peak in the conductance is crossed, such that eventually the resonant chain is completely empty when the applied gate potential becomes sufficiently large.

In an effective charging model the additional splitting of the levels due to the interaction is linear in the repulsive interaction V. By contrast, in our microscopic model the interaction leads to an overall *offset* for the non-central peaks, of the order $\sim V$, while their mutual *distance* is governed by the kinetic energy, of the order $\sim t_D$, as can be seen in Fig. 3.5. Thus this microscopic model exhibits Coulomb blockade behavior where the additional charging of the chain depends on the occupation, and since we use a particle-hole-symmetric interaction also the discharging exhibits Coulomb blockade for the *holes*.

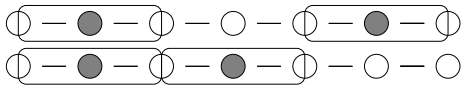

Figure 3.6: Illustration of the reduced lattice picture for strong interaction: The interaction is so strong that the fermions avoid each other, but otherwise move freely. This can be modeled by hard-core free fermions on a lattice of the reduced size $M_S^* = M_S - N_D$.

In the large interaction limit $V \gg t_D$ a simple picture explaining this behavior can be given. In this limit the effect of one fermion in the system on the others is to limit the space available for the other fermions. However the other fermions still move freely on the remaining lattice, as illustrated in Fig. 3.6. Thus the kinetic energy of the fermions can be approximated by freely moving hardcore fermions on a lattice of a reduced size, $M_S^* = M_S - N_D$. In this approximation the interacting fermions are described by effective hard-core particles of the size of the interaction range, compare Refs. [68, 69]. Formalizing this the addition spectrum in Eq. (3.4) can be expressed as

$$\mu_g^{N_D-1\to N_D} = V - 2t_D\Big(\sum_{n=1}^{N_D-1}\cos(\frac{\pi n}{M_S-(N_D-1)}) - \sum_{n=1}^{N_D}\cos(\frac{\pi n}{M_S-N_D})\Big), \quad (3.5)$$

where N_D should be small enough that the chain is still in a delocalized state – i.e., the zero gate peak is not described by this model.

In Tab. 3.1 we show a comparison of resonance positions as predicted by the reduced lattice (RL) model in Eq. (3.5), as predicted by exact diagonalization (ED) of the isolated chain, and resonances found in our DMRG calculations for interaction strengths $V = 5$, 20, and 30. The position of the outermost resonance from $0 \to 1$ particle fits well for both predictions, while the next ones from $1 \to 2$ and $2 \to 3$ deviate somewhat. The RL prediction for the transition $2 \to 3$ is not expected to be accurate since $N_D = 3$ is a localized charge density wave like state. Further the central resonance is not described by this picture as the transition is between two localized states, and the resonance is anyway pinned to zero gate potential by the particle-hole symmetry. The comparison in Tab. 3.1 shows a fair agreement such that the simple model captures the essential features of the Coulomb blockade renormalization of the resonances in the large interaction limit.

Resonance width

The conductance spectra in Fig. 3.5 show that within the weakly interacting regime of the model, $V = 1.0$, the interaction does not lead to any significant

Table 3.1: Table of resonance positions of the $M_S = 7$ site chain with interaction strengths $V = 5, 20, 30$, $\gamma = 0.5$, and $t' = t_{L/R} = 0.5$ as predicted by the reduced lattice (RL) model (Eq. (3.5)), by exact diagonalization (ED) of the isolated chain, and as found from the conductance peaks in our DMRG calculations using the real-space setup. The RL prediction for $N_D = 3$ is not expected to be accurate since the chain is in a localized charge density wave like state.

V	5			20			30		
N_D	1	2	3	1	2	3	1	2	3
RL	6.73	5.50	2.76	21.73	20.50	17.76	31.73	30.50	27.76
ED	6.77	5.88	3.85	21.75	20.63	18.03	31.74	30.59	27.94
DMRG	6.76	5.79	3.66	21.74	20.59	17.97	31.74	30.60	27.95

change of the resonance width, whereas the position of the resonances exhibit Coulomb blockade behavior.

By contrast in the strongly interacting regime there is a strong renormalization of the resonance width. The position again demonstrates Coulomb blockade renormalization, and *additionally* the resonances are sharpened significantly by the interaction. For the central peak this can be understood from a simple argument: At zero gate potential two configurations are energetically equivalent, having 3 and 4 fermions in the chain respectively. As soon as a small potential is applied one of the two becomes favorable, and a single (localized) state is selected, hence suppressing transport very quickly and resulting in a narrow resonance.

In the infinite system length limit and for interaction strengths larger than $V = 2$ the model studied here is an insulator [70, 71, 72, 73], and from the data presented we see how the insulator evolves; rather than being due to a suppression of the resonant value by the interaction it is by a suppression of the resonance *widths*. The resonant value of the conductance remains unitary, but the width of the resonances are strongly suppressed by the interaction.

While weak repulsive interaction does not influence the width of the resonances significantly compared to the non-interacting case, the strong repulsive interaction strongly reduces the resonance width. Thus strong interaction *within* the finite chain tends to suppress the transport compared to the non-interacting case, in the sense that the off-resonance transport is reduced by the interactions.

3.1.3 Real- vs momentum-space leads

In order to illustrate the accuracy of the momentum-space compared to the real-space leads we have recalculated some of the results for a resonant

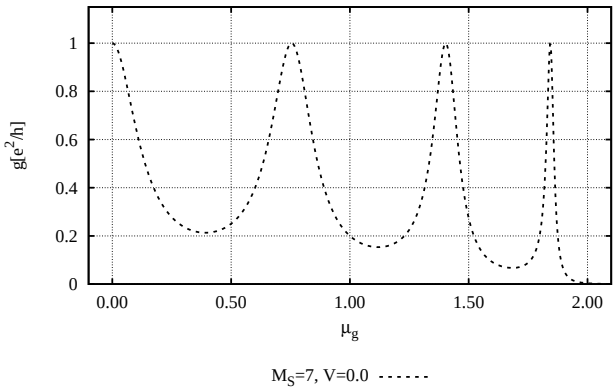

(a) $M_S = 7$ and $V = 0.0$. Exact diagonalization calculation.

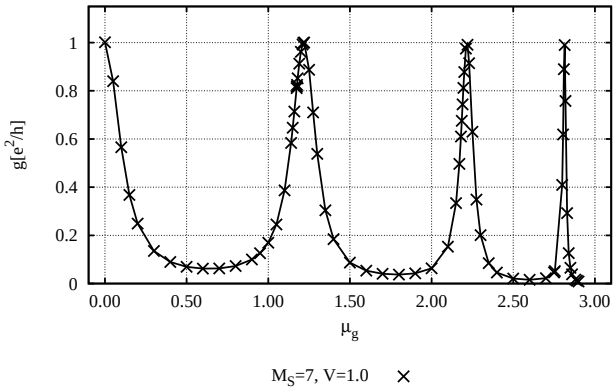

(b) $M_S = 7$ and $V = 1.0$. DMRG calculation.

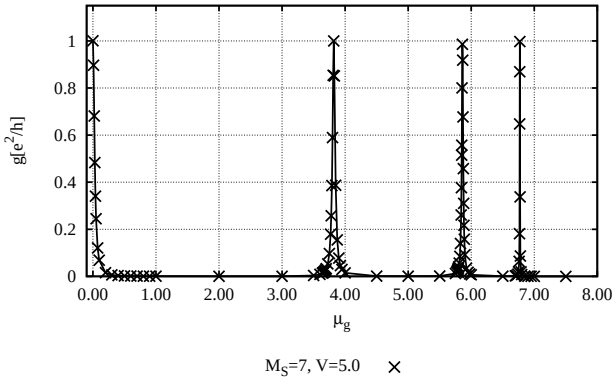

(c) $M_S = 7$ and $V = 5.0$. DMRG calculation.

Figure 3.7: Conductance, g, versus gate potential μ_g for a resonant $M_S = 7$ site chain. The calculations were performed using the momentum-space leads and the parameters $t' = t_{L/R} = 0.5$ and $t_D = 1$. A total of 120 sites was used in the momentum-space leads, corresponding to 40 logarithmically scaled sites and 20 linearly scaled sites per lead. For the non-interacting system exact diagonalization was used, while the interacting data are DMRG calculations. Note that the interaction is *not* smoothed over the contacts – i.e., $\gamma = 0.0$. The lines added to the DMRG results are guides to the eye.

$M_S = 7$ site chain using the momentum-space DMRG setup and using $\gamma = 0$. The plots for $V = 0$, $V = 1$, and $V = 5$ are shown in Fig. 3.7, where lines connecting the DMRG data points have been added as a guide to the eye.

It is clearly seen that the momentum-space leads enable sufficient accuracy to resolve the resonances and reach the unitary limit perfectly even for the outermost sharp resonances. Further we are able to investigate the *shape* of the resonances. In Fig. 3.8 for $V = 1$ and Fig. 3.9 for $V = 5$ we show a zoom in on each of the 4 resonances found for positive gate potential. To each figure is fitted a Lorentzian of half width w centered at $\mu_g = \mu_0$, where the actual parameters are specified in the figures. The agreement between the Lorentzian and the DMRG data is good, showing that indeed the shape of the resonances remains roughly Lorentzian in both regimes. Plotting the conductances on a logarithmic scale for $V = 5$ reveals that there are deviations in the low conductance regimes, such that the shape is not perfectly Lorentzian.

Since the momentum leads enabled an improved energy resolution of the resonances the linewidths can be extracted, and an overview of the widths and positions is given in Tab. 3.2. For convenience we also give the widths in units of the corresponding non-interacting resonance widths. It is seen that the width renormalization in the weakly interacting regime is moderate while in the strongly interacting regime there is a strong reduction of the resonance width, as also evident from the real-space calculations presented in Fig. 3.5.

A note regarding the fitting of Lorentzians in the non-interacting and weakly interacting cases: The resonances are not well separated from each others, as in the strongly interacting case. Thus the tails of the resonances overlap, making the fitting somewhat ambiguous. The fits presented where performed focusing on the top of each resonance where the effect of tail is minimal, which of course reduces the fitting window.

3.1.4 Conclusions

In this part of the thesis we have considered transport through an interacting resonant chain consisting of 7 sites, using DMRG evaluations of the Kubo formula for conductance. This combined approach is capable of handling strong correlations, and we have used it to study the effects on transport properties of repulsive interaction mainly within the resonant chain. We have shown that repulsive interaction can have a major impact on the transport properties; the results presented show that in the weakly interacting regime the resonance width is not significantly changed by the interaction compared to the non-interacting case, while in the strongly interacting regime interactions have a significant effect on the resonance widths, suppressing the off-resonance transport strongly.

The off-resonance transport suppression by the interaction is a precursor

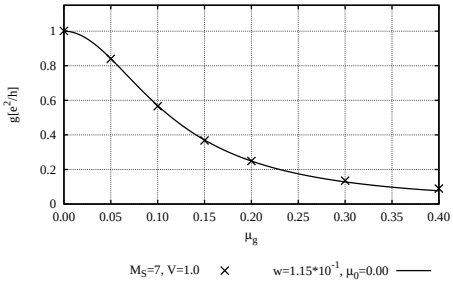

(a) Lorentzian fitted to the central resonance with parameters $w = 1.15\ 10^{-1}$ and $\mu_0 = 0.0$.

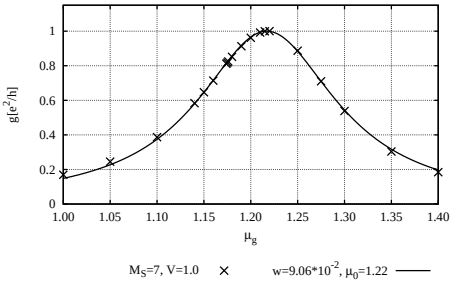

(b) Lorentzian fitted to the first resonance with parameters $w = 9.06\ 10^{-2}$ and $\mu_0 = 1.22$.

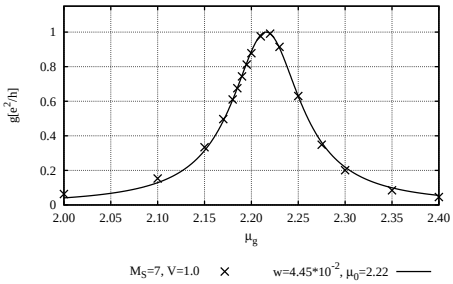

(c) Lorentzian fitted to the second resonance with parameters $w = 4.45\ 10^{-2}$ and $\mu_0 = 2.22$.

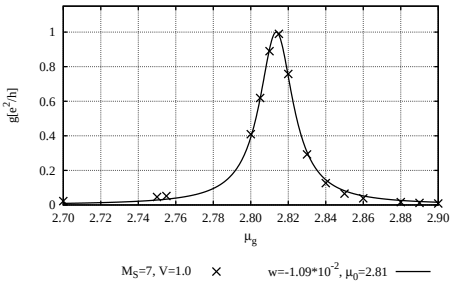

(d) Lorentzian fitted to the third resonance with parameters $w = 1.09\ 10^{-2}$ and $\mu_0 = 2.81$.

Figure 3.8: A zoom in on each of the 4 resonances of a resonant $M_S = 7$ site chain for positive gate potential and weak interaction $V = 1.0$, $t' = t_{L/R} = 0.5$, $t_D = 1$, and $\gamma = 0.0$. To each DMRG calculation is fitted a Lorentzian of half width w and centered at $\mu_g = \mu_0$, where the actual values are given in the plots and reproduced in Tab. 3.2. It is seen that the line shape remains roughly Lorentzian, although the tails of the resonances overlap and give rise to deviations.

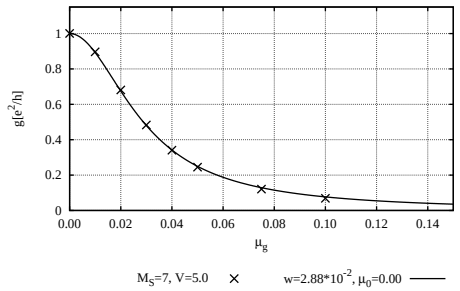

(a) Lorentzian fitted to the central resonance with parameters $w = 2.88\ 10^{-2}$ and $\mu_0 = 0.0$.

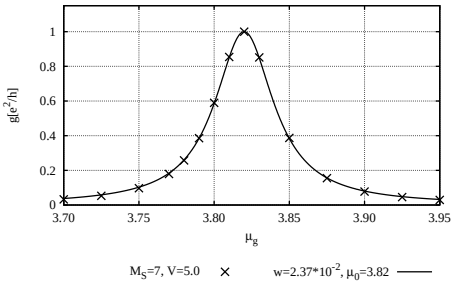

(b) Lorentzian fitted to the first resonance with parameters $w = 2.37\ 10^{-2}$ and $\mu_0 = 3.82$.

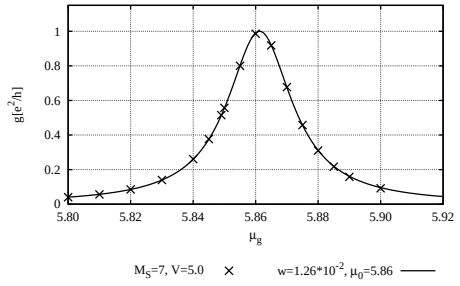

(c) Lorentzian fitted to the second resonance with parameters $w = 1.26\ 10^{-2}$ and $\mu_0 = 5.86$.

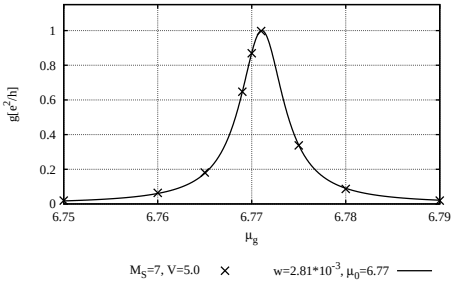

(d) Lorentzian fitted to the third resonance with parameters $w = 2.81\ 10^{-3}$ and $\mu_0 = 6.77$.

Figure 3.9: A zoom in on each of the 4 resonances of a resonant $M_S = 7$ site chain for positive gate potential and strong interaction $V = 5.0$, $t' = t_{L/R} = 0.5$, $t_D = 1$, and $\gamma = 0.0$. To each DMRG calculation is fitted a Lorentzian of half width w and centered at $\mu_g = \mu_0$, where the actual values are given in the plots and reproduced in Tab. 3.2. It is seen that the line shape remains roughly Lorentzian.

Table 3.2: Table of resonance positions and widths of an interacting $M_S = 7$ site chain with parameters $\gamma = 0.0$, $t' = t_{L/R} = 0.5$, and $t_D = 1.0$. For comparison the widths of the interacting cases are additionally given in units of the corresponding non-interacting resonance widths. It is seen that the width renormalization in the weakly interacting regime is moderate, while in the strongly interacting regime there is a significant reduction of the resonance widths.

V	0.0			
μ_0	0.0	0.75	1.40	1.84
w	$1.35\ 10^{-1}$	$1.13\ 10^{-1}$	$6.43\ 10^{-2}$	$1.83\ 10^{-2}$
V	1.0			
μ_0	0.0	1.22	2.22	2.81
w	$1.15\ 10^{-1}$ $\sim 0.85\ w_{V=0}$	$9.06\ 10^{-2}$ $\sim 0.80\ w_{V=0}$	$4.45\ 10^{-2}$ $\sim 0.69\ w_{V=0}$	$1.09\ 10^{-2}$ $\sim 0.60\ w_{V=0}$
V	5.0			
μ_0	0.0	3.82	5.86	6.77
w	$2.88\ 10^{-2}$ $\sim 0.21\ w_{V=0}$	$2.37\ 10^{-2}$ $\sim 0.21\ w_{V=0}$	$1.26\ 10^{-2}$ $\sim 0.20\ w_{V=0}$	$2.81\ 10^{-3}$ $\sim 0.15\ w_{V=0}$

of the formation of an insulating state when the system is infinitely long and the interaction V exceeds the value 2 [73]. The insulator is formed by a reduction of the *width* w of the resonances, while the resonant value of the conductance remains unitary.

By performing essentially the same calculations representing the leads in real- and momentum-space we have illustrated the difference in accuracy between these two setups. The increased accuracy of the momentum-space setup enabled a study of the individual resonances, extracting widths and positions, and showing that the line shapes remain roughly Lorentzian in both regimes.

In both the weakly and strongly interacting regimes the microscopic model studied displays Coulomb blockade renormalization of the resonance positions, where the charging of the model depends on the occupation and interaction strength. In the limit of strong interaction we have given a simple picture for the resonance position and explained the sharpening of the resonances.

3.2 Interacting resonant level models

Perhaps the simplest possible model in a transport setup is a single spinless resonant level coupled to leads. Including nearest neighbor interaction only *within* the nanostructure makes this model generically non-interacting. Allowing additionally interaction on the contact links defines the model we denote by the interacting resonant level model (IRLM). The motivation for studying resonant level models with interaction on the contact links is the physically realistic situation that the interaction inside the transport region does not vanish abruptly in the contacts, and the resonant level model is a simple model incorporating this effect.

Resonant level models in various formulations are common textbook examples because of their simplicity [27], which also make them a good testing ground for new methods and approaches. For the IRLM in particular we would like to mention two recent contributions, Refs. [64, 65] using the scattering Bethe ansatz, and Ref. [74] using a perturbative approach. While we find the same qualitative behavior as both these groups, it is our belief that our approach covers regimes and aspects not accessible by the other approaches. While Ref. [74] has problems reaching the unitary limit we get it perfectly, and Ref. [64] does not yet cover the case of having the level resonant, and thus cannot target the infinitesimal voltage regime we are considering. Most of the results presented in this section were published in Ref. [75].

In the previous section it was shown that strong interaction inside the nanostructure itself suppresses the off-resonance transport. In this section we show that even a small leak of interaction into the contacts can increase the off-resonance transport significantly, and that the resonance width shows a non-monotonic dependence on the interaction in the weak coupling limit that we target here.

In this part we use the enhanced DMRG scheme where part of the leads are put in momentum-space, see Chap. 2.3.4 for details. This facilitates a much higher energy resolution which is needed for these calculations. An example setup is shown in Fig. 3.10 illustrating a four site resonant chain. We include a part of the lead in real-space to account for local – i.e., high-energy physics. The nanostructure is denoted by S, while the combined nanostructure and real-space sites in the leads are denoted the extended system, S_E, with M_E real-space sites in total. In the figure the interactions and hopping matrix elements are indicated, and note that the gate potential μ_g is only applied to the nanostructure.

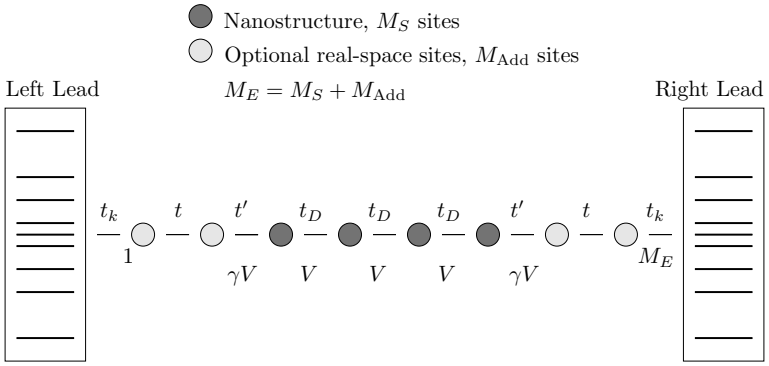

Figure 3.10: General layout in the momentum-space setup. The interacting chain is coupled to non-interacting leads via hopping matrix elements $t' = t_{L/R}$. The hopping matrix elements and interaction inside the chain is given by t_D and V respectively and the leaking of interaction into the contacts is governed by γ. The leads are modeled by M_{Add} sites kept in real-space, close to the chain, and then coupled to momentum-space leads via discretization dependent hopping matrix elements t_k, such that the real-space site couples to *all* momentum-space sites. There is full flexibility to choose the discretization scheme appropriate for the calculation, and the direct coupling to the low-energy sector prevents problems with trapping of fermions in the low-energy sector.

The Hamiltonian is $H = H_{RS} + H_{MS} + H_T$,

$$\begin{aligned} H_{RS} &= \sum_{j\in S} \mu_g c_j^\dagger c_j - \sum_{j,j-1\in S_E} \left(t_j c_j^\dagger c_{j-1} + \text{h.c.}\right) \\ &\quad + \sum_{j,j-1\in S_E} V_j \Big(n_j - \frac{1}{2}\Big)\Big(n_{j-1} - \frac{1}{2}\Big), \qquad (3.6a) \\ H_{MS} &= \sum_{k\in L,R} \varepsilon_k c_k^\dagger c_k, \qquad (3.6b) \\ H_T &= -\sum_{k\in L} \left(t_k c_k^\dagger c_1 + \text{h.c.}\right) - \sum_{k\in R} \left(t_k c_k^\dagger c_{M_E} + \text{h.c.}\right), \qquad (3.6c) \end{aligned}$$

where $c_\ell^\dagger$ and c_ℓ are the (spinless) fermionic creation and annihilation operators at site ℓ and $n_\ell = c_\ell^\dagger c_\ell$ is the local density operator at site ℓ. H_{RS}, H_{MS}, and H_T denote real-space, momentum-space, and tunneling Hamiltonians respectively, and the indices 1 and M_E denote the first and last site in S_E. We use a finite bandwidth for the leads, such that the band ranges from $-D$ to D in energies, and mostly consider a particle-hole-symmetric cosine-band between ± 2.

Using the momentum-space DMRG framework reviewed in Chap. 2.3.4 we have calculated the linear conductance of the interacting resonant level model and interacting chains of $M_S = 3$ and $M_S = 5$ sites, both including

interaction on the contact links. The IRLM without interaction on the contact links is completely non-interacting, while for the 3 and 5 site chains two different interactions are present, V inside the chain and γV on the contact links, such that the parameter γ models the leak of the interaction into the contacts.

In the calculations presented for the interacting resonant level model and the short resonant chains considered here we typically keep up to $m = 800$ states per block, leading to typical target space dimensions of $600.000 - 640.000$ states. A total of 120 sites was used in the momentum-space leads, corresponding to 40 logarithmically scaled sites and 20 linearly scaled sites per lead.

First we consider the simplest model where the transport region consists of a single level, and demonstrate the non-monotonic transport enhancement for this model. We then proceed and consider short resonant chains, and find the same kind of behavior for these extended systems.

3.2.1 The interacting resonant level model

In this part we consider the simplest case of a single resonant level interacting with the neighboring lead sites, and $\gamma = 1$ for this model such that the full interaction is on the contact links. Using the momentum-space DMRG setup we have calculated the conductance of this model, and the resulting spectra are shown in Fig. 3.11 for two different couplings to the leads. To each set of DMRG data is fitted a Lorentzian with a width w, where the specific values are given in the figures. We find in general that the shape of the resonances remain Lorentzian, but with a strong and non-monotonic renormalization of the width by the interaction. For example with $t' = t_{L/R} = 0.01$ and $\gamma V = 1.0$ the resonance width is a factor of 10 larger compared to the non-interacting case.

For repulsive contact interactions below the Fermi velocity, $\gamma V < v_F = 2$, we find a strong increase in the resonance width, that become up to an order of magnitude larger than the non-interacting result. However, for repulsive interaction larger than the Fermi velocity, $\gamma V > v_F = 2$, the off-resonance transport is once again suppressed when increasing the interaction.

In order to investigate the dependence of the resonance width and position on the band cutoff in the leads, we have performed calculations on a non-particle-hole-symmetric model, such that the resonance is no longer pinned at $\mu_g = 0$ by the particle-hole symmetry. In Fig. 3.12 we have used a linear band in order to keep the Fermi velocity fixed, and varied the bandwidth an order of magnitude to investigate what sets the scale for the width renormalization. It is apparent that the result is independent of the cutoff parameter D, and we conclude on this basis that the Fermi velocity rather than the band cutoff sets the relevant scale in the model.

For completeness we have also performed calculations on the interacting

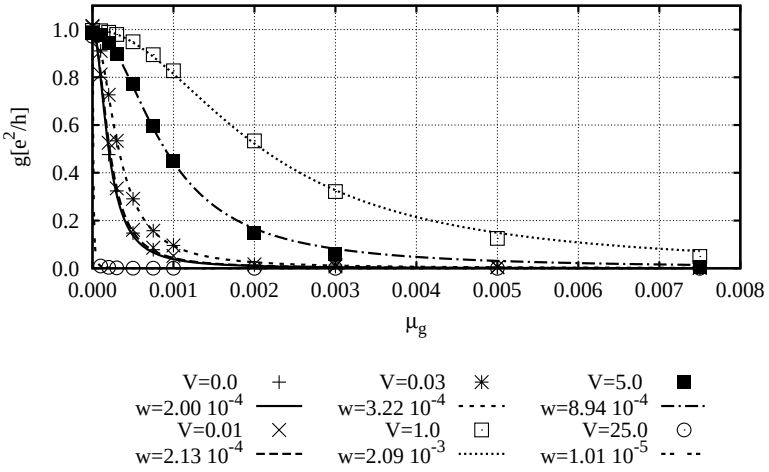

(a) $t' = 0.01$

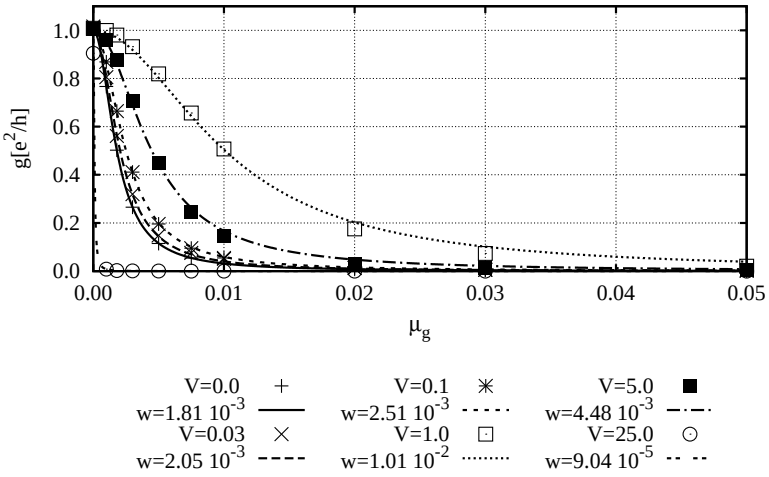

(b) $t' = 0.03$

Figure 3.11: Conductance of the interacting resonant level model with $\gamma = 1$ for two different couplings to the leads, and the leads modeled by a cosine-band between ± 2. To each set of DMRG data has been fitted a Lorentzian of half width w at half maximum. The repulsive contact interaction results in a non-monotonic behavior for the resonance width versus the interaction.

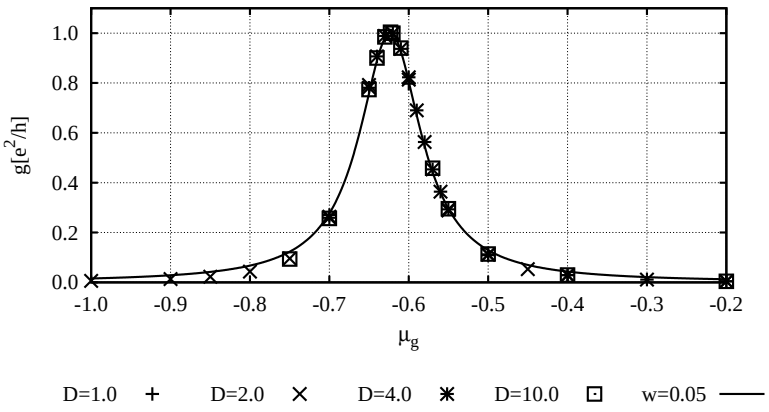

Figure 3.12: Conductance of the non-particle-hole-symmetric interacting resonant level model with $\gamma = 1$, $t' = t_{L/R} = 0.1$, and the leads modeled by a linear band between $\pm D$. To the DMRG data has been fitted a Lorentzian of half width w at half maximum. The different data sets fall on the same Lorentzian curve illustrating that the resonance position and width are independent of the cutoff.

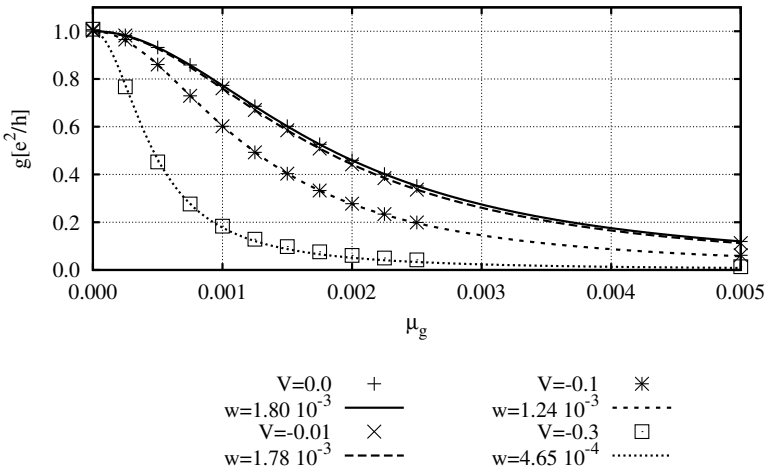

Figure 3.13: Conductance of the interacting resonant level model with attractive interaction, $\gamma = 1$, $t' = t_{L/R} = 0.03$, and the leads modeled by a cosine-band between ± 2. To each set of DMRG data has been fitted a Lorentzian of half width w at half maximum. The attractive contact interaction suppresses the off-resonance transport even for weak interaction strengths.

Table 3.3: Table of resonance widths of the interacting resonant level model. The resonance displays a strong and non-monotonic dependence on the resonance width for both values of the coupling.

(a) Resonance width w for $t' = t_{L/R} = 0.01$ versus V.

V	w
0.0	$2.00\ 10^{-4}$
0.01	$2.13\ 10^{-4}$
0.03	$3.22\ 10^{-4}$
1.0	$2.09\ 10^{-3}$
5.0	$8.94\ 10^{-4}$
25.0	$1.01\ 10^{-5}$

(b) Resonance width w for $t' = t_{L/R} = 0.03$ versus V.

V	w
-0.3	$4.65\ 10^{-4}$
-0.1	$1.24\ 10^{-3}$
-0.01	$1.78\ 10^{-3}$
0.0	$1.81\ 10^{-3}$
0.03	$2.05\ 10^{-3}$
0.1	$2.51\ 10^{-3}$
1.0	$1.01\ 10^{-2}$
5.0	$4.48\ 10^{-3}$
25.0	$9.04\ 10^{-5}$

resonant level model for attractive interaction using $t' = t_{L/R} = 0.03$, as seen in Fig. 3.13. Using an interaction of ten times the hopping, $V = -0.3$, reduces the resonance width by a factor of 4, and the attractive interaction thus suppresses the off-resonance transport strongly. The attractive interaction could for instance be realized by means of a substrate, such that the screening cloud of a particle attracts other particles. For convenience we have collected the resonance widths of the IRLM for the different parameters used in Tab. 3.3.

It was suggested by Borda *et al.* [74] that the explanation for the transport enhancement should be found in the densities of the neighboring lead sites. It was argued that a repulsive interaction keeps the first lead sites empty such that electrons can easily tunnel in, go through the structure and leave again through the drain electrode [74]. In order to test this explanation we have calculated the density of the dot, n_d, and the average density of the first lead sites, n_c, versus the interaction strength of the IRLM for two different finite values of the gate potential, $\mu_g = 0.0002$ and $\mu_g = 0.0005$.[2] The results are shown in Figs. 3.14. The large increase in resonance width is found in the interval $0 < V < 2$, while larger interactions again suppress the off-resonance transport. In this interaction interval we find a charging of the dot, and the lead density *increases* slightly rather than decreases. Thus it appears that the suggestion in Ref. [74] is not the correct mechanism.

In the very strongly interacting regime where the transport is again

[2]Using $\mu_g = 0.0$ would result in strict half filling for each site due to the particle-hole symmetry.

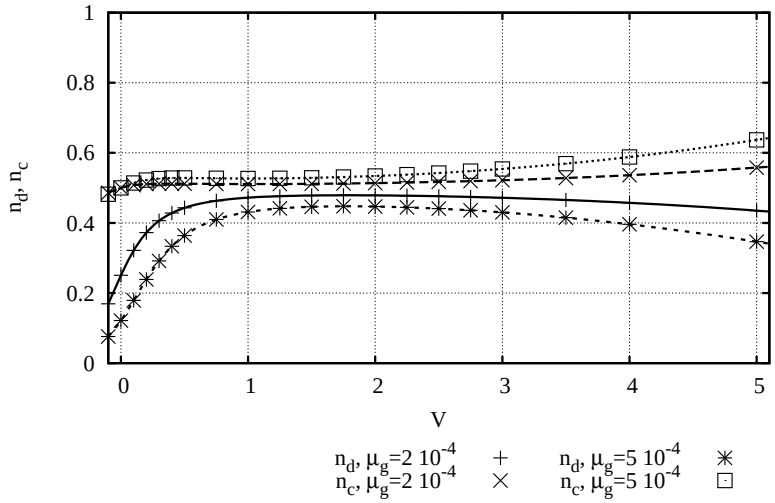

(a) Zoom in of the range where the maximum in interaction is found.

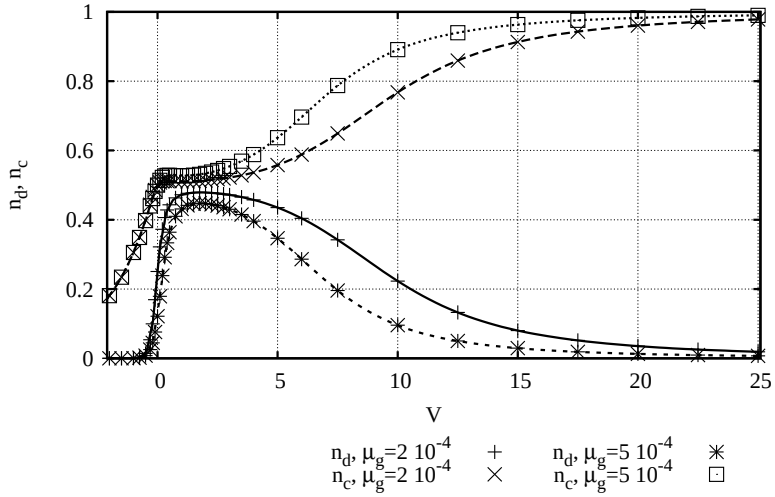

(b) Full range of interactions strengths.

Figure 3.14: Density of the dot, n_d, and the average density of the first lead sites, n_c, versus interaction strength of the interacting resonant level model for two finite values of the gate potential μ_g. Due to the finite gate potential the resonant level is depleted in the non-interacting case. The repulsive interaction on the contact links initially increases the density towards half filling, and for stronger interaction strengths again depletes the level. Hence the densities do follow the conductance to some extent but the leads are not depleted by the increasing interaction as suggested by Borda *et al.* [74], rather charge is built up in the leads close to the resonant level.

suppressed the calculated densities indicate a buildup of charge close to the level, while the level itself is emptied. It is apparent from Fig. 3.14 that the density and the conductance are correlated, but it remains an open question what the governing mechanism is [75].

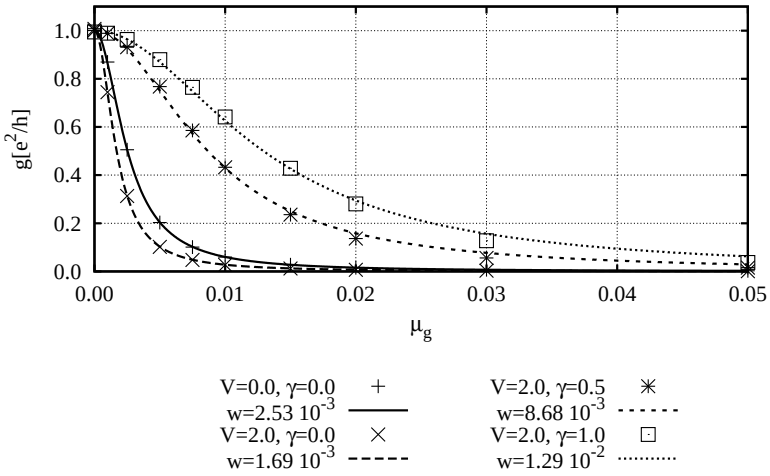

Figure 3.15: Conductance of an interacting resonant $M_S = 3$ site chain with coupling $t' = t_{L/R} = 0.05$ to the leads, $t_D = 0.5$, and the leads modeled by a cosine-band between ± 2. To each set of DMRG data has been fitted a Lorentzian of half width w at half maximum. The non-monotonic dependence on the resonance width is absent for the resonant chain with this strength of the interaction since the contact interaction is limited in magnitude by $V = 2.0$. The increase is present, however, indicating that the increase by contact interaction is stronger than the corresponding decrease due to interactions inside the chain.

3.2.2 Resonant chains with contact interaction

To investigate if the transport enhancement is a special feature of the single resonant level we have performed calculations for resonant $M_S = 3$ and $M_S = 5$ site chains. Within these models two different interactions are present, the nearest neighbor density-density interaction V within the chain, and the leaking of this interaction onto the contact links γV.

Figs. 3.15 and 3.17 show for different interaction strengths that the central peak of the conductance spectrum for the $M_S = 3$ site chain exhibits the same qualitative behavior as the single resonant level. The suppression of transport by the interaction inside the chain, as demonstrated in Chap. 3.1, is apparent in the figures when $\gamma = 0$. Nevertheless a small leak of the interaction into the contacts results in a significant enhancement of the off-resonance transport. For $V = 2.0$ the width of the resonance for $\gamma = 1.0$ is almost an order of magnitude larger than for $\gamma = 0.0$, which is comparable to the single level case. For $V = 3.0$ and $V = 5.0$ the suppression for $\gamma = 0$

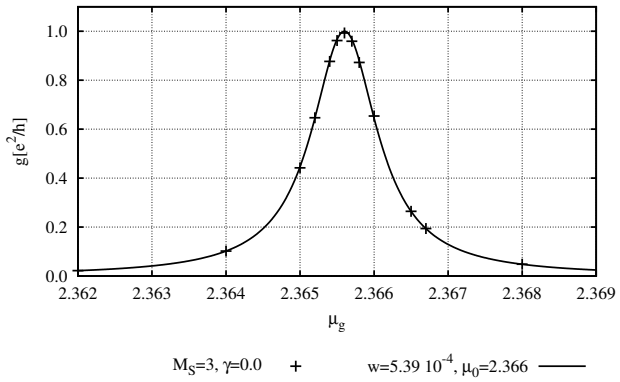

(a) $V = 2.0$ and $\gamma = 0.0$

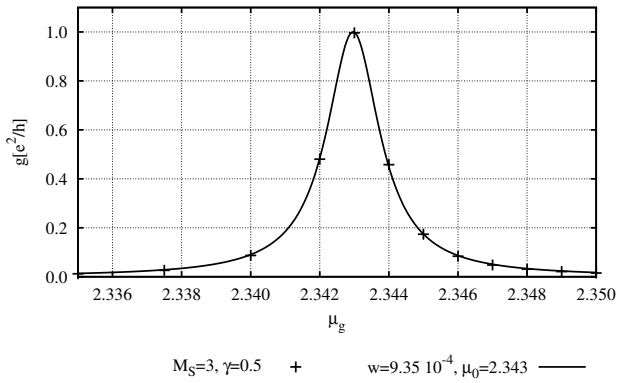

(b) $V = 2.0$ and $\gamma = 0.5$

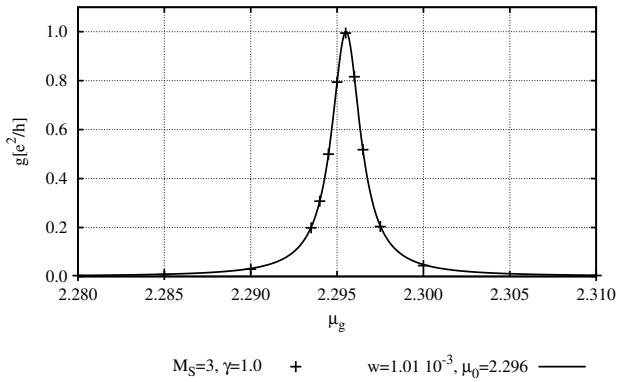

(c) $V = 2.0$ and $\gamma = 1.0$

Figure 3.16: The finite gate potential resonance of an interacting resonant $M_S = 3$ site chain with coupling $t' = t_{L/R} = 0.05$ to the leads, $t_D = 0.5$, and the leads modeled by a cosine-band between ± 2. The interaction $V = 2.0$ is spread on the contact links by γ. To each set of DMRG results is fitted a Lorentzian with half width w at half maximum, and located at $\mu_g = \mu_0$, and the specific values are given in the figures. The increase in resonance width is present for the finite gate resonances, however the increase is less pronounced, and additionally the position of the resonances is changed by the interaction. Notice the different μ_g-scales used in the plots. The positions and widths are collected in Tab. 3.4.

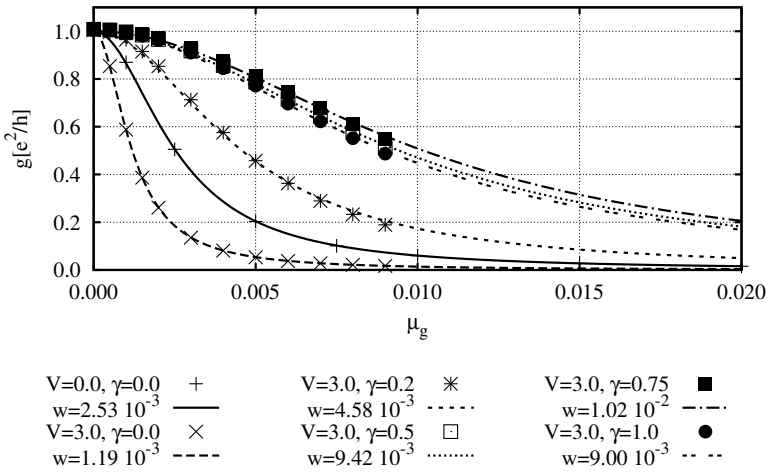

(a) $V = 3.0$

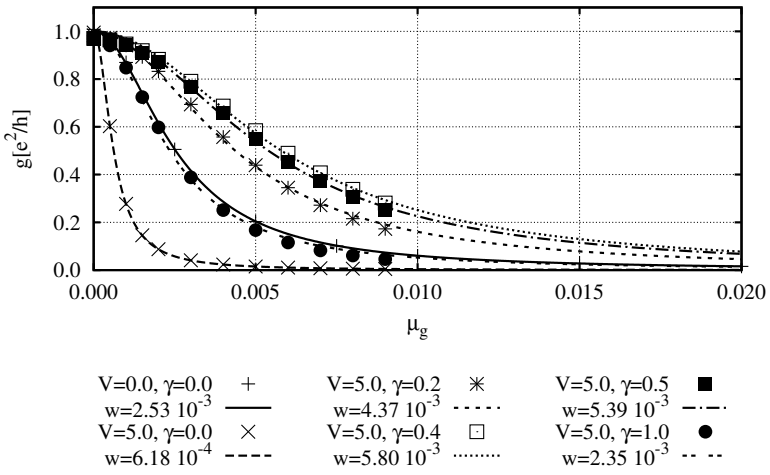

(b) $V = 5.0$

Figure 3.17: Conductance of an interacting resonant $M_S = 3$ site chain with coupling $t' = t_{L/R} = 0.05$ to the leads, $t_D = 0.5$, and the leads modeled by a cosine-band between ± 2. Two different interactions V were used, and the interaction is spread onto the contact links by γ. To each set of DMRG data has been fitted a Lorentzian of half width w at half maximum. These systems display a non-monotonic behavior in the resonance width indicating that the increase is stronger than the corresponding decrease due to interactions inside the chain.

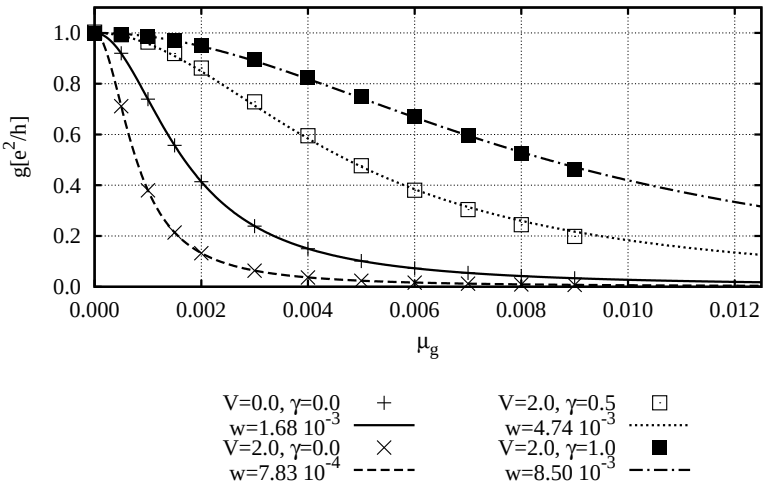

Figure 3.18: Conductance of an interacting resonant $M_S = 5$ site chain with coupling $t' = t_{L/R} = 0.05$ to the leads, $t_D = 0.5$, and the leads modeled by a cosine-band between ± 2. The interaction used is $V = 2.0$ and it is spread onto the contact links by γ. To each set of DMRG data has been fitted a Lorentzian of half width w at half maximum. The $M_S = 5$ site chain displays a similar increase in resonance width as the IRLM.

is comparably stronger than for $V = 2.0$, but the enhancement is still significant, and the maximal resonance widths are found for $\gamma = 0.75$ and $\gamma = 0.4$ respectively, consistent with a maximum value found for $\gamma V \sim v_F = 2.0$.

Since the contact interaction is limited in magnitude by V the non-monotonic dependence on the resonance width is only found for sufficiently large values of V. In Fig. 3.15 the non-monotonicity is absent since $\gamma V < 2$, whereas in Figs. 3.17 the non-monotonicity is clearly visible when $\gamma V > 2$.

The $M_S = 3$ site chain has additionally a resonance located at finite gate potential, and a natural question to ask is whether this also shows the same non-monotonic behavior versus interaction on the contact links. As the position of the resonance is renormalized by the contact interaction the resonances cannot be represented in the same figure. In Figs. 3.16 we have plotted the resonances as well as Lorentzians fitted to the data. For an easy comparison the extracted resonance widths and positions are collected in Tab. 3.4. The finite gate resonance also shows an increase in the width when including interaction on the contact links, but the increase is not nearly as pronounced as for the central resonance. Whereas the width of the central resonance increases up to an order of magnitude, the width of the finite gate resonance merely increases by a factor of two but does show an increase for repulsive contact interaction.

Finally we have considered the central resonance of an interacting resonant $M_S = 5$ site chain. In the weakly coupled limit this resonance behaves

similarly to the 3 site chain, as seen in Fig. 3.18, such that there is a difference of an order of magnitude between having no interaction on the contact, $\gamma = 0$, and having the full interaction on the contact, $\gamma = 1$.

Thus we have shown that the enhancement by a small interaction on the contacts is stronger than the suppression by a strong interaction inside the chain. Hence the strong and non-monotonic enhancement of the transport by interaction on the contact links is not a peculiarity of the single level model, but a generic feature for systems with interaction on the contacts.

Table 3.4: Table of resonance positions and widths of an interacting resonant $M_S = 3$ site chain with $t' = t_{L/R} = 0.05$ and $t_D = 0.5$. The central peak displays a strong increase in the resonance width, while the similar effect for the finite gate peak is less pronounced. Tab. (a) shows the resonance widths and positions for the interactions $V = 0$ and $V = 2$, while Tabs. (b)-(d) compare directly the width of the central resonance for different parameters.

(a) Resonance width w and position μ_0 for $V = 0$ and $V = 2$, versus γ.

	$V = 0.0$		$V = 2.0$, $\gamma = 0.0$	
μ_0	0.0	0.71	0.0	2.366
w	$2.51\ 10^{-3}$	$1.26\ 10^{-3}$	$1.7\ 10^{-3}$	$5.39\ 10^{-4}$
	$V = 2.0$, $\gamma = 0.5$		$V = 2.0$, $\gamma = 1.0$	
μ_0	0.0	2.343	0.0	2.296
w	$8.7\ 10^{-3}$	$9.35\ 10^{-4}$	$1.3\ 10^{-2}$	$1.01\ 10^{-3}$

(b) Resonance width w for $V = 2.0$ versus γ.

γ	w
0.0	$1.7\ 10^{-3}$
0.5	$8.7\ 10^{-3}$
1.0	$1.3\ 10^{-2}$

(c) Resonance width w for $V = 3.0$ versus γ.

γ	w
0.0	$1.19\ 10^{-3}$
0.2	$4.58\ 10^{-3}$
0.5	$9.42\ 10^{-3}$
0.75	$1.02\ 10^{-2}$
1.0	$9.00\ 10^{-3}$

(d) Resonance width w for $V = 5.0$ versus γ.

γ	w
0.0	$6.18\ 10^{-4}$
0.2	$4.37\ 10^{-3}$
0.4	$5.80\ 10^{-3}$
0.5	$5.39\ 10^{-3}$
1.0	$2.35\ 10^{-3}$

3.2.3 Conclusions

A common paradigm in transport calculations is to make a hard distinction between the interacting transport region and the non-interacting leads. Correlation effects are thus kept within the transport region, and the leads serve simply as structureless reservoirs of particles. For some methods this distinction is principal and essential for the success of the method, while for others it is a reasonable assumption.

In this chapter we have considered transport through a single resonant level and short interacting resonant chains, interacting additionally with the neighboring lead sites via a density-density interaction. The effect of repulsive interaction on the contact links has been studied and it was found that the widths of the resonances have a non-monotonic dependence on the interaction strength. For the models considered in this chapter even a small leak of the interaction into the contacts influences the off-resonance transport strongly. We have shown this feature to be stable against the suppression of transport by interaction within the resonant chains themselves. The resonance at zero gate potential as well as the finite gate resonances display a width dependence on the interaction, where for the latter the effect is less pronounced. Finally by considering a non-particle-hole-symmetric model we have shown that these conclusions are independent of the cutoff.

The results presented in this chapter thus challenge the common division between transport region and leads. The stability of the transport enhancement suggests that this feature is universal, and demonstrates that great care should be taken when partitioning the system, particularly regarding the interactions.

Chapter 4

Spinful models

Electronic equipment as we know it from consumer products is based on manipulating the charge degree of freedom of the electrons constituting the current in the circuits. The development since the late 60's within the electronic industry has followed an exponential increase in the number of transistors in CPU's, and a corresponding exponential decrease in the feature size in for instance memory cells. This impressive relation was first predicted in 1965 by co-founder of Intel Corporation Gordon E. Moore and is commonly referred to as Moore's law [5].

As an illustration of the status of the technological development in the industry current production line CPU's feature structures of 45 nm. However successful the silicon industry has been in keeping up the speed of development it is clear that this cannot continue indefinitely. In fact the International Technology Roadmap for Semiconductors[1] (ITRS) predicts for many known manufacturing processes and designs that the limit of existing technology will be reached in the coming years. The colorcoded schematics released by ITRS has lead to the name "the red brick wall" for this event as more and more fields in the schematics become red, indicating that no known solutions exists for the advancement of a given technology. It is clear that the industry is aware of these problems, and are struggling to find suitable solutions to sustain Moore's law.

The electron has two different degrees of freedom, the charge and the spin. In recent years another field has emerged, primarily within fundamental science, manipulating the spin rather than the charge degree of freedom [76]. This field of research is commonplace referred to as spintronics, and the hope is to be able to construct analogs of electronic circuitry using spins rather than charges. A precise definition of the field of spintronics is somewhat lacking but we will use it to refer to transport where the spin can be manipulated by external means. In this work a simple model that exhibits this kind of behavior is considered. In order to approach the topic 'from below' it is important to construct simple models exhibiting the essential mechanisms at play in more complicated structures. The model we consider is known as the ferromagnetic Anderson model with an applied magnetic field ($\vec{B}$-field) [77, 78], abbreviated the FAB model.

4.1 The ferromagnetic Anderson model with an applied magnetic field

In the simplest form the model considers transport through a single resonant level subject to an external magnetic field, and with spin-polarized leads. The magnetic field couples to the spin degree of freedom and hence the spin can be manipulated by an external handle. In one limit the FAB model acts

[1] The ITRS is a report made by the worlds leading chip manufacturing regions to ensure cost-effective advances in the technology, `http://www.itrs.net/`.

as a spin valve where tuning the angle between the external magnetic field and the direction of polarization from 0 to π changes the spin species that is allowed through the dot.

The FAB model is an example of a model that exhibits both coherence and correlation effects. Thus apart from being a spintronics model, the FAB model also exhibits some quite general challenges for the theoretical methods applied to it [79]. This class of models includes effects like the Fano- and Aharonov-Bohm effects such that a successful application of the DMRG method presented in Chap. 2.3 to the FAB would open up further interesting models to consider.

In this chapter we first present the FAB model itself and discuss a tight-binding formulation. We then present the DMRG setup for the model, which involves modeling of the spin-polarized leads, as well as a spin non-conserving interacting resonant level. These technical complications turned out to require a different approach to the conductance than the direct DMRG evaluation of the Kubo formula. The Meir-Wingreen formula [27] was used instead, and an overview of this approach is presented. We then discuss some existing knowledge about the transport behavior of the model, results useful for benchmarking the developed DMRG setup.

Finally the first results for the model are presented and some aspects of the physics are discussed. Due to time constraints we do not present a thorough investigation of the FAB model, rather limit ourselves to presenting a limited amount of data, as well as a comparison with data provided by Jonas N. Pedersen. It will be the target of future work to investigate in detail the behavior of the FAB model, and to perform a more rigorous comparison with other approaches [78, 80]. We therefore conclude the chapter by giving an overview of the future work within the FAB project.

The work on the FAB model presented in this chapter is part of an ongoing effort in collaboration with Ph.D. student Jonas N. Pedersen[2] and Dr. Tomáš Novotný[3].

4.1.1 The model

The FAB model as we consider it here describes a quantum dot with a single spin-degenerate level with bare energy ε_d coupled to two (partially) spin-polarized leads. The level in the dot is split by a magnetic field, $\vec{B}$, applied at an angle ϕ with the direction of magnetization in the leads, as shown schematically in Fig. 4.1. The magnetic field is assumed to interact only with the spin of the dot electrons, leaving the leads unaffected. It has been argued [77] that this type of setup could be realized by using magnetic thin films as leads, such that the magnetic field in the leads is strongly locked to

[2]Mathematical Physics, Lund University, Lund, Sweden.

[3]Department of Condensed Matter Physics, Charles University, Prague, Czech Republic.

the plane of the film, and the addition of a magnetic field to the dot does not perturb the leads significantly.

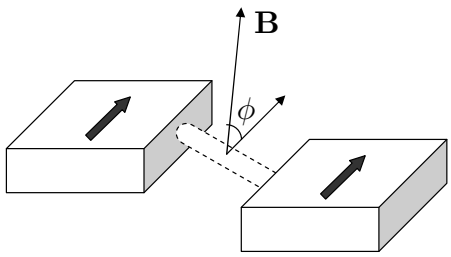

Figure 4.1: Sketch of the ferromagnetic Anderson model with an applied magnetic field. The magnetic field, $\vec{B}$, is applied at an angle ϕ with the direction of the polarization, and interacts only with the spin on the transport level. The model is a simple spintronics model exhibiting both coherence and correlation effects, making the theoretical treatment of the model challenging. Figure from Ref. [77]

Choosing a coordinate system where the magnetization of the leads is along the z-axis, the magnetic field is chosen to rotate in the xz-plane. Letting ϕ denote the polar angle in this coordinate system the magnetic field is given by $\vec{B} = B\,(\sin\phi, 0, \cos\phi)$, where $B = |\vec{B}|$ is the magnitude of the magnetic field. With these choices the Hamiltonian of the FAB model reads $H = H_L + H_R + H_C + H_D + H_B$

$$H_{L,R} = \sum_{k\in\{L,R\},\sigma} \varepsilon_{k\sigma} c^\dagger_{k\sigma} c_{k\sigma}, \tag{4.1a}$$

$$H_C = -\sum_{k\in\{L,R\},\sigma} \left(t_{k\sigma} c^\dagger_{k\sigma} d_\sigma + \text{h.c.} \right), \tag{4.1b}$$

$$H_D = \sum_\sigma \varepsilon_d d^\dagger_\sigma d_\sigma + U n_{d,\uparrow} n_{d,\downarrow}, \tag{4.1c}$$

$$H_B = -\frac{e}{m} \vec{S} \cdot \vec{B}. \tag{4.1d}$$

Notice that excluding H_B from the Hamiltonian corresponds to the Anderson model in the case of unpolarized leads. In the cotunneling limit, $B \gg \Gamma$, it is essential that the onsite interaction is *not* particle-hole-symmetric: As we show later the interacting particle-hole-symmetric FAB model maps onto the non-interacting case with a renormalized magnetic field in this limit.

The Hamiltonian in Eq. (4.1a) represents the leads, and these are treated as non-interacting and spin-polarized, as we discuss in Chap. 4.1.3. Eq. (4.1b) describes the tunneling between the dot and the leads through spin-dependent hopping matrix elements $t_{k\sigma}$. It should be emphasized that in this description the tunneling process is diagonal in the spin of the electrons, in the sense that the spin is *not* flipped in the tunneling process itself.

Eqs. (4.1c) and (4.1d) describe the bare level of the dot, the first being the isolated dot including the onsite Coulomb interaction U, and the latter the interaction of the electron spin with the magnetic field.

Due to the non-collinearity of the polarization and the magnetic field two different spin bases are involved, the spin basis of the leads and the spin basis for the dot. There is a freedom of choice in the basis used for the dot; either a diagonal basis is used such that the dot is spin conserving, but the dot spins are rotated compared to the lead spins, or a non-diagonal basis is used for the dot, where the dot spins and the lead spins are described in the same basis but where the spin on the dot is no longer conserved. We adopt the latter picture using the non-diagonal basis for the isolated dot.

The interaction between the magnetic moment of the electrons on the dot and the magnetic field is represented by Eq. (4.1d): $\vec{S}$ is the spin operator which in first quantization reads $\vec{S} = \frac{\hbar}{2}\vec{\tau}$, where $\vec{\tau}$ is the vector containing the Pauli spin matrices, $\vec{\tau} = \{\sigma_x, \sigma_y, \sigma_z\}$. The second quantized representation of $\vec{S}$ is

$$S_x = \frac{\hbar}{2}\left(d_\downarrow^\dagger d_\uparrow + d_\uparrow^\dagger d_\downarrow\right), \tag{4.2a}$$

$$S_y = i\frac{\hbar}{2}\left(d_\downarrow^\dagger d_\uparrow - d_\uparrow^\dagger d_\downarrow\right), \tag{4.2b}$$

$$S_z = \frac{\hbar}{2}\left(d_\uparrow^\dagger d_\uparrow - d_\downarrow^\dagger d_\downarrow\right). \tag{4.2c}$$

Choosing the coordinate system as described above and using the non-diagonal basis for the dot, the Hamiltonians of the dot H_D and the spin-interaction with the magnetic field H_B are[4]

$$H_D = \sum_\sigma \left(\varepsilon_d - \sigma B\cos\phi\right) d_\sigma^\dagger d_\sigma + U n_{d,\uparrow} n_{d,\downarrow}, \tag{4.3a}$$

$$H_B = -B\sin\phi\left(d_\uparrow^\dagger d_\downarrow + d_\downarrow^\dagger d_\uparrow\right), \tag{4.3b}$$

where $\sigma = 1(-1)$ for spin $\uparrow(\downarrow)$, and the Zeeman splitting of the level is angular dependent. Notice that we have absorbed a diagonal term from H_B into H_D. The spin-flip on the dot for finite angle of the magnetic field, given by $B\sin\phi$, destroys the spin conservation on the dot. Further the polarization of the leads is still unspecified and can be modeled in different ways as will be discussed later.

Despite the apparent simplicity the FAB model contains much complexity due to the splitting of the (otherwise) degenerate spin level on the dot, and the rotated spin basis due to the magnetic field. This opens up the possibility of having two different paths through the dot, and leads to interference effects, such that both correlation and coherence are important. Previous

[4]For convenience we use 'natural' units where $\frac{e\hbar}{2m} = 1$ such that B has the units of energy.

work [77, 78] has focused on two different regimes, (1) strong coupling to the leads without the Coulomb interaction U, and (2) weak coupling to the leads and including the Coulomb interaction U. With words borrowed from Ref. [78] the motivation for studying the FAB model using the DMRG is that "The crossover between these two regimes is an interesting and challenging issue, because a formalism that captures both coherence and correlations on equal footing is needed". The DMRG approach to transport is a good candidate for such a method, and it is the goal of this work to provide a unified DMRG framework for studying both these regimes of the FAB model.

4.1.2 Tight-binding Hamiltonian

In order to apply the DMRG to the FAB model a discretized version of the leads must be formulated. The simplest choice is to model the leads as one-dimensional semi-infinite tight-binding chains, that are discretized appropriately. With this choice and denoting the hopping matrix element between the resonant level and the leads by $t_{L/R,\sigma}$, the Hamiltonian reads $H = H_L + H_R + H_C + H_D + H_B$

$$H_{L,R} = -\sum_{n=1\in\{L,R\}}^{\infty}\sum_{\sigma}\frac{D}{2}\left(c^{\dagger}_{n\sigma}c_{n-1\sigma} + c^{\dagger}_{n-1\sigma}c_{n\sigma}\right), \tag{4.4a}$$

$$H_C = -\sum_{1\in\{L,R\}}\sum_{\sigma}\left(t_{L/R,\sigma}c^{\dagger}_{1\sigma}d_{\sigma} + \text{h.c.}\right), \tag{4.4b}$$

$$H_D = \sum_{\sigma}\left(\varepsilon_d - \sigma B\cos\phi\right)d^{\dagger}_{\sigma}d_{\sigma} + Un_{d,\uparrow}n_{d,\downarrow}, \tag{4.4c}$$

$$H_B = -B\sin\phi\left(d^{\dagger}_{\uparrow}d_{\downarrow} + d^{\dagger}_{\downarrow}d_{\uparrow}\right), \tag{4.4d}$$

where D is the band width of the tight-binding chain representation of the leads.

In order to link different approaches to the model a connection to the effective broadening parameter due to the leads, $\Gamma_{L/R,\sigma}$, must be established. In this particular case it is

$$\Gamma_{L/R,\sigma}(\varepsilon) = -2\ \text{Im}\left[|t_{L/R,\sigma}|^2 g^r_{L/R,\sigma}(1,1,\varepsilon)\right] \tag{4.5}$$

where $g^r_{L/R,\sigma}(1,1,\varepsilon)$ is the surface component of the retarded Greens function of the semi-infinite left (L) or right (R) chain. The surface of the tight-binding chain is the first site, and the Greens function reads [81]

$$g^r_{L/R,\sigma}(1,1,z) = 2\frac{z-\sqrt{z^2-D^2}}{D^2}, \tag{4.6}$$

where $z = \varepsilon + i\eta$ is complex and thus the imaginary part of the Greens function is finite only inside the band between $\pm D$, and is proportional to

the semi-elliptic density of states. In Chap. 4.1.3 we discuss the implementation of the polarization, and explain that half filled leads can be used, corresponding to $\varepsilon = 0$. Thus the correspondence between the broadening $\Gamma_{L/R,\sigma}$ and the hopping matrix element $t_{L/R,\sigma}$ connecting the dot and the leads is

$$\Gamma_{L/R,\sigma} = \frac{4}{D}|t_{L/R,\sigma}|^2, \tag{4.7}$$

and inserting the band width of the tight-binding chain in terms of the hopping matrix element, $D = 2t$, finally

$$\Gamma_{L/R,\sigma} = \frac{2|t_{L/R,\sigma}|^2}{t} \tag{4.8a}$$

$$\Rightarrow t_{L/R,\sigma} = \sqrt{\frac{\Gamma_{L/R,\sigma} t}{2}}. \tag{4.8b}$$

This relation links the parameters of the different methods used to calculate the conductance of the FAB model, making rigorous comparisons of the results of the different methods possible. In this work the parameter $t = 1$ sets the scale for all other parameters.

4.1.3 Modeling the polarization

There is a certain freedom of choice in the modeling of the polarization. Although the polarization is a property of the leads it can be modeled by spin and polarization dependent hopping matrix elements connecting the dot to the leads [78].

Full polarization of the leads is avoided for several reasons. Most prominently full polarization decouples one spin species in a lead completely in the sense that the hopping matrix element between the lead and the resonant level is zero for all angles. Dealing with decoupled Hilbert spaces is undesired as it creates numerical problems such as ill conditioned matrices, making the numerical solution of the resolvent equations hard.

Furthermore there are single points where the model itself is ill-defined for full polarization. At the angles $\phi = 0$ and $\phi = \pi$ the spin-flip process of the dot is inactive due to the prefactor $\sin\phi$. Furthermore due to the full polarization also the hopping matrix element for the minority spin connecting the lead and the dot is zero. Thus the minority spin level is completely decoupled, and hence has a constant occupation. The occupation of the majority spin level, however, depends on the occupation of the minority spin level through the Coulomb repulsion term $Un_{d,\uparrow}n_{d,\downarrow}$, such that the properties of the model for these specific angles depend on the initial conditions of the occupation of the minority spin level.

It should be noted that the qualitative behavior for (large) partial and full polarization are similar except for the problem of the ill-defined points

described above. It is, however, clear that a decreased polarization in the leads tends to wash out the spin dependence in the model, and in the limit of unpolarized leads all spin characteristics are lost.

There are different approaches to modeling the polarization of the leads, from which we have chosen the simplest one to implement in the DMRG setup. Rather than using spin-dependent *filling* in the leads we use half filled leads for both spin species, and model the polarization by modifying the hopping matrix elements connecting the leads and transport region. This is indicated in Fig. 4.2, where we show the DMRG setup using the momentum-space representation of the leads. This choice for the polarization simplifies the DMRG setup significantly as *identical discretizations* can be used for the two spin species in each lead, such that the spin species are again treated equally, apart from the polarization dependent hopping matrix elements t'_σ. With the tight-binding description of the leads the Hamiltonian representing the leads $H_{L/R}$ and the coupling of the dot to the leads H_C are given by

$$H_{L/R} = -\sum_{n=2\in\{L,R\}}^{\infty}\sum_{\sigma} t\left(c^\dagger_{n\sigma}c_{n-1\sigma} + c^\dagger_{n-1\sigma}c_{n\sigma}\right), \tag{4.9a}$$

$$H_C = -\sum_{1\in\{L,R\}}\sum_{\sigma} t^0_{L/R}\sqrt{\frac{1}{2}\big(1+\sigma P_{L/R}\big)}\ \left(c^\dagger_{1\sigma}d_\sigma + \text{h.c.}\right), \tag{4.9b}$$

where the leads are modeled as unpolarized and half filled, and Hamiltonians of the dot H_D and interaction with the magnetic field H_B are given in Eqs. (4.4). The polarization is modeled by different bandwidths (or densities of states at the Fermi edge) of the spin species in the leads, through polarization dependent hopping matrix elements

$$t_{L/R,\sigma} = t^0_{L/R}\sqrt{\frac{1}{2}\big(1+\sigma P_{L/R}\big)}, \tag{4.10}$$

where $\sigma = 1(-1)$ for spin $\uparrow$ ($\downarrow$) and $P_{L/R} \in [-1,1]$ is the polarization in percent of the left (L) and right (R) lead such that $P = \pm 1$ corresponds to full spin up/down polarization and $P = 0$ corresponds to unpolarized leads, and where $t^0_{L/R} = \sqrt{\Gamma^0_{L/R}/2}$ is the 'bare' hopping matrix element at the Fermi edge. Notice that $t = D/2 = 1$ has been chosen to derive the expression and this sets the scale for all other parameters. In all calculations presented we use identical polarization of the two leads, $P_L = P_R = P$, such that the coupling to the left and right leads are identical.

4.1.4 DMRG setup and complications

In the DMRG calculations for spinless models presented in Chap. 3 the leads were always fully polarized in the sense that only a single spin species

was present. By contrast the FAB model utilizes a spinful and (partially) polarized representation of the leads, such that the two spin species are formally no longer equivalent.

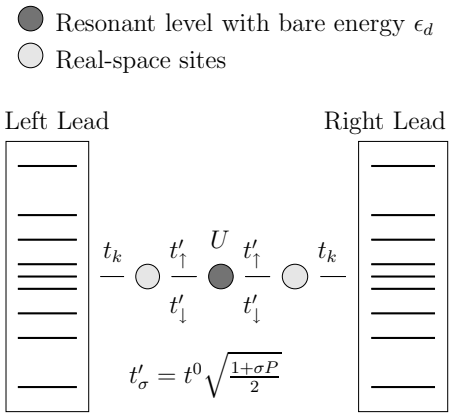

Figure 4.2: Sketch of the DMRG setup for the ferromagnetic Anderson model with a $\vec{B}$-field. Notice the implementation of the polarization through the hopping matrix elements, where $t'_\sigma = t_{L/R,\sigma}$, and the onsite Coulomb interaction U indicated in the figure. In the DMRG evaluation a single lead mapping is used in combination with a momentum-space representation of the single tight-binding lead. t_k indicates a discretization dependent hopping to *all* states in the momentum-space, see also Chap. 2.3.4.

There are a number of technicalities involved in performing DMRG calculations for this model compared to the spinless models considered in previous chapters. Usual DMRG implementations decompose the Hilbert space into subspaces according to quantum numbers, hence decomposing the full Hilbert space into smaller subspaces. The decomposition of the Hilbert space increases the performance of DMRG as it allows to search the solution within the relevant subspaces of the full Hilbert space, effectively neglecting states with different quantum numbers than desired when calculating the target state(s). Contrary to the spinless models and spin-conserving models, the FAB model breaks spin conservation which generally leads to larger Hamiltonian subspaces and decreased performance.

From initial attempts to use the real-space setup evaluating the Kubo formula for conductance directly it became clear that this approach is insufficient as the resolvent equations require a high degree of precision in order to give accurate results. Also, initial attempts to use the momentum-space setup failed as the DMRG did not converge properly in the attempt to evaluate the Kubo formula for conductance. It is a known fact that the DMRG performs best for small site bases, and the spinful site basis is twice the size of the spinless, perhaps being part of the explanation for the poor convergence in the DMRG calculations.

Although the Kubo setup turned out to be unfeasible for the FAB model we were able to calculate the conductance using a different approach: The FAB model is a single impurity model, and hence falls in the category of 'proportional coupling' models. Thus the linear conductance can be calculated from the spectral function using the Meir-Wingreen formula [27], as reviewed in Chap. 2.5.4. The rationale for doing so is purely technical: The spectral function has turned out to have a better finite size scaling, and further can be evaluated within a single lead setup, as discussed in Chap. 2.3.5. This in turn provides smaller superblocks for the DMRG and hence improves performance and accuracy. Using the momentum-space representation of the leads, together with the single lead mapping we were therefore able to perform accurate calculations of the zero frequency spectral function for the FAB model, and hence evaluate the conductance via the Meir-Wingreen formula. Notice that the momentum-space representation of the leads uses a linearization of the energy band around the Fermi edge, which is equivalent to the wide-band limit used in Refs. [77, 78].

Spin resolved conductance

In order to obtain the conductance from the spectral function we make use of the Meir-Wingreen formula [27]. Using DMRG we evaluate the two spin components of the full spectral function in different calculations, and therefore need to recombine the spin resolved spectral functions into a total conductance,

$$g \;=\; \sum_{\sigma} g_{\sigma}. \tag{4.11}$$

Using identical hopping to the left and right leads, $t_{L,\sigma} = t_{R,\sigma} = t'_{\sigma}$, or correspondingly identical polarization of the left and right leads, and utilizing additionally Eq. (2.68) the conductance of the FAB model is calculated as

$$g(\varepsilon_d, \phi) \;=\; \frac{e^2}{h}\Big(|t'_{\uparrow}|^2 A_{\uparrow}(\varepsilon_d, \phi, \omega = 0) + |t'_{\downarrow}|^2 A_{\downarrow}(\varepsilon_d, \phi, \omega = 0)\Big), \tag{4.12}$$

where the polarization enters through the hopping matrix elements as $t'_{\sigma} = t^0\sqrt{\frac{1}{2}(1+\sigma P)}$, and where the polarization is identical in the two leads, $P = P_L = P_R$ as mentioned above. In parts of this work we keep the bare level resonant, $\varepsilon_d = 0$, and focus on the dependence of the angle ϕ. For completeness we present also calculations considering the effect of varying ε_d.

4.1.5 Analytic results

A generalization of the results in [77, 78] to finite polarization of the leads was provided by Jonas N. Pedersen. Specifically a Greens functions result

in the non-interacting limit and a perturbative approach for the cotunneling regime, $B \gg \Gamma$, where the level is significantly split by the magnetic field. In this section we reproduce these results, and later we compare with results obtained using the DMRG setup. These results are derived in the wide-band limit for the density of states, where the real part of the self-energy is zero, which is compliant with the linearized cosine-band used in the DMRG approach.

Firstly the Greens function result for the conductance in the non-interacting limit is

$$g_{\mathrm{GF}} = \frac{e^2}{h}\mathrm{Re}\left[\mathrm{Tr}\left[\mathbf{G}^a\mathbf{\Gamma}_R\mathbf{G}^r\mathbf{\Gamma}_L\right]\right], \tag{4.13}$$

where using the notation from the previous sections the Greens function and broadening matrices are

$$\mathbf{G}^{r/a} = \left[\left[\mathbf{G}_0^{r/a}\right]^{-1} \pm \frac{i}{2}\left(\mathbf{\Gamma}_L + \mathbf{\Gamma}_R\right)\right]^{-1}, \tag{4.14a}$$

$$\left[\mathbf{G}_0^{r/a}\right]^{-1} = \begin{pmatrix} \varepsilon_d - B & 0 \\ 0 & \varepsilon_d + B \end{pmatrix}, \tag{4.14b}$$

$$\mathbf{\Gamma}_{L/R} = \frac{\Gamma_{L/R}}{2}\begin{pmatrix} 1 + P\cos\phi & P\sin\phi \\ P\sin\phi & 1 - P\cos\phi \end{pmatrix}. \tag{4.14c}$$

Notice that this description uses a diagonal basis for the dot such that the Greens function of the isolated dot $\mathbf{G}_0$ is diagonal whereas the coupling matrices $\mathbf{\Gamma}_{L/R}$ are non-diagonal.

The Greens function result is exact, and since the non-interacting limit is not a special case where the DMRG performs better a comparison of the two provides a rigorous benchmark for the DMRG setup, in particular for the finite size effects.

Using again identical polarizations in the two leads, $P_L = P_R = P$, the cotunneling result, valid for $B \gg \Gamma$, is

$$\begin{aligned} g_{\mathrm{COT}} = \frac{e^2}{h}\frac{\Gamma_L^0\Gamma_R^0}{4}\Big((1+P)^2\Big[\frac{\cos^2(\phi/2)}{\varepsilon_d - B} + \frac{\sin^2(\phi/2)}{\varepsilon_d + B + U}\Big]^2 \\ +2(1-P^2)\Big[\frac{-\sin(\phi/2)\cos(\phi/2)}{\varepsilon_d - B} + \frac{\sin(\phi/2)\cos(\phi/2)}{\varepsilon_d + B + U}\Big]^2 \\ +(1-P)^2\Big[\frac{\sin^2(\phi/2)}{\varepsilon_d - B} + \frac{\cos^2(\phi/2)}{\varepsilon_d + B + U}\Big]^2\Big), \end{aligned} \tag{4.15}$$

where $\Gamma_{L/R}^0$ are the bare coupling parameters. In the limit of full polarization ($P = 1$) Eq. (4.15) reduces to the results given in Refs. [77, 78].

In Chap. 4.1.6 we use the Greens function expression to verify the accuracy of the DMRG setup in the non-interacting limit, and in Chap. 4.1.7 compare results obtained from the DMRG setup with the cotunneling result for the interacting case.

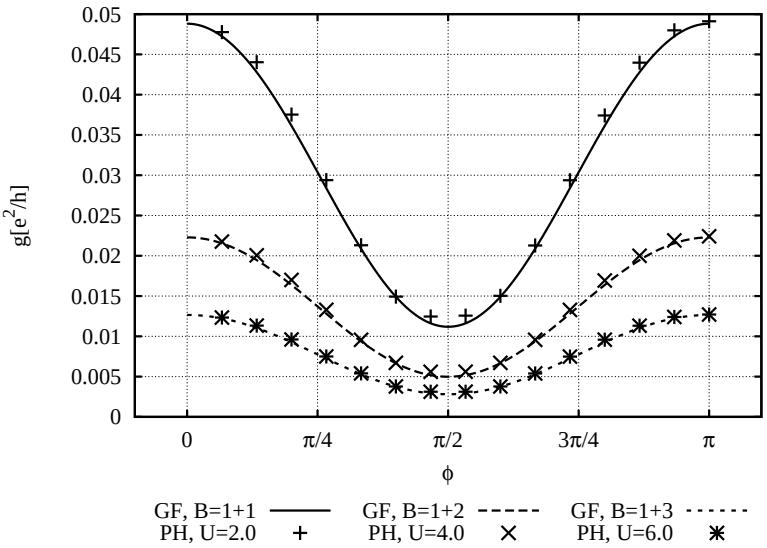

Figure 4.3: Greens function ('GF') and DMRG ('PH, U') results for the conductance versus angle ϕ for the FAB model with $P = 0.8$, $t_0' = 0.5$, $\varepsilon_d = 0$, and $B = 1$, and using a particle-hole-symmetric interaction. In the cotunneling limit this model maps onto the non-interacting model with renormalized magnetic field strength $\tilde{B} = B + \frac{U}{2}$. The discrepancy is attributed to not being completely in the cotunneling limit.

Particle-hole symmetry in the cotunneling limit

While attempting DMRG calculations on the FAB model it was realized that particle-hole symmetry plays a peculiar role for this model in the cotunneling limit $B \gg \Gamma$. In order to illustrate this we use for simplicity the fully polarized result ($P = 1$) for the cotunneling conductance in Eq. (4.15),

$$g_{\mathrm{COT}} \;=\; \frac{e^2}{h}\Gamma_L^0\Gamma_R^0\left[\frac{\cos^2(\phi/2)}{\varepsilon_d - B} + \frac{\sin^2(\phi/2)}{\varepsilon_d + B + U}\right]^2. \tag{4.16}$$

The effect of particle-hole symmetry is a compensating potential for each level on the dot compared to the non-particle-hole-symmetric interaction,

$$U\left(n_\uparrow - \frac{1}{2}\right)\left(n_\downarrow - \frac{1}{2}\right) \;=\; Un_\uparrow n_\downarrow - \frac{U}{2}\left(n_\uparrow + n_\downarrow\right) + \frac{U}{4}, \tag{4.17}$$

such that, apart from a constant that is neglected, the difference to the non-particle-hole-symmetric interaction is the local compensating potential $-\frac{U}{2}$ for each spin level on the dot, or correspondingly a renormalization of the bare energy level ε_d for the dot. Inserting $\varepsilon_d \to \varepsilon_d - \frac{U}{2}$ in the cotunneling

expression Eq. (4.16) yields

$$g_{\mathrm{COT}} = \frac{e^2}{h}\Gamma_L^0\Gamma_R^0\left[\frac{\cos^2(\phi/2)}{\varepsilon_d - \frac{U}{2} - B} + \frac{\sin^2(\phi/2)}{\varepsilon_d + \frac{U}{2} + B}\right]^2, \tag{4.18}$$

which is the non-interacting result with a renormalized magnetic field $\tilde{B} = B + \frac{U}{2}$. Comparing with the more general and more complicated expression for partial polarization Eq. (4.15) it is clear that the conclusion also holds in this case.

Hence the effect of a particle-hole-symmetric interaction in the cotunneling limit of the FAB model is to renormalize the magnetic field. The conductance in this case thus stays symmetric around $\phi = \frac{\pi}{2}$, as may be seen from Eq. (4.16) with $U = 0$ and as will be discussed in Chap. 4.1.6.

This result was found numerically as well, as shown in Fig. 4.3 for different strengths of the Coulomb interaction. The figure shows DMRG calculations of the conductance using a particle-hole-symmetric interaction, and Greens function calculations with a renormalized strength of the magnetic field, $\tilde{B} = B + \frac{U}{2}$. The two data sets agree reasonably, the disagreement attributed mainly to not being completely in the cotunneling regime, but we have not investigated this issue in further detail.

4.1.6 Results

Using the momentum-space representation of the leads in the DMRG setup we have calculated the spectral function for the FAB model, and using the Meir-Wingreen formula in Eq. (4.12) evaluated the conductance of the FAB model. We have varied the angle ϕ between the magnetic field and the polarization direction, for different values of the magnetic field strength B, the onsite Coulomb interaction strength U, and the bare energy level ε_d.

As can be seen from the Hamiltonian in Eq. (4.4) the model is symmetric around $\phi = \pi$ since $\cos(2\pi - \phi) = \cos\phi$ and $\sin(2\pi - \phi) = -\sin\phi$ such that only the spin-flip term acquires an insignificant phase. Therefore we confine our studies to angles in the interval $\phi \in [0, \pi]$, and the interval $\phi \in [\pi, 2\pi]$ is found by reflecting the results given here around $\phi = \pi$.

In order to determine the discretization used for the leads exact diagonalization calculations for the conductance have been performed, and compared to the Greens function results in the non-interacting limit, Eq. (4.13). By virtue of the exact diagonalization the only error present in this approach is the error due to the finite size of the leads. The results are shown in Fig. 4.4 for two different magnetic field strengths B, and a total of 55 sites were used in the single lead setup evaluation of the spectral function, 35 logarithmically and 20 linearly scaled sites. The figure shows excellent agreement between the exact diagonalization and the Greens function results, such that

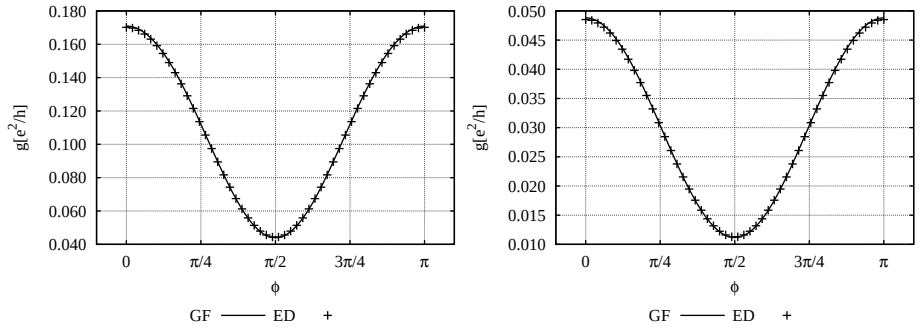

(a) $B = 1$ (b) $B = 2$

Figure 4.4: Comparison of exact diagonalization ('ED') and Greens function ('GF') results for the non-interacting FAB model with parameters $P = 0.8$, $t^0_{L/R} = 0.5$, $\varepsilon_d = 0$, and for two different magnitudes of the magnetic field. The agreement is excellent, demonstrating the capability of the discretization scheme to handle the FAB model. The exact diagonalization calculation was performed with 55 sites in a single lead setup, corresponding to 35 logarithmically and 20 linearly scaled sites. Notice the different g-scales.

the modeling of the leads is sufficient for resolving the FAB model, although upon closer inspection there are minor finite size deviations.

Having benchmarked the DMRG setup in the known limit of $U = 0$ we turn to the interesting regime of finite interactions. In Figs. 4.5 and 4.6 we show the results of the DMRG calculations on the FAB model, keeping the bare level resonant, $\varepsilon_d = 0$, and varying the strength of the magnetic field and the interaction. The calculations presented in each figure were performed keeping the strength of the magnetic field B fixed and varying the interaction strength U and the angle ϕ, where the specific parameter values are given in the plots.

In Fig. 4.7 we show calculations having the bare level off-resonance, $\varepsilon_d \neq 0$, which could be realized by applying a gate potential to the transport level. The strength of the magnetic field was kept fixed, $B = 1$, while the interaction strengths used were $U = 0$ and $U = 2$.

All the DMRG calculations presented in this chapter were performed using 55 sites in the single lead, corresponding to 35 sites scaled logarithmically and 20 sites scaled linearly around the Fermi edge. We keep up to $m = 600$ states per block in the DMRG truncation, and typical target space dimensions are in the range $750.000 - 900.000$ states. To each set of DMRG results in the figures is fitted a spline as a guide to the eye.

In the following we consider the effect of various parameters on the behavior of the model. In some limits simple arguments suffice to explain the behavior and also certain trends can be explained.

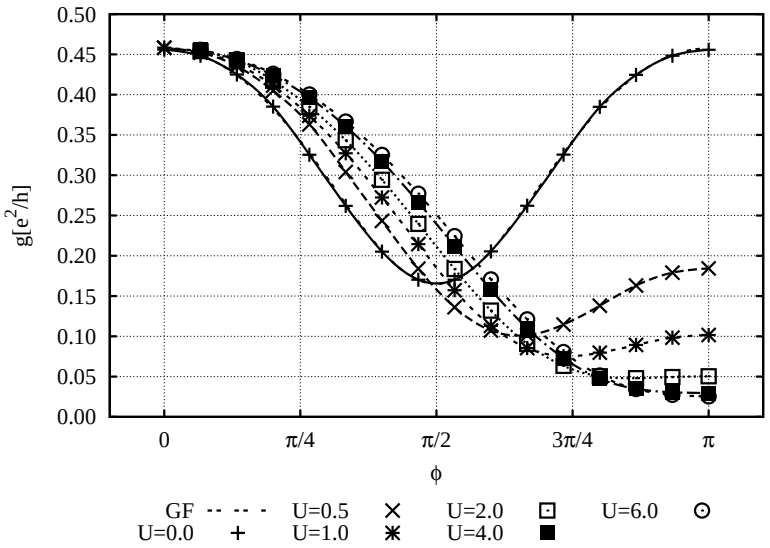

Figure 4.5: Greens function ('GF') and DMRG ('U') results for the conductance versus angle ϕ for the FAB model with $P = 0.8$, $t_0' = 0.5$, $\varepsilon_d = 0$, and $B = 0.5$. To each set of DMRG results is fitted a spline as a guide to the eye. The Greens function result is exact for $U = 0$, and the DMRG results for $U = 0$ are virtually identical to the Greens function results, demonstrating the accuracy of the setup.

Magnetic field

Applying a magnetic field splits the (otherwise) degenerate resonant level $\varepsilon_d = 0$ on the dot, and increasing the magnitude of the magnetic field naturally increases this splitting. Thus, at small angles and for $\varepsilon_d = 0$, the increasing magnetic field pushes the levels further away from the Fermi edge where the transport takes place and lowers the conductance of the system. In Figs. 4.5 and 4.6 this trend is most easily observed by comparing the values of the conductance at $\phi = 0$. For $B = 0.5$ (Fig. 4.5) this value is ~ 0.45 whereas for $B = 2$ (Fig. 4.6(b)) it is reduced by almost a factor of 10 to ~ 0.045 in units of e^2/h. In the cotunneling limit, Eq. (4.15), the dependence on the strength of the magnetic field is seen to be $g \sim 1/B^2$.

Noninteracting limit

In the non-interacting limit the model exhibits single particle behavior. Consider the case where the bare level is resonant, $\varepsilon_d = 0$. Starting with $\phi = 0$ essentially only a single level in the dot takes part in the transport due to the collinearity of the polarization of the leads and the spin basis on the dot ($\sin\phi = 0$). Hence the two paths through the dot are very different in the sense that the path going through the majority spin level has high probability, while the path going through the minority spin level is suppressed due

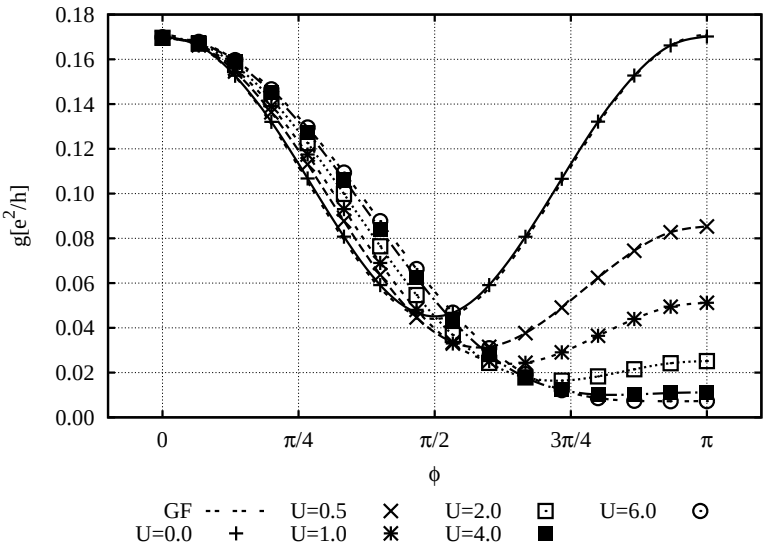

(a) Conductance versus angle for $B = 1$.

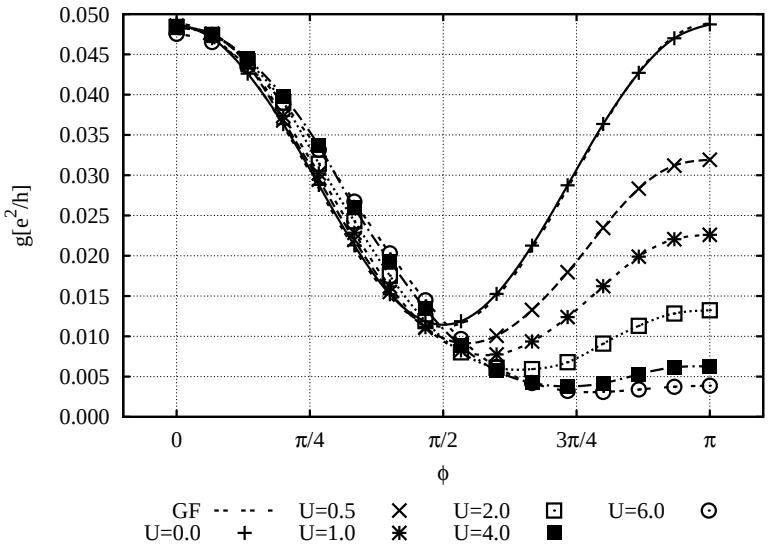

(b) Conductance versus angle for $B = 2$.

Figure 4.6: Greens function ('GF') and DMRG ('U') results for the conductance versus angle ϕ for the FAB model with $P = 0.8$, $t_0' = 0.5$, $\varepsilon_d = 0$, and $B = 1$ and $B = 2$. To each set of DMRG results is fitted a spline as a guide to the eye. The Greens function result is exact for $U = 0$, and the DMRG results for $U = 0$ are virtually identical to the Greens function results, demonstrating the accuracy of the setup.

to the polarization.

As the angle ϕ increases the two paths through the dot become more and more equal since the dot states come closer to the Fermi edge and both levels partake in the transport since the spin-flip is activated. The strong dip in the conductance at the point $\phi = \pi/2$ has been interpreted as destructive interference between the paths [78], which at this point are equally probable since the level splitting at this point is zero, $\cos\phi = 0$ for $\phi = \pi/2$, and the spin-flip rate is maximal, $\sin\phi = 1$. These features are clearly visible in the cotunneling limit, Eq. (4.15), where the two terms cancel (partially) depending on ϕ.

In Chap. 3 it was found for the resonant level models that the lineshape of the resonances was symmetric with respect to the gate potential, such that the relevant quantity for the linear response transport is the distance between the level through which the transport takes place and the Fermi energy in the leads, and whether the level is below or above is insignificant. This in turn explains the symmetry around $\phi = \pi/2$ in the non-interacting case, as increasing the angle above $\pi/2$ reverses the roles of up and down spins on the dot since $\cos(\pi - \phi) = -\cos\phi$ and $\sin(\pi - \phi) = \sin\phi$.

Finite interaction

It is apparent from the DMRG results shown in Fig. 4.5 and 4.6 that for $\varepsilon_d = 0$ the conductance at $\phi = 0$ is nearly independent of the interaction on the dot. At this particular point the minority spin channel is essentially closed by the polarization since the spin-flip on the dot is inactive ($\sin\phi = 0$ for $\phi = 0$), and thus this level remains empty since the spin basis on the dot is aligned with the direction of polarization. Hence only the majority spin level takes part in the transport while the minority spin level remains unoccupied, making the transport independent of the interaction.

The suppression of transport at $\phi = \pi$ for strong interaction (large U) can also be understood. At this angle the role of $\uparrow$ and $\downarrow$ on the dot are reversed compared to $\phi = 0$, such that the minority spin site becomes filled and transport through the majority spin is suppressed by U. Hence the transport is essentially given by the minority spin in the leads, and thus suppressed by the polarization. In previous work using full polarization [78] the conductance indeed goes to zero in the limit of large U, as also apparent from the cotunneling result in Eq. (4.15) using $P = 1$.

In the large U limit the FAB model acts effectively as a spin valve; by tuning the angle of the magnetic field from $\phi = 0$ to $\phi = \pi$ the conductance is changed from a large value to a very small value, illustrating which spin is allowed through the dot. This is similar to a valve since one can open and close the transport for the spin-species by varying ϕ.

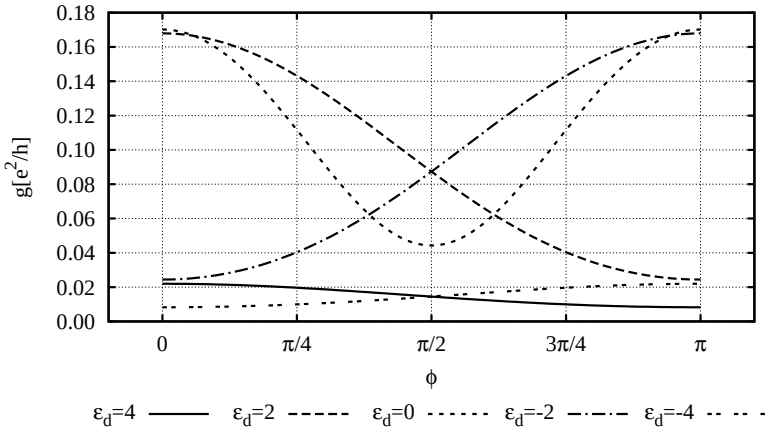

(a) Exact diagonalization for $B = 1$ and $U = 0$

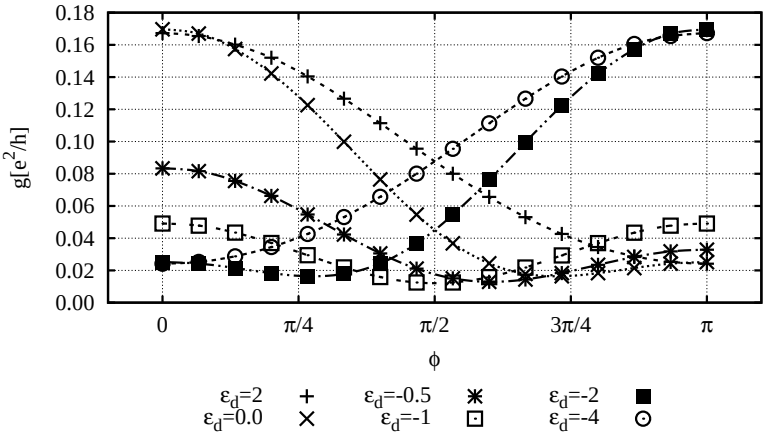

(b) DMRG for $B = 1$ and $U = 2$

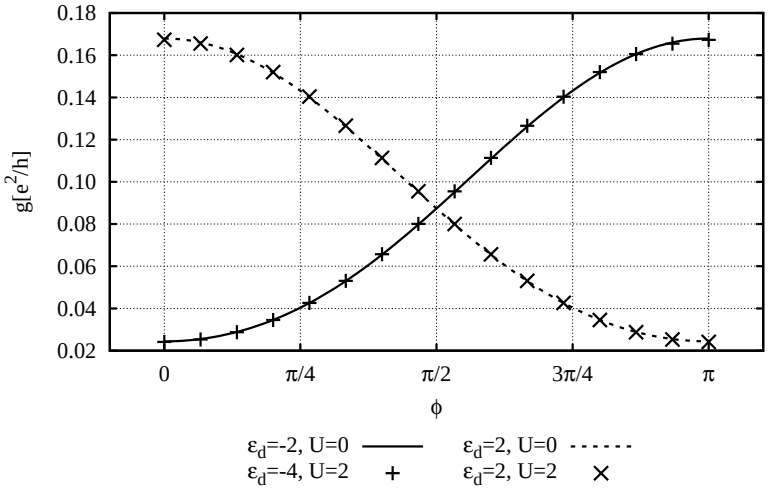

(c) Comparison of DMRG ($U = 2$) and exact diagonalization ($U = 0$) for $B = 1$

Figure 4.7: Effect of varying the bare energy level ε_d on the conductance in both the non-interacting and interacting cases. A comparison of the two data sets is given, showing that the interacting case for some values of ε_d maps onto the non-interacting case with renormalized ε_d.

Bare energy level

So far we have kept the bare energy level resonant, $\varepsilon_d = 0$. To investigate the dependence on the bare energy level ε_d we have performed DMRG and exact diagonalization calculations varying this parameter. In Fig. 4.7 we present DMRG data for the interacting case with parameters $B = 1$ and $U = 2$, and exact diagonalization calculations for the non-interacting case with $B = 1$.

Considering initially the non-interacting case, Fig. 4.7(a), the effect of a finite ε_d is to put the bare level off-resonance, which could be realized by use of a gate potential. Thus the splitting by the magnetic field and the broadening by the leads have to cover the distance to the Fermi edge in order for transport to take place. Consider for example the non-interacting cases of $\varepsilon_d = \pm 2$, as these are reflections of each other around $\phi = \pi/2$. Starting with $\varepsilon_d = 2$ for $\phi = 0$ the conductance is large since the majority spin level is at $\varepsilon = 1$ and the minority spin level is at $\varepsilon = 3$. Thus the transport is mainly through the majority spin level and hence supported by the polarization. At $\phi = \pi$ the Zeeman splitting is opposite such that the transport is mainly through the minority spin level, while the majority spin level is far away from the Fermi edge, and the cross-over from $\phi = 0$ to $\phi = \pi$ is gradual. In the case of $\varepsilon_d = -2$ the dependence on ϕ is reversed such that at $\phi = 0$ the transport is mainly through the minority level, while at $\phi = \pi$ it is mainly through the majority spin level.

Focusing on the difference between the case of $\varepsilon_d = 0$ and $\varepsilon_d = 2$ at $\phi = 0$ in the interacting case, Fig. 4.7(b), we can explain the deviations between the results; in the case of $\varepsilon_d = 0$ the two spin levels are symmetrically below and above the Fermi edge, and therefore both levels partake in the transport, modulus the given polarization. This is not the case for $\varepsilon_d = 2$, where only one level partakes, and thus the difference between the results in these two limits is attributed the transport through the minority spin level in the case of $\varepsilon_d = 0$.

Turning on the interaction, $U = 2$, and keeping the bare level resonant, $\varepsilon_d = 0$, we rediscover the spin-valve behavior. Gating the bare energy level off-resonance potentially changes this behavior significantly; tuning the level above the Fermi edge, $\varepsilon_d = 2$, does not change this behavior qualitatively, since the transport through the minority level is in any case suppressed by the polarization. By contrast tuning the level sufficiently below the Fermi edge, e.g. $\varepsilon_d = -2$ and $\varepsilon_d = -4$, reverses the role of the spin-species such that the transport is also changed. The results presented in Fig. 4.7(b) qualitatively follow results presented in Ref. [78].

It turns out that for some combinations of the interaction U and the bare energy level ε_d the conductance maps onto the non-interacting limit with renormalized bare energy level ε_d. This is shown numerically in two different cases in Fig. 4.7(c), where the comparison between exact diagonalization for

the non-interacting case ($U = 0$) and DMRG calculations for the interacting case ($U = 2$) shows perfect agreement.

Consider the non-interacting case of $\varepsilon_d = -2$ and keep for simplicity $\phi = 0$; the splitting of the bare level by the magnetic field with $B = 1$ gives the spin levels $\varepsilon_\uparrow = -3$ and $\varepsilon_\downarrow = -1$, such that the transport is mainly through the spin down level. Similarly the interacting case of $\varepsilon_d = -4$ and $U = 2$ gives the spin levels $\varepsilon_\uparrow = -5$ and $\varepsilon_\downarrow = -3$. Since the spin up level is far below the Fermi edge, and hence filled, the transport is through the spin down level, and hence subject to the Coulomb repulsion. This gives an effective spin down level at $\varepsilon = -1$, which is essentially the same situation as the non-interacting case above.

Thus in general the interacting case for $\varepsilon_d < -B$ maps onto the non-interacting case with $\tilde{\varepsilon}_d = \varepsilon_d + U$, while the interacting case for $\varepsilon_d > B$ maps onto the non-interacting case with the same bare energy level $\tilde{\varepsilon}_d = \varepsilon_d$, in agreement with Fig. 4.7(c).

4.1.7 Comparison to cotunneling results

A side goal of the DMRG approach to the FAB model was a comparison of the results obtained with other approaches to the same model. Specifically comparing with the cotunneling approach of Pedersen *et al.* [78] in the limit where this approach is valid – i.e., for large magnetic fields $B \gg \Gamma$, where the resonant level is split significantly.

The cotunneling results in Eq. (4.15) are obtained as perturbation theory in the coupling Γ, assuming full occupation of one level on the dot. Therefore the cotunneling results are valid in the limit of a large magnetic field $B \gg \Gamma$ such that the broadening by the leads is small. Thus we compare the cotunneling and the DMRG results for the magnetic field-strengths $B = 1$ and $B = 2$, and expect the cotunneling results to deviate from the DMRG results in the former case since this is not completely in the cotunneling limit.

The comparisons are shown in Figs. 4.8. As expected the cotunneling result for $B = 1$ deviates more significantly from the DMRG results than for the $B = 2$ case, particularly in the high conductance regions. Since we have benchmarked the DMRG against exact diagonalization in the non-interacting limit and found excellent agreement the discrepancy between the cotunneling and DMRG results is attributed to not being completely in the cotunneling regime, such that the approximation inherent in the cotunneling result is not fully justified. This demonstrates the strength of the DMRG approach, that it applies to all parameter regimes equally well, and verifies qualitatively the range of validity of the perturbative approach in the cotunneling regime.

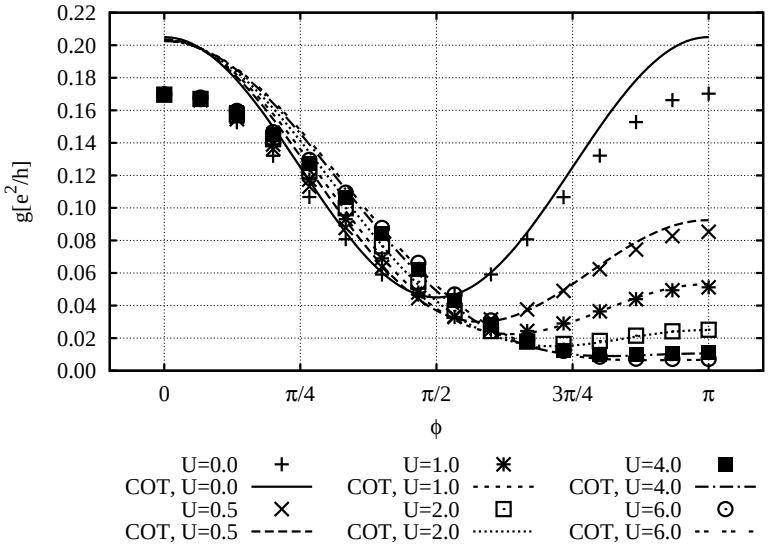

(a) $B = 1$

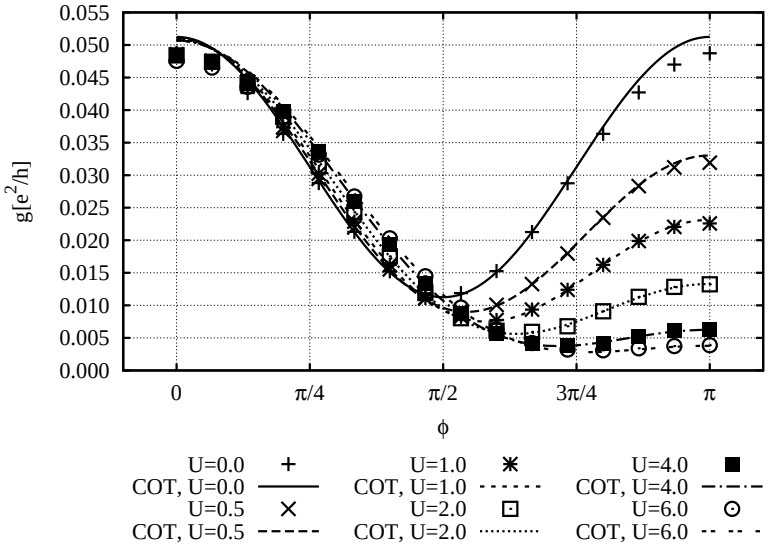

(b) $B = 2$

Figure 4.8: DMRG ('U') and cotunneling ('COT') results for the conductance versus angle ϕ for the FAB model with $P = 0.8$, $t_0' = 0.5$, $\varepsilon_d = 0$, and two values of the magnetic field strength $B = 1$ and $B = 2$. The agreement is expected to be better for larger magnetic fields as the cotunneling data relies on a large splitting of the level, as is evident from the figure. The cotunneling result is given in Eq. (4.15).

4.1.8 Conclusions

In this chapter we considered a spintronics model, the FAB model, consisting of a single level subject to an external magnetic field, and coupled to spin-polarized leads. The magnetic field is applied at an angle ϕ with respect to the direction of polarization in the leads, such that the spin channels can be opened and closed by varying this angle, and the model therefore exhibits both coherence and correlation effects.

We presented the DMRG framework used in calculating the conductance of this model. Compared to the setup used in Chap. 3 the complications consist of a spinful basis, the modeling of spin-polarized leads, and the non-conservation of spin on the dot. It turned out that a direct evaluation of the Kubo formula for conductance was unfeasible, and we devised a different approach to calculate the conductance; the momentum-space DMRG setup was used to evaluate the spectral function for the transport level, and the conductance was then calculated using the Meir-Wingreen formula in Eq. (4.12).

In order to benchmark the DMRG calculation of the conductance we used the Greens function result in Eq. (4.13), valid in the non-interacting limit. Comparing the two approaches confirmed the high accuracy of the DMRG method, and enabled the determination of the necessary lead size.

Using the DMRG scheme we presented results for the linear conductance $g(\phi)$ of the FAB model, varying the magnetic field strength B, the onsite interaction U, and the bare energy level ε_d. The effects of B, U, and ε_d were discussed and it was demonstrated that using a particle-hole-symmetric interaction in this model maps onto the non-interacting result with a renormalized strength of the magnetic field.

Since the DMRG is non-perturbative and can handle strong correlations the developed framework treats both the coherence and the correlation correctly. Thus the full parameter space can be targeted by this method, and we presented initial results for the difficult regime where $B \sim \Gamma^0$. As an illustration we compared perturbative results in the cotunneling limit, Eq. (4.15), to the DMRG results and found a fair agreement in the limit where the perturbative approach is valid. For small magnetic fields the perturbative approach is not expected to be accurate, and the DMRG results quantitatively confirm this.

4.1.9 Outlook

In this chapter we presented the DMRG framework and initial calculations on the FAB model. However the model has a large parameter space that we have not yet investigated. The goal of the project was to provide a non-perturbative DMRG framework for treating the FAB model, and we demonstrated the capability of the developed setup to do just that for the

polarization used so far, $P = 0.8$.

In the future the parameter space of the model will be investigated in more detail. It is for example still unknown how far the DMRG setup can be pushed towards full polarization, and also the dependence on the bare energy level ε_d, or the dependence on the bare hopping matrix element t^0 of the model have not yet been investigated completely. A regime where both coherence and interaction effects are significant is found when $\Gamma^0 = 2[t^0]^2 \sim B$. To our knowledge this regime has not been treated in the literature so far. We presented initial calculations in this regime but further studies are needed to gain a full understanding of the model.

On a slightly longer time scale it would be interesting to expand the model beyond the single resonant site. Depending on the actual choice of extended transport region this may conflict with the Meir-Wingreen approach used in this work, complicating these calculations somewhat. This is, however, not a principal limitation since the Kubo approach is valid but currently unfeasible, such that more work is needed to make that approach feasible.

Chapter 5

Conclusions

5.1 Summary

In this chapter we give a summary of the major outcome of this thesis. We reviewed a new non-perturbative approach to transport in strongly correlated systems, using the density matrix renormalization group (DMRG) method. In the following we sum up the main lines of the method (Chap. 2), and the results for spinless (Chap. 3) and spinful (Chap. 4) models. The method presented is widely applicable such that many possible extensions of the project exist. For the models already considered there are open ends, and we briefly discuss these, as well as possible extensions of this work.

5.1.1 DMRG implementations

In this thesis we presented a setup using the density matrix renormalization group (DMRG) method to calculate transport through interacting nanostructures in the linear source-drain voltage regime. The DMRG is a Hilbert space decimation method, that seeks an optimally projected Hilbert space. Hence a generic feature is that it deals with finite rather than infinite systems, such that some consideration must be made to apply it to a transport setup. On the other hand the DMRG method is capable of handling strong correlations rigorously, such that both correlation and coherence effects can be studied within a unified framework. The developed method targets the linear regime in applied source-drain voltage and uses the DMRG to evaluate either the Kubo formula for conductance or the single particle Greens functions, from which the conductance can be evaluated via the Meir-Wingreen formula. The evaluations of the Kubo formula and the Greens functions are approximation-free apart from the DMRG truncation error, which for one-dimensional systems with short range interactions and hopping can be made very small.

In this thesis two different representations of the leads have been presented, in real- and momentum-space respectively. It was demonstrated that while the real-space leads are simpler to implement the momentum-space leads provide a faster and more accurate setup. The reason for this is the flexibility of the momentum-space leads to tailor the discretization of the lead to the problem at hand. Since the real-space system couples directly to the low-energy states in the momentum-space leads much lower energy scales can be addressed, and no scaling of the boundaries is needed, leading to an overall faster setup. By contrast a similar reduction of the finite size level splitting in the real-space leads is numerically cumbersome and eventually leads to instabilities.

The physics targeted in this thesis deals with the linear response regime in the source-drain voltage. For this type of calculations an accurate discretization is necessary at the Fermi edge, where the transport takes place. In the momentum-space representation of the leads we used a combined log-

arithmic and linear discretization in order to reach the unitary limit for the conductance on-resonance. We use the logarithmic discretization to cover a large energy window, and switch to a linear discretization on the very low-energy scale close to the Fermi edge. This discretization is beyond the capability of for example NRG calculations, and we emphasize that the unitary limit is only reached in this setup when including the linear discretization.

When using the DMRG method in a transport setup we face two different sources of errors; the error committed by describing transport on a finite system (the finite size error), and the error committed when using DMRG to truncate the Hilbert space. We presented benchmark schemes for both types of errors in the non-interacting limit, exact diagonalization for the truncation error, and Greens function calculations for the finite size error, providing in total a rigorous test for the developed DMRG approach. Furthermore the exact diagonalization scheme provides a fast approach to determining the free parameters of the model, for instance for the discretization of the leads.

The momentum-space representation of the leads gives full flexibility for the choice of discretization such that more sophisticated discretization schemes can be used. We discussed the evaluation of the frequency resolved single particle Greens function, where a fine-grained discretization is needed at two energies, such that NRG type logarithmic discretizations are insufficient. However, making full use of this flexibility is left for future applications of the method.

5.1.2 Interacting resonant 7 site chain

The first physical model considered in Chap. 3.1 of this thesis, was an interacting resonant 7 site chain, including repulsive interaction mainly inside the chain. Using the real-space representation for the leads we presented calculations of the conductance versus gate potential, studying the effects of the interaction inside the chain. We presented the parameter determination for the real-space setup, and showed that for weak interaction the widths of the resonances in the spectrum remain largely unchanged compared to the non-interacting limit, whereas the positions of the resonances were found to be renormalized by the interaction, such that this microscopic model exhibits Coulomb blockade behavior.

For the strongly interacting case the picture is different. The positions of the resonances are still renormalized, and additionally the widths are significantly reduced. Thus the model not only displays Coulomb blockade behavior, but also shows a significant sharpening of the resonances in the strongly interacting limit. This illustrates that the transition to the insulating regime for $V > 2$ in the infinite system limit is not through a reduction of the conductance on-resonance, but rather through a reduction of the resonance *width*.

For the strongly interacting limit we provided a simple picture for the

renormalized positions of the resonances, the reduced lattice model. In this model the electrons interact so strongly that the effect of one electron on the others is to limit the available space, such that the electrons effectively move freely on a lattice of a reduced size. Upon comparison with the DMRG data this model was shown to explain the resonance positions with reasonable accuracy.

Finally to illustrate the improved energy resolution we presented recalculations of the 7 site chain using the momentum-space representation of the leads. Whereas the real-space setup failed to reach the unitary limit on-resonance the calculations using the momentum-space reached it perfectly, even for the sharp outermost resonances. The improved resolution of the momentum-space calculations further made the extraction of the widths of the resonances possible, such that quantitative statements could be made for the trends seen from the real-space calculations.

5.1.3 Interacting resonant level models

The interacting resonant level models considered in Chap. 3.2 are seemingly simple models consisting of short interacting resonant chains, with an additional density-density interaction to the neighboring sites in each lead. Whereas we studied the effects of interaction inside the resonant chain considered in Chap. 3.1, the interacting resonant level models have the interaction V inside the chain, and γV on the contact links, and we focused on the effect of the interaction on the contact links.

The interacting resonant level model (IRLM) considered in Chap. 3.2.1 is the simplest possible model with just a single resonant level. It is useful for benchmarking new methods due to its simplicity, and we mentioned the recent approaches to this model, the scattering Bethe ansatz [64, 65] and perturbation theory in the coupling [74].

The conductance of the IRLM in the non-interacting limit is a height normalized Lorentzian of half width at half maximum $w = 2t'^2$, where $t' = t_{L/R}$ is the hopping matrix element coupling the resonant level to each lead. We studied the dependence of the interaction on the resonance width for the IRLM in the limit of weak coupling to the leads, using the momentum-space representation for the leads.

Interestingly the widths of the resonances show a strong and non-monotonic dependence as the strength of the repulsive interaction increases from the non-interacting limit. The models considered are in the weak coupling limit in the sense that the hopping matrix element connecting the resonant level to the leads is small, typically $t' = t_{L/R} = 0.01$. Starting from the non-interacting limit and increasing the interaction strength to $\gamma V = 1$ the width of the resonance *increases* by an order of magnitude. Increasing further the strength of the interaction the width of the resonance is again reduced, and for $\gamma V = 25$ the width is *reduced* by an order of magnitude

compared to the non-interacting limit.

It was suggested in a recent paper by Borda *et al.* [74] that this non-monotonic dependence was linked to a density depletion of the first sites in the leads. This hypothesis was tested in the linear source-drain voltage regime, and no significant signatures were found in the density profile of either the resonant level itself or the neighboring lead sites. In the regime of interaction strengths where the large and non-monotonic change in the resonance widths occur there is a slight charging of the lead sites, rather than a depletion, therefore it appears that the suggested mechanism is incorrect, at least in the parameter regime considered here. For very large interaction strengths the resonant level is depleted, such that there is a correlation between the densities and the transport but it remains an open question what the governing mechanism is [75].

In Chap. 3.1 it was shown that strong repulsive interaction inside the transport region leads to a reduced resonance width, whereas for the single site model considered in Chap. 3.2.1 repulsive interaction on the contact links leads to an increased resonance width. To investigate if the enhancement of the off-resonance transport is a special feature of the IRLM – i.e., to compare the strengths of these two oppositely directed effects, we considered in Chap. 3.2.2 transport through short resonant chains including a leak of the interaction onto the contact links. These resonant chains thus feature two interaction strengths, V inside the chain, and the leaking of this interaction onto the contact links γV, such that $\gamma = 0$ corresponds to no interaction, and $\gamma = 1$ corresponds to the full interaction on the contact links.

The results presented for the short resonant chains show that the enhancement of the off-resonance transport by the interaction on the contact links is *stronger* than the corresponding suppression by the interaction inside the chain. Thus for a resonant 3 site chain with $t' = t_{L/R} = 0.05$, interaction $V = 2$, and $\gamma = 0$ the resonance width for zero gate potential is *reduced* by 30%, while for $\gamma = 1$ it is *increased* by 400%, both compared to the completely non-interacting case $V = 0$. Since the leaking interaction γV is bounded in magnitude by the interaction inside the resonant chain the non-monotonic behavior is not observed for small values of V. For larger interaction strengths, $V = 3$ and $V = 5$, the non-monotonic behavior is rediscovered for the short resonant chains.

The resonant 3 site chain has additionally a resonance located at finite positive gate potential, and it was shown that this resonance displays a similar enhancement of the off-resonance transport, although the enhancement is less pronounced. The study of these resonances is complicated by the fact that the position is renormalized by the interaction on the contact links, and therefore has to be determined in addition to the resonance width.

Finally it was shown that the results remained unchanged when varying the band cutoff. Thus the enhancement was demonstrated to be a stable feature, supporting the conclusion that the off-resonance enhancement by

contact interactions is a universal feature.

This conclusion challenges the division commonly used in transport calculations between transport region and leads, where all interaction and correlation effects are kept inside the transport region. The results presented in this chapter demonstrate that care should be taken when making this division, as even a slight leaking of the interaction into the contacts results in significantly changed off-resonance transport properties.

5.1.4 The ferromagnetic Anderson model with an applied magnetic field

In Chap. 4.1 we considered a spintronics model known as the ferromagnetic Anderson model with an applied magnetic field $\vec{B}$, abbreviated the FAB model. The model consists of a spinful resonant level coupled to partially spin-polarized leads, and with a magnetic field applied to the resonant level at an angle ϕ with the direction of the polarization of the leads. The work on the FAB model is part of an ongoing collaboration with Ph.D. student Jonas N. Pedersen (Lund, Sweden) and Dr. Tomáš Novotný, (Prague, Czech Republic).

Apart from being a spintronics model the FAB model also exhibits both coherence and correlation effects, and in the general case both these effects require a rigorous treatment. Previous work [77, 78] has targeted two different regimes, the non-interacting but strongly coupled, and the weakly coupled but interacting regime. The aim of this work was to provide a uniform framework for treating all regimes of this model, and the method for this is the developed DMRG setup.

In Chap. 4.1 a scheme for calculating the conductance of the FAB model was presented. Specifically the modeling of the spinful and polarized leads makes the setup different from the spinless models considered in Chap. 3. Due to technical difficulties in the DMRG calculations a direct evaluation of the Kubo formula was unfeasible, and the conductance was instead calculated using a DMRG evaluation of the single particle Greens function in combination with the Meir-Wingreen formula. This approach makes a mapping from the usual two lead setup onto a single lead setup possible, such that the total lead size is effectively halved.

Comparing exact diagonalization calculations of the conductance with Greens function results for different strengths of the magnetic field the parameters of the lead were determined in Chap. 4.1.6. Using this lead discretization and keeping the bare level resonant, $\varepsilon_d = 0$, while varying the strength B of the magnetic field, and the onsite Coulomb interaction U, the conductance of the FAB model versus the angle ϕ of the magnetic field was calculated. The results presented were both in the cotunneling limit, and in the interesting regime where correlations and coherence both are important. It was shown that in the strongly interacting limit the FAB model behaves

as a spin valve, where rotating the magnetic field from $\phi = 0$ to $\phi = \pi$ changes the spin species allowed through the transport region.

Also the effect of having the bare level off-resonance was considered. This opens up the possibility of having transport through a single level only, and in some cases the behavior of the interacting case is the same as the behavior in the non-interacting limit with a renormalized bare energy level.

In the cotunneling limit, given by $B \gg \Gamma$, where the bare resonant level on the dot is split by a large magnetic field, perturbation theory in the coupling applies. Perturbative results similar to the ones presented in Ref. [78], but generalized to finite polarization in the leads, enabled a comparison of the DMRG calculations and the perturbative approach, as shown in Chap. 4.1.7. A fair agreement was found for large magnetic fields, while smaller magnetic fields show significant deviations between the two approaches. This demonstrates the range of validity of the cotunneling approach.

In conclusion Chap. 4.1 demonstrated that accurate conductances for the FAB model can be calculated using the developed DMRG approach via the Meir-Wingreen formula. It is left as future work to investigate the parameter space of the model further, and perform rigorous comparisons with other approaches to the FAB model.

5.2 Concluding remarks

This thesis represents the main lines of three years work. Large parts of the work consisted in developing the method itself and the benchmarks for it. We applied the method to a limited number of models, but demonstrated the capability to capture interesting physics. Let us mention three specific issues: (1) The results presented demonstrate Coulomb blockade from a microscopic model, which is beyond the capability of for instance DFT based calculations. (2) We have demonstrated a renormalization of the resonance width by an interaction. (3) For the FAB model a correct description of the coherence is essential, and it has been demonstrated that the method can handle interference in the model. Thus in total we have demonstrated the ability of the DMRG method to handle the important issues of correlation *and* coherence within a transport setup.

A number of interesting problems can be addressed with the developed method and it is the aim to make use of this in the future. Within the models already targeted open questions still remain. Here we discuss some of the open ends and the natural extensions of this work within the developed framework.

The interacting resonant level model (IRLM) as we considered it in Chap. 3.2 is a highly symmetric model, symmetric in hopping matrix elements connecting leads and the resonant level, symmetric in the density-

density interactions with the left and right leads, and also the extended resonant chains considered in Chap. 3.2.2 were symmetric in this sense. It would be relevant to investigate how sensitively the transport enhancement of these models depends on this symmetry. Further it would be interesting to study in more detail the impact of the Fermi velocity on the transport behavior. Additionally the question of the mechanism behind the non-monotonic transport enhancement remains open, and an effort will be devoted to finding an explanation.

The calculations presented for the ferromagnetic Anderson model with an applied magnetic field in Chap. 4.1 are limited to a small part of the parameter space. As the DMRG approach to the model has been shown to yield accurate results a more thorough investigation of the parameter space would be interesting – for instance the effect of having the bare level ε_d off-resonance with the Fermi edge in the leads, or the dependence on the bare coupling Γ^0. It is also an open question how far the method can be pushed towards full polarization of the leads. Finally a more rigorous comparison of the DMRG data with other approaches would be interesting, yielding insight into limitations of the DMRG method as well as limitations of the other methods.

The flexibility of the discretization scheme presented for the momentum-space representation of the leads opens up new problems to be studied. One example of this is the Kondo model in a magnetic field [82]. The magnetic field splits the Kondo peak and a sharp asymmetric resonance is located at a finite frequency $\omega \sim \left|\vec{B}\right|$ [82]. For this model two energy-scales need to be represented accurately in the calculation of the spectral function – energies at the Fermi edge and energies close to the Kondo peak $\sim \left|\vec{B}\right|$. For moderate to large magnetic fields this resonance is well away from the Fermi edge and hence a doubly dense discretization is needed to resolve it. The flexibility for studying this interesting limit of the model is provided by the DMRG setup, whereas the NRG based methods are limited to a single logarithmic discretization and hence do not produce reliable results for finite magnetic fields. This limit of the split Kondo model has not been considered before and a successful application of the DMRG method would be very interesting.

Appendix A

The density matrix renormalization group method

The density matrix renormalization group (DMRG) method is an iterative Hilbert space decimation scheme using a superblock setup where the system is joined with an environment. In this chapter we derive the state selection mechanism, and review the two algorithms used in DMRG calculations. The chapter is based mainly on the Springer Lecture Notes in Physics edited by Peschel *et al.* [14], and the original articles by White [15, 16].

Figure A.1: General superblock setup as originally formulated by White [15, 16] using two central sites. States $|i\rangle$ are system states and states $|j\rangle$ are environment states.

A.1 Retained states

The idea of DMRG is to calculate an optimally projected Hilbert space for the problem at hand. This is done using a superblock setup where the system is joined with an environment. To illustrate the method we consider an arbitrary superblock state $|\psi\rangle$. Using the notation in Fig. A.1, denoting system states by $|i\rangle$ and environment states by $|j\rangle$, this state can be written in product form[1]

$$|\psi\rangle \;=\; \sum_{i=1}^{I}\sum_{j=1}^{J}\psi_{ij}\,|i\rangle\,|j\rangle\,, \tag{A.1}$$

[1]The environment states $|j\rangle$ include the two central sites for simplicity.

where $\sum_{i=1}^{I}$ denotes summation over the complete basis of the system block, and $\sum_{j=1}^{J}$ denotes summation over the complete basis of the environment block. The reduced density matrix (RDM) for the system block is obtained by tracing out the environment degrees of freedom

$$\begin{aligned} \rho_{ii'} &\equiv \sum_{j} \psi^{*}_{i'j}\psi_{ij} \\ &= \sum_{j} \psi_{ij}\psi^{\dagger}_{ji'}, \end{aligned} \tag{A.2}$$

or in matrix notation

$$\rho = \psi\psi^{\dagger}. \tag{A.3}$$

For any *system* block operator A the quantum mechanical average is

$$\begin{aligned} \langle\psi|A|\psi\rangle &= \sum_{iji'j'} \langle j|\langle i|A|i'\rangle|j'\rangle\psi_{i'j'}\psi^{\dagger}_{ji} \\ &= \sum_{ii'} A_{ii'} \sum_{j} \psi_{i'j}\psi^{\dagger}_{ji} \\ &= \sum_{ii'} A_{ii'}\rho_{i'i} \\ &= \mathrm{Tr}\rho A. \end{aligned} \tag{A.4}$$

Normalizing ρ, $\mathrm{Tr}\rho = 1$, and denoting its eigenstates by $|u^{\alpha}\rangle$ and the eigenvalues by $w_{\alpha} \geq 0$ we have $\sum_{\alpha} w_{\alpha} = 1$. For any system operator A we may write the trace in this eigenbasis

$$\langle\psi|A|\psi\rangle = \sum_{\alpha} w_{\alpha} \langle u^{\alpha}| A |u^{\alpha}\rangle . \tag{A.5}$$

The goal is to construct the best possible approximate state, $|\bar{\psi}\rangle \approx |\psi\rangle$, for the superblock using a given number of states. From Eq. (A.5) it is clear that if one particular eigenstate has zero weight, $w_{\alpha} = 0$, *no error* would be made by disregarding the corresponding state $|u^{\alpha}\rangle$ when calculating quantum mechanical averages.

More formally the mathematical goal is to minimize

$$S = \big||\psi\rangle - |\bar{\psi}\rangle\big|^2, \tag{A.6a}$$

$$|\bar{\psi}\rangle = \sum_{\alpha,j} a_{\alpha,j} |u^{\alpha}\rangle |j\rangle , \quad \alpha = 1, \ldots, m < I. \tag{A.6b}$$

by varying over all coefficients $a_{\alpha,j}$ and choosing the best possible orthonormal basis states u^{α}, $\langle u^{\alpha}|u^{\alpha'}\rangle = \delta_{\alpha\alpha'}$.

In order to map the problem of finding the best states and coefficients onto a known form we use a change of basis

$$\begin{aligned} |\bar{\psi}\rangle &= \sum_{\alpha} |u^{\alpha}\rangle \sum_{j} a_{\alpha,j} |j\rangle \\ &\equiv \sum_{\alpha} a_{\alpha} |u^{\alpha}\rangle |v^{\alpha}\rangle , \quad a_{\alpha} |v^{\alpha}\rangle = \sum_{j} a_{\alpha,j} |j\rangle . \end{aligned} \tag{A.7}$$

Switching to matrix notation and using m basis states in the approximate state $|\bar{\psi}\rangle$, the error measure is

$$\begin{aligned} S &= \sum_{ij} S_{ij} \\ &= \sum_{ij} \Big(\psi_{ij} - \sum_{\alpha=1}^{m} a_{\alpha} u_i^{\alpha} v_j^{\alpha} \Big)^2 , \end{aligned} \tag{A.8}$$

a form known from linear algebra. The state vector of the superblock $|\psi\rangle$ is represented by the rectangular (possibly complex) matrix ψ_{ij} defined in Eq. (A.1), and we may write it in singular value decomposition,

$$\psi = UDV^{\dagger}, \tag{A.9}$$

where U and D are $I \times I$ matrices and V is $J \times I$, where I and J are the number of states in the system and environment blocks respectively. U and V are unitary and D is diagonal with positive elements. The connection between U, V, and D can be demonstrated as follows:

$$\begin{aligned} \psi\psi^{\dagger} &= UDV^{\dagger}VDU^{\dagger} \\ &= UD^2U^{\dagger} \Rightarrow \\ U^{\dagger}\psi\psi^{\dagger}U &= D^2 \\ &= \mathrm{diag}(\sigma_1^2, \ldots, \sigma_I^2), \end{aligned} \tag{A.10a}$$

$$\begin{aligned} \psi^{\dagger}\psi &= VDU^{\dagger}UDV^{\dagger} \\ &= VD^2V^{\dagger} \Rightarrow \\ V^{\dagger}\psi^{\dagger}\psi V &= D^2 \\ &= \mathrm{diag}(\sigma_1^2, \ldots, \sigma_I^2). \end{aligned} \tag{A.10b}$$

Hence the elements of D can be found as the square root of the eigenvalues of $\psi\psi^{\dagger}$ or $\psi^{\dagger}\psi$. The columns of U are the corresponding eigenvectors of $\psi\psi^{\dagger}$ while the columns of V are the corresponding eigenvectors of $\psi^{\dagger}\psi$.

Now we see how to minimize S in Eq. (A.8): for a_{α} choose the m largest values of σ_i, for u^{α} choose the corresponding columns of U, and for v^{α} choose the corresponding columns of V. For a given $m < I$ this will be the optimal choice.

From Eq. (A.10a) it is clear that the singular value decomposition is equivalent to diagonalization of the reduced density matrix such that U is the matrix of eigenvectors of ρ. Hence the best possible states to retain are the m largest eigenvalue eigenstates of ρ, or equivalently the m most probable eigenstates of ρ.

If the system is in a mixed state with probabilities W_k,

$$\big|\psi\big\rangle \;=\; \sum_k W_k \big|\psi^k\big\rangle, \tag{A.11}$$

where W_k could be the Boltzmann distribution to simulate temperature, or any other relevant distribution. Each state $\big|\psi^k\big\rangle$ can be written as in Eq. (A.1), and the relevant error measure accordingly

$$S \;=\; \sum_k W_k \sum_{ij} \Big(\psi^k_{ij} - \sum_{\alpha=1}^{m} a^k_\alpha u^\alpha_i v^{k,\alpha}_j\Big)^2. \tag{A.12}$$

We seek a *single set of optimal states*, hence not allowing u^α_i to depend on k, while the environment states are allowed to change with k.

The reduced density matrix is

$$\rho_{ii'} \;=\; \sum_k W_k \sum_j \psi^k_{ij} (\psi^k)^\dagger_{ji'}, \tag{A.13}$$

and a similar optimization procedure gives

$$U^\dagger \rho U \;=\; \mathrm{diag}(\sigma_1^2, \cdots, \sigma_I^2), \tag{A.14}$$

so that the optimal states again are the largest eigenvalue eigenstates of the reduced density matrix, defined in Eq. (A.13).

In conclusion we have shown that the $m < I$ optimal DMRG states are the m largest eigenvalue eigenstates of the reduced density matrix as properly defined in Eq. (A.2) and (A.13).

From the above derivation of the DMRG states it is obvious that the spectrum of the reduced density matrix is linked to the success of the DMRG. If the eigenvalues of ρ decay fast a limited number of states suffices, whereas a slower decay indicate that a larger number of states should be kept to attain the same accuracy. In fact one can use the sum of the truncated eigenvalues as a guideline to the magnitude of the truncation error at each step, but care should be taken since a DMRG calculation consists of very many successive truncations.

It should be noted that the boundary conditions influence the spectrum of the reduced density matrix and generally DMRG performs best for systems with hard-wall rather than periodic boundary conditions [14].

A.2 Algorithms

To implement the idea of optimizing the basis algorithms are needed for building up a system from a sufficiently small size and for improving the description of a given size finite system. In this section we describe how the superblock procedure is combined with the DMRG projection, leading to the two important DMRG algorithms.

In order not to inflate the Hilbert space too much at each step the usual way of adding degrees of freedom is to add one lattice site at a time when building up the system from a small size. In principle not only lattice sites but any other generic and sufficiently small building block of the Hilbert space can be used. The key idea is to divide the system into 4 blocks, a left or system block, two central single sites, and a right block, where the central and right blocks constitute the environment, see also Fig. A.1.

There are two generically different algorithms, the *infinite* and the *finite* system algorithms differing by the choice of the environment block.

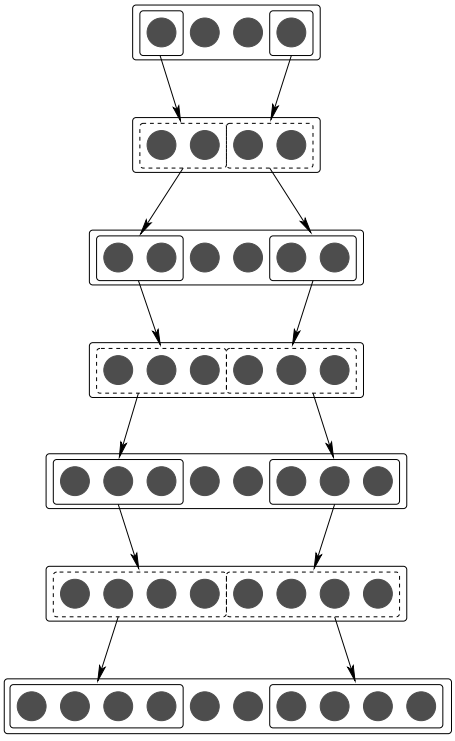

Figure A.2: Schematic representation of the infinite lattice algorithm used to build up the system in DMRG. When the system size becomes sufficiently large each step involves a truncation to a smaller number of states.

A.2.1 Infinite system algorithm

In the infinite system algorithm the system is enlarged by a single site at each step in the algorithm. As environment block a simple choice is to use two single sites joined with a spatial reflection of the system block, as seen in Fig. A.2. This is however not crucial and in the momentum-space setup presented in Chap. 2.2 another choice of environment block is used.

Enlarging both the system and environment block by a single site at each step the superblock size grows by two sites. This has lead to the name *the infinite system algorithm* since the superblock size is not fixed. The algorithm can be formulated as

1. Form a superblock consisting of L sites, where L is small enough that the target state(s) of the superblock Hamiltonian can be calculated exactly.

2. Compute the target state(s) of the superblock Hamiltonian numerically.

3. From the target state(s) construct the reduced density matrix, defined in Eq. (A.2), for the block consisting of the system block and the leftmost central site.

4. Diagonalize the reduced density matrix and collect the desired number of eigenvectors u_α in the truncation matrix U.

5. Transform all system operators to the eigenbasis of the reduced density matrix.

6. Form a superblock of size $L + 2$ using the enlarged system and corresponding environment blocks, and two single sites.

7. Repeat this procedure from step 2, enlarging the superblock size by two sites at each iteration, until the desired superblock size has been reached.

Using the infinite system algorithm a superblock of a desired size can be built in a controlled manner, enlarging the size of the superblock in each step of the algorithm.

A.2.2 Finite system algorithm

Once a superblock of the desired size has been built using the infinite lattice algorithm the environment can be chosen differently. Keeping the size fixed the point of division between the system and environment can be moved back and forth through the superblock improving the accuracy of the description at each sweep. This procedure is illustrated in Fig. A.3. Formally the algorithm is

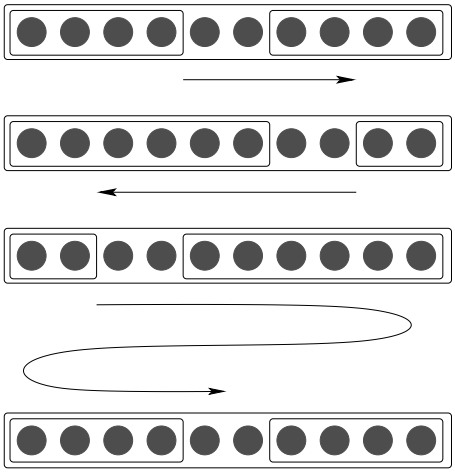

Figure A.3: Schematic representation of the finite lattice algorithm in the DMRG. The finite system algorithm keeps the size of the superblock fixed and shifts the division between system and environment at each step.

1. Use the infinite system algorithm to build up a superblock of the desired size L storing at each step representations of the left and right blocks.
2. Carry out steps 3-5 in the infinite system algorithm, enlarging the size of the system by a single site, and store the representation of the enlarged system block.
3. Form a superblock of unchanged size using the enlarged system block, two single sites and an environment block with one site less. The environment block was found and stored during the build up of the initial superblock using the infinite algorithm.
4. Repeat steps 2-3 until the end of the system is reached. This constitutes the left to right phase in which the left block is enlarged.
5. Reverse the roles of system and environment and move the point of division all the way through the superblock until the opposite end is reached. This is the right to left phase, in which the right block is enlarged.
6. Continue this sweeping until convergence is reached.

The left to right phase improves the description of the left block, while the right to left phase improves the description of the right block.

In the sweeping process the role of the system and environment is switched when reaching the end of the superblock. However, the sweeping is not continued until the environment block is just a single site, rather

it is stopped when the description of the environment block is exact using the number of states kept in the DMRG truncation. For a spinless model 10 sites represented exactly corresponds to 1024 states, while for a spinful model 5 sites represented exactly corresponds to 1024 states, illustrating the different scaling of these two classes of models.

Extracting physical quantities can be done in various ways. Two possibilities are to use the final step to readout values, or to look for a plateau in the readout of the relevant physical quantity during the sweeping, and take the value in the plateau. See also App. D for details about the data extraction used in this work.

A.3 Further details

A large number of technical details should be taken into account when implementing the DMRG efficiently. We will not attempt to provide such details here, but refer to the literature, where a number of reviews and papers discuss these issues. A good starting point is Ref. [14] and the references therein, where wavefunction prediction, decomposition by quantum numbers, etc. are discussed. Also many reviews of the method exist, of which we can mention Refs. [55, 56, 57, 58].

Appendix B

Resolvent formulations

In this Appendix we derive in detail the resolvent expressions for the conductance and the Greens functions evaluated using DMRG in the main text.

For the Kubo formula for conductance the setup is an interacting equilibrium system with Hamiltonian H_0 perturbed by the voltage, represented by the Hamiltonian δH. Hence the interaction picture is well suited for this setup, and we use the notation $\hat{\mathcal{O}}$ for the interaction picture representation of the Schrödinger operator $\mathcal{O}$.

B.1 Linear response conductance

To derive the Kubo formula for conductance in the resolvent form used in this thesis, we start from the general Kubo result for the particle current derived in Chap. 2.4, taking $\hbar = 1$

$$\langle \hat{J}(t) \rangle \;=\; \langle J \rangle_0 - i \int_{-\infty}^{t} \mathrm{d}t' \langle \psi_0 | [\hat{J}(t), \delta\hat{H}(t')] | \psi_0 \rangle, \tag{B.1}$$

where $\delta\hat{H}(t) = -eV_{\mathrm{SD}}(t)\hat{N}(t)$ is the voltage perturbation, $N = \frac{1}{2}(N_L - N_R)$, and $|\psi_0\rangle$ is the ground state of the unperturbed Hamiltonian H_0. The particle current operator at the i'th link is

$$J_i \;=\; -i(t_i^* c_{i-1}^\dagger c_i - t_i\, c_i^\dagger c_{i-1}), \tag{B.2}$$

such that the electric current is

$$I \;=\; -e\langle J \rangle. \tag{B.3}$$

Note that we derive the linear response result in the source drain voltage V_{SD} such that the 'simple' Hamiltonian H_0 contains the full Coulomb interaction.

Usually the equilibrium current is zero, $\langle J \rangle_0 = 0$, and a Fourier transformation yields

$$\begin{aligned}
\langle J(\omega)\rangle &= -i\int_{-\infty}^{\infty} \mathrm{d}t\; e^{i\omega t}\int_{-\infty}^{t} \mathrm{d}t'\; \langle\psi_0|[\hat{J}(t),\delta\hat{H}(t')]|\psi_0\rangle \\
&= ie\int_{-\infty}^{\infty} \mathrm{d}t\; e^{i\omega t}\int_{-\infty}^{\infty} \mathrm{d}t'\theta(t-t')V_{\mathrm{SD}}(t') \\
&\quad \langle\psi_0|\big(\hat{J}(t)\hat{N}(t') - \hat{N}(t')\hat{J}(t)\big)|\psi_0\rangle \\
&= ie\int_{-\infty}^{\infty} \mathrm{d}t\; e^{i\omega t}\int_{-\infty}^{\infty} \mathrm{d}t'\theta(t-t')V_{\mathrm{SD}}(t') \\
&\quad \langle\psi_0|\Big(e^{iH_0t}Je^{-iH_0t}e^{iH_0t'}Ne^{-iH_0t'} \\
&\quad -e^{iH_0t'}Ne^{-iH_0t'}e^{iH_0t}Je^{-iH_0t}\Big)|\psi_0\rangle.
\end{aligned} \tag{B.4}$$

Inserting a complete set of eigenstates of the unperturbed Hamiltonian H_0, $1 = \sum_m |\psi_m\rangle\langle\psi_m|$, we find

$$\begin{aligned}
\langle J(\omega)\rangle &= ie\int_{-\infty}^{\infty} \mathrm{d}t\; e^{i\omega t}\int_{-\infty}^{\infty} \mathrm{d}t'\; \theta(t-t')V_{\mathrm{SD}}(t') \\
&\quad \sum_m \Big(\langle\psi_0|e^{iH_0t}Je^{-iH_0t}|\psi_m\rangle\langle\psi_m|e^{iH_0t'}Ne^{-iH_0t'}|\psi_0\rangle \\
&\quad -\langle\psi_0|e^{iH_0t'}Ne^{-iH_0t'}|\psi_m\rangle\langle\psi_m|e^{iH_0t}Je^{-iH_0t}|\psi_0\rangle\Big) \\
&= ie\int_{-\infty}^{\infty} \mathrm{d}t\; e^{i\omega t}\int_{-\infty}^{\infty} \mathrm{d}t'\theta(t-t')V_{\mathrm{SD}}(t') \\
&\quad \sum_m \Big(\langle\psi_0|J|\psi_m\rangle\langle\psi_m|N|\psi_0\rangle\; e^{i(E_0-E_m)(t-t')} \\
&\quad -\langle\psi_0|N|\psi_m\rangle\langle\psi_m|J|\psi_0\rangle\; e^{-i(E_0-E_m)(t-t')}\Big).
\end{aligned} \tag{B.5}$$

Introducing the short hand notation for the matrix elements, $\langle\psi_0|J|\psi_m\rangle = J_{0,m}$, and similarly for the matrix elements of N we have

$$\begin{aligned}
\langle J(\omega)\rangle &= ie\int_{-\infty}^{\infty} \mathrm{d}t\; e^{i\omega t}\int_{-\infty}^{\infty} \mathrm{d}t'\; \theta(t-t')V_{\mathrm{SD}}(t') \\
&\quad \sum_m \Big(J_{0,m}N_{m,0}\; e^{i(E_0-E_m)(t-t')} - N_{0,m}J_{m,0}\; e^{-i(E_0-E_m)(t-t')}\Big).
\end{aligned}$$

Shifting variables as $t'' = t - t'$ we find

$$\begin{aligned}\langle J(\omega)\rangle &= ie\int_{-\infty}^{\infty} \mathrm{d}t''\ e^{i\omega t''}\theta(t'')\int_{-\infty}^{\infty}\mathrm{d}t'\ e^{i\omega t'}V_{\mathrm{SD}}(t') \\ &\quad \sum_m \Big(J_{0,m}N_{m,0}\ e^{i(E_0-E_m)t''} - N_{0,m}J_{m,0}\ e^{-i(E_0-E_m)t''}\Big) \\ &= ieV_{\mathrm{SD}}(\omega)\int_0^{\infty}\mathrm{d}t\ e^{i\omega t} \\ &\quad \sum_m \Big(J_{0,m}N_{m,0}\ e^{i(E_0-E_m)t} - N_{0,m}J_{m,0}\ e^{-i(E_0-E_m)t}\Big). \end{aligned} \tag{B.6}$$

This formula is the starting point for deriving the resolvent expressions for the conductance.

Current-density correlator

To proceed we insert the convergence factor $e^{-\eta t}$ in Eq. (B.6) to ensure that correlations decay with time, and eventually lead to a broadening in the finite system,

$$\begin{aligned}\langle J(\omega)\rangle &= ieV_{\mathrm{SD}}(\omega)\int_0^{\infty}\mathrm{d}t\ e^{i(\omega+i\eta)t} \\ &\quad \sum_m \Big(J_{0,m}N_{m,0}\ e^{i(E_0-E_m)t} - N_{0,m}J_{m,0}\ e^{-i(E_0-E_m)t}\Big), \end{aligned} \tag{B.7}$$

and perform the integration,

$$\begin{aligned}\langle J(\omega)\rangle &= ieV_{\mathrm{SD}}(\omega)\sum_m \Big[J_{0,m}N_{m,0}\frac{e^{i(E_0-E_m+\omega+i\eta)t}}{i(E_0-E_m+\omega+i\eta)} \\ &\quad -N_{0,m}J_{m,0}\frac{e^{-i(E_0-E_m-\omega-i\eta)t}}{-i(E_0-E_m-\omega-i\eta)}\Big]_{t=0}^{\infty} \\ &= -eV_{\mathrm{SD}}(\omega)\sum_m \Big(J_{0,m}N_{m,0}\frac{1}{E_0-E_m+\omega+i\eta} \\ &\quad +N_{0,m}J_{m,0}\frac{1}{E_0-E_m-\omega-i\eta}\Big). \end{aligned} \tag{B.8}$$

Reinserting the matrix elements gives,

$$\begin{aligned}\langle J(\omega)\rangle &= -eV_{\mathrm{SD}}(\omega) \\ &\quad \langle\psi_0|\Big(J\frac{1}{E_0-H_0+\omega+i\eta}N + N\frac{1}{E_0-H_0-\omega-i\eta}J\Big)|\psi_0\rangle \\ &= -eV_{\mathrm{SD}}(\omega) \\ &\quad \langle\psi_0|\Big(J\frac{E_0-H_0+\omega-i\eta}{(E_0-H_0+\omega)^2+\eta^2}N + N\frac{E_0-H_0-\omega+i\eta}{(E_0-H_0-\omega)^2+\eta^2}J\Big)|\psi_0\rangle\,, \end{aligned} \tag{B.9}$$

such that taking the DC limit $\omega \to 0$ and using that the current operator is purely imaginary[1] we can condense this expression,

$$\begin{aligned}\langle J(\omega)\rangle &= -eV_{\mathrm{SD}}(0) \\ &\quad \langle\psi_0| \left(J\frac{-i\eta}{(E_0-H_0)^2+\eta^2}N + N\frac{i\eta}{(E_0-H_0)^2+\eta^2}J\right)|\psi_0\rangle \\ &= -2eV_{\mathrm{SD}}(0)\ \mathrm{Re}\left[\langle\psi_0| J\frac{-i\eta}{(E_0-H_0)^2+\eta^2}N|\psi_0\rangle\right] \\ &= -2eV_{\mathrm{SD}}(0)\ \langle\psi_0| J\frac{-i\eta}{(E_0-H_0)^2+\eta^2}N|\psi_0\rangle\,. \end{aligned} \tag{B.10}$$

Thus the DC electric current is

$$\begin{aligned} I(\omega\to 0) &= -e\big\langle J(0)\big\rangle \\ &= 2e^2V_{\mathrm{SD}}(0)\ \langle\psi_0| J\frac{-i\eta}{(E_0-H_0)^2+\eta^2}N|\psi_0\rangle\,, \end{aligned} \tag{B.11}$$

and reinserting $\hbar$ the DC conductance is

$$g_{JN} = -\frac{e^2}{h}\langle\psi_0| J\frac{4\pi i\eta}{(H_0-E_0)^2+\eta^2}N|\psi_0\rangle\,, \tag{B.12}$$

which is the form used in the DMRG calculations, and where the position of the current operator can be chosen arbitrarily due to current conservation.

Current-current correlator

The derivation of the current-current correlator starts from the expression in Eq. (B.6),

$$\begin{aligned}&\big\langle J(\omega)\big\rangle = ieV_{\mathrm{SD}}(\omega) \\ &\int_0^\infty \mathrm{d}t\ e^{i\omega t}\sum_m \big(J_{0,m}N_{m,0}\ e^{i(E_0-E_m)t} - N_{0,m}J_{m,0}\ e^{-i(E_0-E_m)t}\big),\end{aligned} \tag{B.13}$$

and reinserting the definition of the matrix elements

$$\begin{aligned}\big\langle J(\omega)\big\rangle &= ieV_{\mathrm{SD}}(\omega)\int_0^\infty \mathrm{d}t\ e^{i\omega t} \\ &\quad \sum_m\Big(\langle\psi_0| J|\psi_m\rangle\langle\psi_m| e^{-iH_0t}Ne^{iH_0t}|\psi_0\rangle \\ &\quad - \langle\psi_0| e^{-iH_0t}Ne^{iH_0t}|\psi_m\rangle\langle\psi_m| J|\psi_0\rangle\Big),\end{aligned} \tag{B.14}$$

[1] See App. D for details on the matrix implementation.

such that the time dependence has been transferred to the density operator. Inverting the time axis yields

$$\begin{aligned}\big\langle J(\omega)\big\rangle &= -ieV_{\rm SD}(\omega)\int_0^{-\infty}\mathrm{d}t\; e^{-i\omega t}\\ &\quad\sum_m\Big(\langle\psi_0|\,J\,|\psi_m\rangle\,\langle\psi_m|\,e^{iH_0t}Ne^{-iH_0t}\,|\psi_0\rangle\\ &\quad-\langle\psi_0|\,e^{iH_0t}Ne^{-iH_0t}\,|\psi_m\rangle\,\langle\psi_m|\,J\,|\psi_0\rangle\Big)\\ &= -ieV_{\rm SD}(\omega)\int_0^{-\infty}\mathrm{d}t\; e^{-i\omega t}\big\langle\psi_0\big|[\hat J(0),\hat N(t)]\big|\psi_0\big\rangle. \qquad \text{(B.15)}\end{aligned}$$

Performing a partial integration in t and inserting the convergence factor $e^{\eta t}$ we find

$$\begin{aligned}\big\langle J(\omega)\big\rangle &= -ieV_{\rm SD}(\omega)\Big(\Big[\frac{e^{-i\omega t+\eta t}}{-i\omega}\big\langle\psi_0\big|[\hat J(0),\hat N(t)]\big|\psi_0\big\rangle\Big]_{t=0}^{-\infty}\\ &\quad-\int_0^{-\infty}\mathrm{d}t\;\frac{e^{-i\omega t}}{-i\omega}\big\langle\psi_0\big|[\hat J(0),\hat{\dot N}(t)]\big|\psi_0\big\rangle\Big), \qquad \text{(B.16)}\end{aligned}$$

where the boundary term was neglected, in $t\to-\infty$ because of the convergence factor and at $t=0$ because the ground state is not current carrying. The time derivative of the density operator is[2]

$$\begin{aligned}\partial_t\hat N_L(t) &= i\Big[H_0,\hat N_L(t)\Big]\\ &= -\hat J_L(t), \qquad \text{(B.17)}\end{aligned}$$

where $J_L=-it_L(c^\dagger_{M_L}d_1-\text{h.c.})$, where M_L denotes the first site in the left lead, and d_1 denotes the first site in the transport region. Keeping the positive current direction fixed we have similarly

$$\begin{aligned}\partial_t\hat N_R(t) &= i\Big[H_0,\hat N_R(t)\Big]\\ &= +\hat J_R(t), \qquad \text{(B.18)}\end{aligned}$$

where $J_R=-it_R(c^\dagger_{M_R}d_{M_S}-\text{h.c.})$, where M_S denotes the last site in the transport region, and M_R denotes the first site in the right lead. Hence we find for the density perturbation

$$\begin{aligned}\partial_t\frac{1}{2}(\hat N_L(t)-\hat N_R(t)) &= -\frac{1}{2}(\hat J_L(t)-\hat J_R(t))\\ &= -\hat J_L(t), \qquad \text{(B.19)}\end{aligned}$$

[2]Notice that the current operator is defined such that it matches the density perturbation – hence the 'peculiar' sign of J_L.

where current conservation in steady state was used such that $J_L = -J_R$ with the notation above.[3] In fact the current operator can be placed anywhere in the system for the same reason.

Thus we have

$$\big\langle J(\omega)\big\rangle \;=\; eV_{\rm SD}(\omega)\int_0^{-\infty}\mathrm{d}t\;\frac{e^{-i\omega t}}{\omega}\big\langle\psi_0\big|[\hat{J}(0),\hat{J}(t)]\big|\psi_0\big\rangle, \qquad \text{(B.20)}$$

Inserting once more a complete set of eigenstates for the Hamiltonian we find similarly to the current-density derivation,

$$\begin{aligned}
\big\langle J(\omega)\big\rangle \;&=\; eV_{\rm SD}(\omega)\int_0^{-\infty}\mathrm{d}t\;\frac{e^{-i\omega t}}{\omega}\sum_m\Big(\,\langle\psi_0|\,J\,|\psi_m\rangle\,\langle\psi_m|\,e^{iH_0t}Je^{-iH_0t}\,|\psi_0\rangle\\
&\quad-\langle\psi_0|\,e^{iH_0t}Je^{-iH_0t}\,|\psi_m\rangle\,\langle\psi_m|\,J\,|\psi_0\rangle\,\Big)\\
&=\; eV_{\rm SD}(\omega)\int_0^{-\infty}\mathrm{d}t\;\frac{e^{-i\omega t}}{\omega}\\
&\quad\sum_m\Big(J_{0,m}J_{m,0}\;e^{i(E_m-E_0)t}-J_{0,m}J_{m,0}\;e^{-i(E_m-E_0)t}\Big)\\
&=\;\frac{eV_{\rm SD}(\omega)}{\omega}\\
&\quad\sum_m J_{0,m}J_{m,0}\Big[\frac{e^{i(E_m-E_0-\omega-i\eta)t}}{i(E_m-E_0-\omega-i\eta)}-\frac{e^{-i(E_m-E_0+\omega+i\eta)t}}{-i(E_m-E_0+\omega+i\eta)}\Big]_{t=0}^{-\infty}
\end{aligned} \qquad \text{(B.21)}$$

and inserting the matrix elements again,

$$\begin{aligned}
\big\langle J(\omega)\big\rangle \;&=\; -\frac{eV_{\rm SD}(\omega)}{i\omega}\Big(\,\langle\psi_0|\,J\frac{1}{H_0-E_0-\omega-i\eta}J\,|\psi_0\rangle\\
&\qquad+\langle\psi_0|\,J\frac{1}{H_0-E_0+\omega+i\eta}J\,|\psi_0\rangle\,\Big),
\end{aligned} \qquad \text{(B.22)}$$

where the complete set of states has been pulled out. This expression however has an apparent divergence in the DC limit, and in order to take the DC limit explicitly a first order expansion in ω is performed.

First order expansion

To avoid the numerically troublesome cancelation of $1/\omega$, and take the DC limit explicitly, a first order expansion in ω of the resolvents is performed.

[3] Notice that this *does not* violate current or particle conservation since the current that flows *out of* the left contact has to flow *into* the right contact.

Starting from the resolvents in Eq. (B.22) we find

$$\begin{aligned}\frac{1}{H_0-E_0-\omega-i\eta}+\frac{1}{H_0-E_0+\omega+i\eta} = \\ \frac{1}{H_0-E_0-i\eta}+\frac{1}{H_0-E_0+i\eta} \\ +\Big(\frac{1}{(H_0-E_0-i\eta)^2}-\frac{1}{(H_0-E_0+i\eta)^2}\Big)\omega+\mathcal{O}(\omega^2). \end{aligned} \tag{B.23}$$

The current must be real, and the prefactor in Eq. (B.22) is purely imaginary, so we seek the imaginary part of this expansion. Thus the zero'th order term vanishes as it should such that the current does not diverge in the DC limit, and we are left with the first order contribution, canceling the diverging prefactor,

$$\frac{1}{(H_0-E_0-i\eta)^2}-\frac{1}{(H_0-E_0+i\eta)^2} \;=\; \frac{4i\eta(H_0-E_0)}{((H_0-E_0)^2+\eta^2)^2}, \tag{B.24}$$

such that finally the particle current is

$$\big\langle J(0)\big\rangle \;=\; -eV_{\mathrm{SD}}(0)\,\langle\psi_0|\,J\frac{4\eta(H_0-E_0)}{((H_0-E_0)^2+\eta^2)^2}J\,|\psi_0\rangle\,, \tag{B.25}$$

and the corresponding DC electric current

$$\begin{aligned} I(0) \;&=\; -e\big\langle J(0)\big\rangle \\ &=\; e^2V_{\mathrm{SD}}(0)\,\langle\psi_0|\,J\frac{4\eta(H_0-E_0)}{((H_0-E_0)^2+\eta^2)^2}J\,|\psi_0\rangle\,. \end{aligned} \tag{B.26}$$

Reinserting finally $\hbar$ the DC conductance is

$$g_{JJ} \;=\; \frac{e^2}{h}\,\langle\psi_0|\,J\frac{8\pi\eta(H_0-E_0)}{\big((H_0-E_0)^2+\eta^2\big)^2}J\,|\psi_0\rangle\,, \tag{B.27}$$

which is the form used in the DMRG. It should be noted that also in this case the current operators need not reside on the same link, but can be placed arbitrarily.

B.2 Single particle Greens functions

Here we derive in detail the resolvent formulations for the single particle Greens functions as used in the DMRG setup reviewed in Chap. 2.5. For consistency we use the notation H_0 for the Hamiltonian although these calculations do not rely on a perturbation in voltage and hence only a single Hamiltonian is relevant.

We Fourier transform the real time definitions of the Greens functions and introduce the usual broadening parameter η. The fermionic Greens functions we consider are defined by

$$
\begin{aligned}
G^{>}_{i,j}(t,t') &= -i\big\langle c_i(t)c_j^\dagger(t')\big\rangle, && \text{(B.28a)}\\
G^{<}_{i,j}(t,t') &= i\big\langle c_j^\dagger(t')c_i(t)\big\rangle, && \text{(B.28b)}\\
G^{r}_{i,j}(t,t') &= -i\theta(t-t')\big\langle\big\{c_i(t),c_j^\dagger(t')\big\}\big\rangle, && \text{(B.28c)}\\
G^{a}_{i,j}(t,t') &= i\theta(t'-t)\big\langle\big\{c_i(t),c_j^\dagger(t')\big\}\big\rangle, && \text{(B.28d)}
\end{aligned}
$$

where we use i and j to denote the generic quantum numbers, and where spin is understood but not written explicitly. The notation $\{A,B\} = AB + BA$ denotes the fermionic anticommutator. In the zero temperature limit the average is a ground state average and this is the limit we consider in this work.

Inserting explicitly the time dependence for the retarded Greens function, it can be written as a single matrix exponential,

$$
\begin{aligned}
G^{r}_{i,j}(t,t') &= -i\theta(t-t')\Big(\big\langle\psi_0\big|e^{iH_0t}c_i\,e^{-iH_0t}e^{iH_0t'}c_j^\dagger e^{-iH_0t'}\big|\psi_0\big\rangle\\
&\quad +\big\langle\psi_0\big|e^{iH_0t'}c_j^\dagger e^{-iH_0t'}e^{iH_0t}c_i\,e^{-iH_0t}\big|\psi_0\big\rangle\Big)\\
&= -i\theta(t-t')\Big(\big\langle\psi_0\big|c_i e^{i(E_0-H_0)(t-t')}c_j^\dagger\big|\psi_0\big\rangle\\
&\quad +\big\langle\psi_0\big|c_j^\dagger e^{-i(E_0-H_0)(t-t')}c_i\big|\psi_0\big\rangle\Big), && \text{(B.29)}
\end{aligned}
$$

where it is evident that the Greens function depends only on a single time argument. Hence the single variable Fourier transform is

$$
\begin{aligned}
G^{r}_{i,j}(\omega) &= -i\int_0^\infty \mathrm{d}t\,\Big(\big\langle\psi_0\big|c_i e^{i(E_0-H_0)t}c_j^\dagger\big|\psi_0\big\rangle\\
&\quad +\big\langle\psi_0\big|c_j^\dagger e^{-i(E_0-H_0)t}c_i\big|\psi_0\big\rangle\Big)\,e^{i(\omega+i\eta)t}\\
&= \Big[\big\langle\psi_0\big|c_i\frac{e^{i(E_0-H_0+\omega+i\eta)t}}{i(E_0-H_0+\omega+i\eta)}c_j^\dagger\big|\psi_0\big\rangle\\
&\quad +\big\langle\psi_0\big|c_j^\dagger\frac{e^{-i(E_0-H_0-\omega-i\eta)t}}{-i(E_0-H_0-\omega-i\eta)}c_i\big|\psi_0\big\rangle\Big]_{t=0}^{\infty}\\
&= \big\langle\psi_0\big|c_j^\dagger\frac{1}{H_0-E_0+\omega+i\eta}c_i\big|\psi_0\big\rangle\\
&\quad -\big\langle\psi_0\big|c_i\frac{1}{H_0-E_0-\omega-i\eta}c_j^\dagger\big|\psi_0\big\rangle, && \text{(B.30)}
\end{aligned}
$$

where the broadening, or convergence, parameter η was introduced in the Fourier transform. This is the desired resolvent form of the Greens function, to which the correction vector DMRG is applicable. Note that the advanced

Greens function is obtained by a Hermitian conjugation of the retarded Greens function, and hence needs no further attention.

Similar manipulations apply for the greater Greens function,

$$\begin{aligned} G^{>}_{i,j}(t,t') &= -i\big\langle\psi_0\big|e^{iH_0t}c_i\,e^{-iH_0t}e^{iH_0t'}c_j^\dagger e^{-iH_0t'}\big|\psi_0\big\rangle \\ &= -i\big\langle\psi_0\big|e^{iE_0(t-t')}c_i\,e^{-iH_0(t-t')}c_j^\dagger\big|\psi_0\big\rangle. \end{aligned} \tag{B.31}$$

Using again a single variable Fourier transformation we find that

$$\begin{aligned} G^{>}_{i,j}(\omega) &= -i\int_{-\infty}^{\infty}\mathrm{d}t\ \big\langle\psi_0\big|c_i\,e^{-i(H_0-E_0)t}c_j^\dagger\big|\psi_0\big\rangle\ e^{i\omega t} \\ &= -2\pi i\big\langle\psi_0\big|c_i\,\delta(\omega-H_0+E_0)c_j^\dagger\big|\psi_0\big\rangle, \end{aligned} \tag{B.32}$$

where the δ function was explicitly inserted. Broadening this δ function to an area normalized Lorentzian of width η to incorporate the finite size broadening we find

$$\begin{aligned} G^{>}_{i,j}(\omega) &= -2i\big\langle\psi_0\big|c_i\,\frac{\eta}{(\omega-H_0+E_0)^2+\eta^2}c_j^\dagger\big|\psi_0\big\rangle \\ &= -2i\ \mathrm{Im}\left[\big\langle\psi_0\big|c_i\,\frac{1}{H_0-E_0-\omega-i\eta}c_j^\dagger\big|\psi_0\big\rangle\right], \end{aligned} \tag{B.33}$$

which is once again the desired resolvent form. Notice that the resolvent needed to calculate $G^{>}$ is identical to the resolvent needed to calculate the retarded Greens function in Eq. (B.30).

Similar manipulations for the lesser Greens function yield

$$G^{<}_{i,j}(t,t') = i\big\langle\psi_0\big|e^{-iE_0(t-t')}c_j^\dagger e^{iH_0(t-t')}c_i\,e^{-iH_0t}\big|\psi_0\big\rangle, \tag{B.34}$$

giving the Fourier transform

$$\begin{aligned} G^{<}_{i,j}(\omega) &= i\int_{-\infty}^{\infty}\mathrm{d}t\ \big\langle\psi_0\big|c_i\,e^{i(H_0-E_0)t}c_j^\dagger\big|\psi_0\big\rangle\ e^{i\omega t} \\ &= 2\pi i\big\langle\psi_0\big|c_i\,\delta(\omega+H_0-E_0)c_j^\dagger\big|\psi_0\big\rangle \\ &= -2i\ \mathrm{Im}\left[\big\langle\psi_0\big|c_j^\dagger\frac{1}{H_0-E_0+\omega+i\eta}c_i\big|\psi_0\big\rangle\right]. \end{aligned} \tag{B.35}$$

Notice that also the resolvent needed to calculate $G^{<}$ is identical to the resolvent needed in the evaluation of the retarded Greens function in Eq. (B.30).

Thus we have shown that evaluating the two resolvents,

$$\big\langle\psi_0\big|c_j^\dagger\frac{1}{H_0-E_0+\omega+i\eta}c_i\big|\psi_0\big\rangle, \tag{B.36a}$$

$$\big\langle\psi_0\big|c_i\,\frac{1}{H_0-E_0-\omega-i\eta}c_j^\dagger\big|\psi_0\big\rangle, \tag{B.36b}$$

enables the calculation of retarded, advanced, lesser, and greater single particle Greens functions.

In the DMRG we thus need to target real- and imaginary parts of the resolvents in Eq. (B.36), specifically we target additionally to the ground state the states

$$\big|\mathrm{Re}_1\big\rangle = \frac{H_0 - E_0 + \omega}{(H_0 - E_0 + \omega)^2 + \eta^2} c_i \big|\psi_0\big\rangle, \tag{B.37a}$$

$$\big|\mathrm{Im}_1\big\rangle = \frac{-\eta}{(H_0 - E_0 + \omega)^2 + \eta^2} c_i \big|\psi_0\big\rangle, \tag{B.37b}$$

$$\big|\mathrm{Re}_2\big\rangle = \frac{H_0 - E_0 - \omega}{(H_0 - E_0 - \omega)^2 + \eta^2} c_j^\dagger \big|\psi_0\big\rangle, \tag{B.37c}$$

$$\big|\mathrm{Im}_2\big\rangle = \frac{\eta}{(H_0 - E_0 - \omega)^2 + \eta^2} c_j^\dagger \big|\psi_0\big\rangle, \tag{B.37d}$$

and from those states the resolvents in Eq. (B.36) can be evaluated as,

$$\big\langle\psi_0\big|c_j^\dagger \frac{1}{H_0 - E_0 + \omega + i\eta} c_i \big|\psi_0\big\rangle = \big\langle\psi_0\big|c_j^\dagger\big(\big|\mathrm{Re}_1\big\rangle + i\big|\mathrm{Im}_1\big\rangle\big), \tag{B.38a}$$

$$\big\langle\psi_0\big|c_i \frac{1}{H_0 - E_0 - \omega - i\eta} c_j^\dagger \big|\psi_0\big\rangle = \big\langle\psi_0\big|c_i\big(\big|\mathrm{Re}_2\big\rangle + i\big|\mathrm{Im}_2\big\rangle\big), \tag{B.38b}$$

from which *all* single particle Greens functions can be calculated.

Appendix C

Greens function solution for resonant chains

In this appendix we consider the Greens function calculation of the conductance of a non-interacting resonant M_S site chain coupled to non-interacting tight-binding leads. For clarity we start with a two site chain as this will make the structure of the calculation clear, and then generalize to the case of M_S sites. In both cases we give explicit expressions for the Greens functions needed in the calculation of the DC conductance.

C.1 Resonant 2 site chain

The Hamiltonian of the problem is

$$H_L = -t\sum_{l=1}^{\infty}\left(c_l^\dagger c_{l+1} + \text{h.c.}\right) \tag{C.1a}$$

$$H_R = -t\sum_{r=1}^{\infty}\left(a_r^\dagger a_{r+1} + \text{h.c.}\right) \tag{C.1b}$$

$$H_S = -t_D\left(d_0^\dagger d_1 + \text{h.c.}\right) + \mu_g\left(d_0^\dagger d_0 + d_1^\dagger d_1\right) \tag{C.1c}$$

$$H_T = -t_L\left(d_0^\dagger c_1 + \text{h.c.}\right) - t_R\left(d_1^\dagger a_1 + \text{h.c.}\right) \tag{C.1d}$$

First we consider the time derivative of the left lead number operator to find the particle current out of the left lead,

$$N_L = \sum_{l=1}^{\infty} c_l^\dagger c_l, \tag{C.2}$$

$$I_L = -e\dot{N}_L = -\frac{ie}{\hbar}[H, N_L], \tag{C.3}$$

$$[H, N_L] = \cdots = -t_L[d_0^\dagger c_1 - c_1^\dagger d_0], \tag{C.4}$$

$$I_L = \langle I_L\rangle = \frac{ie}{\hbar}t_L[\langle d_0^\dagger c_1\rangle - \langle c_1^\dagger d_0\rangle]. \tag{C.5}$$

We therefore define Greens functions as

$$G^{<}_{d_0c_1}(t-t') \equiv i\langle c_1^\dagger(t')d_0(t)\rangle, \tag{C.6a}$$
$$G^{<}_{c_1d_0}(t-t') \equiv i\langle d_0^\dagger(t')c_1(t)\rangle. \tag{C.6b}$$

These Greens functions are defined such that

$$\begin{aligned}[G^{<}_{d_0c_1}(t,t)]^* &= [i\langle c_1^\dagger(t)d_0(t)\rangle]^* \\ &= -i\langle d_0^\dagger(t)c_1(t)\rangle = -G^{<}_{c_1d_0}(t,t),\end{aligned} \tag{C.7}$$

and thus the current can be expressed in terms of these functions

$$\begin{aligned}I_L &= \frac{e}{\hbar}t_L[i\langle d_0^\dagger c_1\rangle - i\langle c_1^\dagger d_0\rangle] \\ &= \frac{et_L}{\hbar}[G^{<}_{c_1d_0}(t,t) + G^{<}_{c_1d_0}(t,t)^*] \\ &= \frac{2et_L}{\hbar}\mathrm{Re}G^{<}_{c_1d_0}(t,t) = -\frac{2et_L}{\hbar}\mathrm{Re}G^{<}_{d_0c_1}(t,t).\end{aligned} \tag{C.8}$$

Thus we seek $G^{<}_{d_0c_1}(t-t')$ and therefore consider the corresponding time ordered Greens function $G^{t}_{d_0c_1}(t-t')$. The definition and equation of motion for $G^{t}_{d_0c_1}(t-t')$ is

$$G^{t}_{d_0c_1}(t-t') = -i\langle T\{d_0(t)c_1^\dagger(t')\}\rangle, \tag{C.9}$$
$$-i\partial_{t'}G^{t}_{d_0c_1}(t-t') = -i\langle T\{d_0(t)[H,c_1^\dagger](t')\}\rangle, \tag{C.10}$$

where an equal time average has canceled due to the step functions implicit in the time ordering. The commutator is easily found,

$$\begin{aligned}[H,c_1^\dagger] &= -t[c_1^\dagger c_2 + c_2^\dagger c_1, c_1^\dagger] - t_L[d_0^\dagger c_1 + c_1^\dagger d_0, c_1^\dagger] \\ &= -tc_2^\dagger\{c_1,c_1^\dagger\} - t_L d_0^\dagger\{c_1,c_1^\dagger\} \\ &= -tc_2^\dagger - t_L d_0^\dagger,\end{aligned} \tag{C.11}$$

and thus the EOM is

$$\begin{aligned}-i\partial_{t'}G^{t}_{d_0c_1}(t-t') &= -t(-i\langle T\{d_0(t)c_2^\dagger(t')\}\rangle) - t_L(-i\langle T\{d_0(t)d_0^\dagger(t')\}\rangle) \\ &\equiv -tG^{t}_{d_0c_2}(t-t') - t_L G^{t}_{d_0d_0}(t-t'),\end{aligned} \tag{C.12}$$

and Fourier transformed

$$\omega G^{t}_{d_0c_1}(\omega) = -tG^{t}_{d_0c_2}(\omega) - t_L G^{t}_{d_0d_0}(\omega), \tag{C.13}$$

where two additional Greens functions have been introduced. These Greens functions must be found separately.

C.1.1 Lead Greens function

In this section we derive the EOM for the Greens functions for the leads. Since the left and right leads are identical in the infinitesimal source-drain voltage regime we derive the Greens function for the right lead only,

$$G^t_{d_0a_2}(t-t') \;=\; -i\langle T\{a_2(t)d_0^\dagger(t')\}\rangle. \tag{C.14}$$

Using again the EOM technique repeatedly we find a series of Greens functions

$$\begin{aligned} i\partial_t G^t_{d_0a_2}(t-t') &= -tG^t_{d_0a_1}(t-t') - tG^t_{d_0a_3}(t-t'),\\ i\partial_t G^t_{d_0a_r}(t-t') &= -tG^t_{d_0a_{r-1}}(t-t') - tG^t_{d_0a_{r+1}}(t-t'), \quad r=2,3,\cdots \end{aligned}$$

Fourier transformation gives $i\partial_t \to \omega$

$$\omega G^t_{d_0a_r}(\omega) \;=\; -tG^t_{d_0a_{r-1}}(\omega) - tG^t_{d_0a_{r+1}}(\omega), \quad r=2,3,\cdots$$

Solving this semi-infinite hierarchy gives a continued fraction representation of the Greens function

$$G^t_{d_0a_2}(\omega) \;=\; \frac{-tG^t_{d_0a_1}(\omega)}{\omega - \frac{t^2}{\omega - \frac{t^2}{\omega - \cdots}}}. \tag{C.15}$$

Defining the self-energy as

$$\Sigma(\omega) \;\equiv\; \frac{t^2}{\omega - \frac{t^2}{\omega - \cdots}},$$

we can use the self similarity to express Σ in closed form,

$$\begin{aligned} \Sigma(\omega) &\equiv \frac{t^2}{\omega - \Sigma(\omega)} \Rightarrow\\ \Sigma^2(\omega) - \omega\Sigma(\omega) + t^2 &= 0 \Rightarrow\\ \Sigma(\omega) &= \frac{\omega \pm \sqrt{\omega^2 - 4t^2}}{2}. \end{aligned} \tag{C.16}$$

In the atomic limit $t \to 0$ we expect to find zero self-energy, and hence the only physical solution is

$$\Sigma(\omega) \;=\; \frac{\omega - \sqrt{\omega^2 - 4t^2}}{2}. \tag{C.17}$$

Thus finally

$$G^t_{d_0a_2}(\omega) \;=\; \frac{-tG^t_{d_0a_1}(\omega)}{\omega - \Sigma(\omega)}. \tag{C.18}$$

C.1.2 Chain Greens function

In this section the Greens function for the chain is derived in a similar fashion as the lead Greens function in the previous section. The definition is

$$\begin{aligned} G^t_{d_0d_0}(t-t') &\equiv -i\langle T\{d_0(t)d_0^\dagger(t')\}\rangle \\ &= -i\theta(t-t')\langle d_0(t)d_0^\dagger(t')\rangle + i\theta(t'-t)\langle d_0^\dagger(t')d_0(t)\rangle, \end{aligned} \tag{C.19}$$

giving the EOM

$$\begin{aligned} i\partial_t G^t_{d_0d_0}(t-t') &= \delta(t-t')\langle d_0(t)d_0^\dagger(t')\rangle + \theta(t-t')\langle \partial_t d_0(t)d_0^\dagger(t')\rangle \\ &\quad +\delta(t'-t)\langle d_0^\dagger(t')d_0(t)\rangle - \theta(t'-t)\langle d_0^\dagger(t')\partial_t d_0(t)\rangle \\ &= 1 + i\theta(t-t')\langle [H,d_0](t)d_0^\dagger(t')\rangle - i\theta(t'-t)\langle d_0^\dagger(t')[H,d_0](t)\rangle. \end{aligned}$$

The commutator is

$$\begin{aligned} [H,d_0] &= [H_S,d_0] + [H_T,d_0] \\ &= t_D d_1 - \mu_g d_0 + t_L c_1, \end{aligned} \tag{C.20}$$

and hence

$$\begin{aligned} i\partial_t G^t_{d_0d_0}(t-t') &= 1 + i\theta(t-t')\langle (t_D d_1 - \mu_g d_0 + t_L c_1)(t)d_0^\dagger(t')\rangle \\ &\quad -i\theta(t'-t)\langle d_0^\dagger(t')(t_D d_1 - \mu_g d_0 + t_L c_1)(t)\rangle \\ &= 1 - t_D G^t_{d_0d_1}(t-t') + \mu_g G^t_{d_0d_0}(t-t') \\ &\quad -t_L G^t_{d_0c_1}(t-t') \Rightarrow \\ (i\partial_t - \mu_g)G^t_{d_0d_0}(t-t') &= 1 - t_D G^t_{d_0d_1}(t-t') - t_L G^t_{d_0c_1}(t-t') \Rightarrow \\ (\omega - \mu_g)G^t_{d_0d_0}(\omega) &= 1 - t_D G^t_{d_0d_1}(\omega) - t_L G^t_{d_0c_1}(\omega). \end{aligned} \tag{C.21}$$

Further the EOM for the introduced Greens functions are found similarly

$$\begin{aligned} i\partial_t G^t_{d_0d_1}(t-t') &= \delta(t-t')\langle d_1(t)d_0^\dagger(t')\rangle + i\theta(t-t')\langle [H,d_1](t)d_0^\dagger(t')\rangle \\ &\quad +\delta(t'-t)\langle d_0^\dagger(t')d_1(t)\rangle - i\theta(t'-t)\langle d_0^\dagger(t')[H,d_1](t)\rangle, \end{aligned}$$

where

$$\begin{aligned} [H,d_1] &= [H_S,d_1] + [H_T,d_1] \\ &= t_D d_0 - \mu_g d_1 + t_R a_1 \end{aligned} \tag{C.22}$$

such that

$$\begin{aligned} i\partial_t G^t_{d_0d_1}(t-t') &= i\theta(t-t')\langle (t_D d_0 - \mu_g d_1 + t_R a_1)(t)d_0^\dagger(t')\rangle \\ &\quad -i\theta(t'-t)\langle d_0^\dagger(t')(t_D d_0 - \mu_g d_1 + t_R a_1)(t)\rangle \\ &= -t_D G^t_{d_0d_0}(t-t') + \mu_g G^t_{d_0d_1}(t-t') \\ &\quad -t_R G^t_{a_1d_0}(t-t') \Rightarrow \\ (i\partial_t - \mu_g)G^t_{d_0d_1}(t-t') &= -t_D G^t_{d_0d_0}(t-t') - t_R G^t_{d_0a_1}(t-t') \Rightarrow \\ (\omega - \mu_g)G^t_{d_0d_1}(\omega) &= -t_D G^t_{d_0d_0}(\omega) - t_R G^t_{d_0a_1}(\omega). \end{aligned} \tag{C.23}$$

Finally the lead Greens function is

$$\begin{aligned} i\partial_t G^t_{d_0a_1}(t-t') &= -tG^t_{d_0a_2}(t-t') - t_R G^t_{d_0d_1}(t-t'), \\ \omega G^t_{d_0a_1}(\omega) &= -tG^t_{d_0a_2}(\omega) - t_R G^t_{d_0d_1}(\omega). \end{aligned} \tag{C.24}$$

C.1.3 Solution for time ordered Greens function

Putting together the EOM's of the previous section leads to the solutions

$$G^t_{d_0a_1}(\omega) = \frac{-t_R G^t_{d_0d_1}(\omega)}{\omega - \Sigma(\omega)}, \tag{C.25}$$

$$G^t_{d_0d_1}(\omega) = \frac{-t_D G^t_{d_0d_0}(\omega)}{\omega - \mu_g - \Sigma_R(\omega)}, \tag{C.26}$$

$$G^t_{d_0d_0}(\omega) = \frac{1}{\omega - \mu_g - \Sigma_{d_0d_0}(\omega)}, \tag{C.27}$$

$$G^t_{d_0c_1}(\omega) = -t_L G^t_{d_0d_0}(\omega) g^t_{c_1c_1}(\omega), \tag{C.28}$$

where the self-energies are defined as

$$\Sigma_{L/R}(\omega) = \frac{t^2_{L/R}}{\omega - \Sigma(\omega)}, \tag{C.29}$$

$$\Sigma_{d_0d_0}(\omega) = \frac{t^2_D}{\omega - \mu_g - \frac{t^2_R}{\omega - \Sigma(\omega)}} - \frac{t^2_L}{\omega - \Sigma(\omega)}, \tag{C.30}$$

and where the lead Greens function is

$$g^t_{c_1c_1}(\omega) = \frac{1}{\omega - \Sigma(\omega)}. \tag{C.31}$$

The Greens function $G^t_{d_0c_1}(\omega)$ should be taken to non-equilibrium by analytic continuation.

C.1.4 Analytic continuation and non-equilibrium

The structure of the time ordered Greens function in non-equilibrium is identically the same as in equilibrium, only the times and time ordering are to be taken on the Keldysh contour.

In the equilibrium case we may restate the result as a convolution in time space

$$G^t_{d_0c_1}(\omega) = -t_L G^t_{d_0d_0}(\omega) g^t_{c_1c_1}(\omega) \Rightarrow \tag{C.32}$$

$$G^t_{d_0c_1}(t-t') = -t_L \int dt_1 G^t_{d_0d_0}(t-t_1) g^t_{c_1c_1}(t_1-t'). \tag{C.33}$$

This result can be taken over to the non-equilibrium case by letting all times be on the Keldysh contour $\mathcal{C}$,

$$G^t_{d_0c_1}(\tau,\tau') \;=\; -t_L \int_{\mathcal{C}} d\tau_1 G^t_{d_0d_0}(\tau,\tau_1) g^t_{c_1c_1}(\tau_1,\tau'). \tag{C.34}$$

By using the rules for analytic continuation [27] we can therefore extract the lesser component as

$$G^<_{d_0c_1}(t-t') = -t_L \int dt_1 \\ \Big[G^r_{d_0d_0}(t-t_1) g^<_{c_1c_1}(t_1-t') + G^<_{d_0d_0}(t-t_1) g^a_{c_1c_1}(t_1-t')\Big], \tag{C.35}$$

and using again the Fourier transformation of a convolution we arrive at,

$$G^<_{d_0c_1}(\omega) \;=\; -t_L\Big[G^r_{d_0d_0}(\omega) g^<_{c_1c_1}(\omega) + G^<_{d_0d_0}(\omega) g^a_{c_1c_1}(\omega)\Big]. \tag{C.36}$$

Thus we need to extract lesser, retarded, and advanced parts of the time ordered Greens functions found previously,

$$g^t_{c_1c_1}(\omega) \;=\; \frac{1}{\omega - \Sigma(\omega)}, \tag{C.37}$$

$$G^t_{d_0d_0}(\omega) \;=\; \frac{1}{\omega - \mu_g - \Sigma_{d_0d_0}(\omega)}. \tag{C.38}$$

Lesser component of $g^t_{c_1c_1}$

The leads are assumed to be in local equilibrium, and hence the fluctuation-dissipation theorem applies. Thus the lesser component of the lead Greens function $g^t_{c_1c_1}$ is given simply by

$$g^<_{c_1c_1}(\omega) \;=\; iA(\omega) n^L_F, \tag{C.39}$$

and similarly for the right lead

$$g^<_{a_1a_1}(\omega) \;=\; iA(\omega) n^R_F. \tag{C.40}$$

The spectral function for the leads is given by

$$A(\omega) \;=\; -2\mathrm{Im}\left[g_{11}(\omega)\right], \tag{C.41}$$

where an explicit expression for the Greens function g_{11} is given later in this chapter.

Lesser component of $G^t_{d_0d_0}$

Expanding the fraction before extracting the lesser component, and regrouping the terms gives the lesser component of the Greens function as [27]

$$G^<_{d_0d_0}(\omega) = \frac{1}{\omega-\mu_g-\Sigma^r_{d_0d_0}}\Sigma^<_{d_0d_0}\frac{1}{\omega-\mu_g-\Sigma^a_{d_0d_0}}, \tag{C.42}$$

where we still need to find $\Sigma^<_{d_0d_0}$ using a similar calculation. Writing

$$\Sigma_{d_0d_0} = \frac{t_D^2}{\omega-\mu_g-\Sigma_R}+\frac{t_L^2}{\omega-\Sigma}, \tag{C.43}$$

we have

$$\begin{aligned}\Sigma^<_{d_0d_0} &= t_D^2\frac{1}{\omega-\mu_g-\Sigma^r_R}\Sigma^<_R\frac{1}{\omega-\mu_g-\Sigma^a_R}\\ &\quad +t_L^2\frac{1}{\omega-\Sigma^r}\Sigma^<\frac{1}{\omega-\Sigma^a},\end{aligned} \tag{C.44}$$

where finally we have to find $\Sigma^<_R$,

$$\begin{aligned}\Sigma_R &= \frac{t_R^2}{\omega-\Sigma},\\ \Sigma^<_R &= t_R^2\frac{1}{\omega-\Sigma^r}\Sigma^<\frac{1}{\omega-\Sigma^a}.\end{aligned} \tag{C.45}$$

Lesser component of $\Sigma(\omega)$

$$\begin{aligned}\Sigma(\omega) &\equiv \frac{t^2}{\omega-\frac{t^2}{\omega-\cdots}}\\ &= t^2g^t_{11}(\omega),\end{aligned} \tag{C.46}$$

where $g^t_{11}(\omega)$ is the isolated lead Greens function. Thus we also have

$$\begin{aligned}\Sigma^<(\omega) &= t^2g^<_{11}(\omega)\\ &= it^2A(\omega)n_F(\omega),\end{aligned} \tag{C.47}$$

where n_F is the Fermi function for the lead in question. Inserting finally the spectral function we have

$$\Sigma^<(\omega) = -2it^2\mathrm{Im}\left[g^r_{11}(\omega)\right]n_F(\omega). \tag{C.48}$$

When calculating the isolated lead Greens function an infinitesimal imaginary part should be remembered. Using results from [81] we can write

$$g_{11}(\omega) = \frac{\omega/2t-\mathrm{sign}(\omega)\sqrt{(\omega/2t)^2-1}}{t}, \tag{C.49}$$

where $\omega\to\omega+i\eta$ gives retarded and $\omega\to\omega-i\eta$ gives advanced Greens function.

Note that the symmetric coupling is not a strict requirement, and non-symmetric coupling would result in different lead self-energies.

C.1.5 Current and conductance

Using the expression from Eq. (C.8) we can now express the current through the left contact as

$$\begin{aligned} I_L &= -\frac{2et_L}{\hbar}\mathrm{Re}G^<_{d_0c_1}(t,t) \\ &= -\frac{2et_L}{\hbar}\mathrm{Re}\int\frac{d\omega}{2\pi}G^<_{d_0c_1}(\omega). \end{aligned} \tag{C.50}$$

Collecting the pieces we find

$$G^<_{d_0c_1}(\omega) = -t_L\big[G^r_{d_0d_0}(\omega)g^<_{c_1c_1}(\omega)+G^<_{d_0d_0}(\omega)g^a_{c_1c_1}(\omega)\big], \tag{C.51}$$

and thus

$$I_L = \frac{2et_L^2}{\hbar}\mathrm{Re}\int\frac{d\omega}{2\pi}\big[G^r_{d_0d_0}(\omega)g^<_{c_1c_1}(\omega)+G^<_{d_0d_0}(\omega)g^a_{c_1c_1}(\omega)\big]. \tag{C.52}$$

The current can be symmetrized by noting that in steady state the current flowing out of the right lead must equal minus the current flowing out of the left lead, $I_R=-I_L$, and thus

$$\begin{aligned} I &= \frac{I_L+I_L}{2}=\frac{I_L-I_R}{2} \\ &= \frac{e}{\hbar}\mathrm{Re}\int\frac{d\omega}{2\pi}\big[t_L^2(G^r_{d_0d_0}g^<_{c_1c_1}+G^<_{d_0d_0}g^a_{c_1c_1})-t_R^2(G^r_{d_1d_1}g^<_{a_1a_1}+G^<_{d_1d_1}g^a_{a_1a_1})\big]. \end{aligned} \tag{C.53}$$

Symmetric coupling

Focusing on the case $t_L=t_R\equiv t'$ and using that the lesser Greens function is imaginary we find

$$\begin{aligned} I &= \frac{et'^2}{\hbar}\mathrm{Re}\int\frac{d\omega}{2\pi}\big[-2i(n_F^LG^r_{d_0d_0}-n_F^RG^r_{d_1d_1})\mathrm{Im}\,[g^r_{11}]+(G^<_{d_0d_0}-G^<_{d_1d_1})g^a_{11}\big] \\ &= \frac{et'^2}{\hbar}\int\frac{d\omega}{2\pi}\Big[2\mathrm{Im}\,\big[\big[n_F^LG^r_{d_0d_0}-n_F^RG^r_{d_1d_1}\big]\big]\,\mathrm{Im}\,[g^r_{11}] \\ &\quad -\mathrm{Im}\,\big[G^<_{d_0d_0}-G^<_{d_1d_1}\big]\,\mathrm{Im}\,[g^a_{11}]\Big]. \end{aligned} \tag{C.54}$$

A few tedious calculations using the free particle result, $g^<_{\ell_1\ell_1}=iA(\omega)n_F^i$, where $A(\omega)=-2\mathrm{Im}\,[g^r_{11}]$, $\ell=a/c$, and correspondingly $i=L/R$, yield the results

$$n_F^LG^r_{d_0d_0}-n_F^RG^r_{d_1d_1} = (n_F^L-n_F^R)G^r_{d_0d_0}, \tag{C.55}$$

$$\mathrm{Im}\,\big[G^<_{d_0d_0}-G^<_{d_1d_1}\big] = (n_F^L-n_F^R)t'^2\big|G^r_{d_0d_0}\big|^2A\;t^2\big|g^r_{11}\big|^2\big[-t_D^2\big|G^r_R\big|^2+1\big], \tag{C.56}$$

where the fact that by symmetry the diagonal retarded and advanced Greens functions for the two sites are identical when $t_L = t_R$ has been used, and where the introduced Greens function is

$$G_R^r = \frac{1}{\omega - \mu_g - \Sigma_R^r}. \tag{C.57}$$

Hence the current is

$$\begin{aligned} I &= \frac{2et'^2}{\hbar}\int \frac{d\omega}{2\pi}(n_F^L - n_F^R)\mathrm{Im}\left[g_{11}^r\right] \\ &\quad \left\{\mathrm{Im}\left[G_{d_0d_0}^r\right] + t'^2\left|G_{d_0d_0}^r\right|^2\mathrm{Im}\left[g_{11}^r\right]t^2\left|g_{11}^r\right|^2\left[t_D^2\left|G_R^r\right|^2 - 1\right]\right\}. \end{aligned} \tag{C.58}$$

Now using that in linear response we can expand the difference in Fermi functions as $n_F^L - n_F^R = eV_{\mathrm{SD}}\delta(\omega)$[1] we finally arrive at,

$$\begin{aligned} I &= \frac{e^2}{\hbar}\frac{V_{\mathrm{SD}}t'^2}{2\pi}\mathrm{Im}\left[g_{11}^r\right] \\ &\quad \times\left\{\mathrm{Im}\left[G_{d_0d_0}^r\right] + t'^2\left|G_{d_0d_0}^r\right|^2\mathrm{Im}\left[g_{11}^r\right]t^2\left|g_{11}^r\right|^2\left[t_D^2\left|G_R^r\right|^2 - 1\right]\right\}\Big|_{\omega=0}, \end{aligned} \tag{C.59}$$

and hence the DC conductance

$$\begin{aligned} g &= \frac{I}{V_{\mathrm{SD}}} \\ &= \frac{e^2}{h}t'^2\mathrm{Im}\left[g_{11}^r\right] \\ &\quad \times\left\{\mathrm{Im}\left[G_{d_0d_0}^r\right] + t'^2\left|G_{d_0d_0}^r\right|^2\mathrm{Im}\left[g_{11}^r\right]t^2\left|g_{11}^r\right|^2\left[t_D^2\left|G_R^r\right|^2 - 1\right]\right\}\Big|_{\omega=0}, \end{aligned} \tag{C.60}$$

where we have absorbed a factor of 2π into $\hbar$ to give h.

C.2 Resonant M_S site chain

The generalization of the derivation in the previous chapter to resonant M_S site chains is straight forward, since the overall structure is the same. The leads are unchanged, but the Greens function of the chain is obviously changed. However the change is somewhat trivial, captured by the self-energy build by iteration in R_i,

$$\Sigma_{d_0d_0}(\omega) = \frac{t_D^2}{\omega - \mu_g - \Sigma_{R_{M_S-1}}(\omega)}, \tag{C.61}$$

$$\Sigma_{R_i}(\omega) = \frac{t_D^2}{\omega - \mu_g - \Sigma_{R_{i-1}}(\omega)}, \tag{C.62}$$

$$\Sigma_{R_1}(\omega) = \frac{t_R^2}{\omega - \Sigma(\omega)}, \tag{C.63}$$

[1] Eg. $\int_{-\infty}^{\infty}(n_F^L - n_F^R)g d\omega = \int_{\mu_R}^{\mu_L} g d\omega \approx g(0)(\mu_L - \mu_R) = eV_{\mathrm{SD}}g(0), \quad \mu_L - \mu_R \to 0.$

where $\Sigma(\omega)$ was found in the previous section.

Thus also $G^{<}_{d_0 d_0}$ changes and a nested product of retarded and advanced Greens functions is found. Using the notation

$$G^{r/a}_{d_0 d_0}(\omega) = \frac{1}{\omega - \mu_g - \Sigma^{r/a}_{d_0 d_0}(\omega)}, \tag{C.64}$$

$$G^{r/a}_{R_{i-1}}(\omega) = \frac{1}{\omega - \mu_g - \Sigma^{r/a}_{R_{i-1}}(\omega)}, \tag{C.65}$$

$$g^{r/a}_{11}(\omega) = \frac{1}{\omega - \Sigma^{r/a}(\omega)}, \tag{C.66}$$

we arrive at the expression

$$G^{<}_{d_0 d_0} = G^{r}_{d_0 d_0}\Big(\prod_{i=M_S-1}^{1} t_D^2 G^{r}_{R_i}\Big)\Sigma^{<}_{R}\Big(\prod_{i=1}^{M_S-1} G^{a}_{R_i}\Big)G^{a}_{d_0 d_0}, \tag{C.67}$$

enabling us to use again the same expressions as used in the preceding section,

$$\begin{aligned} g &= \frac{I}{V_{\mathrm{SD}}} \\ &= \frac{e^2}{h} t'^2 \mathrm{Im}\left[g^r_{11}\right] \times \Big\{ \mathrm{Im}\left[G^r_{d_0 d_0}\right] \\ &\quad + t'^2 \left|G^r_{d_0 d_0}\right|^2 \mathrm{Im}\left[g^r_{11}\right] t^2 \left|g^r_{11}\right|^2 \Big[\prod_{i=1}^{M_S-1} \Big| \frac{t_D^2}{\omega - \mu_g - \Sigma_{R_i}} \Big|^2 - 1 \Big] \Big\} \Big|_{\omega=0}. \end{aligned} \tag{C.68}$$

C.2.1 Matlab implementation

The expressions derived in the previous sections have been implemented in Matlab, and the code is given below. A comparison of the exact diagonalization (ED) calculations and Greens function (GF) calculations for the spinless case with parameters $M_S = 7$, $t' = 0.5$, $t_D = 1$, and $t = 1$ is shown in Fig. C.1.

```
% Syntax: [g, mug] = conductance(MS, t, tD, tLR, mug_min, mug_max)
% 't'   = hopping element in leads
% 'tD'  = hopping element within nanostructure
% 'tLR' = weak link hopping element t_L=t_R=tLR
% 'mug_min/max = interval of external potential
% 'mug_min', 'mug_max', 'tLR' are scaled by parameter 't'
function result=conductance(MS, t, tD, tLR, mug_min, mug_max)

Matr_Size = 10001;
mug = linspace(t*mug_min,t*mug_max,Matr_Size);
tLR = t*tLR;
```

```
Sigma_retarded = t^2*GR_isolated_lead(0, t);
Sigma_R_retarded = tLR^2./(-Sigma_retarded);
Sigma_final_retarded(1,:) = ones(1,Matr_Size)*Sigma_R_retarded;

for k=2:1:MS-1
    temp_retarded = tD^2./(-mug-Sigma_final_retarded(k-1,:));
    Sigma_final_retarded(k,:) = temp_retarded;
end

Sigma_d0d0_retarded = tD^2./(-mug-Sigma_final_retarded(MS-1,:)) ...
                      + tLR^2/(-Sigma_retarded);
G_d0d0_retarded = 1./(-mug-Sigma_d0d0_retarded);

prod_abs = t^2*(abs(1./(-mug-Sigma_final_retarded(1,:)))).^2;

for k=2:1:MS-1
    prod_abs = prod_abs*tD^2 ...
               .* (abs(1./(-mug-Sigma_final_retarded(k,:)))).^2;
end

g = 2*tLR^2*(imag(G_d0d0_retarded) ...
   + tLR^2*(abs(G_d0d0_retarded)).^2 ...
   .*(prod_abs-1).*imag(GR_isolated_lead(0, t)) ...
   .*t^2.*(abs(GR_isolated_lead(0, t))).^2 ...
   ).*imag(GR_isolated_lead(0, t));

result = [mug' g'];

function result=GR_isolated_lead(omega, t)

for k=1:1:length(omega)

    if (abs(omega(k)) < 2*t)

        result(k) = 0.5*omega(k)/t^2 ...
                    - i*sqrt(1-0.25*omega(k).^2/t^2)/t;

    elseif (abs(omega(k)) > 2*t)

        result(k) = 0.5*omega(k)/t^2-sign(omega(k)) ...
                    .* sqrt(0.25*omega(k).^2/t^2-1)/t;

    else
        result(k) = 0;
    end
end
```

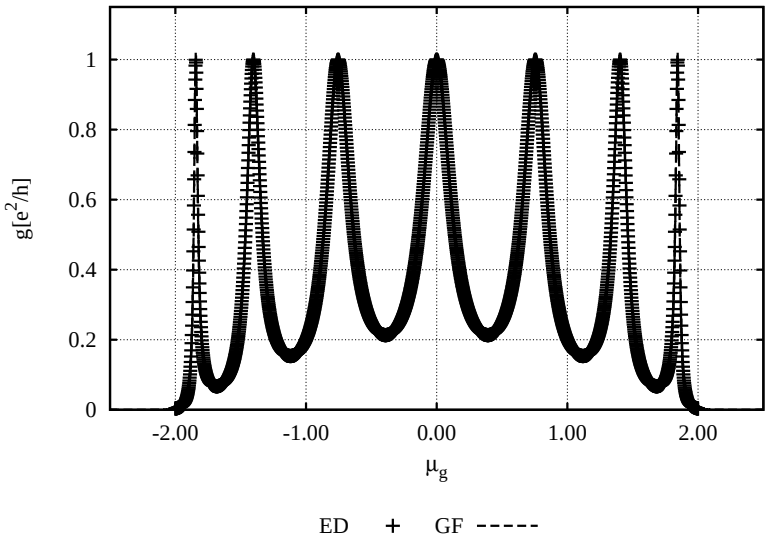

Figure C.1: Comparison of exact diagonalization ('ED') and Greens function ('GF') solution for $M_S = 7$. The parameter values are $t_D = 1$, $t = 1$, $t_L = t_R = 0.5$, and nearest neighbor interaction $V = 0$. The two sets of data are on top of each other, verifying the agreement of the exact diagonalization using the momentum-space setup and the Greens function calculation.

Appendix D

Implementation details

In this chapter we discuss a few implementation details of the `NRG++` code used in this work. We also discuss the hardware requirements, and the calculational time of the different implementations on the machines used in this work.

D.1 Matrix implementations

In the `NRG++` implementation of the DMRG method all matrices are implemented as real, such that the imaginary unit is pulled out explicitly from imaginary components, resulting in real matrices. An example was given in Chap. 2.2.3 where the real and imaginary parts of the correction vectors where targeted explicitly.

Further the implementation of the creation $c_\ell^\dagger$ and annihilation c_ℓ operators are as real matrices, in the site basis give by

$$c_\ell^\dagger = \begin{pmatrix} 0 & 0 \\ 1 & 0 \end{pmatrix}, \tag{D.1a}$$

$$c_\ell = \begin{pmatrix} 0 & 1 \\ 0 & 0 \end{pmatrix}. \tag{D.1b}$$

This in turn implies that operators can be purely real or imaginary, for instance the current operator is defined as

$$J_i = -it_i(c_{i-1}^\dagger c_i - c_i^\dagger c_{i-1}), \tag{D.2}$$

such that when $c_\ell^\dagger$ and c_ℓ are real the current operator is purely imaginary due to the prefactor.

D.2 Extracting results

In the implementation used in this work the results for the targeted quantities are written out during the execution of the code, such that even if the calculation does not finish within the queue limitation of the machine used.

The results vary during the sweeping and the 'correct' values must be extracted. In order to process the large amount of data it is essential to have a (semi) automatic extraction scheme. Each DMRG calculation writes data into separate files, such that a manual extraction is unfeasible. For the calculations presented in Chap. 4 we even have a separate calculation for each spin component, such that we have two output files for each point in a curve.

We use an extraction scheme that searches for a plateau in the extracted physical quantity. By specifying an interval in the sweep for which the extraction should be done – i.e., by sorting away the extreme values in the asymmetric configuration, we can finetune this extraction.

D.3 Real-space leads

The simplest setup uses a real-space representation of the leads. Specifically each lead consists of a tight-binding chain joined with a real-space representation of the Wilson chain. This is done in order to reduce the finite size level splitting as the Wilson chain is exponentially dense around $\varepsilon_F = 0$ for half filling. In this chapter we review a few aspects of the real-space representation for the leads.

D.3.1 Coupling to flat Hamiltonian

In the `NRG++` implementation used we target additionally a flat Hamiltonian – i.e., a homogeneous hopping Hamiltonian, in the initial steps of the DMRG.

This is done to ensure that every site in the system is coupled to the rest of the system via non-vanishing hopping matrix elements, such that there is always a possibility to relax from a given state. Otherwise the system might get trapped in a region of the Hilbert space it cannot get out of due to the lacking coupling. Including this coupling makes the method more stable in the initial sweeps of the method.

After some initial sweeps this coupling is switched off in order to end up with the system targeted in the overall calculation, and a few sweeps are performed to allow the DMRG to converge to this system.

D.3.2 Scaled boundaries

The scaled boundaries, or damped boundary conditions, are introduced to reduce the effect of the hard wall boundary conditions, and provide a better finite size scaling for the leads. The inspiration comes from the hopping Hamiltonian of the Wilson chain. The Wilson chain is exponentially dense around the Fermi edge, and in real-space it corresponds to a tight-binding chain with exponentially damped hopping matrix elements. In the real-

space DMRG setup the leads are modeled by an undamped tight-binding chain joined with a real-space Wilson chain.

The improved finite size scaling due to the scaled boundaries can be traced to two properties; firstly they act as a particle reservoir, since the energy cost of adding or removing a particle from these regions is of the order of the (reduced) hopping elements. Secondly the reduced hopping elements reduce the finite size level splitting at the Fermi energy, hence making possible the use of a much smaller η and reducing the undesired broadening introduced by η.

Using exact diagonalization calculations we have investigated the effect of the scaled boundaries on the finite size level splitting. In Fig. D.1 we have plotted the energy spectrum of the non-interacting system without damping and with exponential damping of varying strengths d, the specific values given in the figure. We damp $M_D = 30$ sites in each lead and the total system size used in this calculation is $M = 150$ sites.

Using a damping factor $d = 1$ corresponds to no damping at all, and the cosine-band is recognized in this case. Turning up the strength of the damping it is apparent from the figure that the spectrum is condensed around $\varepsilon_F = 0$, and for $d = 0.8$ an almost flat dispersion at the Fermi edge is found. This in turn means that the finite size level splitting has been reduced significantly such that now many energy levels are within a small energy window around $\varepsilon_F = 0$ at half filling. This also illustrates why the damped boundary conditions are only effective at exactly half filling, since having a Fermi edge slightly away from $\varepsilon = 0$ would result in a larger level splitting at the Fermi edge.

D.3.3 Interpolation to half filling

When a finite gate potential is applied to the nanostructure the particle number on the structure is changed. As each peak in the conductance spectrum is passed electrons are pushed out of (or pulled into) the nanostructure, hence changing the particle number in the leads.

The discretization scheme used for the leads is only effective around $\varepsilon_F = 0$ corresponding to half filling, as discussed in the previous section. Thus gating the structure inherently pushes the system away from the target of the discretization scheme, hence reducing the accuracy of the calculation.

One way to compensate for this effect is to perform two otherwise identical sets of calculations using different particle numbers, eg. N and $N - 1$, and then interpolate the two sets of results such that the leads are *exactly half filled* [25]. It is important to stress that this is *not* a fitting procedure since there are no free parameters being fitted. It is merely a clever way of keeping the filling in the leads as close to one half as possible.

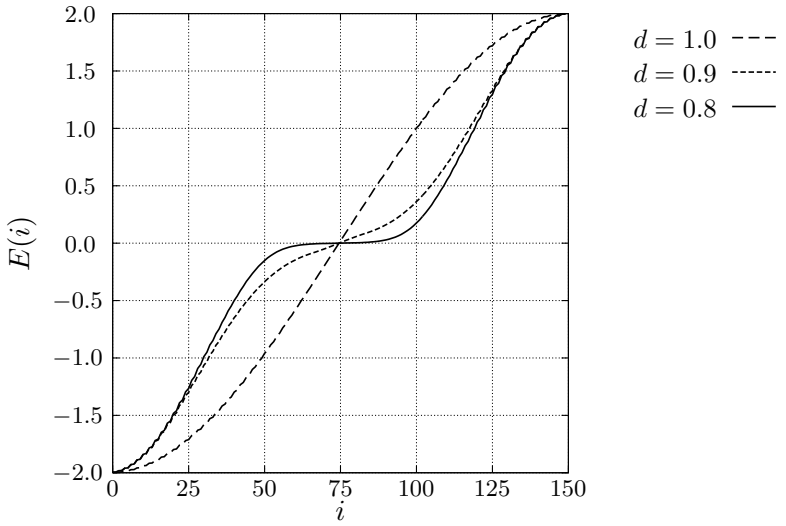

Figure D.1: Plot of the energy spectrum for a non-interacting system with and without scaling of the boundaries, and with the parameters $M_D = 30$ and $M = 150$. The condensation of states around the Fermi level for the half filled system is the rationale for using these boundary conditions in the DMRG.

D.4 Momentum-space leads

D.4.1 Site ordering

The real-space representation for the leads provides a natural ordering of the sites for the DMRG implementation. By contrast the momentum-space representation of the leads does not since it contains long range hopping due to the star configuration, where one site in the real-space part couples to all the momentum-space sites.

Hence there is some degree of freedom in the choice of ordering since the long range hopping anyway blurs the 'natural' ordering. In the implementation used here the layout has been chosen as follows: The real-space part of the setup has been kept entirely in the left block of the DMRG, while both leads have been put in the right block.

With this choice the implementation simplifies since once the left block has been build the DMRG only covers the coupling of the non-interacting leads to the left block, in which the real-space nanostructure is contained. This is naturally only possible if the real-space part of the setup is sufficiently small such that it can be represented exactly. In the real-space setup the density-density interaction also applies between the blocks, which complicates the implementation somewhat.

D.4.2 Preconditioning

When solving linear systems of equations a good preconditioner is essential. Considering a linear set of equations

$$\mathbf{A}x = b, \tag{D.3}$$

the idea of preconditioning is to solve for the 'easy' part of the matrix $\mathbf{A}$ separately, and then afterwards solve the full system.

$$\begin{aligned} \mathbf{A}x &= b, \Rightarrow \\ \mathbf{P}^{-1}\mathbf{A} &= \mathbf{P}^{-1}b, \end{aligned} \tag{D.4}$$

such that one solves for the *preconditioned* matrix $\mathbf{P}^{-1}A$ instead. A good preconditioner fulfills the requirements that the condition number of the preconditioned matrix is smaller than that of the original matrix such that the preconditioned system is easier to solve, the inversion of the preconditioner is fast, and the preconditioner should be cheap to construct. Preconditioning is thus always a matter of a compromise.

We precondition with a Hamiltonian consisting of the separate left and right blocks and the central sites, but *without* the hopping link between them. Hence the Krylov procedure should 'only' take into account the link between these two blocks. This makes the preconditioning somewhat expensive but reduces the memory requirements of the full calculation.

D.4.3 Building up the system

The sites in the momentum-space leads are not equivalent in the sense that they have different energies and couple via different hopping matrix elements. Hence there is a choice to make regarding the labeling, namely in which order do we label the sites within each lead. Or correspondingly, in which order do we build up the system using the infinite lattice algorithm.

In this implementation we can switch between two different schemes. Either we build the lead starting with the sites furthest away from the Fermi edge, or we start with the sites closest to the Fermi edge. In both cases the lead sites are added symmetrically around the Fermi energy, such that the site with energy $\varepsilon_F + \varepsilon$ is added right after the site with energy $\varepsilon_F - \varepsilon$. In the two lead setup the left and right leads are alternated correspondingly.

D.5 Hardware

The DMRG method is a numerically expensive method. It can be viewed as an iterative diagonalization routine seeking an optimally projected Hilbert space. It consists of a number of full diagonalizations of the reduced density matrix of size m and calculations of the ground state (in general target

states) of the Hamiltonian matrix of size $\sim m^2$, where m is the number of retained states in the DMRG. In the calculations presented here a typical number of states is $m = 800$ which illustrates why the DMRG is expensive.

The two implementations of the leads, in real- and momentum-space, have different requirements regarding memory and CPU time. Below we present a few details of typical calculations using these two implementations of the leads.

For both approaches the memory requirement depends on the number of DMRG states kept at each truncation step. Typically 2-4 GB of memory are used in a calculation, depending also on the problem at hand. Most calculations presented in this thesis were performed on computers provided by the Institut für Theorie der Kondensierten Materie[1] (TKM) at Universität Karlsruhe, and in particular using CPU grants of Dr. Peter Schmitteckert.

D.5.1 Real-space leads

As explained in Chap. 2 the real-space implementation of the leads uses a scaling or damping of the boundaries in order to reduce the finite size effects, and this scaling of the boundary is turned on in steps after a full unscaled DMRG calculation. This obviously increases the calculational time needed for the real-space approach compared to a standard non-damped DMRG calculation.

Most of the real-space calculations where performed on the Abacus cluster shared between the Institut für Theorie der Kondensierten Materie (TKM) and the Institut für Theoretische Festkörperphysik[2] (TFP). It is a Linux cluster based on AMD Athlon and Opteron CPU's. Most calculations were performed using the 'long' queue which has an upper limit of 7 days, and occasionally using the 'verylong' queue which is 30 days.

D.5.2 Momentum-space leads

The momentum-space representation of the leads does not rely on a scaling of the boundary to represent the low-energy sector accurately, as the real-space part of the setup couples directly to all momentum-space sites. Therefore this setup is significantly faster, and can address much sharper resonances compared to the real-space setup.

Correspondingly most calculations using the momentum-space setup were performed using the grant of Dr. Peter Schmitteckert on the HP XC4000 of the Scientific Supercomputing Center[3] (SSC) Karlsruhe. The XC4000 has 750 2.6 GHz AMD Opteron quad-core nodes with each 16 GB of memory.

[1] `http://www-tkm.physik.uni-karlsruhe.de/`
[2] `http://www-tfp.physik.uni-karlsruhe.de/`
[3] `http://www.rz.uni-karlsruhe.de/ssck/ssck.php`.

Also the HP XC6000 of the SSC Karlsruhe has been used under the grant of Dr. Schmitteckert. The XC4000 is based on the Itanium 2 dual-core processor, and each thin node has 12 GB of memory. The queue policy of this machine is identical to the XC4000.

Paper A

DMRG evaluation of the Kubo formula
– Conductance of strongly interacting quantum systems

D. Bohr[1,2], P. Schmitteckert[2] and P. Wölfle[2]
[1] MIC – Department of Micro and Nanotechnology, Technical University of Denmark Building 345E, DK-2800 Kgs. Lyngby, Denmark
[2] TKM – Institut für Theorie der Kondensierten Materie, Universität Karlsruhe Wolfgang-Gaede-Str. 1, D-76128 Karlsruhe, Germany
Europhys. Lett., **73** (2), pp. 246-252 (2006)
DOI: 10.1209/epl/i2005-10377-6

Co-author statement

The idea of using the Kubo correlators was due to PW. A first implementation is due to PS. The development of the working scheme including the scaling sweeps is a joint effort of DB and PS. The parameter determination, free fermion comparisons, and Green function benchmarks were done by DB. Interpretation of the results and the writing of the article was a joint effort by all authors.

EUROPHYSICS LETTERS 15 January 2006

Europhys. Lett., **73** (2), pp. 246–252 (2006)
DOI: 10.1209/epl/i2005-10377-6

DMRG evaluation of the Kubo formula —Conductance of strongly interacting quantum systems

D. Bohr[1,2], P. Schmitteckert[2] and P. Wölfle[2]

[1] *MIC - Department of Micro and Nanotechnology, Technical University of Denmark Building 345E - DK-2800 Kgs. Lyngby, Denmark*
[2] *TKM - Institut für Theorie der Kondensierten Materie, Universität Karlsruhe Wolfgang-Gaede-Str. 1, D-76128 Karlsruhe, Germany*

received 8 June 2005; accepted in final form 16 November 2005
published online 9 December 2005

PACS. 73.63.-b – Electronic transport in nanoscale materials and structures.

Abstract. – In this paper we present a novel approach combining linear response theory (Kubo) for the conductance and the Density Matrix Renormalization Group (DMRG). The system considered is one-dimensional and consists of non-interacting tight-binding leads coupled to an interacting nanostructure via weak links. Electrons are treated as spinless fermions and two different correlation functions are used to evaluate the conductance. Exact diagonalization calculations in the non-interacting limit serve as a benchmark for our combined Kubo and DMRG approach in this limit. Including both weak and strong interaction we present DMRG results for an extended nanostructure consisting of seven sites. For the strongly interacting structure a simple explanation of the position of the resonances is given in terms of hard-core particles moving freely on a lattice of reduced size.

Introduction. – During the past decade improved experimental techniques have made production of and measurements on one-dimensional systems possible [1], and hence led to an increasing theoretical interest in these systems. Since its formulation in 1992 [2] the Density Matrix Renormalization Group method (DMRG) has been established as a very powerful, quasi-exact method for numerical calculations of properties of (quasi) one-dimensional systems.

In this paper we present a new approach for calculating linear response conductance for one-dimensional interacting nanostructures coupled to non-interacting tight-binding leads. The method combines Kubo expressions for the conductance with numerical DMRG calculations and is valid for arbitrary interaction strength. It facilitates a unified description of strong and weak interactions and provides conductance directly form a transport calculation, without relying on relations between equilibrium and transport properties.

We employ current-density and current-current correlation functions to calculate the conductance and in the non-interacting case compare to exact diagonalization calculations.

In the strongly interacting limit a simple interpretation of the position of the resonances is given in terms of freely moving hard-core particles on a reduced size lattice [3], and quantitative comparison with numerical DMRG results shows good agreement.

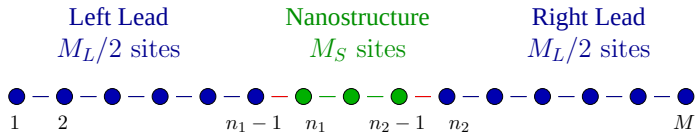

Fig. 1 – One-dimensional interacting nanostructure with M_S sites, coupled to non-interacting tight-binding leads. The total system size is denoted M, the number of lead sites is M_L. The interdot and interlead hopping elements are $t_{\rm Dot}$ and t, respectively, while the contact between the nanostructure and leads are via t_L and t_R.

Model. – We are interested in studying the effect of correlations on transport within a microscopic model of an interacting one-dimensional nanostructure coupled to two non-interacting tight-binding leads, as shown in fig. 1. Electrons are treated as spinless and only nearest-neighbor interaction is considered. The corresponding Hamiltonian is

$$\hat{H}_0 = \hat{H}_{\rm NS} + \hat{H}_{\rm L} + \hat{H}_{\rm C}, \tag{1}$$

$$\hat{H}_{\rm NS} = \sum_{j=n_1}^{n_2-1} U_g c_j^\dagger c_j + \sum_{j=n_1+1}^{n_2-1} \big(- t_{\rm Dot}(c_j^\dagger c_{j-1} + c_{j-1}^\dagger c_j) + V c_j^\dagger c_j c_{j-1}^\dagger c_{j-1}\big), \tag{2}$$

$$\hat{H}_{\rm L} = -t \sum_{i=2}^{n_1-1} (c_i^\dagger c_{i-1} + c_{i-1}^\dagger c_i) - t \sum_{i=n_2+1}^{M} (c_i^\dagger c_{i-1} + c_{i-1}^\dagger c_i), \tag{3}$$

$$\hat{H}_{\rm C} = -t_L(c_{n_1}^\dagger c_{n_1-1} + c_{n_1-1}^\dagger c_{n_1}) - t_R(c_{n_2}^\dagger c_{n_2-1} + c_{n_2-1}^\dagger c_{n_2}) + \\ +\gamma_V V(c_{n_1}^\dagger c_{n_1} c_{n_1-1}^\dagger c_{n_1-1} + c_{n_2}^\dagger c_{n_2} c_{n_2-1}^\dagger c_{n_2-1}). \tag{4}$$

The parameter γ_V controls the smoothing of the interaction on the dot over the contact links as discussed in [4], and U_g is a gate voltage on the structure. In this work we set $t = t_{\rm Dot} = 1$.

Kubo expressions. – Using linear response in applied source-drain voltage, $V_{SD}(t)$, the current is given by

$$\hat{H} = \hat{H}_0 + \delta\hat{H}, \tag{5}$$

$$\langle \tilde{J}_n(t) \rangle = \bar{J} - i \int_{-\infty}^{t} {\rm d}t' \langle \psi_0 | [\tilde{J}_n(t), \delta\tilde{H}(t')] | \psi_0 \rangle, \tag{6}$$

$$\tilde{J}_n(t) = -it_n \big[\tilde{c}_n^\dagger(t)\tilde{c}_{n-1}(t) - \tilde{c}_{n-1}^\dagger(t)\tilde{c}_n(t)\big], \tag{7}$$

where $\hat{H}_0$ is the Hamiltonian in eq. (1), the applied voltage perturbation is $\delta\hat{H}(t) = V_{SD}(t)\hat{N}$, $\tilde{A}(t) = e^{i\hat{H}_0 t}\hat{A}e^{-i\hat{H}_0 t}$ denotes the interaction picture time evolution of the operator $\hat{A}$, and $|\psi_0\rangle$ denotes the ground state. Note that in this approach $\tilde{A}(t)$ contains all correlations of the unbiased structure, since we apply it to the quasi-exact ground state given by the DMRG procedure. The number operator is taken as a symmetric combination of the left and right lead operators, $\hat{N} = \frac{1}{2}(\hat{N}_L - \hat{N}_R)$, and $\bar{J}$ is the equilibrium current included for completeness and henceforth neglected in all numerical calculations.

The Kubo conductance in the DC limit, $g \equiv \frac{e^2}{h}\langle \tilde{J} \rangle / V_{SD}$, can be expressed in terms of two

different correlators,

$$g_{J_j N} = -\frac{e^2}{h}\langle\psi_0|\hat{J}_{n_j}\frac{4\pi i\eta}{(\hat{H}_0-E_0)^2+\eta^2}\hat{N}|\psi_0\rangle, \quad (8)$$

$$g_{JJ} = \frac{e^2}{h}\langle\psi_0|\hat{J}_{n_1}\frac{8\pi\eta(\hat{H}_0-E_0)}{\left[(\hat{H}_0-E_0)^2+\eta^2\right]^2}\hat{J}_{n_2}|\psi_0\rangle, \quad (9)$$

where the positions n_1 and n_2 are defined in fig. 1. Analogous Kubo expressions were used by Louis and Gros in [5], where quantum Monte Carlo calculations for the density-density correlator were performed.

Damped boundary conditions. – To improve the finite-size scaling and to facilitate the use of sufficiently short leads we use exponentially damped boundary conditions, decreasing the hopping elements towards the end of the leads exponentially as shown for the right lead in eq. 10([1]),

$$[-t,\cdots,-t,\underbrace{-t,-t,\cdots,-t}_{M_D}] \rightarrow [-t,\cdots,-t,\underbrace{-td,-td^2,\cdots,-td^{M_D-1},-td^{M_D}}_{M_D}], \quad (10)$$

where $d<1$. The improvement of the finite-size scaling relies on two properties of the DBCs: 1) They allow for use of a smaller η and 2) serve as a particle bath for the nanostructure. The first property is caused by the introduction of exponentially small energy scales in the system thus reducing the finite-size level splitting at the Fermi energy at half-filling. The second property can be understood from the fact that the energy cost of adding or removing a particle from the damped region is of the order of the exponentially small hopping element([2]).

The DBCs introduce two more parameters in the model, the number of damped bonds M_D and the damping factor d, and these must take values such that physical quantities do not depend sensitively on the particular choice.

Numerical calculations. – Before actual numerical calculations can be performed the parameters of the model, M_D, d, and η, must be determined. This is done using exact diagonalization calculations for the non-interacting systems, specifically the resonant value at $U_g = 0$.([3]) For fixed M_D we do indeed find a range of d values that produce essentially identical physical results, indicating the range of validity of the DBCs. Additionally we find that the actual value of M_D is not significant (for reasonably large values) as long as the corresponding value of d is tuned such that the damping at the edge reaches values of the same order of magnitude. The leads used are sufficiently long to keep the damped region separated from the nanostructure, thus allowing Friedel oscillations at the structure edge to decay before reaching the damped region.

The magnitude of the parameter η is bounded by physical arguments; from below by the fact that it should be larger than the finite-size level splitting to allow transport, and from

([1])Modified BCs in connection with DMRG were introduced by Vekic and White in [6] using soft boundary conditions to reduce finite-size effects. Note that exponential damping corresponds to the hopping Hamiltonian in the Numerical Renormalization Group, which models the logarithmic discretization.

([2])In principle properties 1) and 2) of the DBCs could be obtained by using longer non-damped leads. However, these leads would have to be *exponentially long* making such a direct approach impossible.

([3])Considering structures consisting of an odd number of sites has the advantage that the central resonance (by symmetry) remains at $U_g = 0$ for half-filled leads. Due to the bath property of the DBCs it is safe to assume that half-filling is maintained in the parts of the leads that are close to the nanostructure. In contrast, the strongly damped regions act like particle baths and therefore cannot maintain half-filling for non-zero external potential.

above by the broadening of physical results by any finite η, and should thus be much smaller than the width of the resonances we wish to resolve. It is important to note that η is an inherent property of any transport calculation and can only be avoided if one finds a way to obtain transport properties from equilibrium properties.

The conductances in eqs. (8) and (9) are given in terms of ground-state correlators and hence DMRG is directly applicable. To evaluate the correlators we use the correction vector DMRG [7–9] in the zero frequency limit. Calculating, *e.g.*, the correlator in eq. (9) is done by formulating the linear problems,

$$\frac{1}{\hat{H}_0 - E_0 + i\eta}\hat{J}_{n_j}|\psi_0\rangle = |\phi_j\rangle \quad \Rightarrow \quad \hat{J}_{n_j}|\psi_0\rangle = \big[\hat{H}_0 - E_0 + i\eta\big]|\phi_j\rangle, \tag{11}$$

which can be solved for $|\phi_j\rangle$ by a linear solver. Having solved for the correction vector $|\phi_j\rangle$ the conductance is found as the vector overlap,

$$|\phi_j\rangle = |\phi_j^R\rangle + i|\phi_j^I\rangle, \tag{12}$$

$$g_{JJ} = -\frac{8\pi e^2}{h}\langle\phi_1^I|\phi_2^R\rangle. \tag{13}$$

In our DMRG calculations we target apart from the ground state also the real and imaginary parts of the two correction vectors, $|\phi_1\rangle$ and $|\phi_2\rangle$, as well as the states $\hat{N}|\psi_0\rangle$ and $\hat{J}_{n_{1,2}}|\psi_0\rangle$ to ensure that the DMRG basis is suitable for describing the conductance accurately [8, 9].

It should be mentioned that the damped boundary conditions make the convergence rate in numerical calculations much slower. In addition any finite external gate voltage, U_g, changes the particle number in the structure and the excess particles come from the bath property of the DBCs. We therefore face the problem that the damping should be sufficiently strong to provide a reasonable particle bath but at the same time a strong damping decreases the coupling of the highly damped region to the rest of the system. To remedy the slow convergence in the DMRG calculations we turn on the damping in steps and perform several finite system DMRG sweeps for each such damping step. In other words, we perform a complete finite lattice calculation employing typically 11 sweeps and then initiate the scaling sweeps. This allows DMRG to gradually optimize the basis to include the damping in the leads and provides a more gradual decoupling of the damped regions from the rest of the system, thus improving the convergence rate at the cost of more DMRG iterations.

Nevertheless, the resolvent equations, eq. (11), are still ill-conditioned and standard solvers like the Conjugate Gradient Method do not converge. We use instead a preconditioned Davidson-type solver similar to Ramasesha [10] modified with a Gauss-Seidel enhanced block diagonal preconditioner. The DMRG calculations presented in fig. 2 were done using up to $m = 1200$ states. In our DMRG implementation we do not fix the number of states per block to be m but rather fix the dimension of the target space to be at least m^2. In the calculations presented this corresponds to an increase of block states of typically 15%–30%.

Results. – Here we present DMRG and (in the non-interacting limit) exact diagonalization calculations for a single resonant level, fig. 2(a), and a nanostructure consisting of seven sites coupled symmetrically to two non-interacting leads. For the extended structure we present results in the non-interacting limit, fig. 2(b), and for weak and strong interaction, fig. 2(c) and (d).

The spinless single resonant level is generically non-interacting and serves as a testing ground for the approach. The exact result for the conductance in the symmetrically coupled case can be shown to be a Lorentzian of full width $4t'^2$ at half-maximum, where $t' = t_L = t_R$.

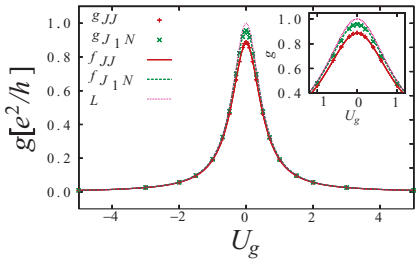

(a) Single resonant level, $M_S = 1$ and $M = 102$. f's denote exact diagonalization results, g's denote DMRG results, and L denotes the exact Lorentzian in the infinite lead limit. The inset shows an enlargement of the resonance peak.

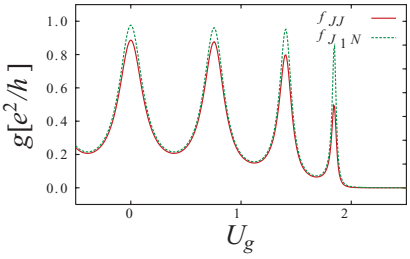

(b) Seven-site nanostructure, $M_S = 7$ and $M = 150$, in the non-interacting limit, $V = 0.0$. Exact diagonalization calculation.

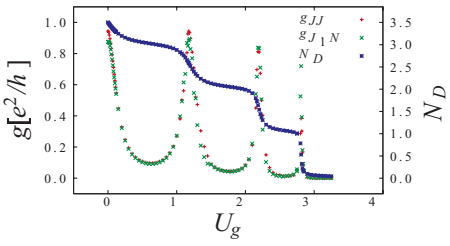

(c) Seven-site nanostructure, $M_S = 7$ and $M = 150$, in the Luttinger-liquid regime, $V = 1.0$.

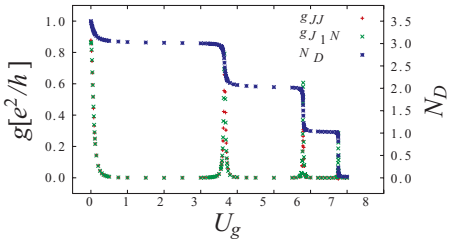

(d) Seven-site nanostructure, $M_S = 7$ and $M = 150$, in the charge density wave regime, $V = 5.0$.

Fig. 2 – Conductance, g, and number of particles on the dot, N_D, *vs.* external potential U_g for a single resonant level and for an extended nanostructure consisting of seven sites. g_{JJ} denotes the current-current correlator, and g_{J_jN} denotes the current-density correlator. The left/right contact hopping elements are $t_{L/R} = 0.5$ and the parameters of the DBCs are $M_D = 30$ and $d = 0.8$. For the calculations above we use $\eta = 1/M_S$. For the interacting spectra notice the offset of resonance positions of the order V as compared to the non-interacting case. The interaction on the nanostructure is smoothed over the contacts with $\gamma_V = 0.5$.

In fig. 2(a) we show exact diagonalization and DMRG calculations for the single resonant level and the two sets are virtually indistinguishable. This verifies that the truncation error introduced by the DMRG is negligible. Furthermore, we have plotted the exact Lorentzian result, and the agreement between the three curves is very good, demonstrating the accuracy of our combined Kubo and DMRG approach.

There is a systematic difference between the current-current and the current-density correlators, specifically close to resonances the current-density correlator generally gives better results. This is due to the additional energy-dependent broadening given by $\hat{H}_0 - E_0$ in the current-current correlator. The opposite is true in the tails where the current-current correlator is more reliable since it is less sensitive to changes of the particle number.

Table I – *Table of peak positions for the $M_S = 7$ site structure with interaction $V = 5, 20, 30$, as predicted by the reduced lattice (RL) model, by exact diagonalization (ED) of the isolated nanostructure, and as found from the conductance peaks in our DMRG calculations. The RL prediction for $N_D = 3$ is not expected to be accurate since the nanostructure is in a localized charge-density-wave–like state. Except for the RL prediction for $V = 5$, $N_D = 3$, all predictions are correct to linear order in t/V.*

V		5			20			30	
N_D	1	2	3	1	2	3	1	2	3
$U_g^{N_D-1\to N_D}$ RL	6.73	5.50	2.76	21.73	20.50	17.76	31.73	30.50	27.76
$U_g^{N_D-1\to N_D}$ ED	6.77	5.88	3.85	21.75	20.63	18.03	31.74	30.59	27.94
$U_g^{N_D-1\to N_D}$ DMRG	6.76	5.79	3.66	21.74	20.59	17.97	31.74	30.60	27.95

In numerical calculations the parameter η is always finite making the expected form of the conductance peaks that of an area-normalized Lorentzian (L_A) of half-width η convoluted with the "bare" physical result. Assuming as a first approximation that the latter is a height-normalized Lorentzian (L_H) of width Γ, the expression for the expected numerical results is of the general form

$$(L_A * L_H)(x) = \frac{\Gamma}{2} \frac{\eta + \Gamma/2}{(x - x_0)^2 + (\eta + \Gamma/2)^2}. \tag{14}$$

To leading order in η the conductance at the resonant level is then given by $g_{\rm res} \approx 1 - 2\eta/\Gamma$, which demonstrates that one needs small η to reach the unitary limit, $g_{\rm res} = 1$. However, η is known from the input and Γ can be extracted from the results. Thus a conductance value on resonance of $1 - 2\eta/\Gamma$ is explained entirely by the broadening by the finite leads and therefore suggests that infinite leads in this case would yield the unitary limit. Our calculations indicate that the peak width is only slightly affected by the interaction on the nanostructure, as long as the nanostructure remains in the Luttinger-liquid regime. However, once the structure is driven into the charge density wave regime the peak width decreases rapidly. A more detailed study of the resonance shapes is considered as future work.

The position of the resonances can be described by the addition spectrum,

$$U_g^{N_D-1\to N_D} \;=\; E_0^{N_D-1} - E_0^{N_D}, \tag{15}$$

where $E_0^{N_D}$ is the energy of the isolated nanostructure occupied by N_D particles. In the large interaction limit the kinetic energy of the particles can be approximated by freely moving fermions on an effective lattice of size $M_S^* = M_S - N_D$. In this approximation one describes the interacting fermions by effective hard-core particles of the size of the interaction range, compare [3, 11]. Thus eq. (15) can be expressed as

$$U_g^{N_D-1\to N_D} \;=\; V + 2t \left(\sum_{n=1}^{N_D} \cos\left(\frac{\pi n}{M_S - N_D} \right) - \sum_{n=1}^{N_D-1} \cos\left(\frac{\pi n}{M_S - (N_D - 1)} \right) \right), \tag{16}$$

where N_D should be small enough that the nanostructure is still in a delocalized state.

In an effective charging model the additional splitting of the levels due to the interaction is linear in the charging interaction V. By contrast, in our microscopic model the interaction leads to an overall *offset* for the non-central peaks, while their mutual *splitting* is governed by the kinetic energy, $\sim t$.

In table I we show a comparison of resonance positions as predicted by the reduced-lattice (RL) model in eq. (16), as predicted by exact diagonalization (ED) of the isolated nanostructure, and resonances found in our DMRG calculations for interaction strengths $V =$ 5, 20, 30. The position of the outermost resonance from $0 \to 1$ particle fits fairly well for both predictions, while the next ones deviate somewhat. The RL prediction for the transition $2 \to 3$ is not expected to be accurate since $N_D = 3$ is a localized charge-density-wave–like state. All exact diagonalization predictions are correct to lowest order in t/V as expected.

Conclusion. – In this work we have presented a new approach for linear conductance calculations of interacting one-dimensional nanostructures, combining linear response for conductance and DMRG. We have benchmarked this new approach against exact diagonalization calculations in the non-interacting case and found excellent agreement, which serves as a real test for the real space DMRG. For the resonant level we also compared our results to the exact Lorentzian result, and found excellent agreement.

For the interacting case we have presented conductance curves for a seven-site nanostructure in both the Luttinger-liquid ($V = 1$) and the charge density wave ($V = 5$) regimes, thus demonstrating the versatility of our approach. We find the largest conductance when the particle number in the structure fluctuates, in agreement with physical intuition.

In the large interaction limit we have shown that a simple picture based on effective hard-core particles moving freely on a reduced size lattice describes the position of the resonances quite well. However, the peak width is strongly decreased by strong interaction.

We expect that further finetuning of the method and numerical parameters will lead to significantly more precise results facilitating calculations for more complicated structures and allow to quantitatively describe resonance peaks for strongly interacting and extended structures.

* * *

This work was performed at TKM, Universität Karlsruhe and we profited from many discussions with colleagues. In particular, we would like to thank F. Evers, G.-L. Ingold, G. Schneider, and R. Werner for their help in clarifying concepts. DB is grateful for the hospitality of TKM during this work. The authors acknowledge the support from the DFG through project B2.10 of the Center for Functional Nanostructures, and from the Landesstiftung Baden-Württemberg under project B710.

REFERENCES

[1] Sohn L. L., Kouwenhoven L. P. and Schön G. (Editors), *Mesoscopic Electron Transport: Proceedings of the NATO Advanced Study Institute* (Kluwer) 1997.
[2] White S. R., *Phys. Rev. Lett.*, **69** (1992) 2863; *Phys. Rev. B*, **48** (1993) 10345.
[3] Gómez-Santos G., *Phys. Rev. Lett.*, **70** (1993) 3780.
[4] Molina R. A., Schmitteckert P., Weinmann D., Jalabert R. A., Ingold G.-L. and Picard J.-L., *Eur. Phys. J. B*, **39** (2004) 107.
[5] Louis K. and Gros C., *Phys. Rev. B*, **68** (2003) 184424.
[6] White S. R. and Vekic M., *Phys. Rev. Lett.*, **71** (1993) 4283; *Phys. Rev. B*, **53** (1996) 14552.
[7] Ramasesha S., *J. Comp. Chem.*, **11** (1990) 545.
[8] Kühner T. D. and White S. R., *Phys. Rev. B*, **60** (1999) 335.
[9] Jeckelmann E., *Phys. Rev. B*, **66** (2002) 45114.
[10] Ramasesha S., Pati S. K., Krishnamurthy H. R., Shuai Z. and Brédas J. L., *Synth. Metals*, **85** (1997) 1019.
[11] Schmitteckert P. and Werner R., *Phys. Rev. B*, **69** (2004) 195115.

Paper B

Strong enhancement of transport by interaction on contact links

D. Bohr[1] and P. Schmitteckert[2]
[1] MIC – Department of Micro and Nanotechnology, Technical University of Denmark Building 345E, DK-2800 Kgs. Lyngby, Denmark
[2] TKM – Institut für Theorie der Kondensierten Materie, Universität Karlsruhe Wolfgang-Gaede-Str. 1, D-76128 Karlsruhe, Germany
Physical Review B **75**, 241103(R) (2007)
DOI: 10.1103/PhysRevB.75.241103

Co-author statement

The initiative for this project was due to PS. The numerics and the writing of the article was a joint collaboration by both authors.

RAPID COMMUNICATIONS

PHYSICAL REVIEW B **75**, 241103(R) (2007)

Strong enhancement of transport by interaction on contact links

Dan Bohr
MIC, Department of Micro- and Nanotechnology, NanoDTU, Technical University of Denmark, DK-2800 Kgs. Lyngby, Denmark

Peter Schmitteckert
TKM, Institut für Theorie der Kondensierten Materie, Universität Karlsruhe, D-76128 Karlsruhe, Germany
(Received 7 March 2007; revised manuscript received 23 May 2007; published 12 June 2007)

Strong repulsive interactions within a one-dimensional Fermi system in a two-probe configuration normally lead to a reduced off-resonance conductance. We show that if the repulsive interaction extends to the contact regions, a strong increase of the conductance may occur, even for systems where one would expect to find a reduced conductance. An essential ingredient in our calculations is a momentum-space representation of the leads, which allows a high energy resolution. Furthermore, we demonstrate that these results are independent of the high-energy cutoff and that the relevant scale is set by the Fermi velocity.

DOI: 10.1103/PhysRevB.75.241103 PACS number(s): 73.63.Kv, 73.23.Hk, 71.10.Pm

I. INTRODUCTION

Constructing a transport theory for strongly correlated systems is one of the major challenges of condensed matter physics. Even though many interesting ideas have been proposed during recent years, no consensus has yet emerged as to the general validity and applicability of the various schemes. With this state of affairs, it is of high importance to establish reliable benchmarks for simple model systems, which then can be used to validate new approaches.

Recently, we presented a method for calculating linear response conductance[1] using the density matrix renormalization group (DMRG) method.[2] A major challenge in this work consisted in minimizing finite-size effects, which was achieved via modified boundary conditions. In this paper, we circumvent these technical problems by reformulating the leads in momentum space. This approach enables us to (i) reach a much higher energy resolution ($\sim 10^{-5}$) and (ii) allows for a greater flexibility in the choice of discretization schemes.

In two recent papers, Mehta and Andrei[3,4] presented nonequilibrium Bethe ansatz results for the interacting resonant-level model (IRLM), where a single spinless level is coupled to a left and a right lead both via a tunneling and a density-density interaction term. However, their work currently excludes the regime of resonant tunneling—i.e., the regime where the conductance is close to unity.[5]

In this work we study the linear conductance of the IRLM on a lattice to provide a benchmark for the universal properties of the model. In addition, we present results for an extended model, where the central region consists of three sites, with a similar interaction as in the IRLM model. As we will show, this model displays the same qualitative behavior as the IRLM. It should be noted that despite its simplicity, the IRLM captures much of the physics of transport through an arbitrary interacting nanostructure provided that only a single level is close to the Fermi energy of the leads, with all other levels well separated and outside the voltage window within which the transport takes place. For perfect coupling, the IRLM model corresponds to the one-dimensional model studied by Vasseur *et al.*[6] and Molina *et al.*,[7] obtained by restricting their nanostructure to a single site. Using the embedding method, they showed that smoothing the ramp of interaction for perfect contacts can compensate for the decrease of transmission due to interaction on the nanostructure. Here we go far beyond the energy resolution attained in previous work and show that interaction on the contact links can lead to strong renormalization effects, enhancing transport beyond the noninteracting system.

II. METHOD AND MODELS

We use the DMRG method to evaluate the linear response conductance of the interacting nanostructure. In previous work,[1] the leads were modeled in *real space* by nearest-neighbor hopping chains. While simple to implement, there are several drawbacks of this method, most prominently the need for "damped boundary conditions" and the resulting problem of trapping of fermions on the Wilson chain (the damped region).[1]

In the present work, we introduce a setup where the leads are described in *momentum space*. Specifically, a short part of the lead close to the nanostructure is represented in real space, accounting for local (i.e., high-energy) physics, while farther away from the nanostructure the lead is represented in momentum space; see Fig. 1. Since the low-energy modes of the momentum leads are now directly coupled to the extended structure (the nanostructure plus additional real-space

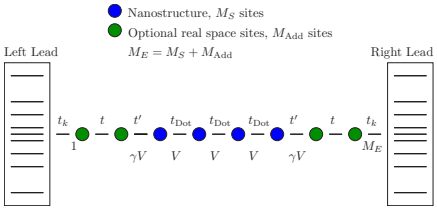

FIG. 1. (Color online) Schematics of the nanostructure extended by real-space sites and attached to momentum-space leads.

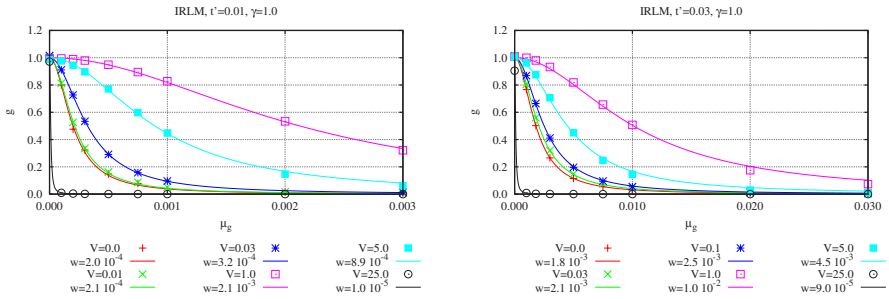

(a) (b)

FIG. 2. (Color online) Conductance versus gate potential for the interacting resonant-level model for a contact hopping of (a) $t'=0.01$ and (b) $t'=0.03$ and contact interaction ranging from zero to 25. To each set of DMRG data, a Lorentzian of half width $2w$ has been added as a guide to the eye. The leads are described with a cosine band between ±2 such that the Fermi velocity is $v_F=2$. In contrast to intradot interaction, the contact interaction enhances the conductance and shows a nonmonotonic behavior versus contact interaction.

sites), as illustrated in Fig. 1, the trapping of fermions on the low-energy sites[1] is avoided and no scaling sweeps are needed. This enables much higher energy resolution, and in the current work we resolve resonances of widths $\mathcal{O}(10^{-5})$.

By virtue of the momentum representation of the leads, the discretization scheme can be chosen arbitrarily to suit the problem at hand. In the present work, we use a logarithmic discretization to cover a large energy range, while switching to a linear discretization for the lowest-energy states in order to describe Fermi-surface physics accurately. The linear discretization on the low-energy scale allows for a better representation of the low-energy physics relevant for transport properties—i.e., excitations created by η.

The models considered in this work are the IRLM and the natural extension of this model to resonant linear chains, defined by the Hamiltonians

$$H_{RS} = \sum_{j\in S} \mu_g \hat{c}_j^\dagger \hat{c}_j - \sum_{j,j-1\in S_E} (t_j \hat{c}_j^\dagger \hat{c}_{j-1} + \text{H.c.}) + \sum_{j,j-1\in S_E} V_j \left(\hat{n}_j - \frac{1}{2}\right)\left(\hat{n}_{j-1} - \frac{1}{2}\right), \quad (1)$$

$$H_{MS} = \sum_{i\in L,R} \epsilon_i \hat{c}_i^\dagger \hat{c}_i, \quad (2)$$

$$H_T = -\left(\sum_{k\in L} t_k \hat{c}_k^\dagger \hat{c}_1 + \sum_{k\in R} t_k \hat{c}_k^\dagger \hat{c}_{M_E}\right) + \text{H.c.}, \quad (3)$$

where $\hat{c}_\ell^\dagger$ and $\hat{c}_\ell$ are the (spinless) fermionic creation and annihilation operators at site ℓ, $\hat{n}_\ell = \hat{c}_\ell^\dagger \hat{c}_\ell$. H_{RS}, H_{MS}, and H_T denote real space, momentum space, and tunneling between real- and momentum-space Hamiltonians, respectively. The symbols S and S_E denote the nanostructure and the extended nanostructure (the full real-space chain), respectively. The indices 1 and M_E denote the first and last sites in S_E. The general setup and the specific values of the hopping matrix elements t_j and the interactions V_j are indicated in Fig. 1, and note specifically the interactions on the contact links, γV. The coupling t_k of the extended real-space structure to the momentum leads is chosen in such a way that in the case of a cosine band it corresponds to a nearest-neighbor hopping chain in real space with a hopping parameter of t. In the following we measure all energies in units of $t=1$.

For a single-site nanostructure and $\gamma=1$ this model reduces to the IRLM. The properties of the leads are defined by the band structure ϵ_k, which can take any form. In this work we use either the cosine band, $\epsilon_k=-2\cos(k)$, or the linear band, $\epsilon_k=2k$. D is a cutoff parameter such that the Fermi velocity $v_F=2$ is kept constant in all work presented here, and the band ranges between energies $-D$ and D. Throughout this work we use the notion of "contact interaction" for interaction on the link between the nanostructure and the leads.

III. RESULTS

The aim of this work is to study the effect of contact interaction. It is known from previous work[1] that strong repulsive interactions within the nanostructure lead to suppression of the transport off resonance due to the formation of a density-wave-like state on the dot.

In Fig. 2, we show results for the conductance versus gate potential for different couplings to the leads and different contact interactions for the IRLM ($\gamma=1$). The calculations have been performed with typically 130 sites in total, $M_E=10$ real-space sites and 120 momentum-space sites. Due to the symmetry of the band, we use a discretization that is symmetric around $\epsilon_F=0$, and further use identical discretization of the two leads. To represent the "large" energy span in the band we use 20 logarithmically scaled sites, and thereafter use 10 linearly spaced sites to represent the low-energy

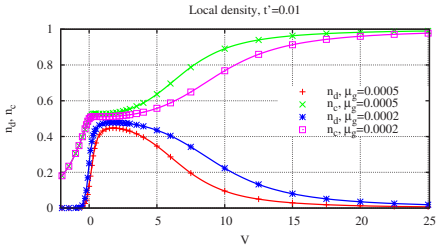

FIG. 3. (Color online) Site occupation n_d of the resonant level and n_c of the real-space sites attached to the level vs the link interaction in the IRLM for $t'=0.01$ and two different gate voltages.

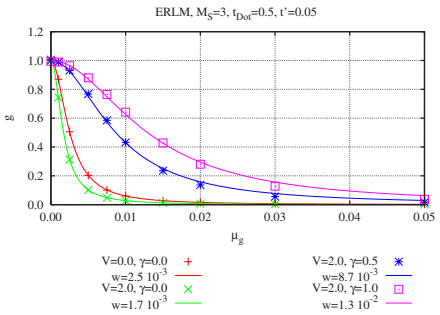

FIG. 4. (Color online) Conductance versus gate potential for a resonant three site chain. To each set of DMRG results a Lorentzian of half width $2w$ has been added as a guide to the eye. The leads are described by a cosine band between ± 2 such that $v_F=2$. The intersite interaction suppresses the transport while the contact interaction is seen to enhance the transport.

scale correctly. In the DMRG calculations presented we used at least 1300 states per block and 10 finite lattice sweeps. To each set of DMRG results in Fig. 2 is added a Lorentzian of half width $2w$ as a guide to the eye.

As the interaction is turned up the width of the resonance is increased far beyond the noninteracting result, up to an order of magnitude larger; e.g., for $t'=0.01$ and $V=1$ the resonance width is increased by a factor of 10. However, for a larger interaction $V>v_F=2$, transport is suppressed, and for very large interactions the width even becomes smaller than the noninteracting resonance. A similar nonmonotonic behavior is observed by Borda *et al.*[8] using a perturbative calculation and is opposite to the one originally reported by Mehta and Andrei,[3] which, however, has been corrected in an erratum.[5] Where preceding work[3–5,8] failed to reach the unitary limit, we demonstrate that indeed the resonant value remains unitary.

Furthermore, by changing the bandwidth D for linear bands we have verified that the relevant energy scale is the *Fermi velocity* v_F of the leads, while the bandwidth D *does not* influence the conductance, as long as $D \gg V$; compare Fig. 5.

Borda *et al.*[8] conclude in their work that "in the case of repulsive interaction the site next to the occupied d level is empty and thus that electron can easily jump to the conduction band," while for attractive interaction fermions accumulate close to the impurity. From that reasoning we would expect an asymmetric conductance curve depending on whether the impurity is filled or depleted. However, this would violate particle-hole symmetry of the model. In Fig. 3, we plot the site occupation n_d of the resonant level and the averaged site occupation n_c of the left and right real-space sites attached to the level. The occupations are plotted versus the contact link interaction for the interacting resonant-level model and for two different gate voltages. The site occupation of the resonant level and the neighboring sites are both enhanced by the repulsive interaction as long as interaction is in the range that enhances the conductance. For stronger interaction the site occupancy of the resonant level is indeed reduced; however, this is the regime where the conductance is reduced. We would like to remark that in the noninteracting case and for a weak contact, $t' \ll 1$, the site occupations of the real-space sites in the leads change only slightly with gate voltage and are all very close to half filling. Thus it seems that the densities of the hybridizing lead levels are *not* the determining quantity for the interaction-induced changes of transport properties.

The strong renormalization of the resonance width and the nonmonotonic behavior is, however, not specific to the IRLM. In Fig. 4, we show results for the center peak of a three-site nanostructure. Without a contact interaction we find that the intradot interaction $V=2.0=4t_{\mathrm{dot}}$ leads to a *suppression* of the transport in agreement with previous results.[1] As in the single-level case already a small contact interaction increases again the width of the resonance at zero gate potential. The enhancement of the conductance by a contact interaction is stronger than the corresponding suppression by the intradot interaction. Therefore, we conjecture that the enhancement of conductance due to the contact interaction is a universal feature, which should also be present in other systems. These findings may also be relevant for disordered structures, where repulsive interaction was found to enhance transport in the case of strong disorder.[9]

Finally, we have considered a non-particle-hole-symmetric IRLM model to address the question of parameter renormalization versus bandwidth cutoff. The non-particle-hole-symmetric model is defined by replacing the $(\hat{n}_j - \frac{1}{2})$ terms in H_{RS} by $\hat{n}_j$. The results are shown in Fig. 5. It is clearly seen from the calculation that varying the cutoff over an order of magnitude does not change the resonance, providing the interaction is *not* cut off by the band. Neither the position nor the width of the resonance peak is influenced by the change of the cutoff D, which is in contrast to the the renormalization group flow that follows from the nonequilibrium Bethe ansatz.[3] There, all transport quantities depend on the cutoff D and the conductance changes with the cutoff. While it is often difficult to compare a field theoretical model, like the IRLM of Mehta and Andrei, with a lattice

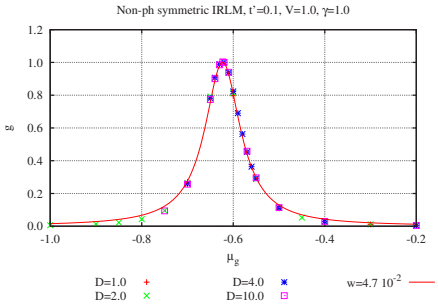

FIG. 5. (Color online) Conductance versus gate potential for a single-site nanostructure without particle-hole symmetry with a contact interaction of $V=1.0$ and a contact hopping of $t'=0.1$ for a linear band with cutoff parameter $D=1.0$, 2.0, 4.0, and 10.0 and constant Fermi velocity, $v_F=2$. The conductance is independent of the cutoff. The solid line is a fit with a Lorentzian of half width $w=4.7\times10^{-2}$.

model, we can at least conclude that the RG flow found in their work is absent in our model with regularized (tight binding) leads and that the relevant energy scale is the Fermi velocity.

IV. SUMMARY

A normal paradigm in transport calculations is to make a principal division between transport region, the nanostructure or "molecule," and leads, where all correlation effects are excluded from the leads.

In this work, we have investigated the influence of an interaction on the contact between a nanostructure and the leads in a simple tight-binding model. Using the nonperturbative DMRG method to evaluate the linear conductance we have demonstrated that a contact interaction significantly influences the transport properties. A repulsive interaction smaller or comparable to the Fermi velocity in the leads enhances the conductance, while a large interaction leads to a suppression of the conductance. Our work shows that even a slight spread of the interaction on the contacts influences the transport strongly. This demonstrates that particular care should be taken in treating the contacts correctly, especially regarding the interaction.

ACKNOWLEDGMENTS

D.B. acknowledges support from the HPC-EUROPA under Project No. RII3-CT-2003-506079, supported by the European Commission. This work also profited from Project 710 of the Landesstiftung Baden-Württemberg and partial support through project B2.10 of the DFG Center for Functional Nanostructures. Parts of the computations were performed on the XC1 and XC2 at the SSC Karlsruhe.

[1] D. Bohr, P. Schmitteckert, and P. Wölfle, Europhys. Lett. **73**, 246 (2006).
[2] S. R. White, Phys. Rev. Lett. **69**, 2863 (1992).
[3] P. Mehta and N. Andrei, Phys. Rev. Lett. **96**, 216802 (2006).
[4] P. Mehta and N. Andrei, arXiv:cond-mat/0702612 (unpublished).
[5] P. Mehta, S. P. Chao, and N. Andrei, arXiv:cond-mat/0703426 (unpublished).
[6] G. Vasseur, D. Weinmann, and R. A. Jalabert, Eur. Phys. J. B **51**, 267 (2006).
[7] R. A. Molina, D. Weinmann, R. A. Jalabert, G.-L. Ingold, and J.-L. Pichard, Phys. Rev. B **67**, 235306 (2003).
[8] L. Borda, K. Vladár, and A. Zawadowski, Phys. Rev. B **75**, 125107 (2007).
[9] R. A. Molina, P. Schmitteckert, D. Weinmann, R. A. Jalabert, G.-L. Ingold, and J.-L. Pichard, Eur. Phys. J. B **39**, 107 (2004).

Bibliography

[1] B. Bransden and C. Joachain, *Quantum Mechanics*. Prentice Hall, 2000.

[2] S. Elliot, *The Physics and Chemistry of Solids*. John Wiley & Sons Inc., 2000.

[3] C. Kittel, *Introduction to Solid State Physics*. John Wiley & Sons Inc., 1996.

[4] M. Tinkham, *Introduction to Superconductivity*. McGraw-Hill Education, 1996.

[5] G. E. Moore, "Cramming more components onto integrated circuits," *Electronics*, vol. 38, 1965.

[6] D. Fedorets, L. Y. Gorelik, R. I. Shekhter, and M. Jonson, "Vibrational instability due to coherent tunneling of electrons," *Europhysics Letters*, vol. 58, no. 1, pp. 99–104, 2002.

[7] N. Neel, J. Kroger, L. Limot, T. Frederiksen, M. Brandbyge, and R. Berndt, "Controlled Contact to a C_{60} Molecule," *Physical Review Letters*, vol. 98, no. 6, p. 065502, 2007.

[8] M. H. Hettler, W. Wenzel, M. R. Wegewijs, and H. Schoeller, "Current collapse in tunneling transport through benzene," *Physical Review Letters*, vol. 90, no. 7, p. 076805, 2003.

[9] R. Stadler, K. Thygesen, and K. Jacobsen, "An ab initio study of electron transport through nitrobenzene: the influence of leads and contacts," *Nanotechnology*, vol. 16, no. 5, pp. 155–160, 2005.

[10] L. P. Kadanoff, "Scaling laws for Ising models near T_c," *Physics 2*, vol. 2, p. 263, 1966.

[11] K. G. Wilson and J. Kogut, "The Renormalization Group and the ϵ Expansion," *Physics Reports*, vol. 12, pp. 75–200, 1974.

[12] K. G. Wilson, "The renormalization group: Critical phenomena and the Kondo problem," *Reviews of Modern Physics*, vol. 47, p. 773, 1975.

[13] F. Anders and A. Schiller, "Real-Time Dynamics in Quantum-Impurity Systems: A Time-Dependent Numerical Renormalization-Group Approach," *Physical Review Letters*, vol. 95, p. 196801, 2005.

[14] I. Peschel, X. Wang, M. Kaulke, and K. Hallberg, *Density-Matrix Renormalization*, vol. 528 of *Lecture Notes in Physics*. Springer, 1999.

[15] S. R. White, "Density matrix formulation for quantum renormalization groups," *Physical Review Letters*, vol. 69, no. 19, pp. 2863–2866, 1992.

[16] S. R. White, "Density-matrix algorithms for quantum renormalization groups," *Physical Review B*, vol. 48, no. 14, pp. 10345–10356, 1993.

[17] K. Hallberg, "Density-matrix algorithm for the calculation of dynamical properties of low-dimensional systems," *Physical Review B*, vol. 52, no. 14, pp. 9827–9830, 1995.

[18] T. D. Kühner and S. R. White, "Dynamical correlation functions using the density matrix renormalization group," *Physical Review B*, vol. 60, p. 335, 1999.

[19] E. Jeckelmann, "Dynamical density-matrix renormalization-group method," *Physical Review B*, vol. 66, p. 045114, Jul 2002.

[20] T. Nishino, "Density matrix renormalization group method for 2d classical models," *Journal of the Physical Society of Japan*, vol. 64, pp. 3598–3601, 1995.

[21] T. Nishino, Y. Hieida, K. Okunishi, N. Maeshima, Y. Akutsu, and A. Gendiar, "Two-dimensional tensor product variational formulation," *Progress of Theoretical Physics*, vol. 105, pp. 409–417, 2001.

[22] S. Yamada, M. Okumura, and M. Machida, "Direct extension of density-matrix renormalization group toward 2-dimensional quantum lattice systems: Studies for parallel algorithm, accuracy, and performance," *arXiv:0707.0159v1*, 2007.

[23] S. R. White and A. E. Feiguin, "Real time evolution using the density matrix renormalization group," *Physical Review Letters*, vol. 93, p. 76399, 2004.

[24] P. Schmitteckert, "Nonequilibrium electron transport using the density matrix renormalization group," *Physical Review B*, vol. 70, p. 121302(R), 2004.

[25] G. Schneider and P. Schmitteckert, "Conductance in strongly correlated 1D systems: Real-Time Dynamics in DMRG," *arXiv:cond-mat/0601389v1*, 2006.

[26] S. L. L., K. L. P., and S. G., eds., *Mesoscopic electron transport: Proceedings of the NATO Advanced Study Institute*. Kluwer, 1997.

[27] H. Haug and A.-P. Jauho, *Quantum kinetics in transport and optics of semiconductors*. Springer series in solid-state sciences, Springer, 1996.

[28] H. Bruus and K. Flensberg, *Many-Body Quantum Theory in Condensed Matter Physics*. Oxford Graduate Texts, Oxford University Press, 2004.

[29] N. S. Wingreen, A.-P. Jauho, and Y. Meir, "Time-dependent transport through a mesoscopic structure," *Physical Review B*, vol. 48, no. 11, pp. 8487–8490, 1993.

[30] N. S. Wingreen and Y. Meir, "Anderson model out of equilibrium: Noncrossing-approximation approach to transport through a quantum dot," *Physical Review B*, vol. 49, pp. 11040–11052, Apr 1994.

[31] S. Kehrein, *The flow equation approach to Many-Particle Systems*, vol. 217 of *Springer Tracts in Modern Physics*. Springer, 2006.

[32] V. Meden, W. Metzner, U. Schollwöck, and K. Schönhammer, "Scaling behavior of impurities in mesoscopic luttinger liquids," *Physical Review B*, vol. 65, p. 045318, 2002.

[33] S. Andergassen, T. Enss, C. Karrasch, and V. Meden, "A gentle introduction to the functional renormalization group: the kondo effect in quantum dots," *Contribution to the Les Houches proceedings 2006*, 2006.

[34] V. Meden and F. Marquardt, "Correlation induced resonances in transport through coupled quantum dots," *Physical Review Letters*, vol. 69, p. 146801, 2006.

[35] J. Favand and F. Mila, "Comparison of tunneling through molecules with mott-hubbard and with dimerization gaps," *The European Physical Journal B*, vol. 2, pp. 293–299, 1998.

[36] O. P. Sushkov, "Conductance anomalies in a one-dimensional quantum contact," *Physical Review B*, vol. 64, p. 155319, Sep 2001.

[37] A. O. Gogolin and N. V. Prokof'ev, "Simple formula for the persistent current in disordered one-dimensional rings: Parity and interaction effects," *Physical Review B*, vol. 50, pp. 4921–4924, Aug 1994.

[38] M. Büttiker, "Four-terminal phase-coherent conductance," *Phys. Rev. Lett.*, vol. 57, pp. 1761–1764, Oct 1986.

[39] R. A. Molina, D. Weinmann, R. A. Jalabert, G.-L. Ingold, and J.-L. Pichard, "Conductance through a one-dimensional correlated system: Relation to persistent currents and the role of the contacts," *Physical Review B*, vol. 67, p. 235306, Jun 2003.

[40] R. A. Molina, P. Schmitteckert, D. Weinmann, R. A. Jalabert, G.-L. Ingold, and J.-L. Pichard, "Residual conductance of correlated one-dimensional nanosystems: A numerical approach," *The European Physical Journal B*, vol. 39, pp. 107–120, 2004.

[41] R. A. Molina, D. Weinmann, and J.-L. Pichard, "Length-dependent oscillations of the conductance through atomic chains: The importance of electronic correlations," *Europhysics Letters*, vol. 67, p. 96, 2004.

[42] C. A. Büsser, G. B. Martins, K. A. Al-Hassanieh, A. Moreo, and E. Dagotto, "Interference effects in the conductance of multilevel quantum dots," *Physical Review B (Condensed Matter and Materials Physics)*, vol. 70, no. 24, p. 245303, 2004.

[43] C. A. Büsser, A. Moreo, and E. Dagotto, "Conductance dip in the kondo regime of linear arrays of quantum dots," *Physical Review B (Condensed Matter and Materials Physics)*, vol. 70, no. 3, p. 035402, 2004.

[44] U. Gerland, J. von Delft, T. A. Costi, and Y. Oreg, "Transmission phase shift of a quantum dot with kondo correlations," *Physical Review Letters*, vol. 84, pp. 3710–3713, Apr 2000.

[45] A. Oguri and A. Hewson, "Nrg approach to the transport through a finite hubbard chain connected to reservoirs," *Journal of the Physical Society of Japan*, vol. 74, pp. 988–996, 2005.

[46] A. Oguri, Y. Nisikawa, and A. C. Hewson, "Determination of the phase shifts for interacting electrons connected to reservoirs," *Journal of the Physical Society of Japan*, vol. 74, no. 9, pp. 2554–2562, 2005.

[47] Y. Nisikawa and A. Oguri, "Numerical renormalization group approach to a quartet quantum-dot array connected to reservoirs: Gate-voltage dependence of the conductance," *Physical Review B (Condensed Matter and Materials Physics)*, vol. 73, no. 12, p. 125108, 2006.

[48] A. Silva, Y. Oreg, and Y. Gefen, "Signs of quantum dot˘lead matrix elements: The effect on transport versus spectral properties," *Physical Review B*, vol. 66, p. 195316, Nov 2002.

[49] R. Peters, T. Pruschke, and F. B. Anders, "Numerical renormalization group approach to green's functions for quantum impurity models,"

Physical Review B (Condensed Matter and Materials Physics), vol. 74, no. 24, p. 245114, 2006.

[50] K. Louis and C. Gros, "Quantum monte carlo simulation for the conductance of one-dimensional quantum spin systems," *Physical Review B*, vol. 68, p. 184424, 2003.

[51] P. Hohenberg and W. Kohn, "Inhomogeneous electron gas," *Physical Review*, vol. 136, pp. B864–B871, Nov 1964.

[52] W. Kohn and L. J. Sham, "Self-consistent equations including exchange and correlation effects," *Physical Review*, vol. 140, pp. A1133–A1138, Nov 1965.

[53] M. Paulsson, T. Frederiksen, and M. Brandbyge, "Inelastic transport through molecules: Comparing first-principles calculations to experiments," *Nano Letters*, vol. 6, no. 2, pp. 258–262, 2006.

[54] P. Schmitteckert and F. Evers, "Exact ground state density functional theory for impurity models coupled to external reservoirs and transport calculations," *arXiv:0706.4253v1*, 2007.

[55] U. Schollwöck, "The density-matrix renormalization group," *Reviews of Modern Physics*, vol. 77, p. 259, 2005.

[56] R. M. Noack and S. R. Manmana, "Diagonalization- and numerical renormalization-group-based methods for interacting quantum systems," vol. 789, pp. 93–163, AIP, 2005.

[57] K. Hallberg, "New trends in density matrix renormalization," *Advances in Physics*, vol. 55, p. 5, 2006.

[58] U. Schollwöck, "Progress in density matrix renormalization: What quantum information is teaching us," *Journal of Magnetism and Magnetic Materials*, vol. 310, pp. 1394–1400, 2007.

[59] S. Ramasesha, "A new algorithm for solving large inhomogeneous linear system of algebraic equations," *J. Comp. Chem.*, vol. 11, pp. 545–547, 1990.

[60] D. Bohr, P. Schmitteckert, and P. Wölfle, "DMRG evaluation of the Kubo formula – Conductance of strongly interacting quantum systems," *Europhysics Letters*, vol. 73, p. 246, 2006.

[61] S. R. White and M. Vekic, "Smooth boundary conditions for quantum lattice systems," *Physical Review Letters*, vol. 71, p. 4283, 1993.

[62] S. R. White and M. Vekic, "Hubbard model with smooth boundary conditions," *Physical Review B*, vol. 53, p. 14552, 1996.

[63] S. Nishimoto, E. Jeckelmann, F. Gebhard, and R. M. Noack, "Application of the density matrix renormalization group in momentum space," *Physical Review B (Condensed Matter and Materials Physics)*, vol. 65, no. 16, p. 165114, 2002.

[64] P. Mehta and N. Andrei, "Nonequilibrium Transport in Quantum Impurity Models: The Bethe Ansatz for Open Systems," *Physical Review Letters*, vol. 96, no. 21, p. 216802, 2006.

[65] P. Mehta, S. Chao, and N. Andrei, "Erratum: Nonequilibrium Transport in Quantum Impurity Models (Bethe-Ansatz for open systems). [Phys. Rev. Lett. 96, 216802 (2006)]," *arXiv:cond-mat/0703426v1*, 2007.

[66] R. Bulla, T. Costi, and T. Pruschke, "The numerical renormalization group method for quantum impurity systems," *arXiv:cond-mat/0701105v1*, 2007.

[67] A.-P. Jauho, N. S. Wingreen, and Y. Meir, "Time-dependent transport in interacting and noninteracting resonant-tunneling systems," *Physical Review B*, vol. 50, no. 8, pp. 5528–5544, 1994.

[68] G. Gómez-Santos, "Generalized hard-core fermions in one dimension: An exactly solvable luttinger liquid," *Physical Review Letters*, vol. 70, p. 3780, 1993.

[69] P. Schmitteckert and R. Werner, "Charge-density-wave instabilities driven by multiple umklapp scattering," *Physical Review B*, vol. 69, p. 195115, 2004.

[70] C. N. Yang and C. P. Yang, "One-dimensional chain of anisotropic spin-spin interactions. i. proof of bethe's hypothesis for ground state in a finite system," *Physical Review*, vol. 150, no. 1, pp. 321–327, 1966.

[71] C. N. Yang and C. P. Yang, "One-dimensional chain of anisotropic spin-spin interactions. ii. properties of the ground-state energy per lattice site for an infinite system," *Physical Review*, vol. 150, no. 1, pp. 327–339, 1966.

[72] C. N. Yang and C. P. Yang, "One-dimensional chain of anisotropic spin-spin interactions. ii. applications," *Physical Review*, vol. 151, no. 1, pp. 258–264, 1966.

[73] P. Schmitteckert, R. A. Jalabert, D. Weinmann, and J.-L. Pichard, "From the fermi glass towards the mott insulator in one dimension: Delocalization and strongly enhanced persistent currents," *Physical Review Letters*, vol. 81, pp. 2308–2311, Sep 1998.

[74] L. Borda, K. Vladar, and A. Zawadowski, "Theory of a resonant level coupled to several conduction-electron channels in equilibrium and out of equilibrium," *Physical Review B*, vol. 75, no. 12, p. 125107, 2007.

[75] D. Bohr and P. Schmitteckert, "Strong enhancement of transport by interaction on contact links," *Physical Review B*, vol. 75, no. 24, p. 241103(R), 2007.

[76] J. König, J. Martinek, J. Barnas, and G. Schön, *Quantum dots attached to ferromagnetic leads: Exchange field, spin precession, and Kondo effect*, vol. 658 of *Lecture Notes in Physics*. Springer Verlag, 2005.

[77] J. N. Pedersen, "Coherent and correlated transport in mesoscopic structures," Master's thesis, Ørsted Laboratory, NBIfAPG, University of Copenhagen, Denmark, 2004.

[78] J. Pedersen, J. Q. Thomassen, and K. Flensberg, "Noncollinear magnetoconductance of a quantum dot," *Physical Review B*, vol. 72, p. 045341, 2005.

[79] A. Aharony and S. Katsumoto, "Focus on interference in mesoscopic systems," *New Journal of Physics*, vol. 9, no. 5, 2007.

[80] I. Weymann and J. Barnas, "Cotunneling through a quantum dot coupled to ferromagnetic leads with noncollinear magnetizations," *The European Physical Journal B*, vol. 46, pp. 289–299, 2005.

[81] D. Bohr, "The Density Matrix Renormalization Group – Applied to mesoscopic structures," Master's thesis, Department of Micro and Nanotechnology, Technical University of Denmark, Denmark, 2004.

[82] A. Rosch, T. A. Costi, J. Paaske, and P. Wölfle, "Spectral function of the Kondo model in high magnetic fields," *Physical Review B*, vol. 68, no. 1, p. 014430, 2003.

[83] M. Andersson, *Numerical Renormalization, Doped Antiferromagnets, and Statistics - Topics in Low Dimensional Physics*. PhD thesis, Department of Theoretical Physics, Chalmers University of Technology, Göteborg University, 2001.

[84] L. Ballentine, *Quantum Mechanics – A Modern Development*. World Scientific, 1999.

[85] R. Landauer, "Electrical resistance of disordered one-dimensional lattices," *Philosophical Magazine*, vol. 57, pp. 863–867, 1970.